DRF

Space Programs Summary No. 37-31, Volume III

for the period November 1, 1964 to December 31, 1964

The Deep Space Network

FACILITY FORM 602
N65-19925 (ACCESSION NUMBER)
105 (PAGES)
CR-57521 (NASA CR OR TMX OR AD NUMBER)
1 (THRU)
07 (CODE)
(CATEGORY)

JET PROPULSION LABORATORY
CALIFORNIA INSTITUTE OF TECHNOLOGY
PASADENA, CALIFORNIA

January 31, 1965

M

GPO PRICE $ _____
OTS PRICE(S) $ _____
Hard copy (HC) $4.00
Microfiche (MF) $0.25

Space Programs Summary No. 37-31, Volume III

for the period November 1, 1964 to December 31, 1964

The Deep Space Network

JET PROPULSION LABORATORY
CALIFORNIA INSTITUTE OF TECHNOLOGY
PASADENA, CALIFORNIA

January 31, 1965

Preface

The *Space Programs Summary* is a six volume, bimonthly publication designed to report on JPL space exploration programs, and related supporting research and advanced development projects. The subtitles of all volumes of the *Space Programs Summary* are:

Vol. I. The Lunar Program (Confidential)

Vol. II. The Planetary–Interplanetary Program (Confidential)

Vol. III. The Deep Space Network (Unclassified)

Vol. IV. Supporting Research and Advanced Development (Unclassified)

Vol. V. Supporting Research and Advanced Development (Confidential)

Vol. VI. Space Exploration Programs and Space Sciences (Unclassified)

The *Space Programs Summary,* Volume VI consists of an unclassified digest of appropriate material from Volumes I, II, and III; an original presentation of the JPL (1) quality assurance and reliability efforts, and (2) environmental- and dynamic-testing facility-development activities; and a reprint of the space science instrumentation studies of Volumes I and II.



W. H. Pickering, *Director*
Jet Propulsion Laboratory

Space Programs Summary No. 37-31, Volume III

Copyright © 1965, Jet Propulsion Laboratory, California Institute of Technology

Prepared under Contract No. NAS 7-100, National Aeronautics & Space Administration

Contents

I. Introduction 1

II. Tracking Stations Engineering and Operations 3
A. Flight-Project Engineering 3
B. Systems Engineering and Integration 4
C. Systems Analysis 13
D. Goldstone Operations 16
E. Canberra 85-ft Antenna Erection 18
References 21

III. Space Flight Operations Facility 22
A. Installation of Orbit Determination Keyboard in the FPAA . . . 22
B. High-Speed Data System 23

IV. RF Systems Development 25
A. S-Band Waveguide Switch Development 25

V. Communications Engineering Developments 29
A. S-Band Implementation for DSIF 29
B. Ground Instrumentation for *Mariner C* Occultation Experiment . . 32
C. Mesa Antenna Range: Anechoic Chamber Facility 32
D. *Mariner C* 100-kw Transmitter 33
Reference 34

VI. Communications Research and Development 35
A. Ground Antennas 35
B. Experimental Closed Cycle Refrigerator for Masers 38
C. Experimental X-Band Lunar Radar Project 40
D. S-Band Planetary Radar Project 56
E. Error Statistics of Inter-DSN Teletype Channels 76
F. Venus Site Operations: Experimental Activities 78
References 85

VII. Advanced Antenna System 86
A. Synopsis 86
B. Static Deflection Test of Instrument Tower to Determine Foundation Modulus 90
C. AAS Elevation Bearing Assemblies 90
D. AAS Elevation Wheel and Primary Reflector Structure 93
E. ½-Scale Model Feed for AAS 99

I. Introduction

The Deep Space Network (DSN) is a precision communication system which is designed to communicate with, and permit control of, spacecraft designed for deep space exploration. The DSN consists of the Deep Space Instrumentation Facility (DSIF), the Space Flight Operations Facility (SFOF), and the DSN Ground Communication System (GCS).

The DSN is a NASA facility, managed by JPL through a contract between NASA and the California Institute of Technology. The Office of Tracking and Data Acquisition is the cognizant NASA office.

It is the policy of the DSN to continuously conduct research and development of new components and systems and to engineer them into the DSN to maintain a state-of-the-art capability.

The DSN has facilities for simultaneously controlling a newly launched spacecraft and a second one already in flight. Within a few months, it will be able to control simultaneously either two newly launched spacecraft plus two in flight, or the operations of four spacecraft in flight at the same time. The DSIF is equipped with 85-ft antennas having gains of 53 db at 2300 Mc and a system temperature of 55°K, making it possible to receive significant data rates at distances as far as the planet Mars. To improve the data rate and distance capability, a 210-ft antenna is under construction at the Goldstone Mars site, and two additional antennas of this size are scheduled for installation at overseas stations.

The DSIF utilizes large antennas, low-noise phase-lock receiving systems, and high-power transmitters located at stations positioned approximately 120 deg around the Earth to track, command, and receive data from deep space probes. Overseas stations are generally operated by personnel of the respective countries. The DSIF stations are:

I.D. No.	Name	Location
11	Goldstone, Pioneer	Goldstone, California
12	Goldstone, Echo	Goldstone, California
13	Goldstone, Venus (R&D)	Goldstone, California
14	Goldstone, Mars (under construction)	Goldstone, California
41	Woomera	Island Lagoon, Australia
42	Canberra (under construction)	Canberra, Australia
51	Johannesburg	Johannesburg, South Africa
59	MTS	Johannesburg, South Africa
61	Madrid (under construction)	Madrid, Spain
71	Spacecraft Monitoring	Cape Kennedy, Florida

The SFOF is located in a three-story building at the Jet Propulsion Laboratory in Pasadena, California, and utilizes operations control consoles, status and operations displays, computers, data processing equipment for analysis of spacecraft performance and space science experiments, and communication facilities to control space flight operations. This control is accomplished by generating trajectories and orbits, and command and control data, from tracking and telemetry data received from the DSIF in near real-time. The SFOF also reduces the telemetry, tracking, command and station performance data recorded by the DSIF into engineering and scientific information for analysis and use by the scientific experimenters and spacecraft engineers.

The DSN Ground Communication System consists of voice, normal and high data rate teletype circuits provided by the NASA World-Wide Communications Network between each overseas station and the SFOF; teletype and voice circuits between the SFOF, Goldstone Stations, and Cape Kennedy; and a microwave link between the SFOF and Goldstone, provided by the DSN.

II. Tracking Stations Engineering and Operations

A. Flight-Project Engineering

1. Surveyor

A full report on the results of the command and data console (CDC)/DSIF compatibility tests has been written by Hughes Aircraft Company; further tests are planned, subject to clarification of DSIF mission support schedules. A prototype interface junction box has been designed and built and is being evaluated before procuring boxes for all *Surveyor* stations. The DSIF/*Surveyor* interface requirements have been updated and expanded and will be issued as the DSN/*Surveyor* interface description, JPL Engineering Planning Document No. 260, covering the entire DSN interface.

The problems arising from *Surveyor* acquisition requirements at DSIF-51 in Johannesburg are being evaluated in detail, and a satisfactory solution is being sought.

2. Pioneer

Integration of the DSIF and *Pioneer* Project ground equipment interfaces has progressed to the point at which cables, connectors, and pin designations are defined, and procurement action on cables and junction boxes has commenced. Also, a revised interface document is being prepared.

The junction boxes will be located at the perimeter of the mission dependent area at each station and will serve to interconnect the standard DSIF cables with the mission dependent cables.

A start has been made toward defining the project's DSIF requirements for compatibility testing to verify the RF and communications interfaces, and to prove the integrity of the spacecraft in the Goldstone spacecraft test facility and at DSIF-71, Cape Kennedy. The project was requested to develop a telecommunications decibel margin control table which is now being reviewed by the DSIF.

3. Lunar Orbiter

A block diagram of the telemetry and command data flow has been finalized and will be used for describing the interface between the DSN and the *Lunar Orbiter* Program.

The DSN/*Lunar Orbiter* interface description document being written will define the electrical and physical characteristics of the interfaces between the DSN and both the spacecraft and ground equipment.

DSIF project personnel are attending design reviews for spacecraft subsystems and ground support equipment to ensure DSN compatibility with the project.

4. Surveyor Dynamic Model AC-5 and -6

Tests to determine compatibility between the *Surveyor* dynamic model transponder and the GSDS S-band system were conducted at the Pioneer site and at Hughes. A draft of the testing program and test results at Goldstone has been prepared.

5. Mariner

Both *Mariner C* and *D* operations were heavily supported during this period. Prior to the actual launchings, all pertinent parameters of the over-all telecommunications system were measured and verified and configurations and operating parameters developed for all stations for each launch.

In addition, acquisition procedures were developed for inclusion in the *Mariner* Tracking Instruction Manual (TIM). These are:

(1) Use of nominal predictions in initial acquisition procedures.

(2) Use of servo monitor scope in initial acquisition procedures.

(3) Initial acquisition for L-S band station configuration.

(4) Initial acquisition for S-band station configuration.

(5) Nonstandard initial acquisition procedure.

(6) Procedure for transfer of transmitter from S-band acquisition aid (SAA) to S-band Cassegrain monopulse feedhorn and bridge system (SCM).

(7) Procedure for transferring spacecraft tracking from one station to another.

(8) Ranging acquisition procedure (preliminary).

Post-mission analysis of DSIF performance during the first launch was carried out and resulted in improvement in the following areas:

(1) Development of a technique for avoiding the possibility of lock onto a spacecraft telemetry sideband.

(2) Modifications to the servoamplifier circuit to prevent blocking due to saturation under conditions of large errors and low signal level.

(3) Analysis of RF carrier suppression due to telemetry power in the limiter passband.

(4) Theoretical analysis of expected up-link acquisition times.

(5) Development of nonstandard acquisition techniques, using specified beam search patterns.

Continuous RF advisor support was provided during the critical portion of the second mission, and a preliminary report containing a detailed analysis of the first 15 hr of the mission has been published.

6. Ranger

Those portions of the *Ranger* documents pertaining to systems engineering considerations were reviewed and were updated where necessary, in preparation for the forthcoming *Ranger* 8 and 9 missions.

B. Systems Engineering and Integration

1. Spacecraft Monitoring Station

Ground has been broken at Cape Kennedy and construction work is under way for the permanent spacecraft monitoring station, DSIF-71. The site has been cleared and forms are in place for the underfloor plenum of the control building and the floor of the generator room.

2. Spacecraft Test Facility

Proposals for the construction of the Phase II version of the spacecraft test facility at Goldstone are being studied. The enclosure will be expanded to $28 \times 28 \times 20$ ft in order to accommodate the *Surveyor* and *Lunar Orbiter* spacecrafts. The enlarged facility is expected to be occupied in May, 1965.

3. JPL Engineering Planning Document No. 256

Progress on the two-volume technical description of the DSIF has been reported previously in JPL Technical Memorandum No. 33-26, now identified as JPL Engineering Planning Document No. 256, Vol. II, which describes the DSIF subsystems. Manuscript copies of 11 of the 14 sections comprising Vol. II have been reviewed, and repro typing is now in progress. Vol. I, which describes the over-all DSIF System, is also in preparation.

4. First Pass Acquisition Procedure Tests

a. Purpose. The tests described herein were made to develop and prove an acquisition procedure which would achieve the following objectives in the shortest possible time after a spacecraft appears above the local horizon.

(1) Good two-way doppler data condition.

(2) Good telemetry data condition.

(3) Good angle data above 10-deg elevation angle.

b. Procedure. The helicopter carrying a standard DSIF transponder was instructed to fly a special flight profile which resulted in an angular tracking rate at the DSIF of approximately 0.05 deg/sec, and to repeat this course 500 or 1000 ft to the east or west of a predetermined "on line" course as instructed. The "on line" course corresponded to the nominal predicted spacecraft track over the station, and 500 and 1000 ft corresponded to approximately 5.5 and 11 deg relative to this line at the horizon.

On several of the runs, the "apparent" frequency received from and sent to the transponder was biased to provide the operators with an opportunity for searching for a new frequency on each run.

A time bias was also introduced on some of the runs where Event A was called prior to the actual occurrence of first visibility. Transponder AGC voltage was called by the pilot immediately as up-link lock was obtained. The acquisition procedure followed by the DSIF operators is shown in Table 1.

The tracking data handling subsystem and the analog portion of the station instrumentation subsystem recorded all of the station performance data required to evaluate the acquisition time under the various conditions of the test.

c. Test results summary. The time in seconds from first visibility to Events B, C, D, and E for all runs is shown in Fig. 1.

Table 1. Spacecraft acquisition procedure

Step	Action	Event	Notes
1	Antenna points to 10 deg above local horizon in the "on line" direction.		Receiver 1 on SCM Receiver 2 on SAA Transmitter on SAA BW: R1; R2 — AGC: 1.18 cps; 4.5 cps — T/M: 4.5 kc; 20 kc — Loop: 48 cps; 152 cps
2	Aircraft first visibility.	A	
3	Receiver 2 on SAA searches frequency window and locks down-link.	B	
4	Transmitter is turned on SAA. Exciter VCO searches frequency window and locks up-link.	C	Receiver 2 will lose lock.
5	Receiver 2 on SAA searches window and relocks the up-link.	D	Good doppler data is now received.
6	Receiver operator presses GOOD DATA switch.		
7	Servo operator selects AUTO TRACK SAA when spacecraft crosses +10-deg line on servo monitor scope.	E	Servo in high-speed integrator BW = 0.2 cps. Immediately after Event D, position of spacecraft relative to beam axes visible on servo operator's scope.
8	R1 on SCM searches frequency window and locks down-link also.	F	This can be done immediately after Event D. Set integrator BW = 0.6 cps.
9	Servo operator selects AUTO TRACK SCM.	G	When R1 AGC is 2.5 v above R2 AGC.
10	Servo operator presses GOOD ANGLE DATA switch.	H	Press when good auto tracking on SCM is achieved.

Table 2. Runs and events achieved

Run	Events achieved	Run	Events achieved
1	B	16	B, E
2	B	17	B, C, D, E
3	B	18	B, C, D, E
4	B, C, D, E	19	B, C, D, E
5	B, C, D, E	20	B, C, D, E
6	B, C, D, E	21	This run aborted because of premature turn-on of transmitter
7	B, C, D, E		
8	B, C, D, E		
9	B, C, D, E		
10	B, C, D, E	22	B
11	B, C, D, E	23	B, E
12	B	24	B, C, D, E
13	B, C, D, E	25	B, C, D, E
14	B	26	B, C, D, E
15	B	27	B, C, D, E

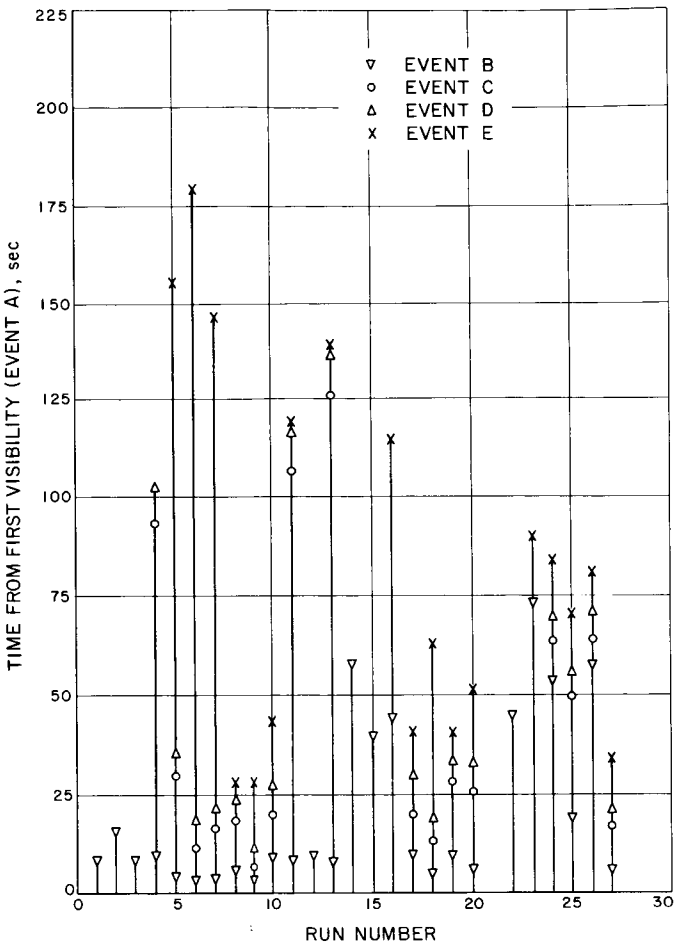


Fig. 1. Time from first visibility to various events

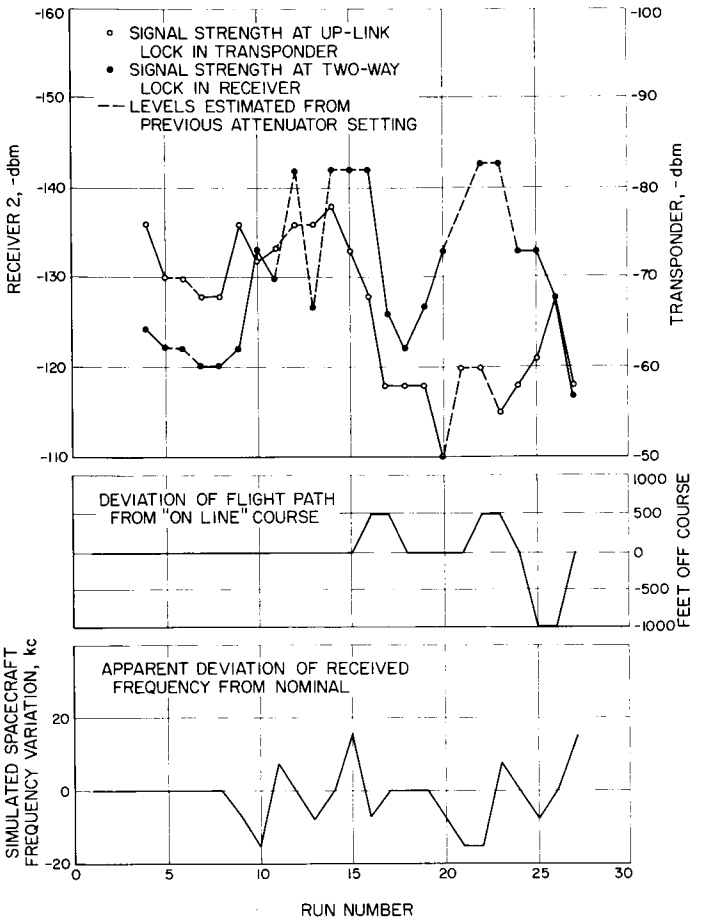


Fig. 2. Parameter variation versus run number

Event B is Receiver 2 on SAA in one-way lock (downlink).

Event C is transmitter on SAA in one-way lock (uplink).

Event D is Receiver 2 on SAA in two-way lock.

Event E is Receiver 1 on SCM in one-way lock (downlink).

These results are summarized in Table 2.

The signal levels into the transponder input[1] and DSIF receiver are shown in Fig. 2, together with the flight path and apparent received frequency deviations for each run.

In the following evaluation of each run, reference is made to Fig. 2 for parameter variation.

[1]The loss between the transponder input connector and the actual receiver is 22 db. Thus, the up-link receiver levels are actually 22 db lower than the input levels given in Fig. 2.

Considering first those runs on which only Event B was achieved:

Runs 1, 2	During these runs, severe leakage between the 50-Mc cables from antenna cage to control building caused receiver malfunction.
Run 3	Signal levels to and from the transponder were probably too low, judged by subsequent performance.
Run 12	Signal strength into transponder was too low.
Runs 14, 15, 16	Signal strength into receiver was probably too low (estimated −142 dbm), although contributing factors could have been flight path and frequency deviations.
Run 21	This run was aborted because of procedural confusion caused by the premature turn-on at DSIF transmitter.

Run 22 Signal strength into the transponder was high (estimated −50 dbm) and flight path was approximately 5 deg E, but the major factor was probably the apparent deviation of the transponder–receiver frequency from nominal (−15 kc). It appears that the exciter operator was, therefore, unable to locate the transponder–receiver frequency in the frequency window.

Run 23 Signal strength into the transponder was high (estimated −55 dbm) and flight path was normal. Transponder–receiver frequency deviation was +7.5 kc. It is, therefore, concluded that the exciter operator was unable to locate the transponder–receiver frequency as in Run 22.

Considering the remaining 17 runs, the following observations are evident from the data given in Figs. 1 and 2.

(1) Two-way lock (D) was established in all cases as:
Minimum time: 12 sec
Maximum time: 136 sec
Average time: 50 sec

(2) On Runs 4–10, Receiver 1 lock (E) was not attempted until after auto track on SAA (F). On subsequent runs, the operator was instructed to lock R1 as soon after Event D as possible. Except on Run 16, where the signal strength was very low, R1 was locked up, typically 10–15 sec after Event D.

(3) On all except Run 13, the signal strength at the transponder input was −76 dbm or greater, and the signal strength at the receiver input was −133 dbm or greater. When either or both signal strengths were less than this value, two-way lock was not achieved. This point is illustrated in Fig. 3, where a datum line has been drawn at the above signal levels. Points well below the datum correspond to short acquisition times, while points near the datum generally have long acquisition times. Acquisition was not achieved in those cases when either up-link or down-link signal levels were above the line.

(4) On Runs 24, 25, and 26 the time bias referred to in paragraph (1) was removed before the acquisition point was plotted in Fig. 3. The conformity at the resulting two-way lock times to the general pattern is evident.

(5) The acquisition times do not show any obvious dependence on flight path variations. Any effect due to flight path is probably reflected in the signal strength relationships described above.

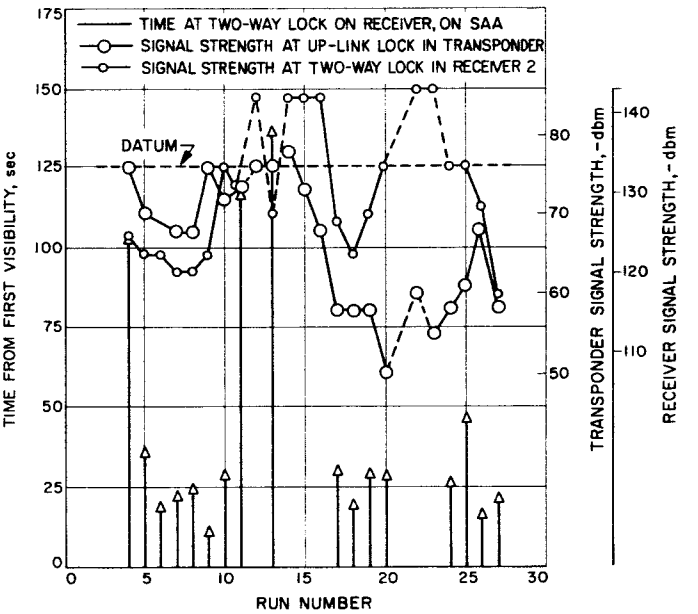


Fig. 3. Variation of signal strength and lock time versus run number

(6) The acquisition times do not show any obvious dependence on frequency variations. The location of the spacecraft frequency in the "window" must obviously influence the lock times, but it appears that the effect is masked by the much stronger effect of signal strength variations.

Angle tracking was accomplished on all runs on which two-way lock was first achieved, as shown in Fig. 4.

Auto track on the SAA was accomplished as soon as the helicopter reached 10 deg above the horizon (average time, 154 sec; average rate, 0.06 deg/sec), and auto track on the SCM was achieved shortly after (average time, 35 sec).

d. Conclusions. These tests, and evaluation of the data, lead to these conclusions:

(1) The time from first visibility to two-way lock on the SAA depends strongly on both the up-link and down-link signal strengths. Two-way lock will not be achieved when either the transponder received signal strength is less than −76 dbm (−98 dbm at DSIF test transponder input) or the ground received signal strength is less than −133 dbm. If both signal strengths exceed these values, acquisition will be achieved in a time which depends directly on the difference between the actual signal levels and the minimum levels referred to above.

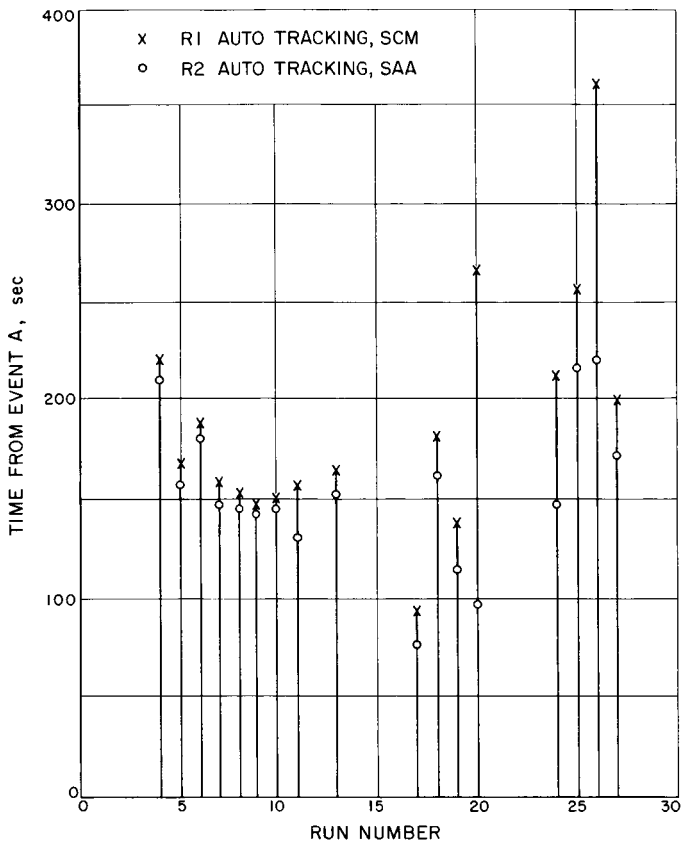


Fig. 4. Time to auto track condition versus run number

The signal-to-noise ratios in the loop bandwidths corresponding to these levels are:

S/N for −133 dbm in 2 B_L = 450 cps; on SAA parametric amplifier = 16 db

S/N for −98 dbm in 2 B_L = 233 cps; in transponder = 18 db.

(2) Flight path variations (up to ±11 deg) and transponder frequency offsets do not exert a strong influence on two-way lock time.

(3) Within the constraints mentioned above, two-way lock can be achieved in the following times from first visibility:

Minimum time: 12 sec

Maximum time: 136 sec

Average time: 50 sec.

(4) Auto track on the SAA can be accomplished reliably when the spacecraft reaches 10 deg above the horizon (assuming prior two-way lock on the SAA). Average time for typical angular rates of 0.06 deg/sec is 156 sec.

(5) Angle track on the SCM can be accomplished shortly after angle track on SAA. Average time, 35 sec.

(6) The procedure described results in good doppler data at the earliest possible time after first visibility, reliable auto track condition at 10 deg above the horizon, and good angle data some 35 sec later.

5. Suitcase Telemetry

All components of the suitcase telemetry equipments have been received and checked out. The equipments were packed and sent to Johannesburg where a crew from the mobile tracking station was checked out in equipment operation. One set of equipment was left at Johannesburg while the other was taken to the Fort Dauphin area, Malagasy Republic.

The Johannesburg Station, with the advantages of real time administrative communications, was able to acquire *MC-2* at a signal level of about −142 dbm. No data were obtained, however, since the level is below telemetry threshold. *MC-3* was acquired and tracked for about 3.5 min. Malagasy was unable to acquire the signal from *MC-2*, but did acquire *MC-3* and recorded data for 2.5 min. Equipment difficulties reduced the length of the track and degraded the data. Some equipment deficiencies were noted and will be corrected. The basic concept of a station searching an azimuth sector for a spacecraft using only trajectory predictions and having no real time communications has been proven. A complete report of the test will appear in a future *SPS*.

6. S-Band Receiver AGC Calibration Analysis

The analysis compares a theoretical evaluation of the root sum square (rss) errors intrinsic in calibrating the AGC loop of the receiver in terms of signal strength received at a reference point, with data taken on the S-band receiver at the Pioneer site. The comparison between theoretical and actual was taken only for the traveling wave maser (TWM) and parametric amplifier modes with the effective loop noise bandwidth ($2B_{LO}$) equal to 12 cps.

The analysis illustrates an inordinate spread of data points at the AGC voltages analyzed in the report (viz, 5 to 10 db for both strong and weak signals on the TWM and parametric amplifier) from data taken over several

months, while the theoretical estimates indicate the spread should be

(1) TWM–rss (3σ) = ± 1.27 db

(2) Parametric amplifier–rss (3σ) = ± 1.64 db

The abnormal spread in data indicated that standardized AGC calibration procedures and careful operator techniques need to be established in the DSIF. A preliminary calibration procedure was included in the Appendix of the analysis.

7. Mariner 4 Carrier Lock Verification Procedure

A simplified operational procedure has been developed wherein carrier lock on a telemetry sideband can be detected and corrected.

A 70-cps RC low-pass filter was inserted, via a tee, into the telemetry video output line of the GSDS S-band receiver (Fig. 5). The filter consisted of a 100 kΩ resistor and a 0.33-μf capacitor mounted between two coaxial connectors.

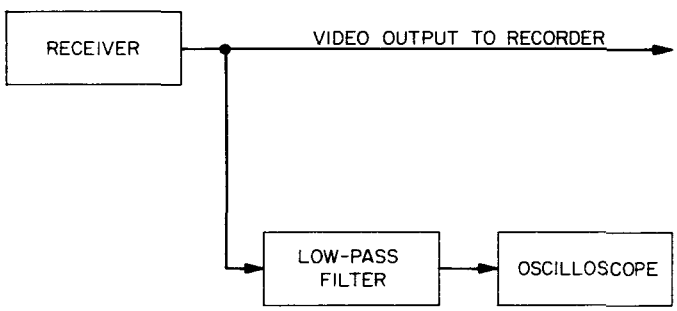


Fig. 5. Sideband filter connections

The filter is high impedance and causes negligible loading on the telemetry output. The output from the filter was connected to an oscilloscope with the vertical sensitivity set at 0.2 v/cm and the sweep speed set at 20 msec/cm.

If the receiver is locked to the carrier, the telemetry video output contains the telemetry subcarrier frequency only, which is much higher than the filter cutoff frequency, and the oscilloscope shows only noise. If the receiver is locked to a telemetry subcarrier sideband which is being biphase modulated at a rate 33⅓ bits/sec, the video output contains the biphase modulation rate which is passed by the filter and presented on the scope. Fig. 6 compares carrier lock with sideband lock at two signal strengths with the receiver reference channel set for a 152-cps threshold loop bandwidth which has a carrier threshold of −160 dbm at 50°K system temperature.

This technique allows detection of sideband lock down to receiver carrier power levels of 15 db above threshold.

8. Station Control and Monitor Console, Phase I

A prototype station control and monitor console (SMC) has been completed and installed at the Pioneer site interim S-band facility building. The console, which provides a central point for the station manager to carry out his normal duties, was designed to satisfy three primary requirements:

(1) To display information for the station manager that will indicate any nonstandard situation which may be detrimental to the operation of the station and to the acquisition of data.

(2) To display information frequently requested by DSIF operations control.

(3) To display other information that will assist the station manager in maintaining a smooth operation.

a. Description. The console for the prototype SMC is shown in Fig. 7. It is composed of five equipment racks with accommodations for standard 19-in. display, control, and communications panels to be mounted above the desk top which is approximately 9 ft in over-all length and can accommodate either a two- or three-man operation. The electronics control and power units, and connector patch panels, are located in the lower part of the five bays.

In addition to the console, the prototype SMC subsystem consists of the following functional units:

(1) Antenna position display

(2) Greenwich Mean Time display

(3) Countdown time assembly

(4) System status display

(5) Subsystem status display

(6) Microwave switch mode display

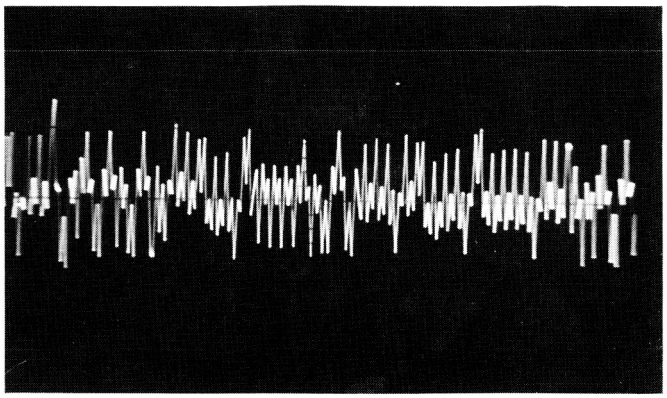
(7) Connector and patching assembly

(8) Station intercommunication panels

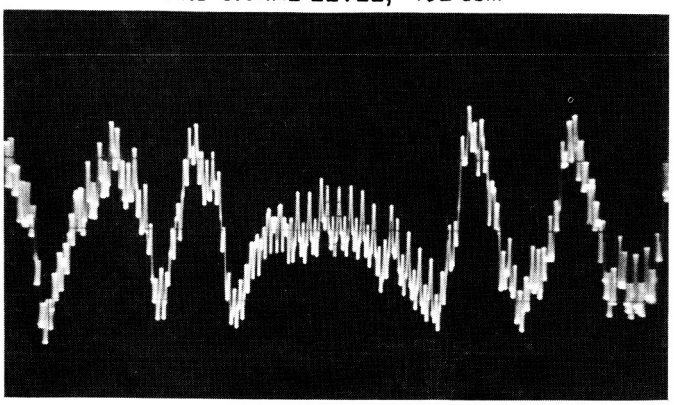
(9) Interstation communications panels

The displays for these assemblies are shown in Figs. 8–13.

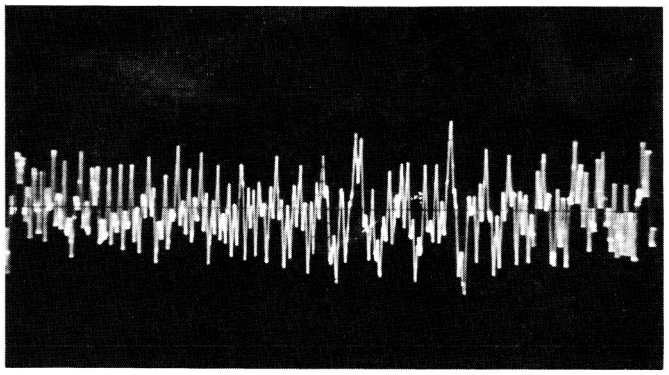
CARRIER SIGNAL LEVEL, -100 dbm



FIRST SIDEBAND SIGNAL LEVEL, -102 dbm



CARRIER SIGNAL LEVEL, -144 dbm



FIRST SIDEBAND SIGNAL LEVEL, -146 dbm

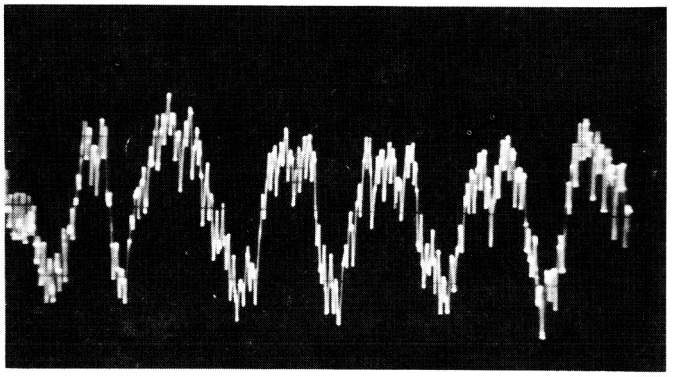


Fig. 6. Comparison of carrier lock with sideband lock, receiver bandwidth at 152 cps and threshold —160 dbm

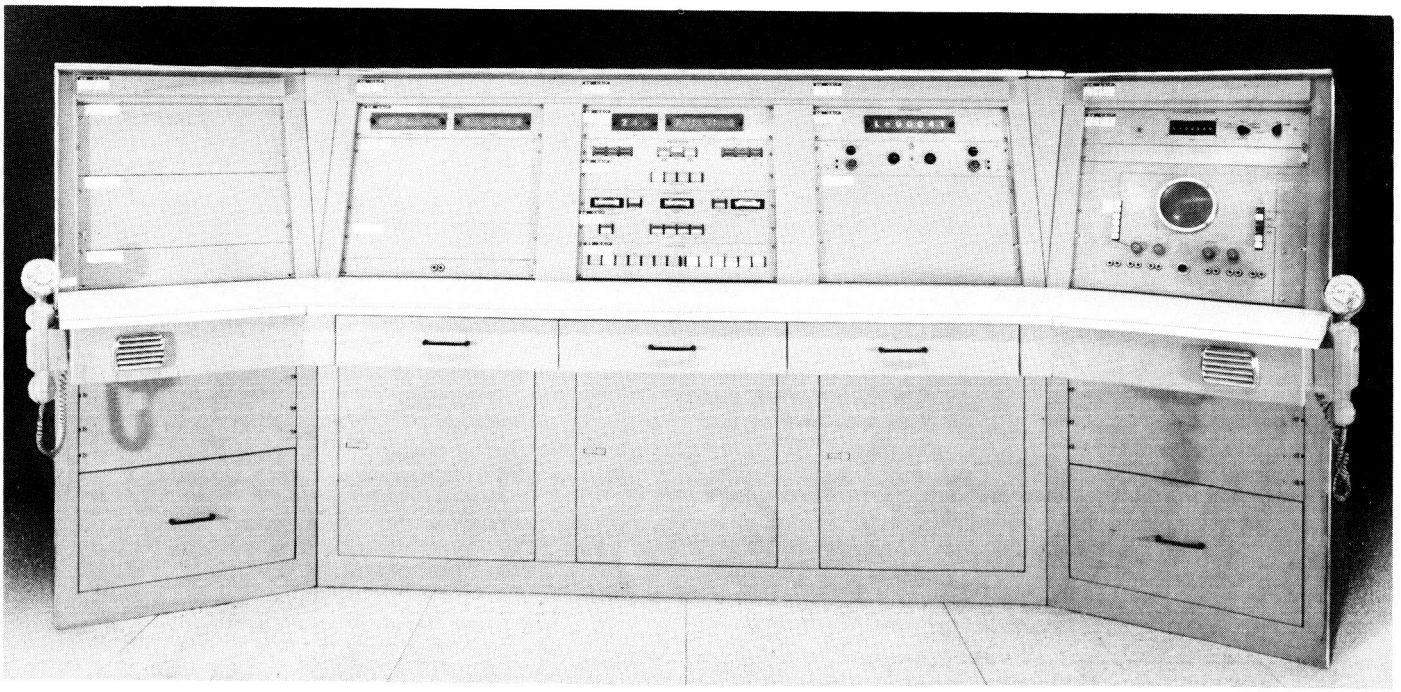


Fig. 7. Prototype station control and monitor console

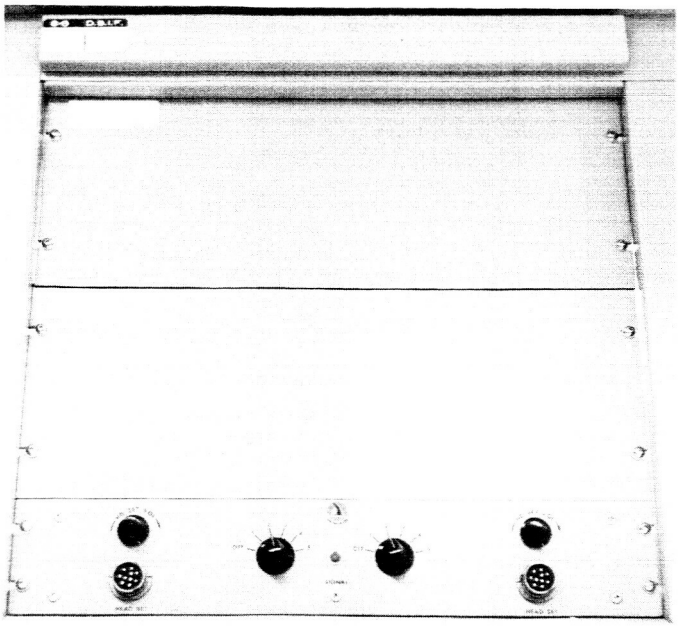


Fig. 8. Headset control panel

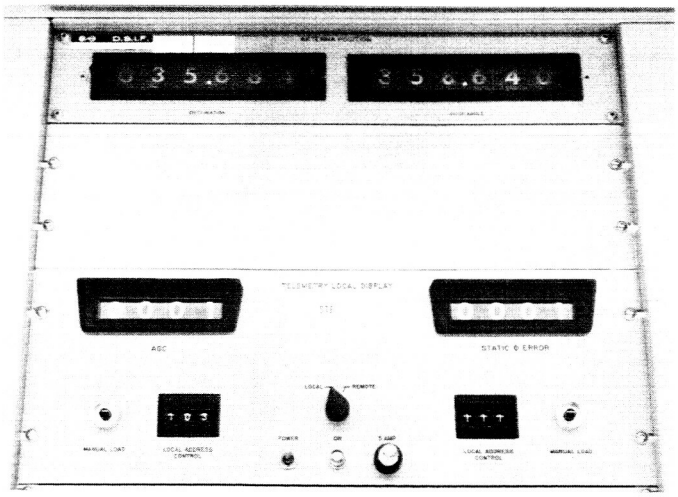


Fig. 9. Antenna position display panel and telemetry local display panel

b. Functional units. The following paragraphs provide a functional description of the displays, beginning with the bay at the extreme left (Fig. 8) and proceeding to the bay at the extreme right (Fig. 12) and from top to bottom. The blank panels are for future expansion of the SMC display capability.

Fig. 8. Headset control panel: provides control for two headsets.

Fig. 9. Antenna position display panel: provides declination and hour angle readout to third decimal place.

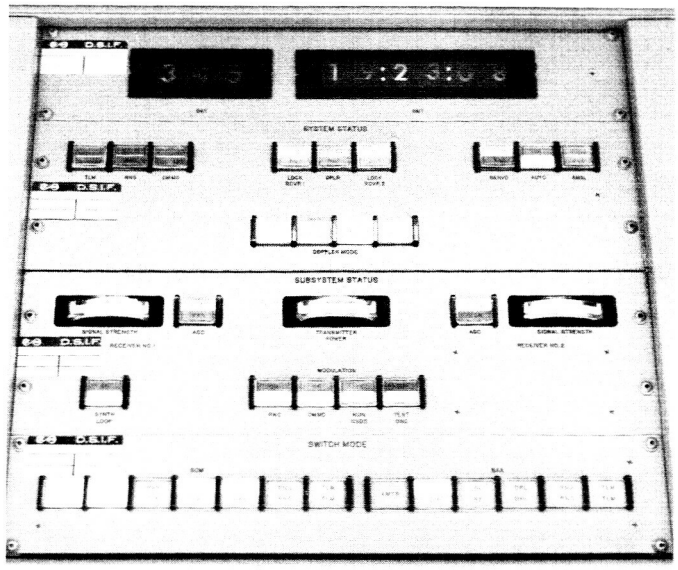


Fig. 10. Mode, time, and status display panels

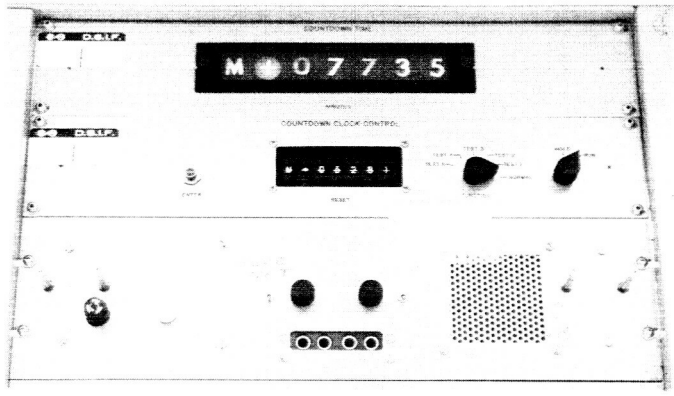


Fig. 11. Countdown time, countdown clock control and TAC-COM panels

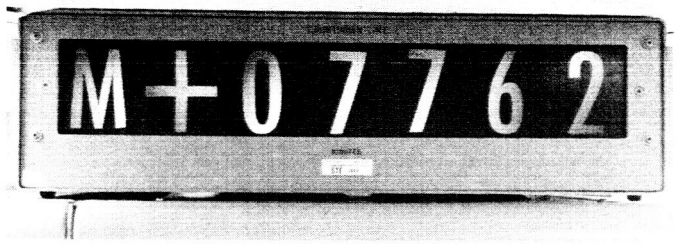


Fig. 12. Remote countdown time display

Telemetry local display: provides display of spacecraft telemetry parameters. With the REMOTE–LOCAL switch in the LOCAL position, the two parameters displayed are under the control of the mission decom equipment, and normally will display spacecraft AGC and

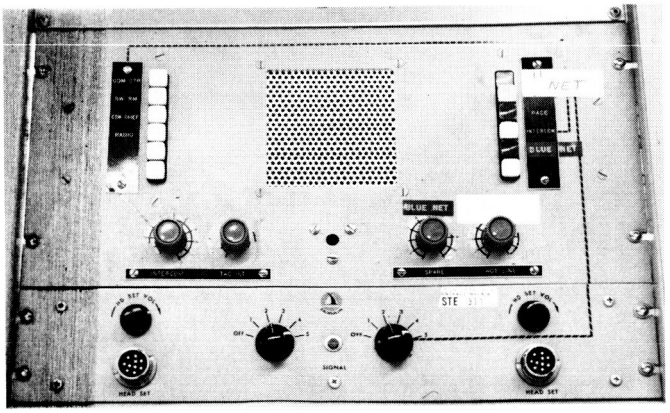


Fig. 13. Station intercommunications panel with headset control panel

static phase error. However, the local address control digiswitch assembly provides for selection of any telemetry data word by setting the appropriate address. In the REMOTE switch position, the telemetry display is connected to, and data display controlled by, the digital portion of the station instrumentation subsystem computer.

Fig. 10. Greenwich Mean Time display (days, hours, minutes, seconds).

System status display panel displays:

(1) Telemetry (TLM) receiving or not receiving.

(2) Range tracking (RNG) tracking or not tracking.

(3) Spacecraft command (CMMD) transmitting or not transmitting.

(4) Phase lock of Receiver 1 and 2, in-lock or out-of-lock.

(5) Receiver doppler condition (DPLR) good or bad.

(6) Servocontrol antenna error signals (SERVO) from SCM or SAA.

(7) Tracking (AUTO) in or out.

(8) Tracking angle data (ANGL) good or bad.

(9) Doppler mode:

C1, one way.

C2, two way.

C3, pseudo two way.

C_o3, coherent pseudo two way.

Subsystem status panel: displays the following operating conditions:

(1) Received signal strength meters, Receivers 1 and 2; indicates AGC voltage, 0 to −10 v.

(2) Transmitted power meter, to be calibrated in kilowatts.

(3) Receiver gain control (AGC) Receivers 1 and 2; AGC or MAN.

(4) Transmitter synthesizer loop lock (SYNTH) in-lock or out-of-lock.

(5) Transmitter modulation:

Ranging (RNG) . . . on-off.

Command (CMMD) . . . on-off.

Non-GSDS. . . on-off.

Test OSC . . . on-off.

Switch mode panel: displays the operating configuration of the DSIF system. Two sets of lights are used to display either SCM or SAA operation. Each set displays the same data, except for the SCM which has an additional light to indicate when the TWM is in use. The panel displays the following operating conditions, and all are pertinent to operation in either SCM or SAA mode:

(1) Transmitter operation, (XMTR) to SCM or SAA.

(2) Antenna operation:

SCM to maser (TWM).

SCM to parametric amplifier (PAR).

SCM directly to receiver (DIR).

SAA to parametric amplifier (PAR).

SAA directly to receiver (DIR).

(3) Receiver 1 or 2 in use (R1) or (R2).

(4) Which receiver is supplying doppler (DPL) data.

(5) Which receiver is supplying ranging (RNG) data.

(6) Which receiver is supplying telemetry (TLM) data.

Fig. 11. Countdown time panel: provides for counting from −99999 to 00000 to +99999 min. The clock is designed to accept a 1-pulse/min pulse from the DSIF frequency and timing subsystem (FTS). In addition, one of the five letters, L, I, X, M, and T can be displayed in the extreme left display position.

Countdown clock control panel: enables the operator to set the clock to any desired counting position in either

plus or minus time. A series of ten-position switches is provided for setting each decimal digit. By placing the HOLD-RUN switch to HOLD, and positioning the desired number sequence on the switches, the numbers can be entered on the countdown time display by pushing the ENTER button. The counting sequence at 1 count/min is then resumed by placing the HOLD-RUN switch to RUN. A remote display identical to, and driven from, the countdown time display is mounted on top of the servo rack (Fig. 12).

Tactical communications panel (TAC-COM): provides voice circuits for real time coordinating of DSIF operations through DSIF net control in the SFOF, and reporting DSIF status to SFOF.

Fig. 13. DSIF Station intercommunications panel: also includes TAC-COM capability described in previous paragraph.

c. Modifications to SMC prototype. The production phase of the SMC has been initiated; however, the follow-on SMC will reflect several changes, primarily to the console configuration. The console height has been reduced to 45 in. to provide better visibility for the station manager; the desk surface has been increased to a 21-in. depth. Also, changes have been made in some of the panel nomenclature to provide a better understanding of switch identification and functions. The countdown clock design will be modified to read out time in hours, minutes, and seconds in order to be compatible with standard SFOF designs.

C. Systems Analysis

1. Estimate of the Nominal Earth-to-Spacecraft Up-Link Acquisition Times

Prior to the *Mariner* 1964 launches, an investigation was made to estimate the nominal Earth-to-spacecraft up-link acquisition times involved in the *Mariner 4* flight to Mars. Three flight periods are considered: (1) first pass acquisition (refer to Section B, p. 5); (2) midcourse maneuver; and (3) encounter.

The time to be specified will be comprised of the *propagation time* of the radiated signal and the *search time* necessary to locate the spacecraft lock-up frequency. For a practical assessment of the up-link acquisition time, the down-link propagation time should be added to the above estimate in order that two-way acquisition will occur, verifying the up-link acquisition.

The total up-link acquisition time can be expressed by the following relationship:

$$T_{tot} = T_p + (f_w/\dot{f}_{sw}) \pm (f_w/\dot{f}_d) \quad (1)$$

where

T_{tot} = total up-link acquisition time, sec

T_p = propagation time, sec

f_w = frequency window to be searched, cps

$\dot{f}_{sw}$ = operator sweep rate, cps^2

$\dot{f}_d$ = nominal doppler rate experienced by the spacecraft, cps^2

Also, the frequency rate components are related as follows:

$$\dot{f}_{sw} \pm \dot{f}_d \pm \Delta\dot{f}_d < \dot{f}_{max} \quad (2)$$

or

$$T_{tot} \geqq f_w/\dot{f}_{max} + T_p$$

where

$\Delta\dot{f}_d$ = the change in doppler rate experienced by the spacecraft relative to the nominal doppler rate for a specific case.

$\dot{f}_{max}$ = maximum tolerated frequency rate of the spacecraft receiver, beyond which the spacecraft theoretically is unable to obtain phase lock.

In using this relationship, the following assumptions will be made:

(1) The frequency window represents an estimate of the maximum uncertainty of the lock-up frequency of the spacecraft transponder. This value includes spacecraft frequency (crystal oscillator), doppler prediction uncertainty estimates, and includes the effect of a doppler shift of the lock-up frequency during the acquisition process.

(2) The $f_w/\dot{f}_{sw}$ factor represents the time necessary for the operator to sweep once through a given frequency window. However, this value does not include the time necessary to zero the static phase error in the spacecraft receiver, which is acknowledged via telemetry.

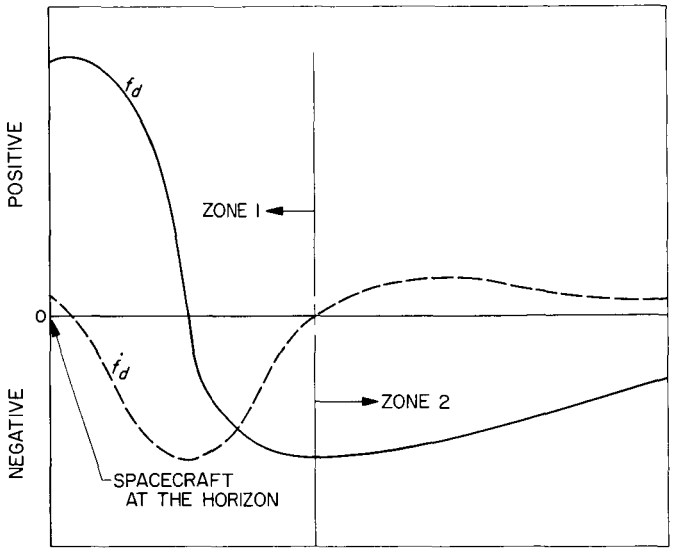


Fig. 14. Typical example of f_d and $\dot{f}_d$ curves for first pass at Woomera

(3) Using Fig. 14 and separating the time into two chronological zones: (a) If the operator attempts up-link acquisition in Zone 1, he should search from a higher frequency to a lower frequency; and (b) in Zone 2 he should start his search from a lower frequency sweeping to the higher predicted frequency. This technique will minimize relative doppler rates. The most probable search condition will occur in Zone 2 with the spacecraft doppler rate $\dot{f}_d$ aiding the operator sweep rate.

The $\dot{f}_{max}$ represents the spacecraft transponder frequency rate limitation during acquisition with the restriction that the maximum tolerated phase error is 15 deg. Using ½ rad for this restriction has been suggested (Ref. 1); however, the effect of noise in the receiver is not included in this reference.

The down-link propagation time should be added to the total up-link acquisition time to yield an estimate of the time of up-link acquisition from the start of the search to confirmation of up-link acquisition. It is assumed that initiation of command system lock-up required up-link RF lock verification.

For the first pass acquisition and midcourse sequence, the operator should sweep at no more than 200 cps^2 at the carrier frequency, and if the spacecraft's ranging channel is *on*, the operator can listen for the down-link audio frequency beat of the up-link unlocked carrier frequency (while sweeping the frequency window). Table 3 illustrates typical up-link lock acquisition time.

Table 3. Estimated acquisition times

Flight period	Frequency window f_w, cps	Operator sweep rate f_{swr}, cps^2	Up-link acquisition time T_{tot}, sec	Time from start of search to up-link acquisition verification, sec
1. First pass acquisition	10,000	200.0	42.0	42.1
	5,000	200.0	16.0	16.1
	3,000	200.0	12.0	12.1
2. Midcourse maneuver				
(a) 3 days	1000	200.0	≈9.0	≈12.0
(b) 10 days	1000	200.0	13.0	22.0
3. Encounter	100	≈0.0	≈1000 (or 16.7 min)	≈1733.0 (or 29.0 min)

For several passes before encounter phase, a very slow sweep rate may be required in order to obtain up-link lock. However, by the time the spacecraft has reached the encounter phase, the operator's *a priori* knowledge should allow presetting of the transmitter VCO frequency, thereby letting the spacecraft transponder acquire lock by itself. This is denoted as the pull-in time of the phase lock loop receiver. Ref. 1 gives the relationship for pull-in time for a second-order loop (perfect integration) as follows:

$$t = \frac{27\,(\Omega)^2}{256 B_L{}^3}, \text{ sec}$$

where

Ω = difference between the signal frequency and the VCO center frequency, rad/sec

and

B_L = loop noise bandwidth, cps (10 cps for the *Mariner 4* transponder).

For the encounter phase Ω equals approximately 100 cps and using the loop noise bandwidth at threshold of spacecraft transponder then yields:

$$t = \frac{27\,(100)^2\,(2\pi)^2}{256\,(10)^3} = 41.6 \text{ sec}$$

Ref. 1 does not take into account noise effects or doppler rate capability and the fact that the loop filter is an imperfect integrator. Nevertheless, this value will probably not exceed 100 sec.

From plots of Eq. (1), it is estimated that the up-link acquisition should occur within 20 min of station first view, more likely within 15 min.

This theoretical development to an operational problem necessitates an experimental program to verify the acquisition time and technique presented in the analysis. So far, the numbers generated for the first acquisition and midcourse phases of *Mariner 4* have been verified in a qualitative manner. Actual performance of the S-band stations during the later phases of the *Mariner 4* mission will be reported in a future *SPS*.

2. Initial Values for Sequential Estimation

This article applies the sequential method of R. Kalman (Ref. 2) to the estimation of a random variable imbedded in noise. The random variable, x, is fixed for any single experiment, but its value varies over the ensemble of experiments. A single experiment is the observation of a scalar sequence of values of $\phi(t)$, $\{\phi_i\}$ where

$$\phi(t) = x + n(t) \tag{1}$$

The goal is to provide the best possible estimates of x for $i = 0, 1, 2, \cdots, n$, assuming that the noise $n(t)$ is of zero mean and variance Γ. We consider the effect of the initial estimate on the set of best estimates.

In Ref. 2, Kalman presents a general iterative solution for the optimal estimate of the state of a dynamic system excited by noise. Related and equivalent results, in which the noise enters directly into the observations, are presented by Pfeiffer (Ref. 3), and Ho (Ref. 4). In all cases the best estimates are given by a system of difference equations which yield a new best estimate and a new estimate of its covariance in terms of the previous values and the observation at that time. With x_i and Λ_i representing the estimate and its variance, direct application of these results to the example discussed above yields:

$$x_{i+1} = x_i + \frac{\Lambda_i(\phi_{i+1} - x_i)}{\Lambda_i + \Gamma} = \frac{x_i\Gamma + \Lambda_i\phi_{i+1}}{\Lambda_i + \Gamma} \tag{2}$$

and

$$\Lambda_{i+1} = \Lambda_i - \frac{\Lambda_i^2}{\Lambda_i + \Gamma} = \frac{\Lambda_i\Gamma}{\Lambda_i + \Gamma} \tag{3}$$

Dividing Eq. (2) and (3) and examining x_1/Λ_1 and x_2/Λ_2 yields:

$$\frac{x_n}{\Lambda_n} = \frac{x_0}{\Lambda_0} + \frac{1}{\Gamma}\sum_{i=1}^{n}\phi_i, \tag{4}$$

where x_0 and Λ_0 are the initial or *a priori* values. Solving for Λ_n in terms of x_n and substituting in Eq. (2) yields a difference equation for x_i alone. By inspection of the first few terms, the solution can be found and easily verified to be:

$$x_n = \frac{x_0\Gamma + \Lambda_0\sum_{i=1}^{n}\phi_i}{\Gamma + n\Lambda_0} \tag{5}$$

This and Eq. (4) yield:

$$\Lambda_n = \frac{\Lambda_0\Gamma}{n\Lambda_0 + \Gamma} \tag{6}$$

The limit as $n \to \infty$ of the estimate is the mean of the observations; that of the variance is zero. This holds for any initial estimates of the parameter and the variance of the estimate. However, the effect of different choices of the initial estimates is significant.

For any single experiment whose actual value of the parameter is x, the expected value of the sequential estimate will be:

$$E(x_n) = \frac{x_0\Gamma + n\Lambda_0 x}{\Gamma + n\Lambda_0} = x + \frac{(x_0 - x)\Gamma}{\Gamma + n\Lambda_0} \tag{7}$$

Thus, x_n is a biased estimate of x, with bias

$$(x_0 - x)/(\Gamma + n\Lambda_0).$$

The bias is asymptotically zero and can be reduced by increasing the initial variance Λ_0.

An attempt to eliminate the bias, by choosing for x_0 a function of the first few observations whose expected value is x (such as the mean), was not fruitful. If we set

$$x_0 = \frac{1}{r}\sum_{i=1}^{n}\phi_i \tag{8}$$

and use Eq. (5) for $(r + 1)$ and on,

$$x_n = \frac{\frac{\Gamma}{r}\sum_{i=1}^{r}\phi_i + \Lambda_0\sum_{i=r+1}^{n}\phi_i}{\Gamma + (n - r)\Lambda_0} \tag{9}$$

But

$$\Lambda_0 \equiv E[(x - x_0)^2] = E\left[\left(\frac{1}{r}\sum_{i=1}^{r}n_i\right)^2\right] = \frac{1}{r}E[n_i^2] = \frac{\Gamma}{r}$$

Consequently Eq. (9) reduces to

$$x_n = \frac{1}{n}\sum_{i=1}^{n}\phi_i.$$

If the best *a priori* estimate of x (its mean over the ensemble of experiments $\bar{x}$) is known and used as initial

estimate, the expected value of the bias over the ensemble of experiments will be zero. However, in many cases $\bar{x}$ is not known. Furthermore, the estimation in a single experiment may be of great importance as in the case of a parameter of a missile trajectory, so use of the *a priori* best estimate does not help eliminate the bias.

D. Goldstone Operations

The launch of *Mariner 4* on November 28, 1964 culminated months of preparation at the Pioneer site. In those months, the control building wings were erected, local and overseas S-band systems were assembled and tested, and personnel were trained to operate equipment for the *Mariner*–Mars mission. After the success of *Ranger 7*, the Echo site gave to the Pioneer site full support which continued until the midcourse maneuver of *Mariner 4* was accomplished. During the last two weeks of December, Echo personnel began the preliminary system preparation for the *Ranger 8* and *9* missions, scheduled for early 1965.

1. Mariner 1964

Prior to the launch of *Mariner 3*, scheduled for November 4, 1964, the Pioneer site participated in Mission Simulation Test No. 1. All subsystems functioned properly and preparations for *Mariner* 1964 were completed. *Mariner 3* was launched on November 5, 1964 but failed soon after launch. Pioneer unsuccessfully attempted to acquire the vehicle during the first view period.

In the interval between the *Mariner 3* and *Mariner 4* launches, there was additional system testing. Operational testing of receiver spare modules was performed, and the receiver was retuned for operation on Channel 21.

Practice countdown exercises were conducted by station personnel to verify continued operational readiness. Pioneer participated in successful DSIF operational readiness tests on November 19 and 24.

Mariner 4 was launched from Cape Kennedy. Pioneer attempted to "hear" the spacecraft as it went into the injection orbit, but terrain features at Goldstone raised the eastern horizon too high to accomplish the reception. First acquisition of the spacecraft occurred late in the evening of November 28. Canopus lock was delayed until November 30 and Pioneer initiated the commands which caused the Canopus sensor to unlock from other stars. The view period ended for Pioneer prior to Canopus lock, which occurred after Woomera had taken over the track.

Two midcourse maneuvers were initiated. The first occurred on December 3 and was inhibited almost immediately when the spacecraft performed an unscheduled roll. The second, on December 4, successfully completed the midcourse correction, and a close-up flyby of Mars is expected. Scientific, engineering, and cruise-mode data are being recorded in near-real time, and the tracking has settled into a normal mission operation.

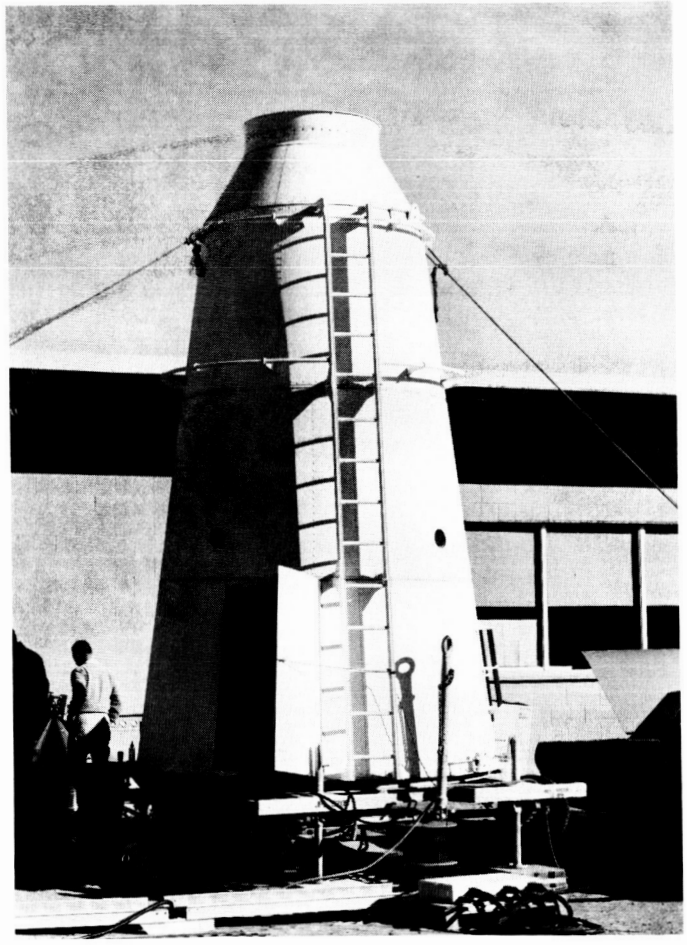


Fig. 15. Madrid Cassegrain cone test setup at Pioneer site

2. Equipment

The S-band system for the Madrid, Spain Station was assembled and tested in late December at the Pioneer site (*SPS 37-30*, Vol. III, p. 3). The Madrid Cassegrain cone, tested on the Echo site 85-ft antenna, was installed just outside the south wall of the Pioneer S-band wing (Fig. 15), and the parametric amplifier (Fig. 16) was installed in the basement to permit closed loop interface testing of the receiver equipment. With the Pioneer 85-ft antenna in full use for *Mariner* 1964 tracking, all future tests of the Madrid S-band system involving the antenna will be performed at the Madrid Station to which equipment will be sent early in 1965.

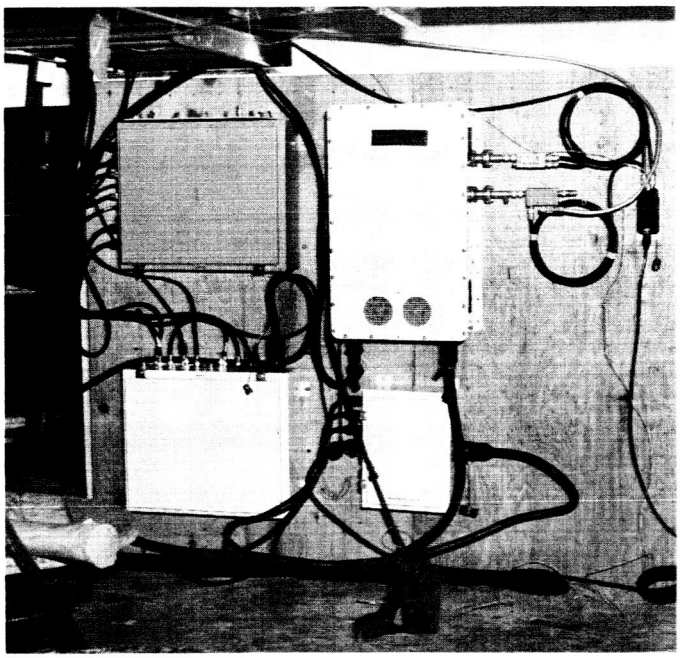


Fig. 16. Madrid parametric amplifier test setup at Pioneer site

The S-band system for DSIF-71, Cape Kennedy, is being partially assembled and tested at the Pioneer site. The equipment will be shipped to the Cape early in 1965, and final assembly and complete system testing will be accomplished there.

3. Ranger Preparations

During November and the first two weeks of December, Echo site personnel contributed full support to the Pioneer site for the launch of *Mariner 3*, and the subsequent launch and tracking of *Mariner 4*. Since the L-band system was being held in standby with the completion of *Ranger 7*, the time was used to recable the 85-ft antenna, and to perform cone testing of the Madrid S-band Cassegrain cone. In addition, star track tests were performed with a radiometric Cassegrain cone under development in the Goldstone microwave support section.

In December, preliminary L-band system testing was begun. Cable loss calibrations of the new cabling installed on the antenna were completed. During the last two weeks in December, operations personnel were withdrawn from the *Mariner* mission to complete the L-band system preparations for the *Ranger 8* systems and operational readiness tests scheduled for early 1965.

The RCA video group has been conducting continuous testing, and has been performing minor modifications to the video equipment in readiness for *Ranger 8*.

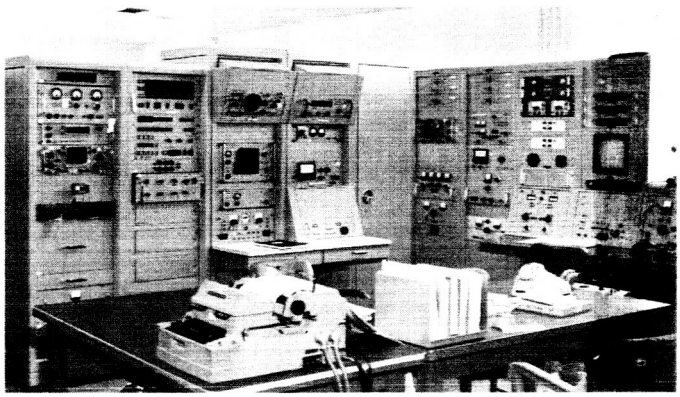


Fig. 17. Exciter installation for 100-kw transmitter at Venus site

4. Mariner 1964 100-kw Cone Transmitter

The exciter for the *Mariner* 1964 100-kw Cassegrain cone transmitter (*SPS 37-30*, p. 5) has been installed in the Venus Site control room (Fig. 17). Personnel from the Goldstone microwave support section, who partially designed and fabricated the exciter, have been conducting system tests of the exciter and transmitter. Testing has included ground testing of the cone transmitter, and antenna testing with the full 100-kw capability. A modification was initiated to provide a listening capability in addition to the transmitting function, and is currently being installed and tested.

5. Construction

The underground telephone cable (*SPS 37-30*, p. 6) linking the Echo, Pioneer, and Mars sites and the airport

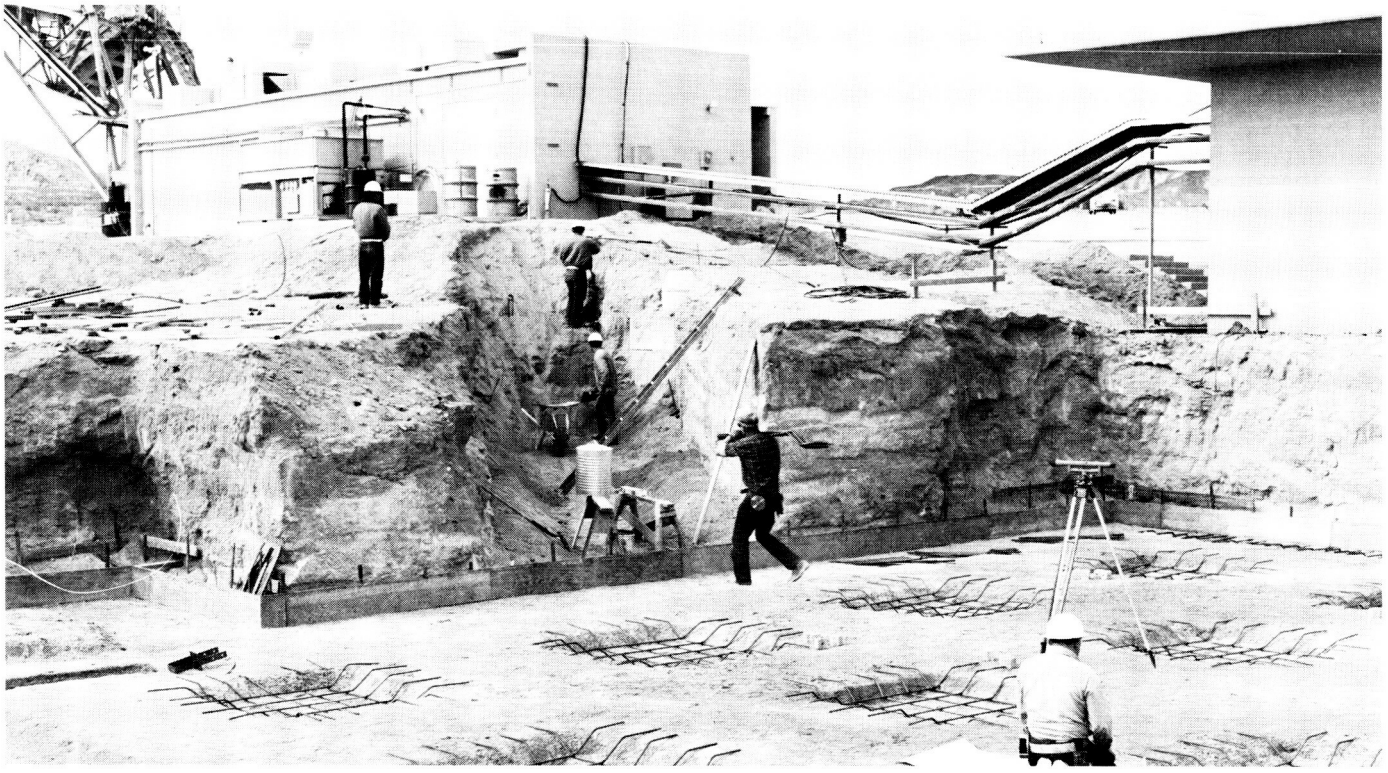


Fig. 18. S-band wing excavation at Echo site

was completed. Construction of the S-band wing to the present control building at Echo has started. The basement excavation (Fig. 18) has been completed and the footings and support pads have been placed.

E. Canberra 85-ft Antenna Erection

Construction of the Canberra, Australia, 85-ft polar-mounted antenna was completed November 6, 1964, bringing DSIF-42 closer to operational status. Completion of the four-month task now gives the Canberra Station an antenna which incorporates all the new DSIF features embodied in the recent Retrofit Program (new TX-E1 cage, truss quadripod, counterweight cages, air conditioning, acquisition aid subsystem, etc.).

The Canberra antenna also has the new high-performance S-band surface panels, increased hour angle coverage, a four-legged pedestal, a beefed up structure for improved surface tolerance and general stiffness, and modified hour angle and declination drive skids for adjustability and improved stiffness.

Figs. 19–26 show the Canberra antenna at various stages of completion:

Fig. 19 shows the foundation piers for each pedestal leg being framed up before pouring the cement.

Fig. 20 shows the start of erection of the antenna's steel portion, the pedestal legs having just been placed.

Fig. 21 shows the completed pedestal prior to installation of the hour angle drive skids.

Fig. 22 shows the completed four-legged pedestal and polar wheel, with both the HA and Dec drive skids in place.

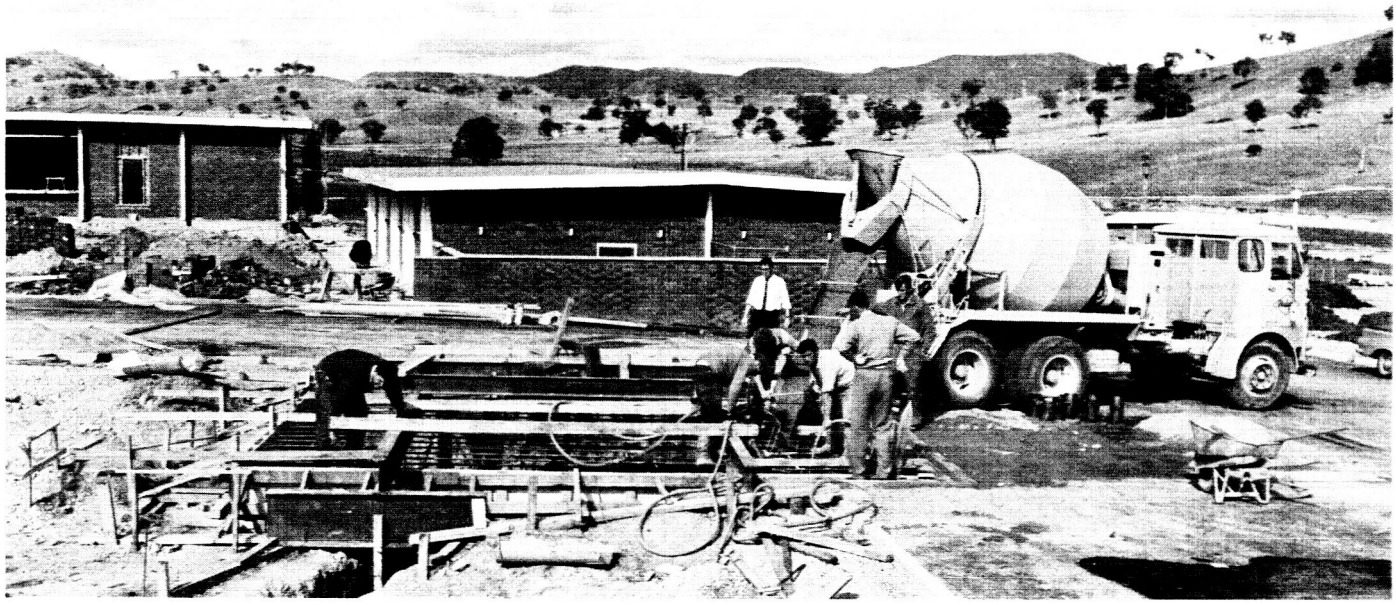


Fig. 19. Placing pedestal leg foundation

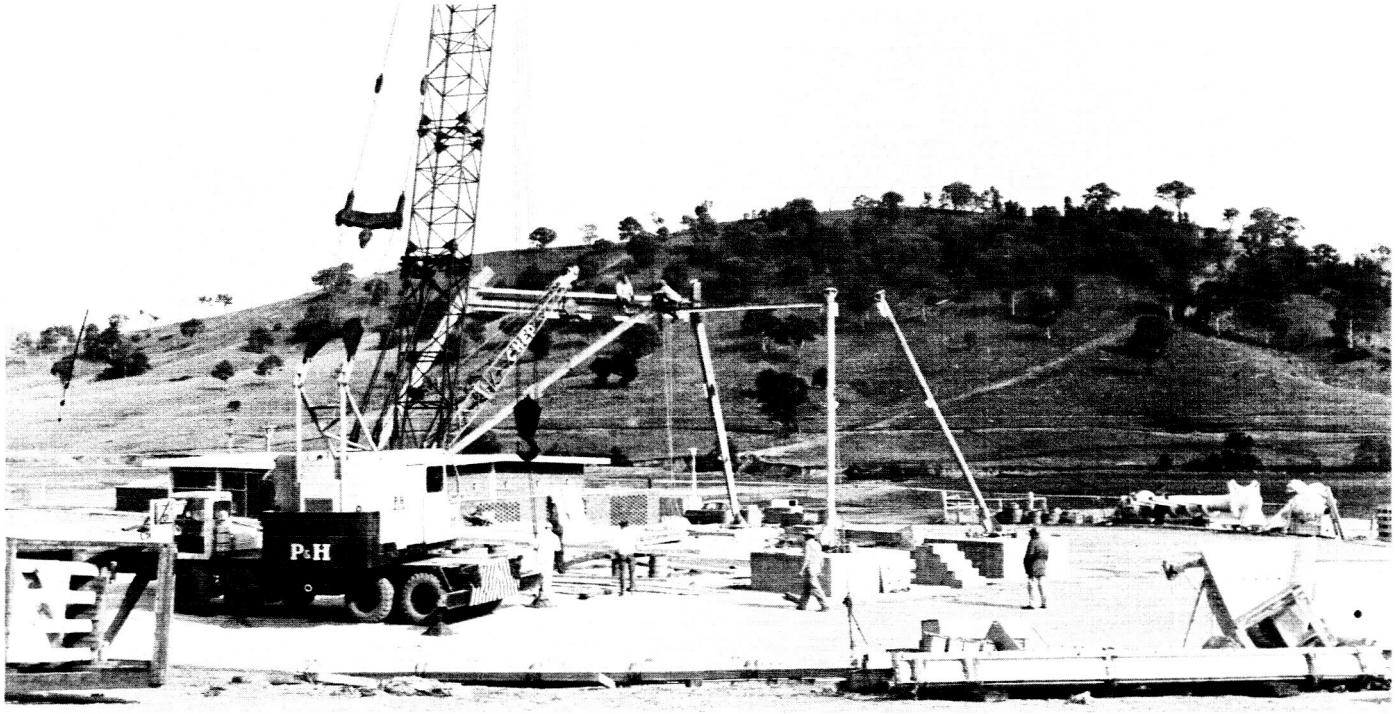


Fig. 20. Pedestal leg placement completed

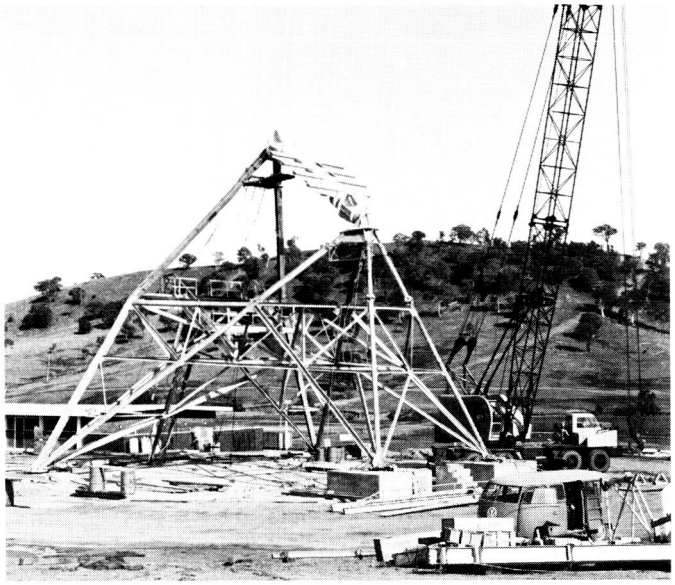


Fig. 21. Four-legged pedestal prior to drive skid installation

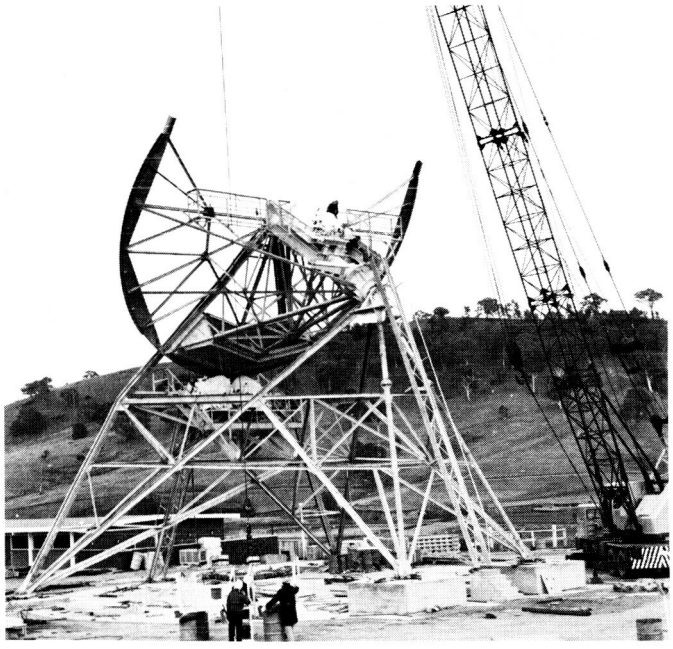


Fig. 22. HA-Dec drive skids in place

Fig. 23 shows the antenna structure just before installation of dish elements.

Fig. 24 shows the antenna structure with the dish substructure, electronics room, etc., installed.

Fig. 25 shows the antenna after installation of the new high-tolerance S-band panels on the dish.

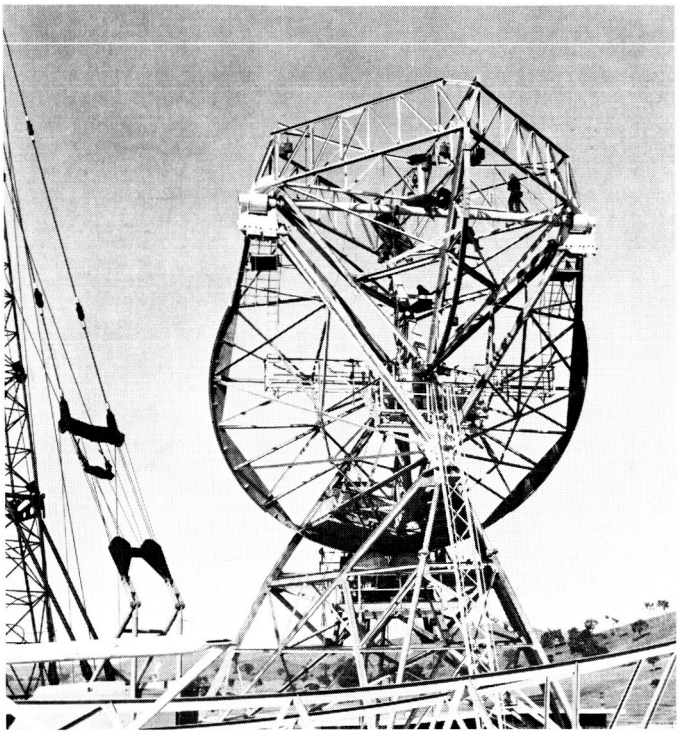


Fig. 23. Antenna structure ready for dish installation

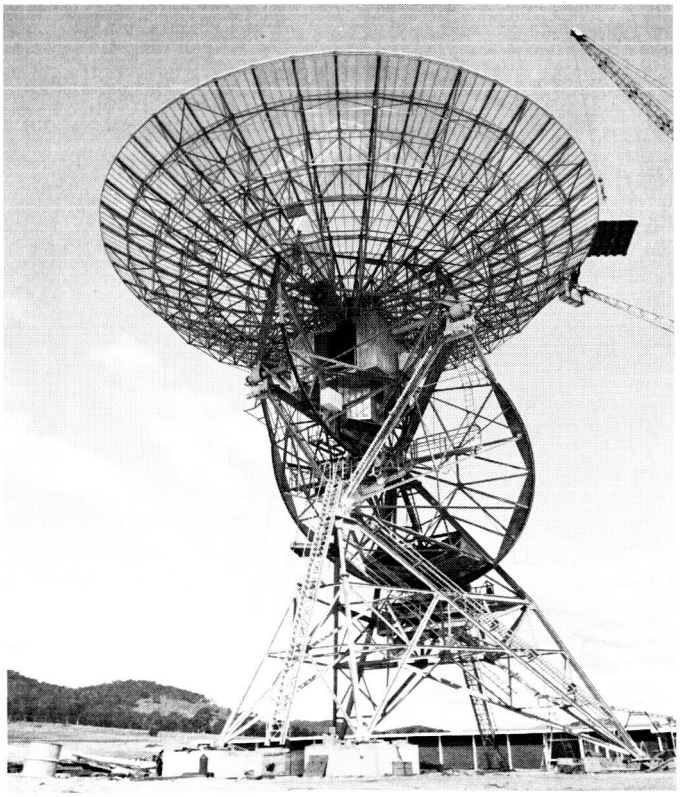


Fig. 24. Antenna dish, partially installed

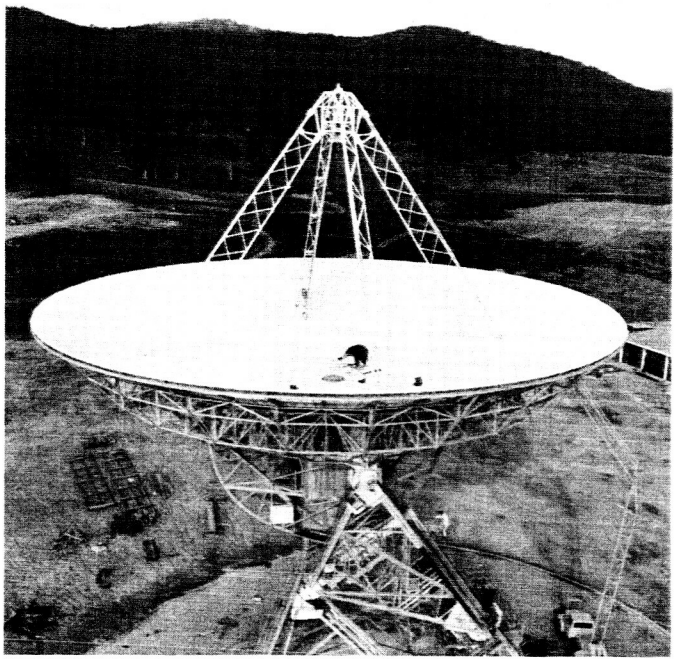


Fig. 25. Antenna dish with high tolerance S-band panels installed

Fig. 26 shows the completed antenna, along with its support hardware and buildings.

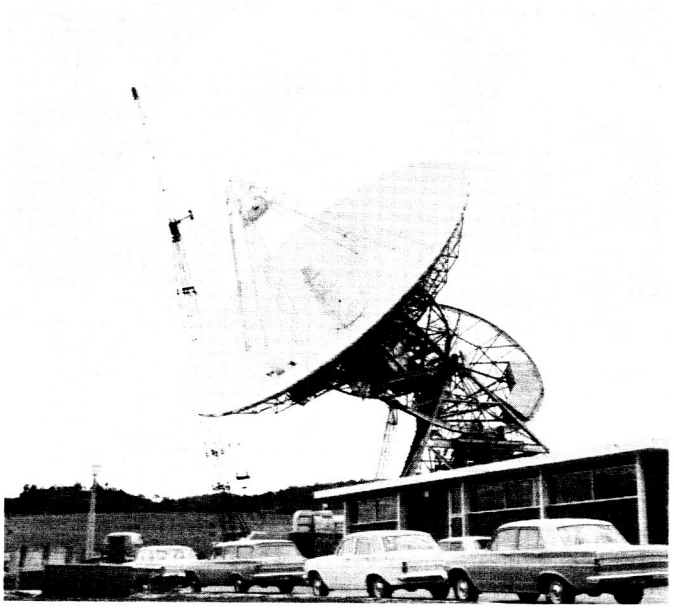


Fig. 26. Antenna installation completed

A preliminary review of the acceptance test data indicated that the new four-legged polar antenna not only exceeds its design criteria but apparently has an X-band quality surface.

References

1. Viterbi, A. J., *Acquisition Range and Tracking Behavior of Phase-Locked Loops,* External Publication No. 673, p. 19, Jet Propulsion Laboratory, Pasadena, California, July 14, 1959.

2. Kalman, R. E., "A New Approach to Linear Filtering and Prediction Problems," American Society of Mechanical Engineers, *Journal of Basic Engineering,* p. 35, March 1960.

3. Pfeiffer, C. G., "Sequential Estimation of Correlated Stochastic Variables," Technical Report No. 32-445, Jet Propulsion Laboratory, Pasadena, California, July 1, 1963.

4. Ho, Yu Chi, "On the Stochastic Approximation Method and Optimal Filtering Theory," *Journal of Mathematical Analysis and Applications,* Vol. 6, pp. 152–154, 1962.

III. Space Flight Operations Facility

A. Installation of Orbit Determination Keyboard in the FPAA

A keyboard input device has been designed and implemented at JPL for use in the flight path analysis area (FPAA) of the SFOF. This device replaces the existing control panel/control logic configuration used in updating the orbit determination display; a display containing rows and columns of remotely controlled digital information. The purpose of the display is to present orbital and miss parameter information when the spacecraft is in close proximity to the Earth immediately after launch and during other critical phases of the mission.

Such a keyboard entry device was required to shorten the time element involved in updating the display, especially during earlier phases of a mission when orbital trajectories have shorter periods due to the spacecraft's relative closeness. The previous control panel configuration (Fig. 1) contained thumbwheel switches for the digital data. A study made, comparing the update time of the existing thumbwheel configuration to the ten-key key-

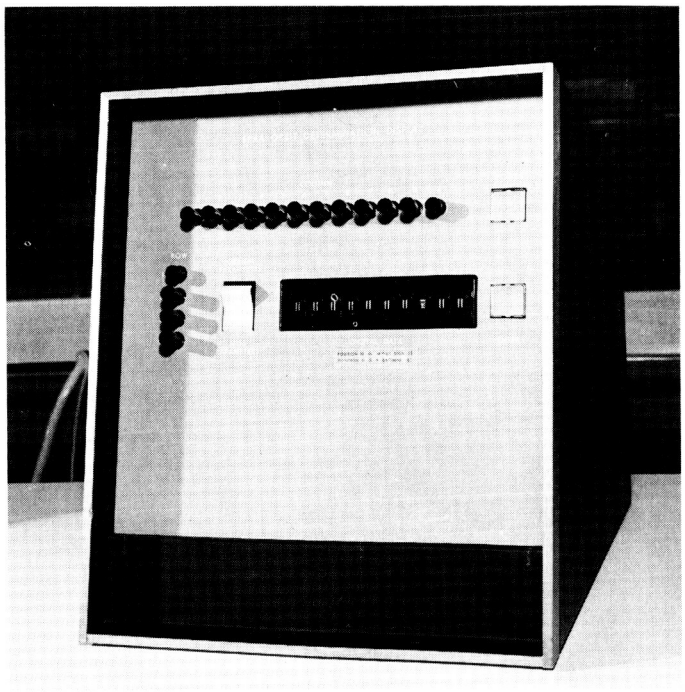


Fig. 1. Previous control panel configuration employing thumbwheel switches

board, resulted in favoring the keyboard as it was found to be four to eight times faster, depending on the operator.

The new configuration consists of three units: a remote control panel (Fig. 2); a card-cage containing digital control logic [*and* and *or* gating, binary-coded decimal/decimal (BCD-Deci) and Deci/BCD decoding, and a shift register]; and a power supply.

Briefly, an updating operation will consist of selecting a column and a row, "inserting" a selected array of ten digits into a shift register and then entering these into the display proper. Electrically, the process consists of the keyboard (being a decimal input) feeding a decoder card which changes the signals to BCD. This enables information to be entered into the shift register as it is a 4-bit by 10-digit matrix. The output of the shift register is also BCD. These signals are decoded with BCD to decimal converter cards prior to entry into the display which has a decimal input. Actuation of the display digital data unit (DDU) readouts, accomplished through relay logic, consists of "homing" in on the "hot" decimal lines provided by the decoder cards. These actuate relays contained within the readouts, breaking the AC circuit driving the DDU motor, and stopping the unit at the proper number selected.

The new device provides the same functions as the original system with the additional capability of clearing the shift register in the event of error and maintaining a given configuration of digital information in the shift register if two or more groups of ten DDU's are to be updated alike.

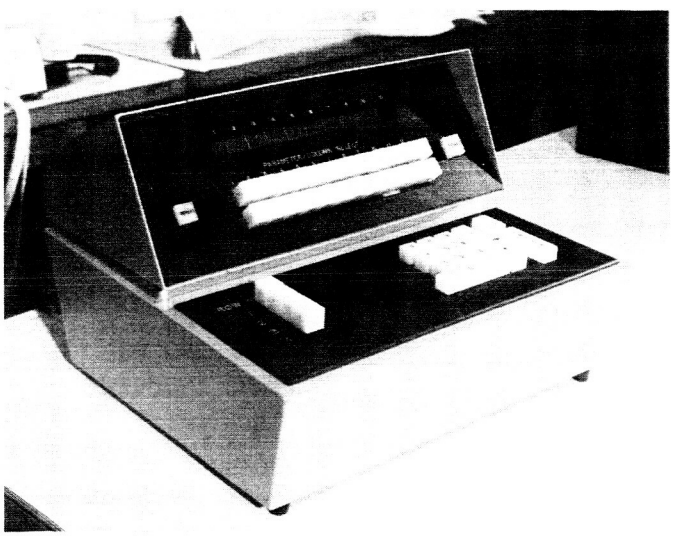


Fig. 2. New keyboard control panel

The largest design problem involved integrating the new control logic into the present system. This was solved by adhering to the existing wiring pattern behind the display and designing the new control system "around" existing cabling and wirelists so that the display "sees" the same inputs as before. The temporary storage of data aspect had been changed, however, i.e., thumbwheel switches to keyboard/shift register.

This system has been tested and is fully operational. Evaluation of the system based on time-and-motion studies is favorable.

In conclusion, the remote-controlled semiautomatic displays in the SFOF will probably be computer-driven eventually. The keyboard control logic configuration is designed so that this could be accomplished with the computer drive and serve as a manual override.

B. High-Speed Data System

This is part of a continuing series of articles describing implementation of various portions of the SFOF.

The high speed data system (HSDS) to be discussed is presently utilized in the transmission of real time telemetry data from the DSIF stations to the SFOF. After performing data encoding, the HSD transmitter phase reversal modulates an audio tone which is passed over high-quality voice transmission lines to the SFOF receiver. To be investigated are the errors which occur between HSD transmitter and receiver.

The problem of evaluating error performance over a data transmission link is often insurmountable because of the random nature of the digital signals being passed. Fortunately, operational high speed data system design allows on-line performance monitoring of any type of random data.

Basically, error performance may be checked in two ways:

(1) During nonoperational periods, exact error count is determined by means of an integral test facility (ITF). A fixed signal is fed to the transmitter which, after transmission to the SFOF, is compared to a

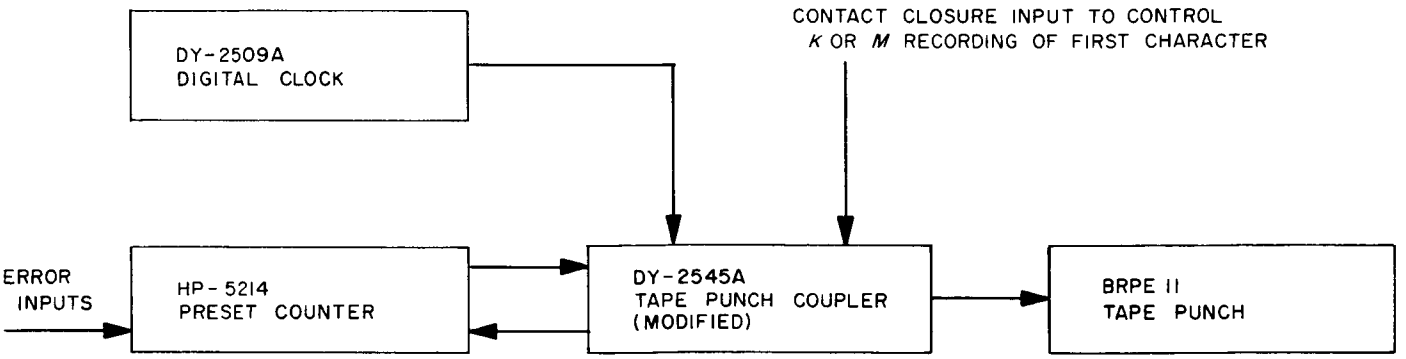


Fig. 3. DY-6691 counter–timer system for JPL

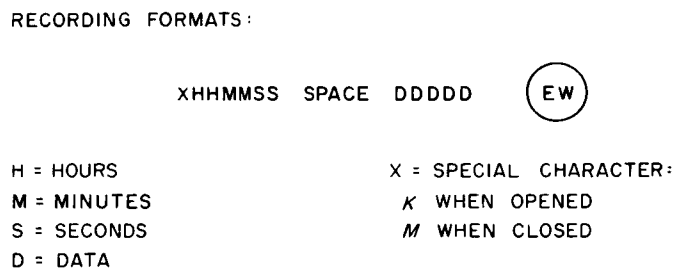


Fig. 4. Recording formats

like signal generated within the receiver. Any errors present are fed as voltage pulses to the error-counting equipment.

(2) During operational periods a relative error rate may be measured. Due to nine to five coding of the digital data, code groups are selected so that it is impossible for two logic *one's* to appear consecutively in the 9-bit data. Consequently, a fixed percentage of errors will appear as 9-bit consecutive *one's*. These consecutive *one's* are detected within the receiver and are routed as voltage pulses to monitoring equipment.

The error monitoring equipment consists of a counter, digital clock, and high speed paper tape punch, (Fig. 3). In operation, on command from the counter, error count and GMT are punched on the paper tape in the general format shown in Fig. 4. The paper tape, with its error data, provides a permanent record of line error characteristics.

In practice, the counter issues punch commands in either of two modes:

(1) By setting the unit to TIME INTERVAL, errors are read out in switch selectable increments of time.

(2) If the counter is in PRESET mode, errors and GMT are read out whenever the number of errors reaches a preset amount.

A computer program to reduce the error data reads the paper tape and provides outputs of error rate and performance evaluation. Thus, the error data may be used to provide a basis for more efficient data coding schemes.

IV. RF Systems Development

A. S-Band Waveguide Switch Development

1. Summary

Development has been completed of two- and three-position WR-430 waveguide switches used to calibrate the traveling wave maser, select antenna feeds for the parametric amplifier, select loads for the transmitter, and control antenna polarization. Prototype and production models have been tested and are being manufactured.

2. Background

Prior to 1963, there existed at JPL a requirement for several WR-430 waveguide switches to perform maser calibrations and radiometry switching at 2388 Mc, and transmitter load selection for the Venus radar antenna at the same frequency and a power level of 100 kw continuous wave (CW) or greater.

A survey of the market at that time indicated that no switches were available which would provide both high performance and high reliability. The most serious fault with available switches was the inferior performance of various drive mechanisms and control/indicator circuits. Therefore, JPL initiated both in-house and contractor-supported development programs to provide several switches of acceptable performance. As a result of these efforts, a new control/indicator circuit was developed, and marginally acceptable microwave performance was obtained in a three-position switch for radiometric work. The geneva drive mechanism for this switch, however, did not perform satisfactorily until the switching speed was reduced to 1.5 sec. For high power operation, a two-position switch was obtained by purchasing an acceptable switch without drive and assembling to it a unique drive mechanism which has performed satisfactorily on the Venus radar antenna, but which is slow and not readily adaptable to a three-position switch.

3. GSDS Development

Early in 1963 it became apparent that the S-band conversion of the DSIF would require more than 50 waveguide switches for transmitter load selection, maser calibration, and antenna polarization selection. Ease of fabrication and assembly, simplicity of field maintenance, and minimal necessity for spare parts dictated that all waveguide switches in the DSIF be as nearly identical as possible. It was decided to initiate a new procurement for

two prototype WR-430 waveguide switches (one two-position and one three-position) that would be essentially identical except for rotor and body layout, and which would use the well-proven control/indicator circuit developed at JPL and shown in Fig. 1 (as modified slightly for the production switches).

A survey was made of possible drive mechanisms, including all known switch drives then commercially available and the unique JPL drives. Since no one drive mechanism was outstanding, or even entirely satisfactory, the choice of drive was left unspecified in the request for proposals.

Out of nine requests there were two acceptable proposals; Ramcor, Inc. of Long Island, New York, was selected on the basis of slightly lower cost, and because Ramcor at that time was marketing an S-band switch with good microwave performance.

Immediately after award of this prototype switch contract in May 1963, a device manufactured by Commercial Cam & Machine Co. of Chicago, Illinois, came to the attention of JPL. This device, an indexing cam with zero backlash and a modified trapezoidal output acceleration for uniform input, appeared so promising that JPL directed Ramcor to investigate the device and use it for

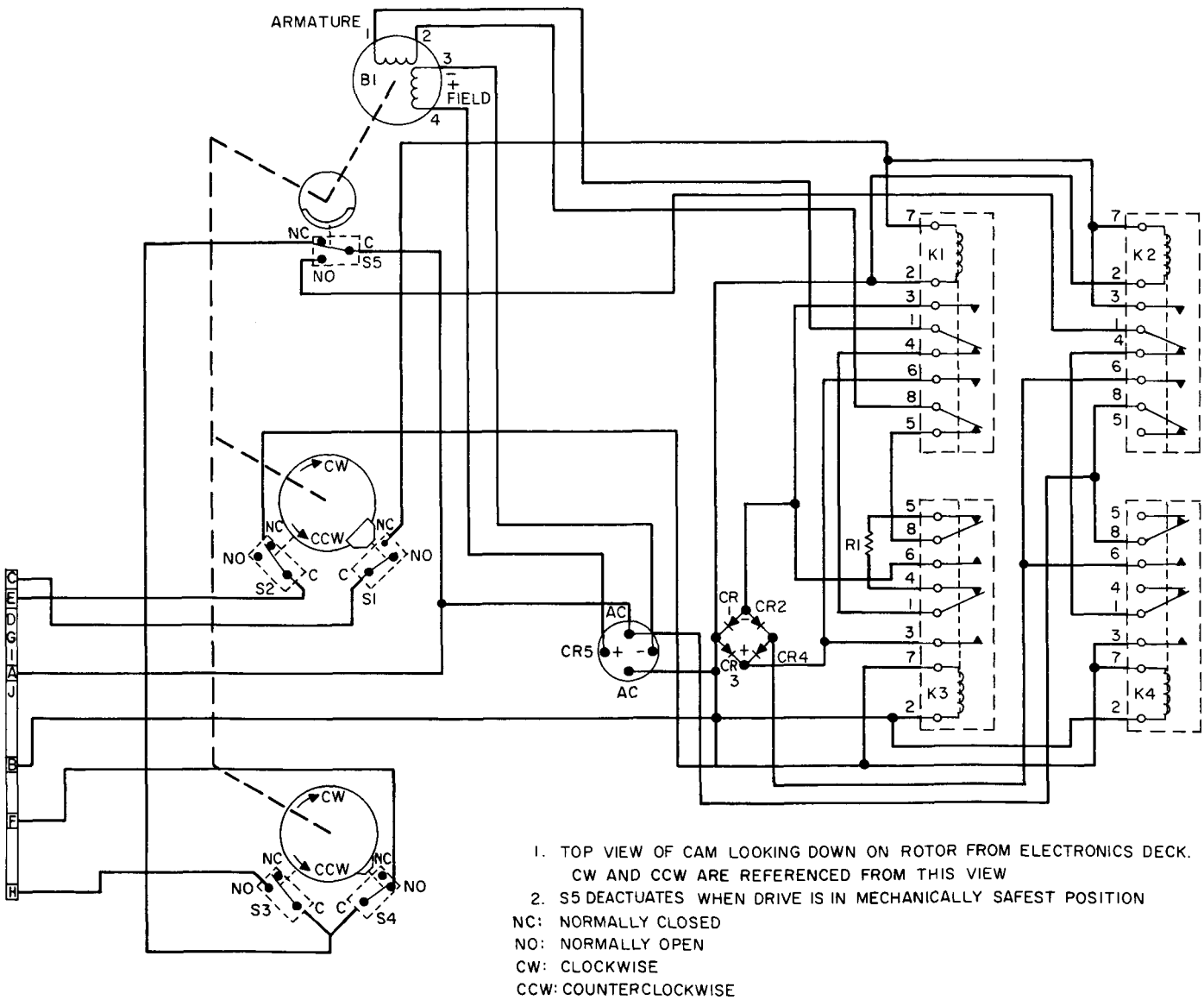


Fig. 1. Schematic diagram of waveguide switch (two-position)

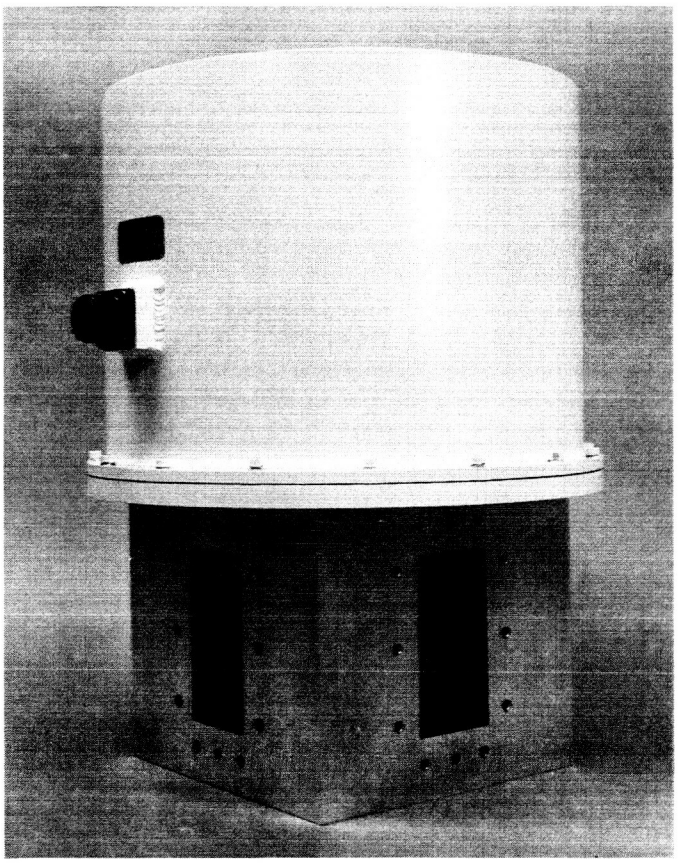


Fig. 2. Two-position WR-430 waveguide switch

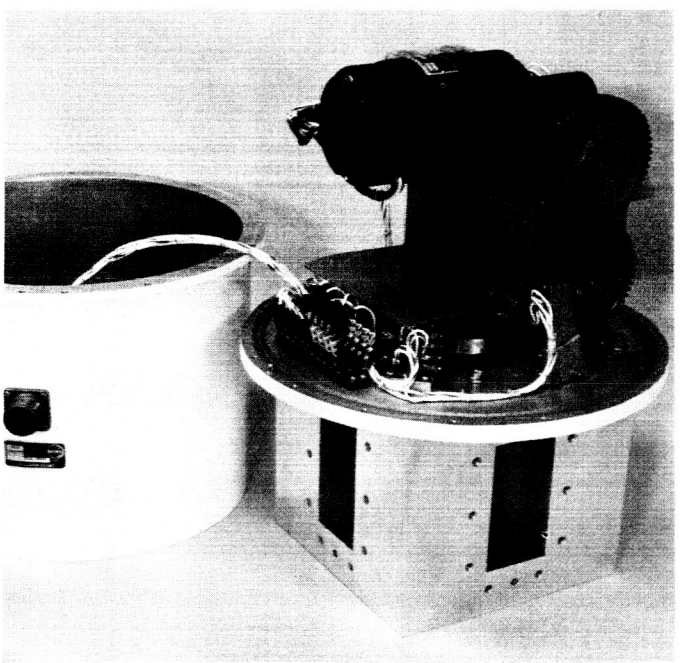


Fig. 3. Waveguide switch with cover removed

the switch drive, if possible. The device was successfully incorporated in both prototype switches, and after acceptance testing of the units at JPL, a production contract was awarded with only minor changes in the prototype design.

4. Results

A production model of the resulting two-position switch is shown in Figs. 2–4. In Fig. 3 may be seen the microswitch (S5) which rides on the lower transfer gear, and two of the four microswitches which ride the follower plate. Fig. 4 presents a close-up of the two-piece drive mechanism consisting of cam and follower plate.

The cam is driven through the transfer gears and a 30:1 gear reducer by a ¼-hp DC motor. The follower plate, with its preloaded roller bearing followers, is bolted and pinned directly to the rotor. The rotor and body are each machined from solid 7075-T6 aluminum forgings.

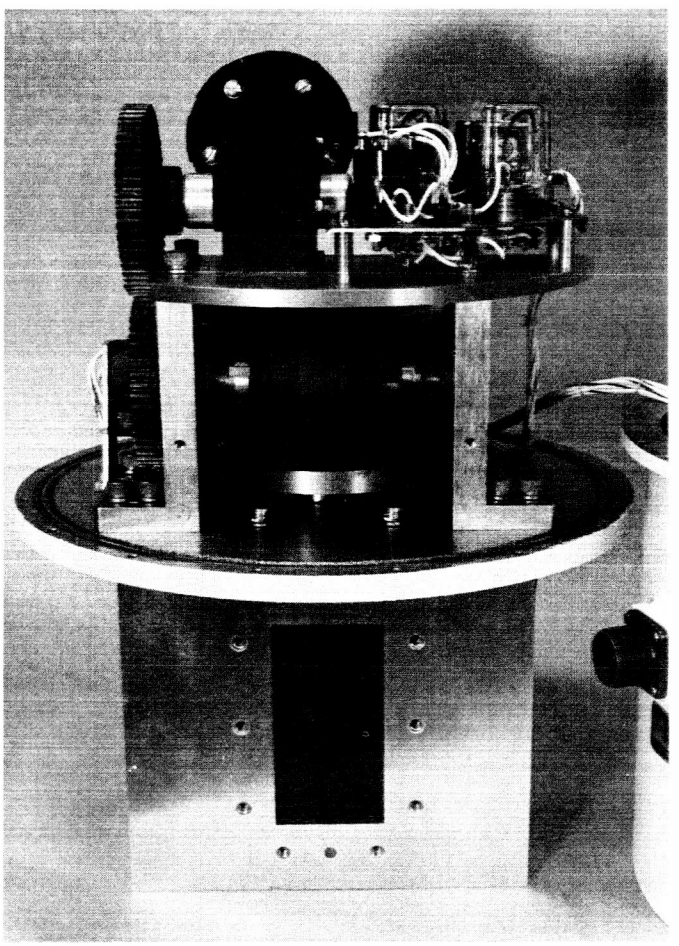


Fig. 4. Close-up of drive mechanism

The three-position switch (not shown) uses an identical drive system, except that it has eight microswitches for position control/indication. The three-position switch time between adjacent ports (one revolution of the cam) is 0.2 sec from command to verified indication. The two-position switch time between adjacent ports is 0.4 sec because the cam must rotate twice to turn the rotor 90 deg.

The VSWR of each switch is 1.01 at 2100 Mc; at 2300 Mc it is 1.01 for the three-position switch and 1.045 for the two-position switch. The isolation of each switch is greater than 60 db over this frequency band, and insertion losses vary from 0.02 to 0.035 db.

A total of 96 two- and three-position switches has been received and many have been in operation since January, 1964.

Two failures have occurred:

(1) A defective relay was discovered in one switch; replacement corrected the fault.

(2) Water was inadvertently allowed to enter one switch. During several months of storage and overseas shipment, corrosion occurred, causing an electrical failure in the control circuit. The switch was replaced.

In normal operation, no switch is required to handle more than 10 kw CW. However, all switches in the high-power waveguide runs are routinely tested at 17 kw CW, and one switch was successfully tested at 100 kw CW at 2388 Mc for more than 50 hr. No power failures have ever occurred in any switch. Typical use of these switches in the DSIF is described in *SPS 37-28*, Vol. III, p. 30.

V. Communications Engineering Developments

A. S-Band Implementation for DSIF

1. Traveling Wave Maser (TWM)

After several disturbing failures in the closed-cycle refrigerators (CCR) of the TWM/CCR assembly, all systems are now in satisfactory operation. Defects in the unit, problems with the compressor, and inadequate operator training have contributed to many apparent system failures. A memo, to up-date operator training while the instruction manual is being completed, is being prepared.

2. Acquisition Aid for DSIF

As part of the DSIF S-Band Implementation Project, an S-band acquisition aid subsystem (ACQ) has been developed for the 85-ft antennas. The first three systems, for Pioneer, Woomera, and Johannesburg, are now operational. The fourth subsystem, for Canberra, is presently being installed.

The DSIF-41 (Woomera) acquisition subsystem was successfully used during the recent *Mariner 4* tracking mission. The events recorded are given in Table 1.

Table 1. Events during *Mariner 4* first acquisition at DSIF-41

Event	Time: hr, min, sec
1. Receiver lock achieved	15:10:46.5
2. Spacecraft line-of-sight above local horizon	15:11:01.5
3. Servo auto track on acquisition antenna	15:12:00.9
4. Servo switchover to auto track on main antenna	15:12:10.7
5. Smooth tracking on main antenna	15:12:40
The total time of approximately 2 min for this sequence of events is well within the original design goal of 5 min for acquisition.	

3. Acquisition Aid for Ascension Island

An S-band acquisition antenna system is required for the DSIF-72 (Ascension Island) station. This system will facilitate acquisition of *Surveyor* immediately after appearance above the local horizon.

The required function of the DSIF-72 acquisition system is basically the same as for the existing 85-ft antennas at Goldstone, Woomera, and Johannesburg. Because of the large size and weight of the microwave equipment in these systems, however, it is not practical to use the same

design on the 30-ft DSIF antenna. An additional factor favoring a microwave redesign for Ascension Island is that the angular tracking rates and dispersions are somewhat different from those typically observed at the other DSIF stations, thereby possibly dictating a different gain/beamwidth optimum for the acquisition antenna.

Fig. 1 is a block diagram of the DSIF-72 acquisition aid system. Preliminary designs have been completed for the major components, and prototype units are being fabricated.

The transmitter horn is located outboard of one antenna elevation bearing to provide for: (1) convenient installation of the waveguide run to the electronics room; (2) alleviation of the problem of mechanical interference with the pedestal at low elevation angles; and (3) relative freedom from blockage by the 30-ft antenna apex and quadripod structure. A dominant mode conical feedhorn will be used as the radiating element. By using detachable sections to construct the associated horn flare, with the radome on the smallest section, it may be possible to have a variable beamwidth which may be chosen prior to each tracking mission. A series of scale model feedhorns is being fabricated to investigate this technique; it is presently anticipated that a half-power beamwidth range of 10 to 30 deg may be obtained, with a corresponding gain range of 24 to 14 db above isotropic.

The 2295-Mc tracking antenna poses a somewhat more complex design problem. A preliminary look at the question of optimum half-power beamwidth for reliable

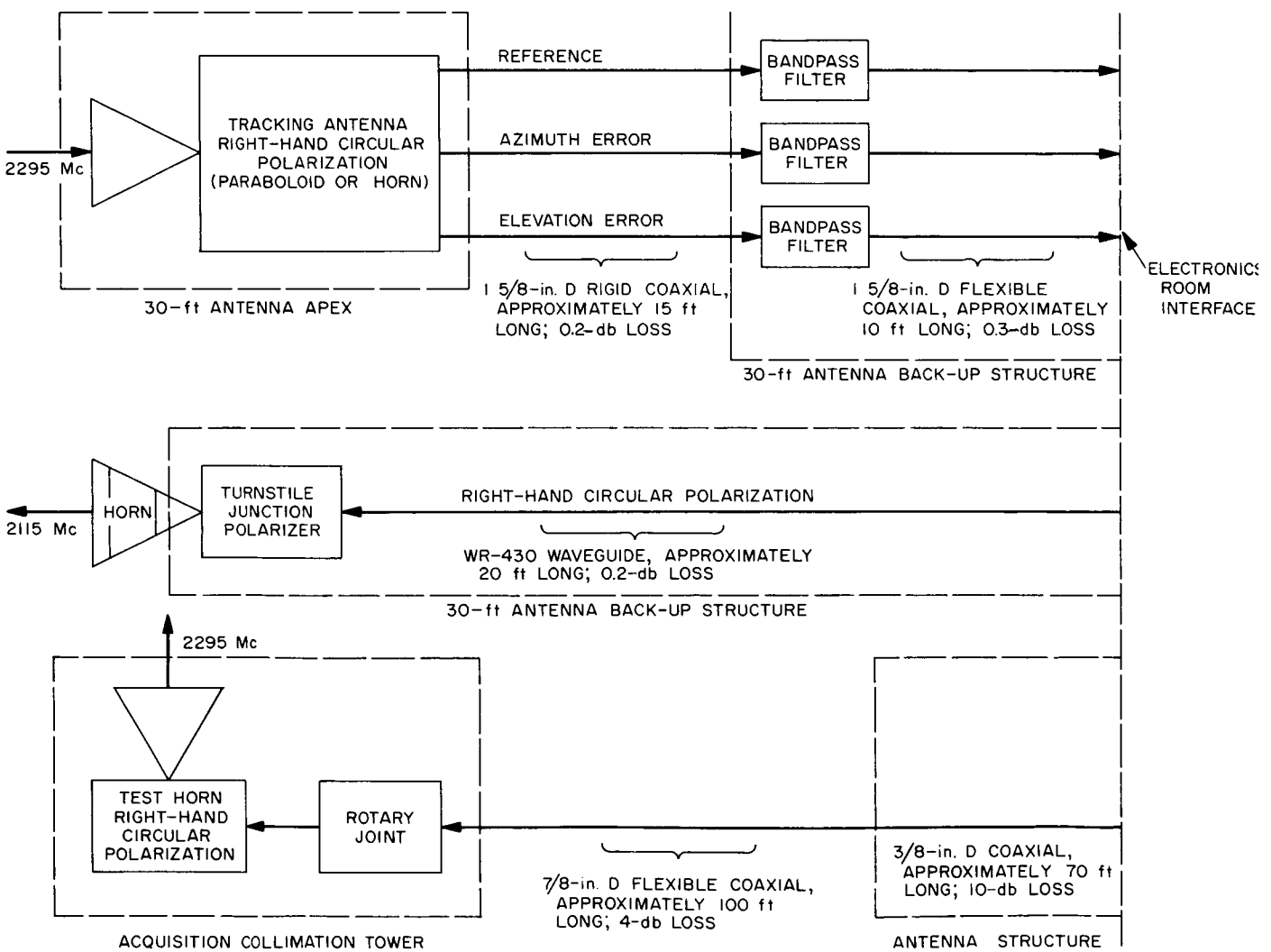


Fig. 1. DSIF-72 acquisition aid block diagram

acquisition indicates a range of 10 to 20 deg. For beamwidths less than 15 deg, the front-fed paraboloid appears to be the most practical type of antenna configuration; for beamwidths greater than 15 deg, the five-horn and multimode horn approaches appear best. Pending completion of the beamwidth optimization study, both the paraboloid and horn approaches are being considered.

A preliminary design for a suitable monopulse paraboloid feed has been completed. It has been shown previously by Hannan (Ref. 1) that a monopulse feed should have an error channel aperture width, in the null plane, approximately equal to the reference channel aperture width. In the error plane, the error channel aperture width should be approximately twice the reference channel width. A feed with these characteristics can be made to have high reference channel efficiency, high error channel slope, and low sidelobes in all channels.

A feedhorn having the desired characteristics is shown in Fig. 2; the associated bridge circuitry is shown in Fig. 3. This approach has the additional advantage (over the conventional four-horn feed) of having only one hybrid junction associated with each error channel, and hence much less severe problems associated with mismatches, dissipative losses, physical size and temperature stability. A possible problem area, however, is the noise temperature contribution due to coupling between the ambient terminations and the reference channel output; this effect will be investigated with a prototype feed presently being fabricated.

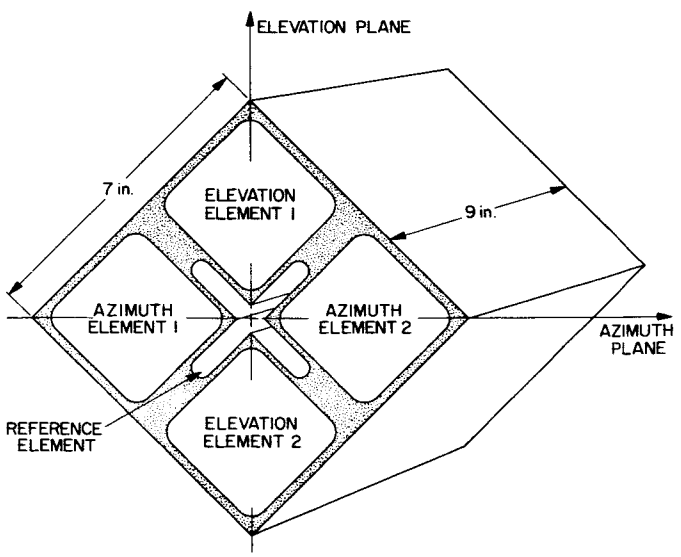


Fig. 2. Prototype monopulse feed configuration

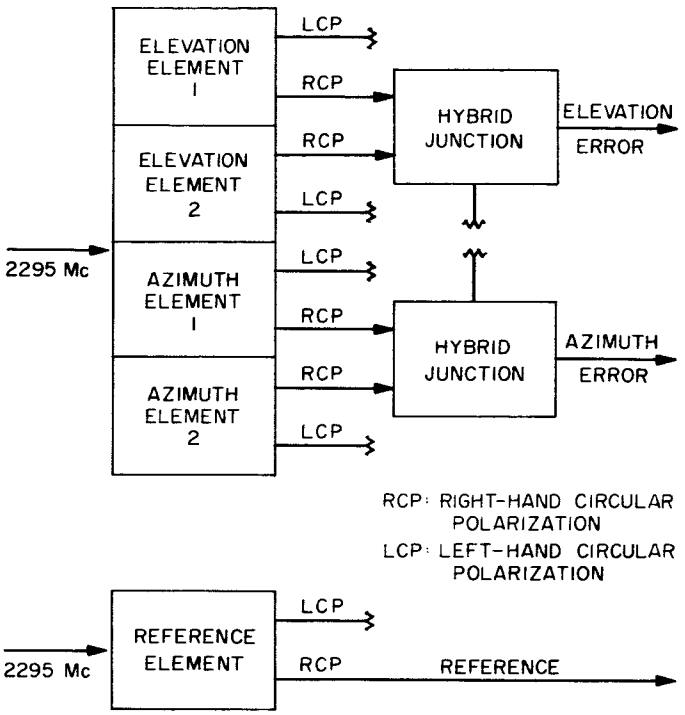


Fig. 3. Prototype monopulse bridge circuitry

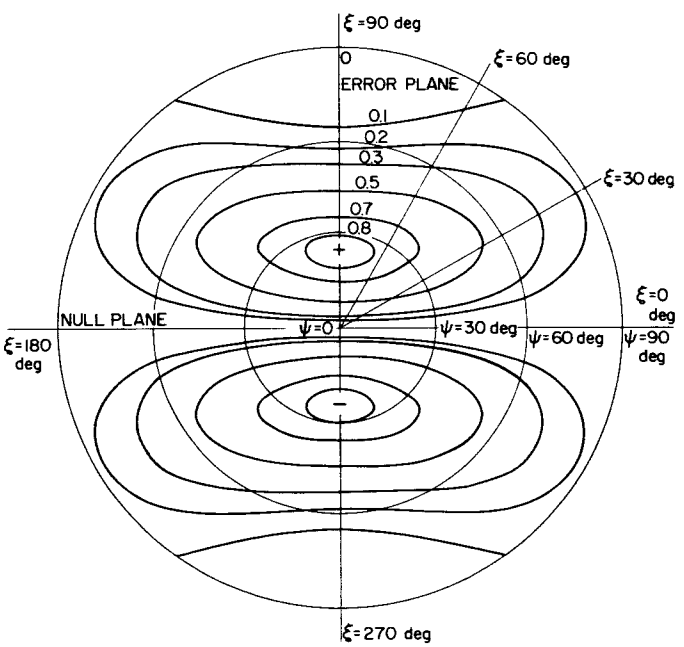


Fig. 4. Error channel aperture distribution

The error channel aperture illumination calculated for the prototype feed is shown in Fig. 4. Contours of constant aperture field are shown as a function of the feed polar and azimuthal pattern angles ψ and ξ, respectively.

It is clear from Fig. 4 that the aperture is efficiently utilized, while at the same time a strong tapering is introduced at the aperture edges, resulting in low error channel sidelobes. The secondary performance to be expected from this type of feed is presently being quantitatively investigated, utilizing the IBM 7094 Radiation Program (*SPS 37-21*, Vol. III, pp. 28–30).

If scaled down in angle (larger aperture), Fig. 4 indicates the type of error channel performance to be expected from a five-horn acquisition antenna. Thus, for beamwidths larger than 15 deg, a suitable approach appears to be the use of the basic feed unit with horn flare extensions rather than with a paraboloid. It is presently planned to investigate both approaches experimentally.

B. Ground Instrumentation for *Mariner C* Occultation Experiment

The *Mariner C* occultation experiment places unique demands on the measurement capabilities of the DSIF. The principal quantities to be measured are doppler frequency and received power versus time of the *Mariner* spacecraft S-band radio signal.

For the experiment, the second channel of the standard DSIF S-band receiver (described in *SPS 37-30*, Vol. III, pp. 34–35) will be used in a constant frequency, constant gain mode; the first receiver channel will be used in its normal phase lock mode and with essentially conventional doppler and signal amplitude instrumentation.

Essentially, the occultation experiment measures small perturbations of frequency and power produced by the planetary atmosphere. To make meaningful measurements, it is necessary to have good data about the steady state. Experiments are being conducted to measure the drift rate and stability of the *Mariner* spacecraft auxiliary oscillator by measuring the inflight one-way doppler and comparing it to the orbital predictions and obtaining the residuals. If evaluation of the data indicates a requirement, stability and drift tests will be conducted with the type-approval radio system in the environmental test facility. These tests would be designed to determine frequency stability and drift dependence on temperature.

It is also necessary to measure the actual inflight spectrum of the *Mariner* transponder in two-way lock. This will be accomplished with the receiver configuration described in *SPS 37-30*.

Measurements will be made to determine the spectral content of the S-band receiver dynamic automatic gain control (AGC). This data will be used to analyze the steady state stability of the power received from *Mariner C*.

C. Mesa Antenna Range: Anechoic Chamber Facility

Construction of the anechoic chamber building (*SPS 37-24*, Vol. III, pp. 97–99) at the Mesa Antenna Range has been completed. The structure is an addition to Building 212 (Fig. 5); it has been expanded to the west (Figs. 6 and 7). The new building houses two anechoic chambers, required control rooms, necessary assembly space, a control room for two outdoor ranges, and office space.

Lining the chambers with RF-absorbent material will be accomplished in four steps:

(1) Commercially available RF-absorber will be evaluated and tested to show which absorber is most efficient over the widest range of angles of incidence.

(2) A study by a commercial engineering company will determine the effect of baffling on the reduction of RF-reflections in the chambers. In this study, the following baffle configurations will be investigated: a transverse iris; a pair of transverse fences in either plane; pyramidal backwall; backwall at an angle; and different shapes of longitudinal baffling on all four surfaces.

(3) After checking the data provided by Steps (1) and (2), the smaller (K-band) chamber will be lined; the K-band chamber will then undergo tests to determine its performance.

(4) The X-band chamber will be lined, using information provided by Step (3) to make any possible

improvements in the installation of lining in the large chamber.

Present planning calls for both chambers to be lined and in operation by mid-1965.



Fig. 5. Building 212 before construction of addition

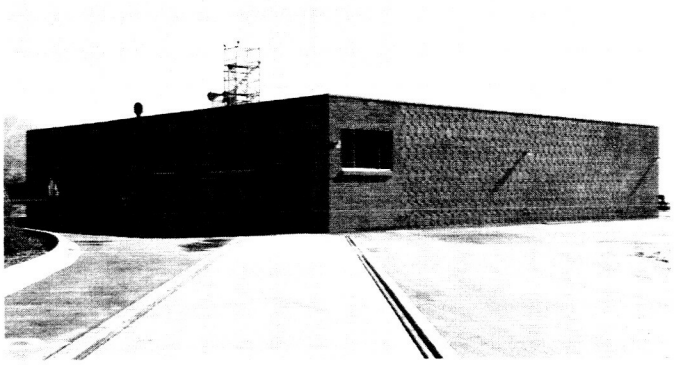


Fig. 6. Anechoic chamber addition viewed from the west

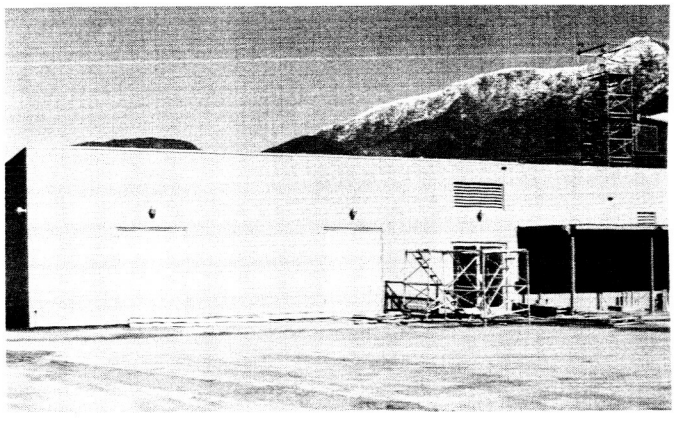


Fig. 7. South view of anechoic chamber addition

D. *Mariner C* 100-kw Transmitter

1. Introduction

A ground transmitter power of 100 kw continuous wave (CW) will be required for the *Mariner C* program under certain operating conditions. The complete transmitter program to meet this requirement consists of a 100-kw klystron amplifier subassembly, a ground test and checkout facility, and specialized controls for this installation.

2. Klystron Amplifier Subassembly

During this reporting period the klystron amplifier subassembly was operated in the cone test facility to obtain operating time on the components and to train personnel. At the same time, additional measurements were made to evaluate the subassembly.

As described in *SPS 37-30*, Vol. III, p. 36, the waveguide VSWR was calculated by measuring the forward and reflected power. To obtain a check on these measurements (Fig. 8) the VSWR was measured from the klystron out through the feedhorn for both Amplifier Number 1 and Number 2, using a reflectometer. The ratios, contained in brackets in Fig. 8, were obtained as described

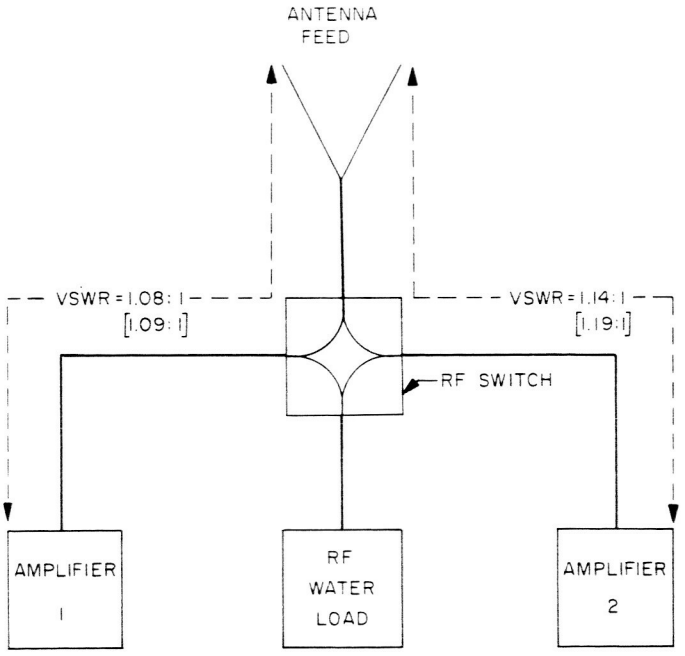


Fig. 8. VSWR measurements, *Mariner C* amplifier subassembly

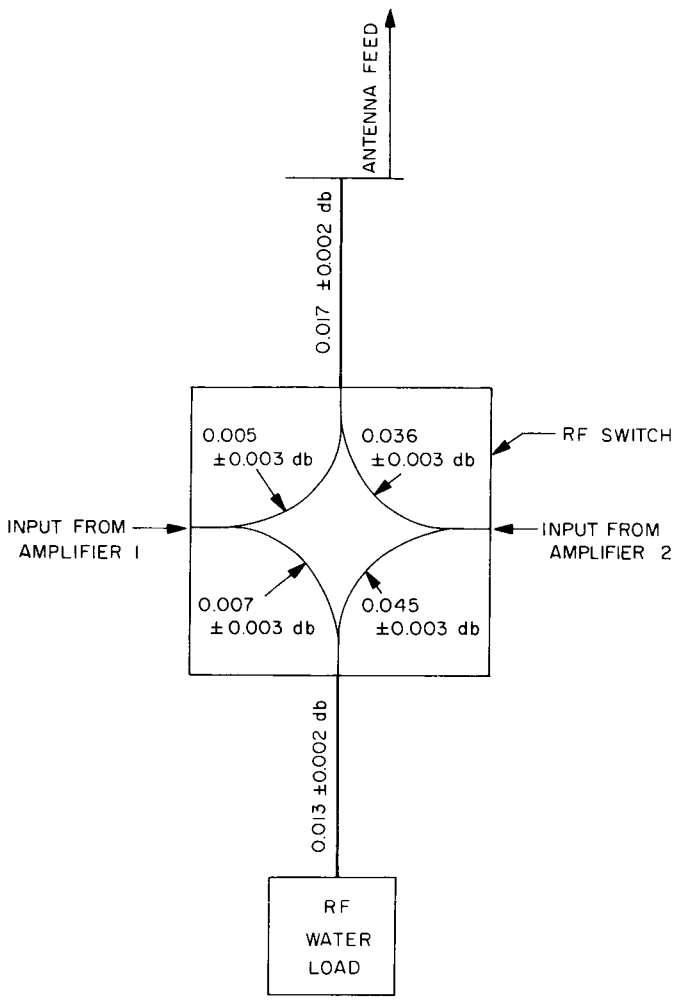


Fig. 9. Insertion loss measurements, *Mariner C* amplifier subassembly

in *SPS 37-30*. After the original measurements were made, calibration of the reflected power coupler on Amplifier 2 was checked and a 2-db error found in the coupling factor. If the original calculations are corrected for this error, the VSWR of Amplifier 2 out through the feedhorn was computed to be 1.14:1, which is in agreement with the reflectometer measurements.

Waveguide insertion loss measurements also were made to determine the amplifier RF power coupled into the antenna feed, together with the possible uncertainty of this measurement (Fig. 9). The water flow through the RF load can be measured to ±1 gal/min and the temperature differential of the water can be measured to ±0.1 deg. The uncertainty of the water load measurement is, therefore, ±0.026 kw. It was assumed that 1 kw is lost by radiation through the water load and associated waveguide. Results of these measurements are given in Table 2.

Table 2. Output power calculations

Amplifier 1		+db	−db
Power into water load	80.04 dbm	0.001	0.001
Insertion loss, load to switch	0.013 db	0.002	0.002
Insertion loss, through switch	0.007 db	0.003	0.003
Power into switch from Amplifier 1	80.060 dbm	0.006	0.006
Insertion loss, switch input to output	0.005 db	0.003	0.003
Insertion loss, switch output to antenna feed	0.017 db	0.002	0.002
Power into antenna feed from Amplifier 1	80.038 dbm	0.011	0.011
Amplifier 2			
Power into water load	80.04 dbm	0.001	0.001
Insertion loss, load to switch	0.013 db	0.002	0.002
Insertion loss, through switch	0.045 db	0.003	0.003
Power into switch from Amplifier 2	80.098 dbm	0.006	0.006
Insertion loss, switch input to output	0.036 db	0.003	0.003
Insertion loss, switch output to antenna feed	0.017 db	0.002	0.002
Power into antenna feed from Amplifier 2	80.045 dbm	0.011	0.011

Reference

1. Hannan, P. W., "Optimum Feeds for All Three Modes of a Monopulse Antenna I: Theory II: Practice," *IRE Transactions on Antennas and Propagation*, Vol. AP-9, No. 5, pp. 444–461, September 1961.

VI. Communications Research and Development

A. Ground Antennas

1. Antenna Instrumentation

A transportable instrumentation system is being developed for use in research and development testing of the structural and mechanical properties of large ground antennas. It has been used in a measurement program on the 85-ft antenna at the Goldstone Venus site; it will be used extensively during the alignment and testing of the 210-ft-diameter Advanced Antenna System (AAS). This facility was first used on the AAS Project during the recent initial lift-off and rotation testing of the azimuth hydrostatic bearing. During those tests it was used to measure and record the bearing film heights. There is a detailed description of the instrumentation system in *SPS 37-20*, Vol. III, pp. 31–34, and progress reports have been made in subsequent issues.

Because the major transportable instrumentation facility will be used continuously on the AAS Project during 1965, a small simplified transportable instrumentation facility is being prepared for use on other needed instrumentation work at Goldstone. The small facility is completely wired and awaits installation of data equipment, delivery of which is approximately 85% complete.

A data reduction program is being developed for reducing data obtained with the transportable instrumentation systems whenever the data logging systems are used (*SPS 37-30*, Vol. III, pp. 37–38). The recording format is identical for both systems, thus permitting standardization of the reduction program. This data reduction program is now being used to reduce measurement of surface waviness of the reflector panels and the dead-load deflection measurements on the 85-ft Az–El antenna. Some of the results of the dead-load deflection measurements have been reported (*SPS 37-27*, Vol. III, p. 54; and *SPS 37-24*, Vol. III, p. 33 and pp. 39–43).

During this reporting period, a digital plotting system was first used to plot results of laboratory and field testing of the film height probes used in the AAS hydrostatic bearing evaluation. The plotting system is compatible with the data recording system and produces 11- by 27-in. point plots of high accuracy from key-punch, or punched paper tape.

Tests are now underway at JPL and in the field to ascertain the reliability and stability of the film height measurement system for use in the interlock and/or alarm circuitry of the azimuth drive system.

2. Radio Calibration Techniques: Simultaneous Lobing Radiometric Tracking System

a. Summary. The S-band systems for the DSIF 85-ft and future 210-ft antennas will use simultaneous lobing angle tracking feed systems. A radiometer which could be used with the tracking feed would be a useful device for angle pointing and gain calibrations of the antenna system using radio star sources.

On the night of September 26–27, 1964, an experimental tracking radiometer was successfully operated at the Pioneer site of the Goldstone Tracking Station using the 85-ft antenna and the S-band receiver system. The results of this experiment can be found in *SPS 37-30*, Vol. III, pp. 42–44.

b. Recent work. After operation of the experimental simultaneous lobing radiometer at the Pioneer site, it was decided that the unit should be repackaged for ease of operation as a potential DSIF demonstration prototype. This has been done.

An analysis of the simultaneous lobing radiometer is given in *SPS 37-30*, Vol. III, pp. 38–42, in which it is shown that the output voltage from the radiometer is given by

$$V_{dc\,D} = 2AB\left(\frac{\omega_0}{\theta_0}\right)\left(\cos\theta_0 \sin\frac{BW}{2\omega_0}\theta_0\right).$$

Verification of this expression was obtained by setting up a step delay line at the IF frequency in one channel of the radiometer. The system was set up using a 10-Mc IF center frequency and a 6-Mc bandwidth. The results of this experiment are shown in Fig. 1 along with a plot of the theoretical curve. With the bandwidth and center frequency previously stated, the theoretical curve becomes

$$V_{dc\,D} = AB\left(\frac{4\pi \times 10^7}{\theta_0}\right)\left(\cos\theta_0 \sin\frac{12\pi \times 10^6}{4\pi \times 10^7}\theta_0\right)$$

$$= AB\left(\frac{4\pi \times 10^7}{\theta_0}\right)(\cos\theta_0 \sin 0.3\theta_0)$$

$$= AB\,(12\pi \times 10^6)(\cos\theta_0)\left(\frac{\sin 0.3\theta_0}{0.3\theta_0}\right).$$

Since the experimental curve had a peak of 1450 mv, the coefficient in the above expression was normalized to 1450, giving

$$V_{dc\,D} = 1450\,(\cos\theta_0)\left(\frac{\sin 0.3\theta_0}{0.3\theta_0}\right) \quad \text{millivolts.}$$

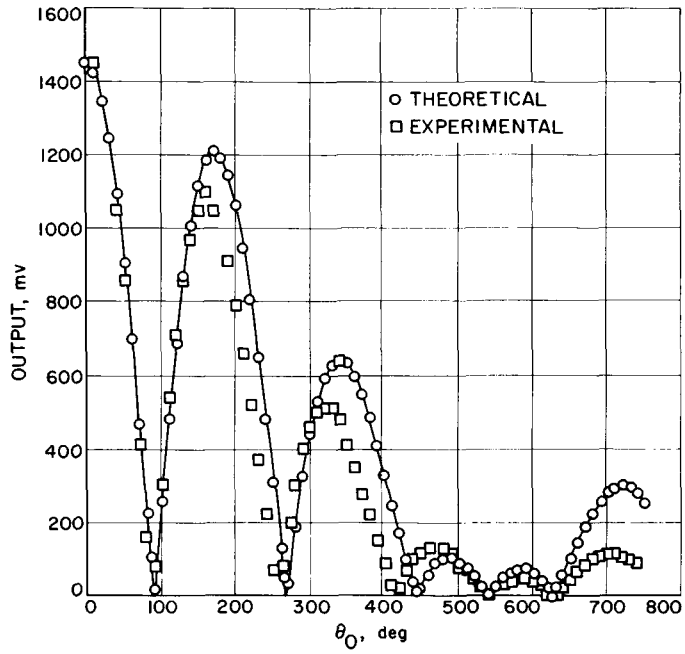


Fig. 1. Theoretical and experimental output from simultaneous lobing radiometer versus relative delay between channels

In order to obtain better agreement with the experimental curve, this expression was further modified, with the aid of an IBM 1620 computer to

$$V_{dc\,D} = 1450\,[\cos(1.008\theta_0)]\left[\frac{\sin(0.33333\theta_0)}{0.33333\theta_0}\right].$$

This result indicates that the delay line used was actually 0.8% longer than marked, and that the bandwidth of the system is approximately 6.6 Mc rather than 6 Mc.

3. Precision Drive System for 30-ft Antenna

The design, fabrication, and installation of the new precision servo drive system for the 30-ft Az–El antenna at the Goldstone Venus site has been reported previously (*SPS 37-26*, Vol. III, pp. 23–24; *SPS 37-28*, Vol. III, p. 46; and *SPS 37-29*, Vol. III, pp. 41–45). The definitive testing of the system to obtain over-all transfer functions has not been completed; however, some tracking data are available. During the 20- to 24-Gc Venus black body radiation experiments, some tracking performance information was accumulated. Fig. 2 is a typical record of the slave mode tracking error recorded during the Venus experiment. The error signal recorded, which is the signal fed to the servo valve, is the difference between the computed

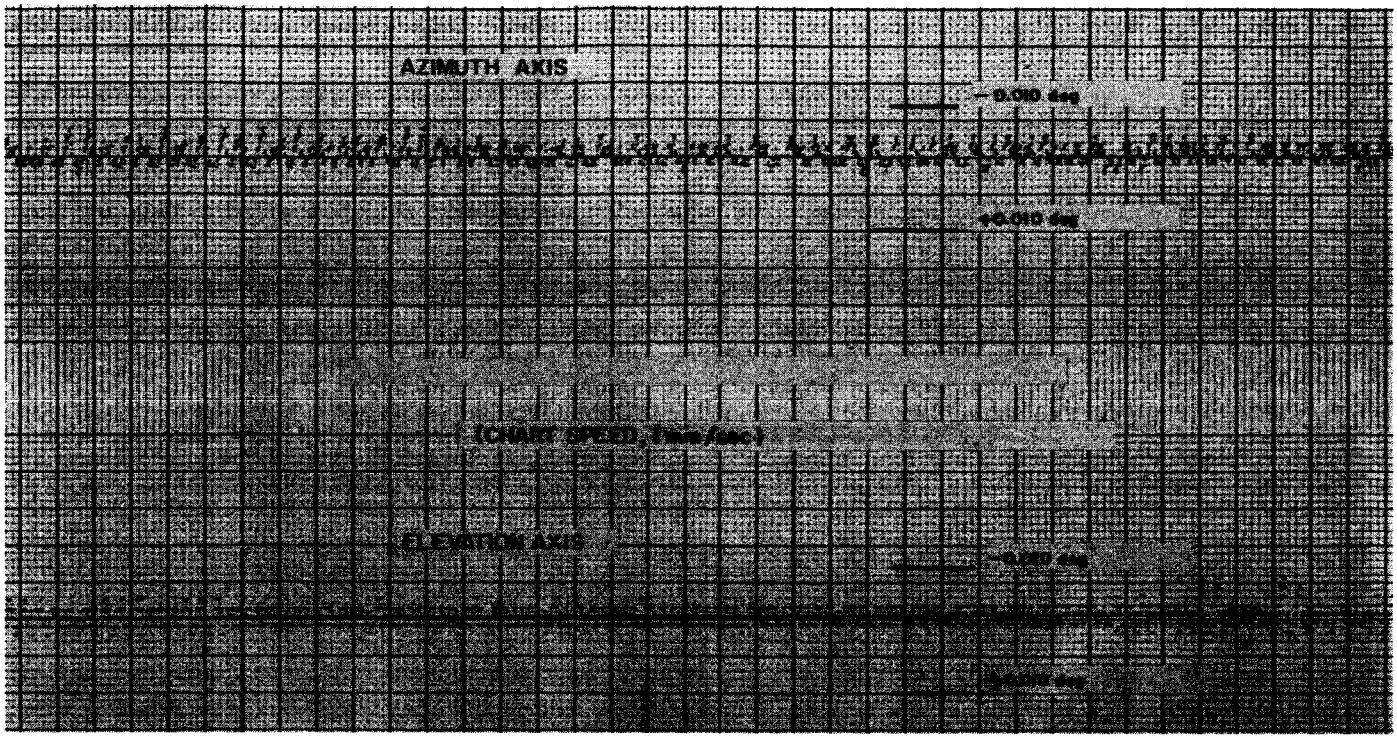


Fig. 2. Typical tracking error during Venus experiment

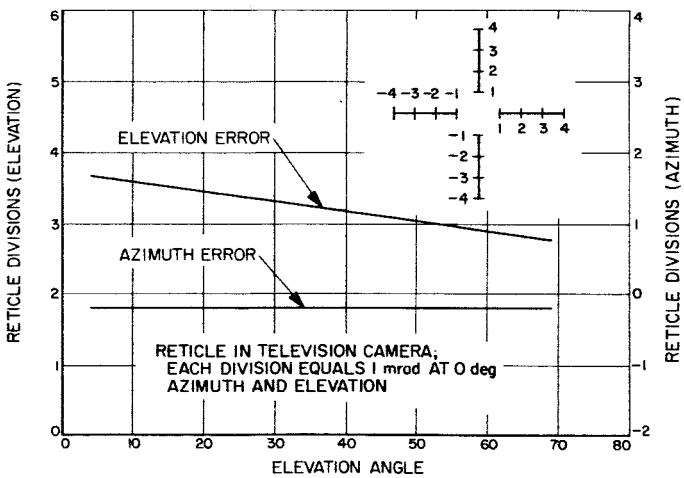


Fig. 3. Relation between RF axis and TV optical axis

ephemeris from the SDS 910 computer and the antenna data readout system. The servo system in the slave-track mode is a Type II system with an integration time constant equivalent to a bandwidth of approximately 0.1 cps. The record (Fig. 2) was made near the meridian crossing of the planet; the rates in elevation were very close to zero, and the azimuth rates were approximately 0.008 deg/sec.

During the Venus experiment, a record was made of the visual position of the planet on the boresight TV camera corresponding to the on-planet position of the antenna RF axis. Fig. 3 is a plot of the data. The information used to generate this figure was obtained in the first 5 days of tracking, and during the course of the experiment it was regularly rechecked. No attempt was made to remove the error, only to record it; the errors were removed during data reduction.

A hydraulic rotary joint is used to carry high-pressure fluid across the azimuth axis to the elevation drive motors. The original design of the rotary joint required pressure at all times to provide sealing of the fluid; also, the compression of the high-pressure Chevron packing was not accomplished by positive means. Some modifications have been made to improve the joint performance; in the modified design shown in Fig. 4, all of the original major components were utilized (the three inner shells, as well as the outer Chevron packing glands). Positive pressure on the packing is obtained by the sizing of the back-up rings. This sizing operation is accomplished by several assembly and test cycles, optimizing minimum driving torque with maximum allowable leakage. The leakage is not external; however, it is retained and returned to the reservoir. One set of "quad-rings" was removed in the

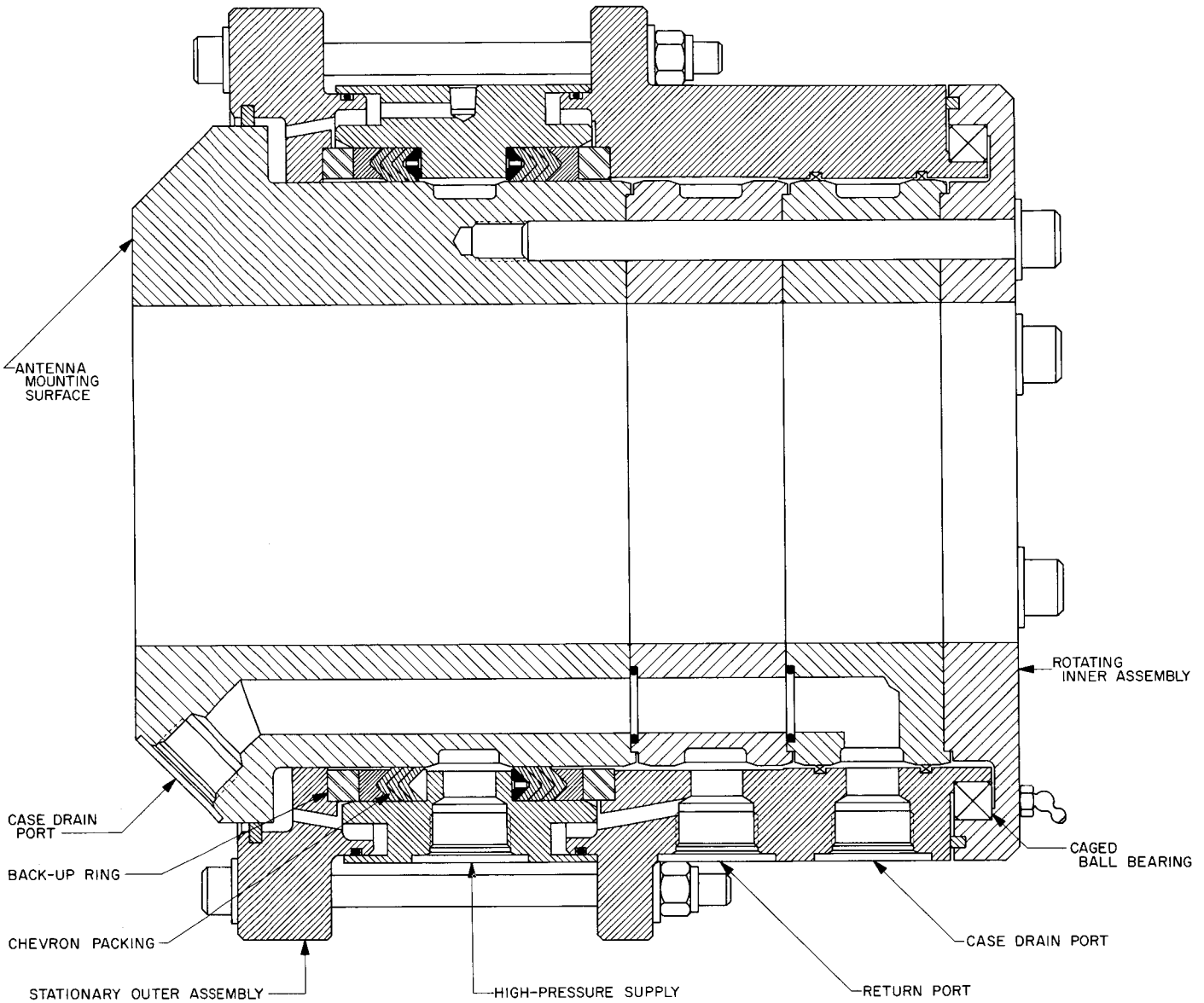


Fig. 4. Modified rotary joint

redesign to reduce drive torque. By placing the return cavity between two already dynamically sealed cavities and adding static seals to atmosphere, the removal was accomplished. In addition, a caged ball bearing was added to control concentricity of the inner and outer assembly and to control preload. This bearing replaces a row of plain balls that afforded only partial concentricity control. The method of restraint was also redesigned, eliminating any loading on the assembly other than a torsional couple. This is accomplished by diametrically opposed restraining rods that accept only tension and compression. The modified rotary joint will be installed on the antenna early this Spring.

B. Experimental Closed Cycle Refrigerator for Masers

1. Introduction

In a continuing effort to provide the DSIF with more reliable cryogenic refrigerators for low-noise amplifiers and related cold load instrumentation, a feasibility demonstration version of a new helium refrigerator has recently been operated.

The new machine uses the Gifford cryomatic gas balancing technique (U.S. Patent 3,119,237) to provide the

refrigeration needed to cool helium gas to 16°K; the gas is then allowed to expand in a Joule-Thompson (J-T) stage and cools itself to 4.2°K. The advantage of the gas balancing technique over more conventional designs is that of increased reliability resulting from a simpler driving arrangement for the engine. The thermodynamic cycle used is similar to the Gifford-McMahon cycle used in the A. D. Little cryodyne.

The feasibility model was developed through a joint effort between JPL and Professor W. E. Gifford of Syracuse University. Professor Gifford is a consultant to JPL under a study contract.

2. Current Activities

A feasibility model of an advanced refrigerator for cooling a maser has been built and is currently being tested. The guiding philosophy has been to design a refrigerator which is as simple as possible. Not only can increased reliability result from this, but equally important is the possibility of concomitant reduction in fabrication costs. Fortunately, the performance of the new machine also appears better than previous designs.

The principal features of the refrigerator are as follows:

(1) 750-mw refrigeration capacity at 4.4°K.

(2) No-load cool-down time of 2½ hr.

(3) Elimination of all controls on refrigerator. (All control functions can be performed at compressor.)

(4) Motor driven valve assembly contains only one moving part.

A compatible compressor assembly is now under construction.

a. Theory of operation. Since this is a first reporting of the project, a concise but complete qualitative description of the refrigerator will be given.

All cryogenic refrigerators which achieve liquid helium temperatures make use of cooling by expansion of helium gas in a J-T process. However, it is necessary to first cool the gas to below the inversion temperature (~30°K) before this process can be used. (Above the inversion temperature the J-T process will produce heating.) Various schemes have been proposed and tried; these schemes generally differ only in the way in which the helium gas is cooled for the J-T expansion, preferably to 16°K or lower. The principal advantage of the Gifford gas balancing machine as compared with the others is that of simplicity resulting from the fact that all critical moving parts are at ambient temperature.

b. Gas balancing refrigeration method. Fig. 5 shows schematically a single-stage machine. A compressor supplies helium gas to the refrigerator via a small motor driven control valve; the following cycle occurs at a rate of 1 to 2 cps.

(1) High-pressure gas is admitted to V_1; this drives the piston P downward along with the displacer D (made of insulating material).

(2) With high pressure continuing to be applied to V_1, the valve now permits gas to fill the regenerator R and V_2.

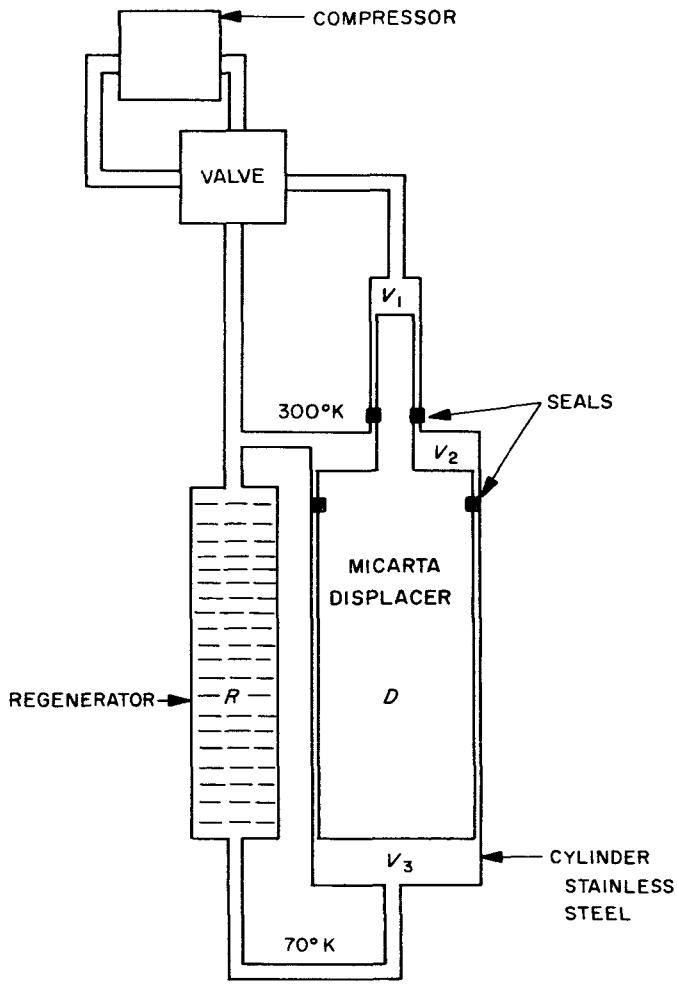


Fig. 5. Schematic diagram of single-stage "gas balancing refrigerator"

(3) With high pressure continuing to be applied to V_2 and R, the valve now connects V_1 to the low-pressure line. This causes the displacer to move up and displace the gas from V_2 to V_3. The gas actually deposits a quantity of heat Q with the regenerator material as it moves into V_3.

(4) With low pressure remaining at V_1, the valve now connects V_2, V_3, and R to the low pressure. The high-pressure gas then expands out of V_3, giving a refrigeration effect Q_r equal to the product of the displaced volume and pressure difference. The gas expands out through the regenerator where it picks up some of the previously deposited heat Q_1. Note that the displacer does no mechanical work as is done in the more familiar Collins cryostat.

(5) The cycle is completed when step (1) is repeated. This causes the cold gas to be driven out of V_3 through the regenerator, which it further cools by picking up the remainder of the heat Q_1 previously deposited there.

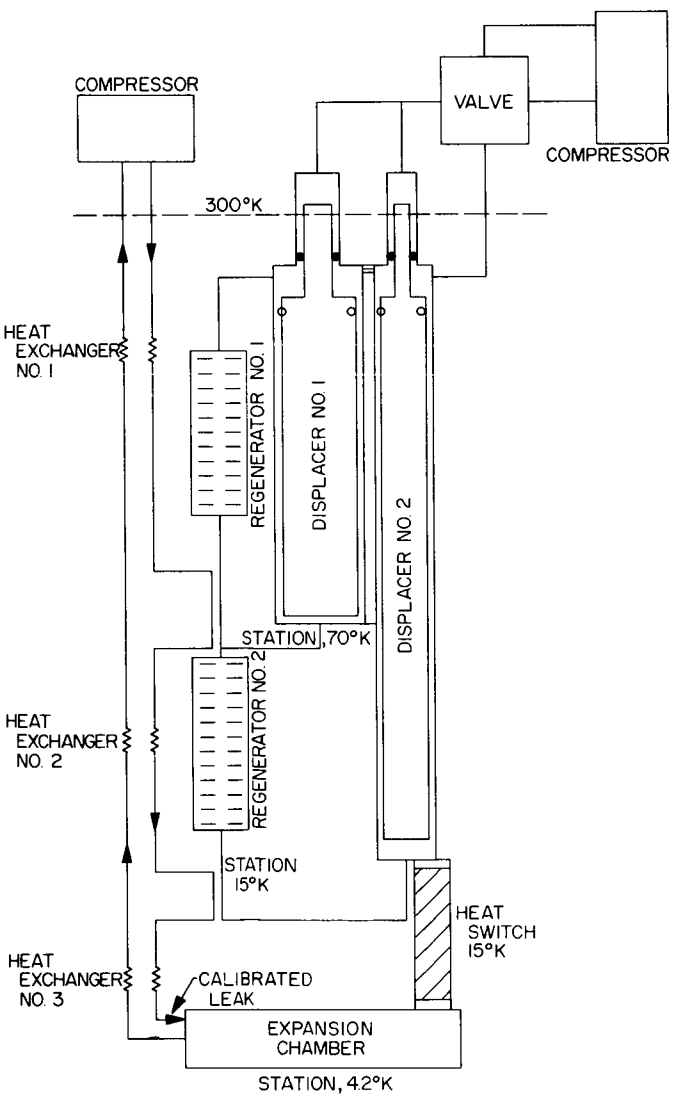


Fig. 6. Two-stage machine with J-T expansion stage added

A single-stage machine will provide refrigeration at 60 to 70°K; a second stage, as shown in Fig. 6, is used to provide cooling to 15 to 17°K, which is required for the J-T circuit.

c. The J-T stage. Fig. 6 shows a two-stage engine with a J-T circuit added for the final refrigeration to 4.2°K. Helium gas, compressed to approximately 20 atm, is cooled by the 60° and 15°K stations, then allowed to expand to 1 atm. A liquid–gas mixture is produced in the 4.2°K station for cooling the maser. The cold gas returns to the compressor through three heat exchangers and helps to cool the incoming gas. The J-T process is simple to utilize, but the success depends on the efficiencies of the heat exchangers.

The thermal switch between the 15° and the 4°K stations is required to initially cool the latter stage to 15°K so that the J-T process may be initiated. Schematically, the newly developed switch is shown in Fig. 7. A tube filled with hydrogen gas contains two sets of copper plates in proximity to each other; one set of plates is in contact with the 15°K station; the other with the 4°K station. The hydrogen gas provides good heat conduction until the entire structure is cooled to around 15°K; at this point the hydrogen is solidified, and the two stations are then thermally isolated as required.

Another innovation has been the use of a fixed J-T valve to simplify the machine. A calibrated leak is used to provide the required flow rate of gas. This eliminates a few mechanical linkages and reduces the chances for gas leaks.

C. Experimental X-Band Lunar Radar

1. Black Body Measurements of the Moon

a. Summary. During recent tests with an experimental X-band radar at the Goldstone Venus site, thermal radiation measurements of the Moon were made. The antenna temperature from the Moon was approximately 120°K.

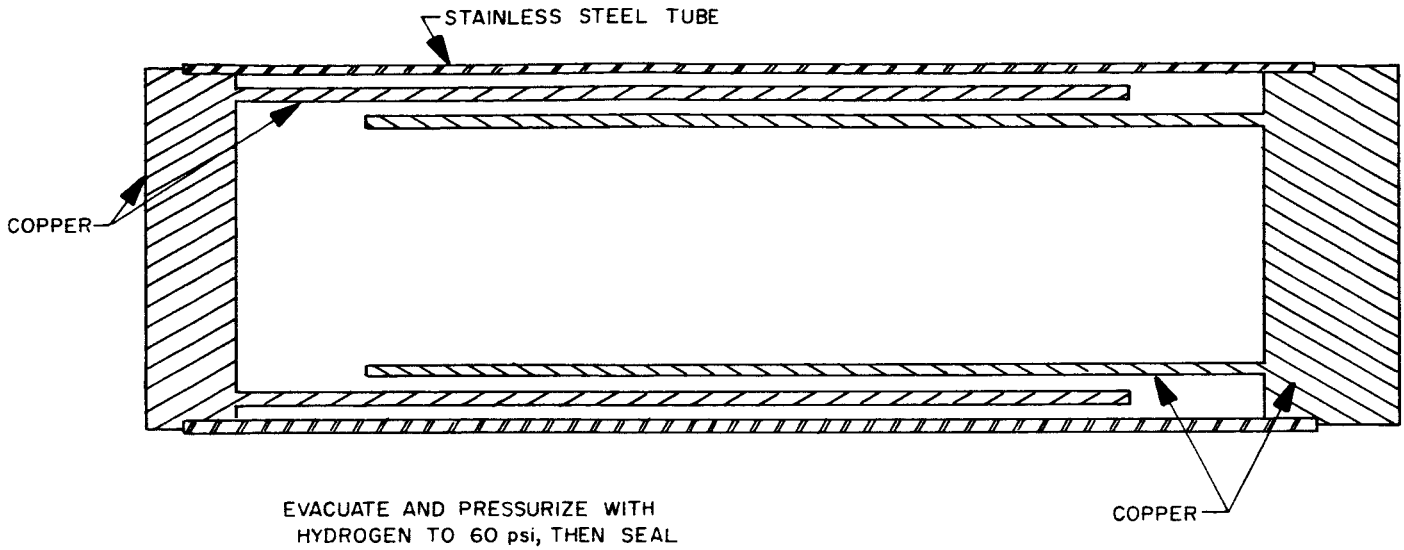


Fig. 7. Cross-sectional view of heat switch

b. Recent work. The 8448-Mc maser and instrumentation mounted on the 30-ft antenna at the Goldstone Venus site (*SPS 37-30*, Vol. III, pp. 50–53) was used for black body measurements of the Moon. The microwave instrumentation is shown in Fig. 8. The receiving system was used as a "total power" radiometer to take standard "half drift curves" of the Moon. With the maser switched to the antenna, the Moon was tracked and the total power recorded. When the antenna stopped tracking the Moon, the time and antenna position were noted. After the Moon drifted out of the antenna beam, the maser input was switched to the ambient and liquid nitrogen cooled termination, respectively. For the sample recording shown in Fig. 9:

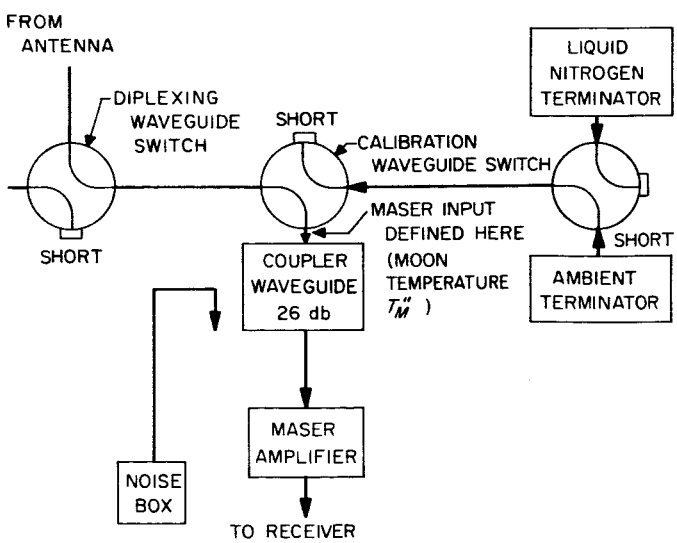


Fig. 8. Block diagram of X-band maser instrumentation

Date	November 7, 1964
Time	22:35 GMT
Azimuth	183.9 deg
Elevation	30.1 deg
Receiver, 3-db bandwidth	9 Mc
Recorder time constant	0.1 sec

The liquid nitrogen cooled termination has been calibrated (*SPS 37-30*, Vol. III, pp. 56–61). For this typical recording, with an ambient temperature of 19.7°C, the difference between the ambient and cryogenic termination is 195.7°K. The increase in system temperature defined at the maser input is 121.9°K. This is the Moon temperature, T_M', defined at the maser input. A graph of the measurements made between October 27 and November 8 is shown in Fig. 10. The weather was cloudy during the measurements of November 3 and 7. The average measured temperature (not including that taken during cloudy weather) was 120°K. To refer these temperatures to the Moon to obtain the actual measured Moon temperature, T_M, corrections must be made for the waveguide loss between the maser and the antenna, antenna beam efficiency, and atmospheric loss.

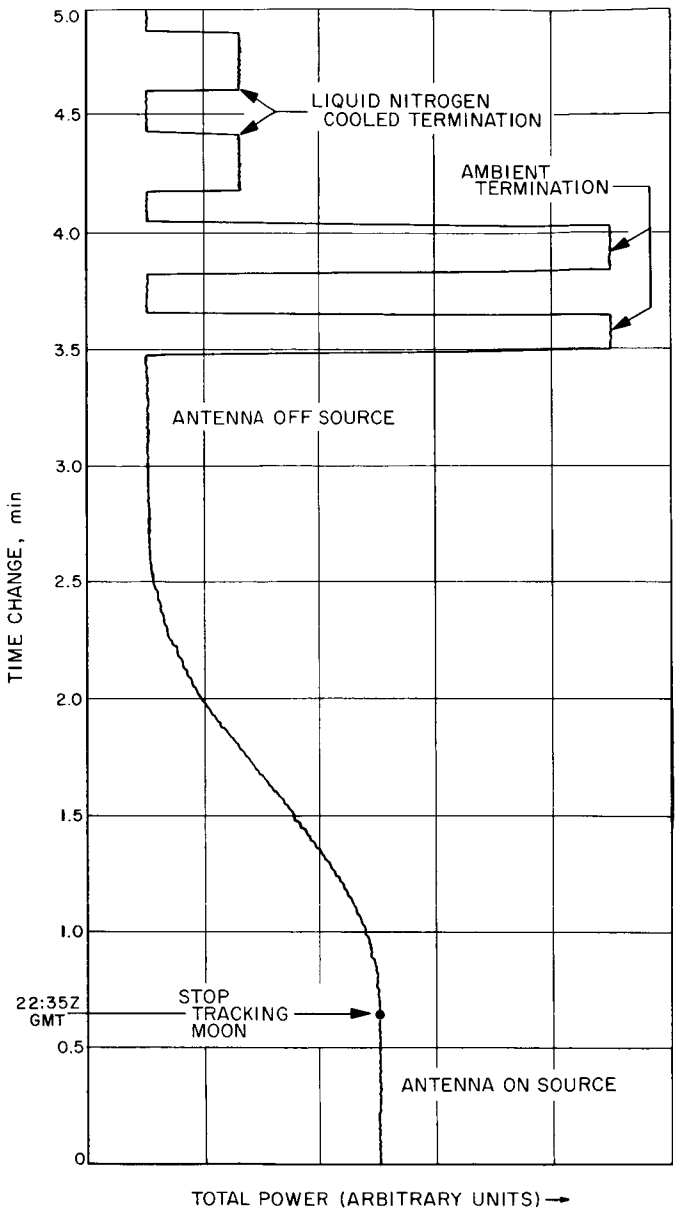


Fig. 9. X-band "half drift curve" of Moon taken with Venus site 30-ft antenna, November 7, 1964

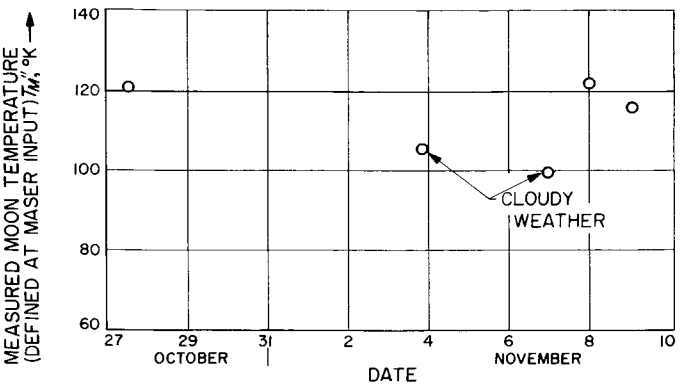


Fig. 10. Measured Moon temperature (defined at maser input) versus date

2. Feed Performance

a. Summary. The feed for the X-band lunar/planetary radar is a Cassegrain configuration consisting of a 24λ diameter hyperboloidal subreflector illuminated with a dual mode horn. The horn is excited in either a circular polarization (CP) mode or linear polarization (LP) mode through the use of a turnstile junction polarizer.

Experimental data using this feed, as installed on the Goldstone Venus site 30-ft reflector, have been previously reported in *SPS 37-30*, Vol. III, pp. 61–63. During November 1964, far-field radiation patterns of the system were obtained.

b. Recent work. Far field radiation patterns of the X-band 30-ft reflector system have been obtained using the Tiefort Mountain collimation tower. Because the collimation tower is approximately 13 mi from the radar site, the $2D^2/\lambda$ minimum range requirement of 3 mi is well satisfied. Rotatable linear polarization was used on the collimation tower source, and 30-ft reflector patterns were taken as a function of polarization and plane of cut.

Fig. 11 shows azimuth E- and H-plane patterns of the system, while Fig. 12 depicts elevation E- and H-plane performance. Because some initial radar data has been collected using the Moon as a target, the average Moon diameter has been plotted for convenience. A comparison of Figs. 11 and 12 shows some degradation of symmetry in the elevation plane, particularly in the first sidelobe levels and depth of second nulls. In Fig. 12 the truncated (right) side occurs when the reflector is oriented to look below the local horizon (−1.1 deg) at the local terrain. It is, therefore, difficult to ascertain whether the cause of the asymmetry is due to gravity-induced structural deflections and/or rotation (tilt) of the hyperboloidal subreflector-quadripod assembly or ground reflections.

Some evidence exists suggesting that deflections are the cause. As reported in *SPS 37-21*, Vol. III, p. 24 and *SPS 37-23*, Vol. III, p. 34, a previous X-band (8450-Mc) Cassegrain feed has been evaluated on the Goldstone 30-ft reflector. Elevation plane patterns obtained during the 8450-Mc study also show asymmetric sidelobes with approximately the same amplitude unbalance, but with opposite sense; i.e., the sidelobe observed with the reflector looking at the local terrain was higher rather than lower, as Fig. 12 shows. The significant difference between

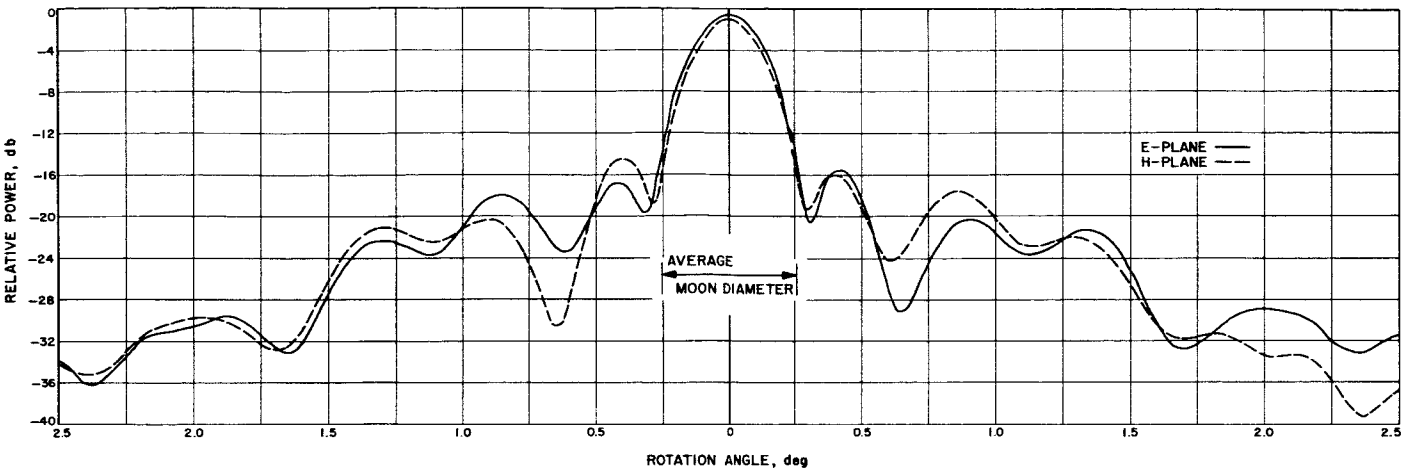


Fig. 11. 8448-Mc, 30-ft reflector azimuth patterns

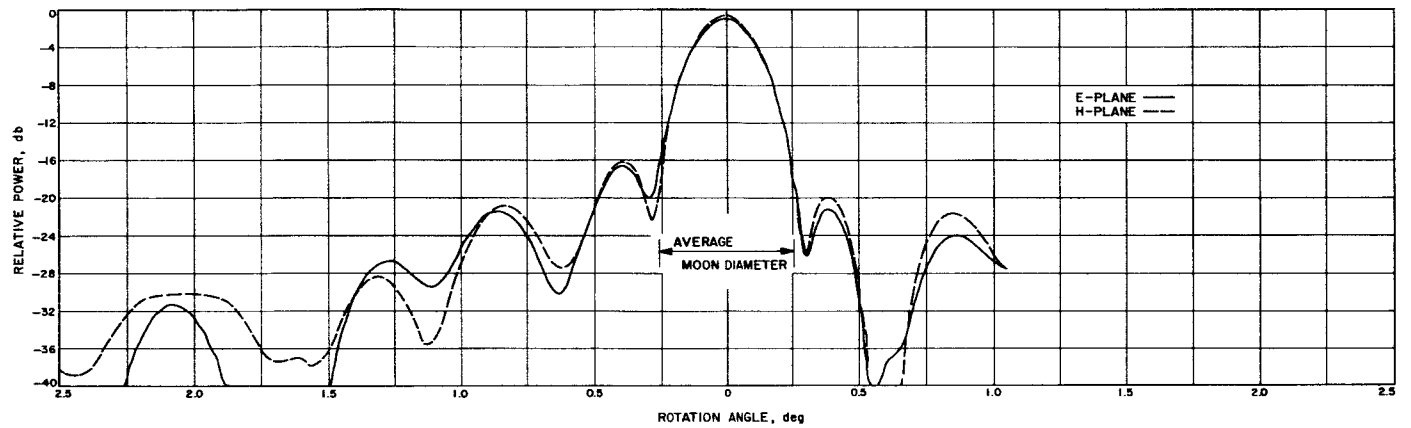


Fig. 12. 8448-Mc, 30-ft reflector elevation patterns

the two X-band hyperboloid positioner–quadripod assemblies used is shown in *SPS 37-21*, Vol. III, Figs. 21 and 27, which depict the 6-ft reference antenna mounted at the quadripod apex, on the feed positioner. It is felt that the 6-ft reference antenna did act in a counterweight fashion during the 8450-Mc tests. During the recent 8448-Mc radar tests, the 6-ft antenna was deleted, therefore increasing the possibility of hyperboloid translation and/or tilt. Monopulse Cassegrain work conducted at 16 Gc, reported in *SPS 37-30*, Vol. III, p. 110 also without the counterweight, supports this hypothesis.

Figs. 13 and 14 illustrate 45-deg plane patterns for the radar system, as a function of polarization. 45-deg plane patterns are obtained by slewing the reflector simultaneously in azimuth and elevation at the same rates, from starting offsets of equal magnitude in azimuth and elevation, thereby driving the structure through the collimation tower boresight. The axial symmetry in Figs. 13 and 14 is considered poor for X-band wavelengths, but is expected to improve at higher elevation angles.

Prior to the pattern measurements, the RF boresight coordinates for the Tiefort Mountain collimation tower were re-evaluated. Table 1 shows the RF boresight coordinates measured in November 1964; for completeness, previous determinations reported in *SPS 37-30*, Vol. III, are repeated. It is apparent from Table 1 that a significant (0.025 deg) offset was required in azimuth after

Table 1. Tiefort Mountain RF boresight coordinates, 8448 Mc

Date (1964)	Polarization	Azimuth, deg	Elevation, deg
November	Vertical	79.577	0.762
November	Horizontal	79.570	0.757
October	Vertical	79.598	0.764

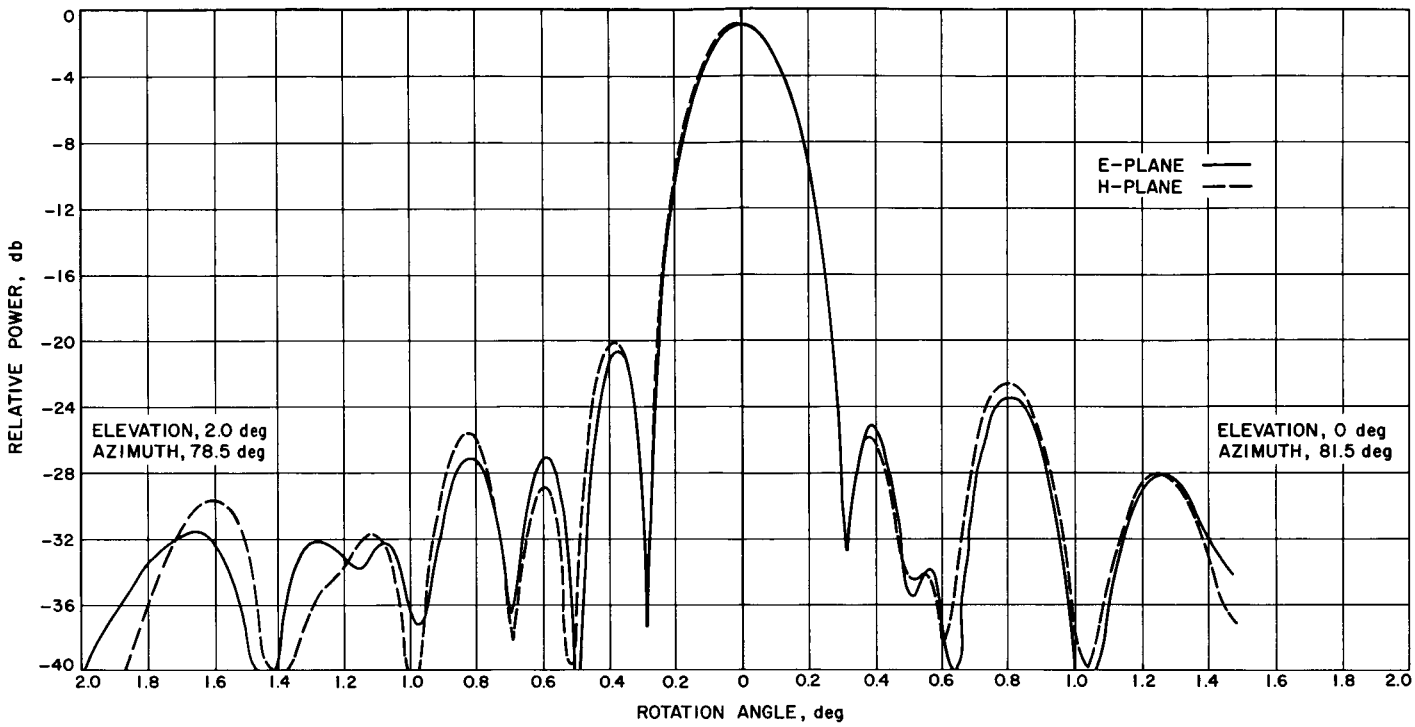


Fig. 13. 8448-Mc, 30-ft reflector 45-deg plane patterns, S–N

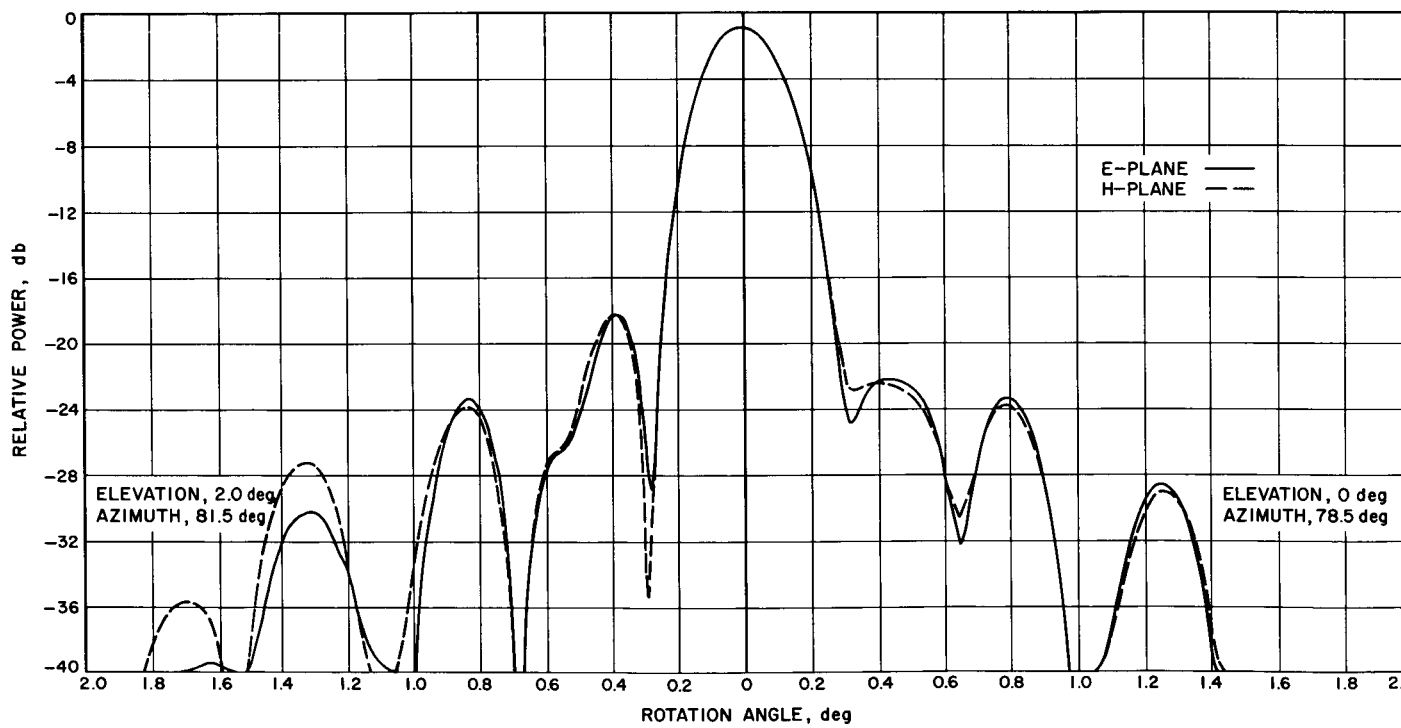


Fig. 14. 8448-Mc, 30-ft reflector 45-deg plane patterns, N–S

1 mo of operations. Elevation boresighting appears to be reasonably repeatable.

Half-power beamwidths have been reduced from the recorded patterns. An estimated uncertainty of ±0.030 in. on the recorded patterns amounts to ±0.005 deg in half-power beamwidth. Table 2 summarizes beamwidth data.

Table 2. 8448-Mc radar, half-power beamwidths

Plane of cut	Polarization plane	Half-power beamwidth, deg
Azimuth (79.5 deg)	E	0.270
	H	0.255
45 deg N–S[a]	E	0.243
	H	0.247
45 deg S–N	E	0.252
	H	0.250
Elevation (0.8 deg)	E	0.252
	H	0.250

[a]North–South.

Silver (Ref. 1) has shown the half-power beamwidth for a uniformly illuminated circular aperture for the case of interest here to be 0.227 deg, while a tapered illumination of the form $(1 - r^2)$ will produce a secondary beam of 0.283 deg.

In summary, the characteristics of the X-band radar 30-ft antenna, based on pattern evidence, appear to be quite reasonable. Some asymmetry has been observed in the far-field patterns, but this is expected to improve with increasing elevation angle. An unexplained phenomenon in Table 2, the somewhat broader azimuth plane beamwidth, remains. Preparations are being made for a future absolute gain measurement.

3. X-Band Transmitter

a. Introduction. The X-band 8.448-Gc high-power lunar transmitter was assembled at JPL and installed on the 30-ft antenna at the Venus site, GTS. The transmitter was operational for approximately a 1-mo period, and produced output powers as high as 9.5 kw. After initial troubleshooting, the transmitter operated reliably and the klystron accumulated a total of 324 filament hours and 159 beam operating hours. The completed transmitter cabinet is shown in Fig. 15, the monitor cabinet in Fig. 16, and antenna building control equipment in Fig. 17.

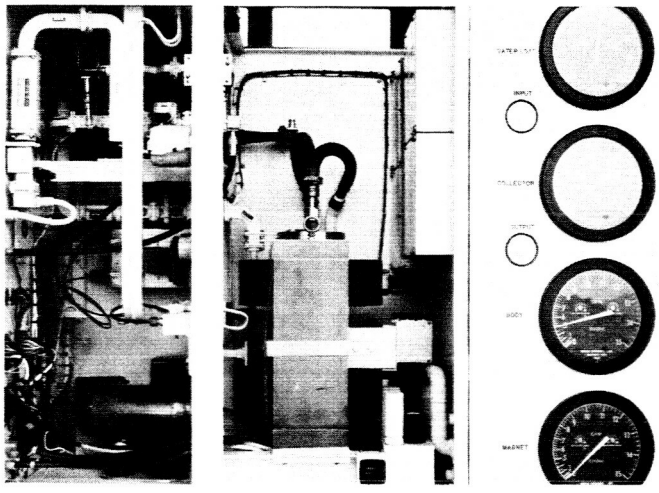


Fig. 15. X-band transmitter, covers removed

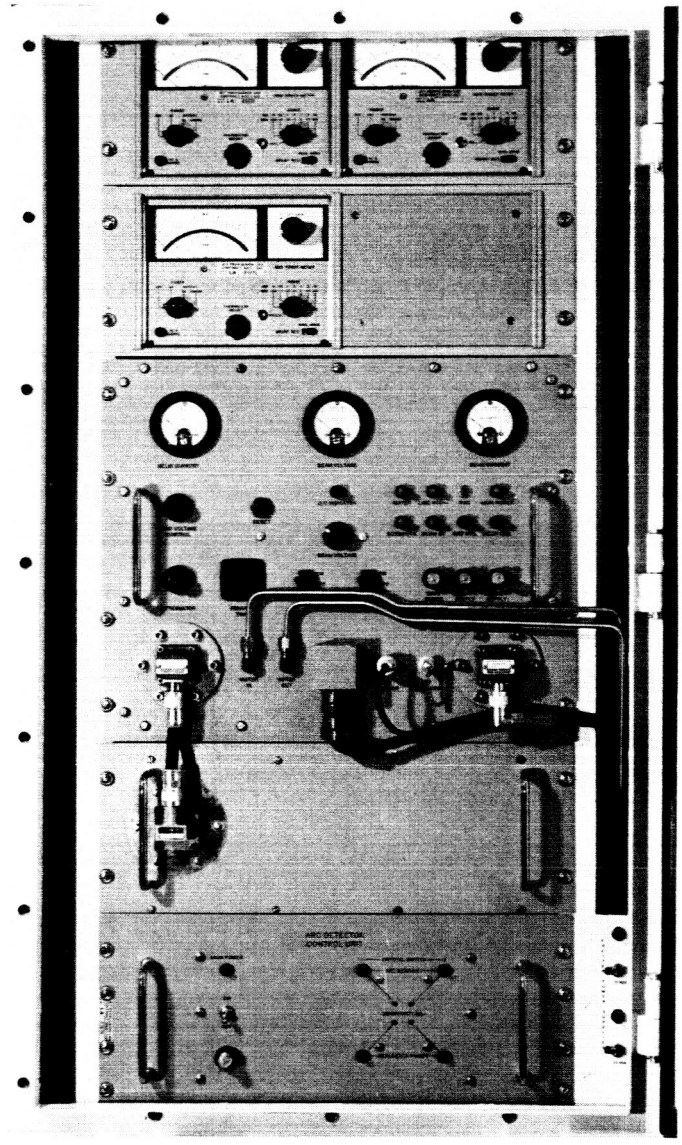


Fig. 16. Monitor cabinet

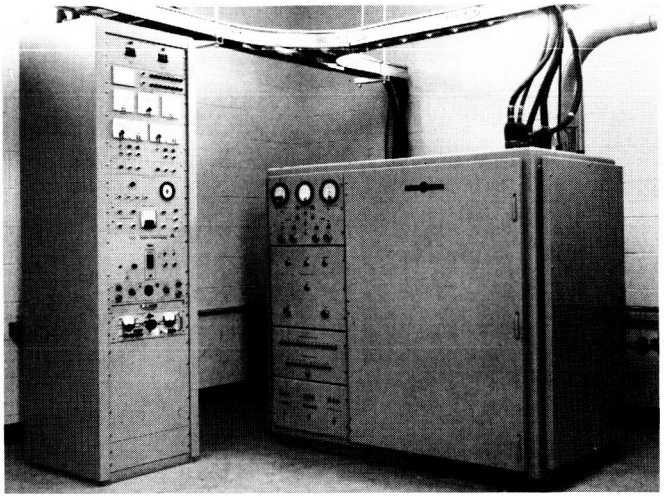


Fig. 17. Control equipment

System transmitter tests and the principal problem areas encountered in the installations are primarily discussed in this report.

b. VA 849G klystron. The transmitter used a VA 849G klystron that developed a maximum power output of 9.5 kw at 18.2 kv and 1.95 amp. The klystron is rated at over 20-kw output at 25 kv and 3 amp, but was run at the reduced power because of power supply limitations. The gain curve of the klystron is shown in Fig. 18. The curve's output power is relative rather than absolute because the output power meter was not calibrated with the water load when the data was taken. Later, after klystron retuning and calibration, a full 9.5 kw was obtained. The klystron survived approximately 10 waveguide arcs caused by malfunction of the waveguide switches, but did not develop any internal arcs during the experiment.

c. Traveling wave tube amplifier. The transmitter used a traveling wave tube (TWT) amplifier (*SPS 37-27*, Vol. III, p. 81) as a power amplifier for driving the klystron. The measured gain characteristics of the amplifier are shown in Fig. 19. During initial testing of the amplifier, the well regulated, but complex, filament power supply failed twice because of high-voltage turn-on transients; the filament supply floats at nearly −2700 v. The filament supply was replaced with a less complex supply that incorporated bypass capacitors across each transistor element. The new supply operated reliably for the remainder of the experiment.

TWT noise reduction. The noise generated in the TWT amplifier during the transmit off or receive mode increased the receiver system noise by 130°K. The Litton L-3472 TWTs used in the amplifier had a published noise figure of 37 db which is typical for other TWTs of similar power output. This high noise output was reflected in a change of receiver system noise temperature from 63°K

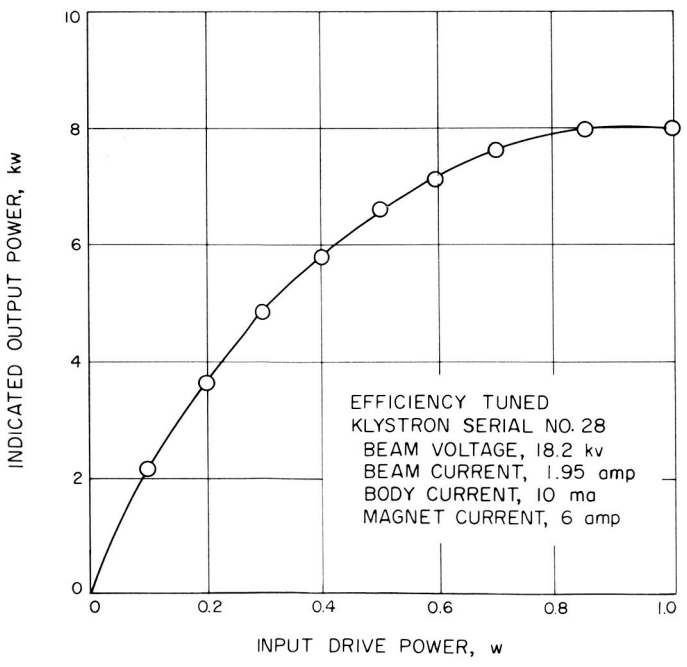


Fig. 18. Klystron 849G input versus output power

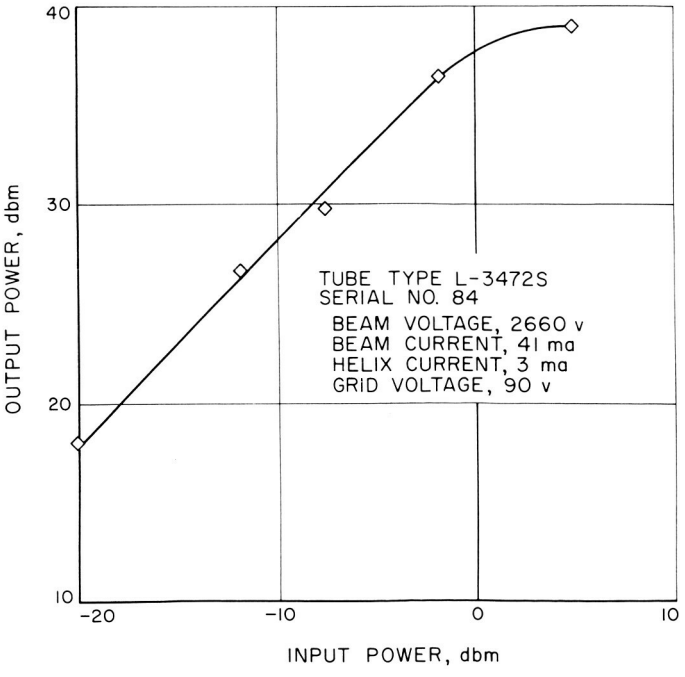


Fig. 19. X-band TWT amplifier gain curve

(exciter chain and TWT turned off) to 194°K (exciter chain off, TWT on). The klystron beam was at 18.2 kv, and the klystron was operating in the water load for the test. Subsequently, a coaxial switch was installed between the TWT output and the input to the klystron. This allowed the TWT noise output to be terminated into a 50-ohm load instead of the klystron during the receive mode, and reduced the receiver system noise temperature degradation to 4°K. The coax switches were not designed for X-band use and had nearly 10-db loss; the transmitter power dropped from a high of 9.5 kw to approximately 6 kw with the loss of klystron drive power. Instability of the switches sometimes caused the output power to drop as low as 4 kw. The remainder of the experiment was run with the coaxial switch unit and lower power because of a net gain in the signal-to-noise of the received spectrum over that obtained without the coaxial switch unit. A new exciter under construction will provide adequate drive for full output.

TWT failures. After 250 hr of operation, TWT 84 became gassy and ceased to function. A spare TWT was installed, but it too had become gassy during storage. The TWT amplifier was then replaced with an Alfred TWT amplifier for the remainder of the experiment.

Present plans call for a small three-cavity klystron amplifier having a gain of 30 db and an output power up to 30 w to replace the TWT amplifier for future experiments.

d. Arc detector. A primary problem area of the transmitter was the arc detector. The arc detector system was the same as that used on the 100-kw S-band planetary radar transmitter except for the light amplifier unit which uses photomultipliers instead of photocells. After the light amplifier, test light, reflected power amplifier and associated circuitry were installed according to the manufacturer's instructions, the arc detector would not "fire" when an arc was simulated by shining a test light on the klystron window. Investigation revealed that the manufacturer's recommended 25-deg angle at which the light enters a hole in the side wall of the output waveguide did not permit the light to shine on the center of the klystron window; the waveguide was reworked and the hole angle changed to 15 deg. Additional modifications were required on the light amplifier (increasing photo multiplier load resistances, etc.) to lower its threshold sensitivity before the light amplifier unit worked properly.

The reflected power amplifier circuitry was modified by the addition of isolation coaxial resistors between the reflected power amplifiers and RF crystal detectors. The crystal detectors used had internal built-in resistor networks that provided a low impedance path to ground. The reflected power amplifiers were designed for use with simple crystal detectors having high dc impedance to ground.

Except for two failures of transistors in the reflected power amplifier, the arc detector system operated properly for the remainder of the experiment.

e. Antenna multiplier chain. The ×60 multiplier chain (140.8 Mc to 8.448 Gc) consisting of a VHF amplifier, ×15, and ×4 is shown in Fig. 20. The modules are mounted in a RF shielded container and are rack-mounted in the transmitter monitor cabinet directly below the TWT amplifier (Fig. 16).

f. Corona tests. Prior to connecting the antenna-mounted equipment to the beam power supply, all devices subject to beam voltage were tested for corona effects using a commercial high-voltage corona testing machine. The results of the tests are as follows:

Device	Test voltage, kv	Corona current, μa	Arc-over voltage, kv
Filament rectifier	60	0	60
Filament transformer	40	0	>40
Series limiter	40	20	>40
Klystron 849G installed in magnet	40	100	>40

g. Filament rectifier. In order to ensure minimum spurious modulation of the RF output, dc power on the klystron's heater or filament supply must be used. The transmitter uses a single-phase, full wave rectifier and filter assembly to rectify the 400-cycle output of the filament transformer. The assembly and its corona shield are shown in Fig. 21. The assembly also contains protective diodes to prevent beam current from flowing through and burning out the klystron heater in case of a filament transformer short to ground.

h. Series limiter. Klystrons can be severely damaged during an internal cathode-to-anode or cathode-to-body arc if not properly protected by a current limiting resistor or crowbar device. Although the transmitter's power supply has beam and body meter contacting relays that

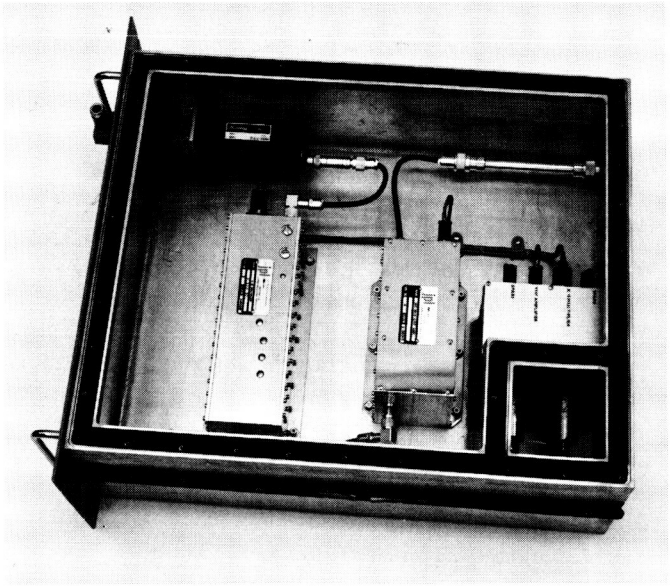


Fig. 20. Frequency multiplier chain (×60), antenna-mounted component

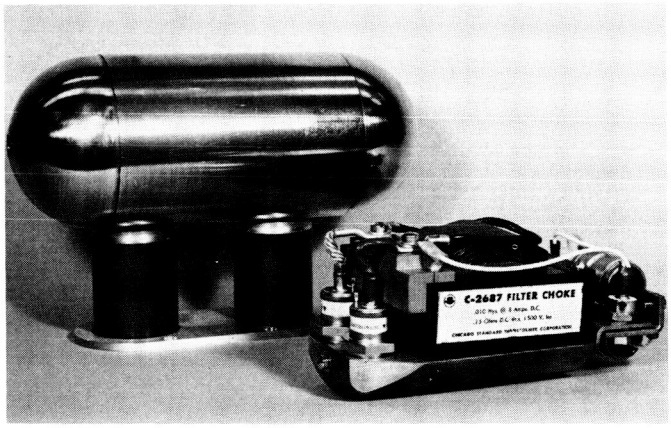


Fig. 21. Filament rectifier–filter

drop out a contactor in the primary side of the high-voltage klystron, the response time of approximately 100 msec is much too slow to suitably protect the klystron from peak currents. The transmitter employs a 100-ohm series limiting resistor network (six 600-ohm resistors in parallel). The series limiter is shown in Fig. 22.

The primary function of the series limiter is to limit peak currents and powers to finite values. Assuming a klystron arc has a 1-ohm impedance, the peak current is limited to 18.2 kv ÷ 100 ohm or 182 amp. The energy dissipated is also reduced. The principal energy storage component is a 1-μf capacitor in the output of filter network of the power supply. This capacitor stores 165 joules of

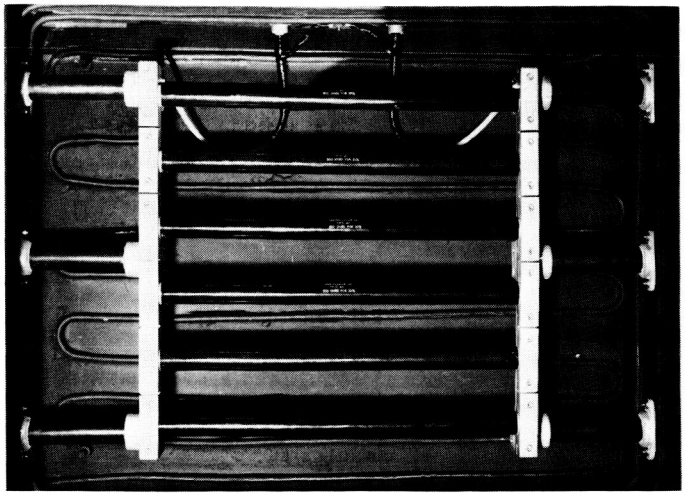


Fig. 22. Beam current, series limiting resistor

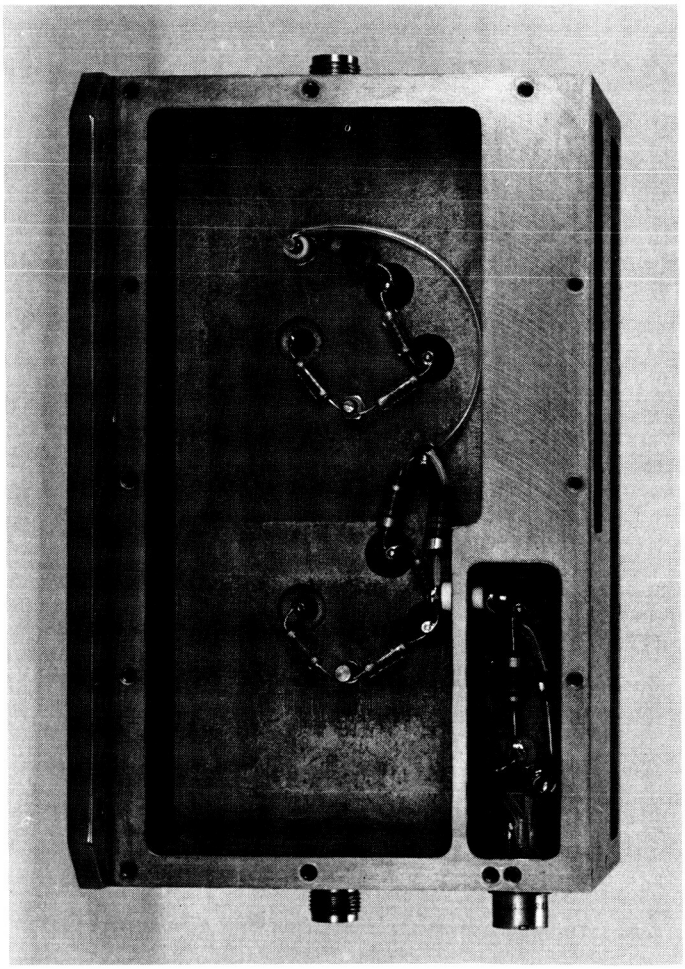


Fig. 23. ×4 frequency multiplier

energy at 18.2 kv, but the energy dissipated in the tube is reduced to 1.65 joules with the 100-ohm series limiter in the circuit again assuming a 1-ohm arc impedance.

Since the resistor assembly dissipates 400 w with a normal beam current of 2 amp, the housing containing the series limiter is water cooled.

4. Multiplier Chains

a. Introduction. A program for development and evaluation of varactor multipliers for use in receiver local oscillator chains, exciters, and signal generators has been in progress for some time. Progress has been reported in *SPS 37-29*, Vol. III, p. 86 (*Solid State Frequency Multipliers and Modulators*) and *SPS 37-28*, Vol. III, p. 75 (*Multiplier Chains*). All units for the X-band multipliers have been received and evaluated, and the results of system tests are covered in *SPS 37-30*, Vol. III. With the exception of the final ×4 multiplier to X-band, all units performed satisfactorily. In-house work is proceeding on a redesign of this unit. Based on the results of the X-band multipliers, a decision was reached to replace the vacuum tube units in the S-band exciter and receiver with varactor multipliers. Documentation for procurement of these units is well underway, and documentation for procurement of additional X-band units, if required, is complete. Recommendations for modification of existing VHF amplifiers for use with these chains have been made.

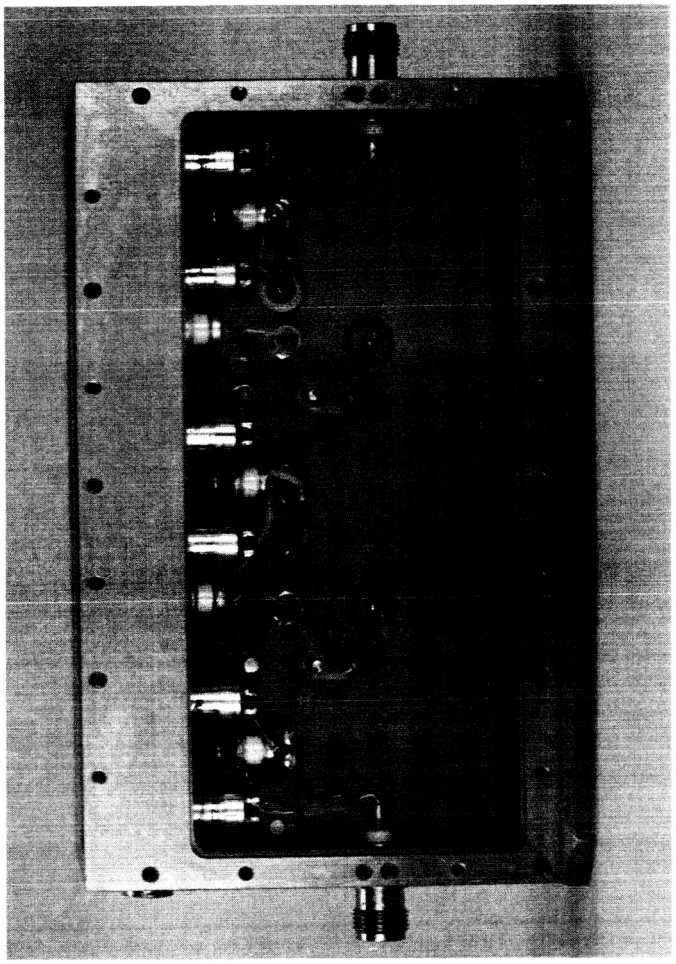


Fig. 24. VHF amplifier

b. Module development and documentation. Module development has been completed on all but the X-band ×4 multiplier, which was purchased as a stock item. Additional line filtering and RF cover plate rework have been incorporated, in the VHF amplifier and ×15 multiplier modules, to meet RF interference specifications. These and a few minor mechanical modifications, considered desirable, have been included in the final documentation consisting of photographs, schematic diagrams, and mechanical fabrication drawings. Work on supplementary documentation necessary for the procurement of S-band components is in progress, and will include the modification of standard types, recommended below, wherever feasible.

c. Initial ×4 frequency multiplier and VHF amplifier. Photographs of the ×4 frequency multiplier and VHF amplifier with cover plates removed are shown in Figs. 23 and 24, respectively. Both units consist of two solid-state stages and are mechanically identical. Bias and resonant circuit component values associated with individual stages are selected for operation as a doubler or

Table 3. Electrical performance of initial ×4 frequency multiplier and VHF amplifier

Characteristics	× 4 frequency multiplier		VHF amplifier	
	Specification limits	Performance, three units	Specification limits	Performance, five units
Center frequency, Mc	35.0 to 35.3	35.17 to 35.18	140 to 141.2	140 to 141
Impedance, ohms	50	50	50	50
VSWR	<1.1	<1.1	<1.1	<1.1
Power levels, dbm				
Input	13	13	8	8
Output	8.5 ±1	8.4 to 9.0	23 ±1	22 to 23
Bandwidth, Mc				
3 db	2.2 (minimum)	2.28 to 2.41	20 (minimum)	23.8 to 25.1
1 db	—	1.61 to 1.86	—	17.4 to 19.3
Limiting action output variation for 8-db input variation, db	—	Not applicable	2 (minimum)	2.0

amplifier as required. In the case of S-band chains, the first stage of the initial frequency multiplier operates as an amplifier, the second stage as a ×5 multiplier.

Table 3 indicates the range of the electrical performance of the three frequency multipliers and five amplifiers produced. Figs. 25 and 26, respectively, show a plot of the input/output characteristic and an oscillograph trace of the frequency response of a representative VHF amplifier. All modules meet JPL requirements, but it is felt that the degree of limiting of the VHF amplifiers could profitably be increased beyond the marginal value orginally specified, since more than adequate keying ratio has been achieved. To this end, the basic three-stage amplifier which is being developed for booster and distribution requirements could be standarized for use in future procurement.

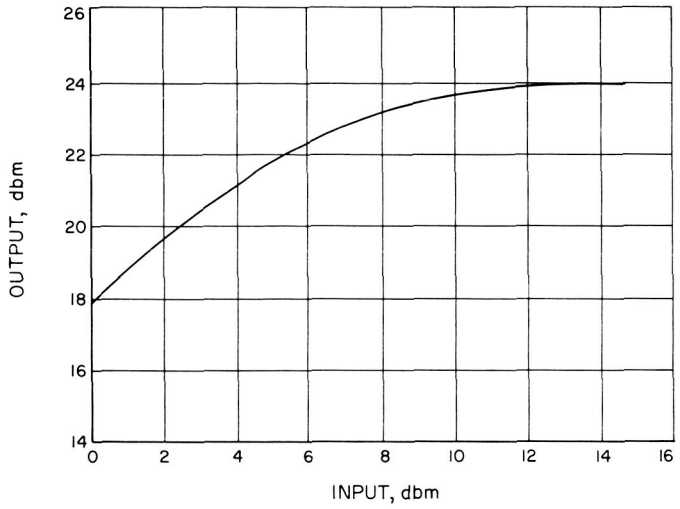


Fig. 25. Input/output characteristic of VHF amplifier

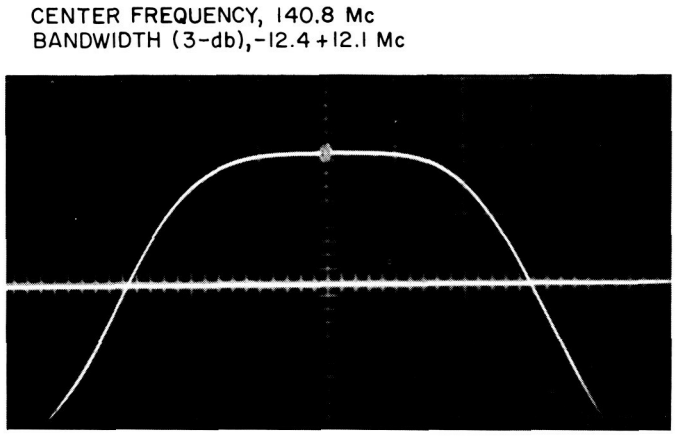


Fig. 26. Oscillograph trace of VHF amplifier frequency response

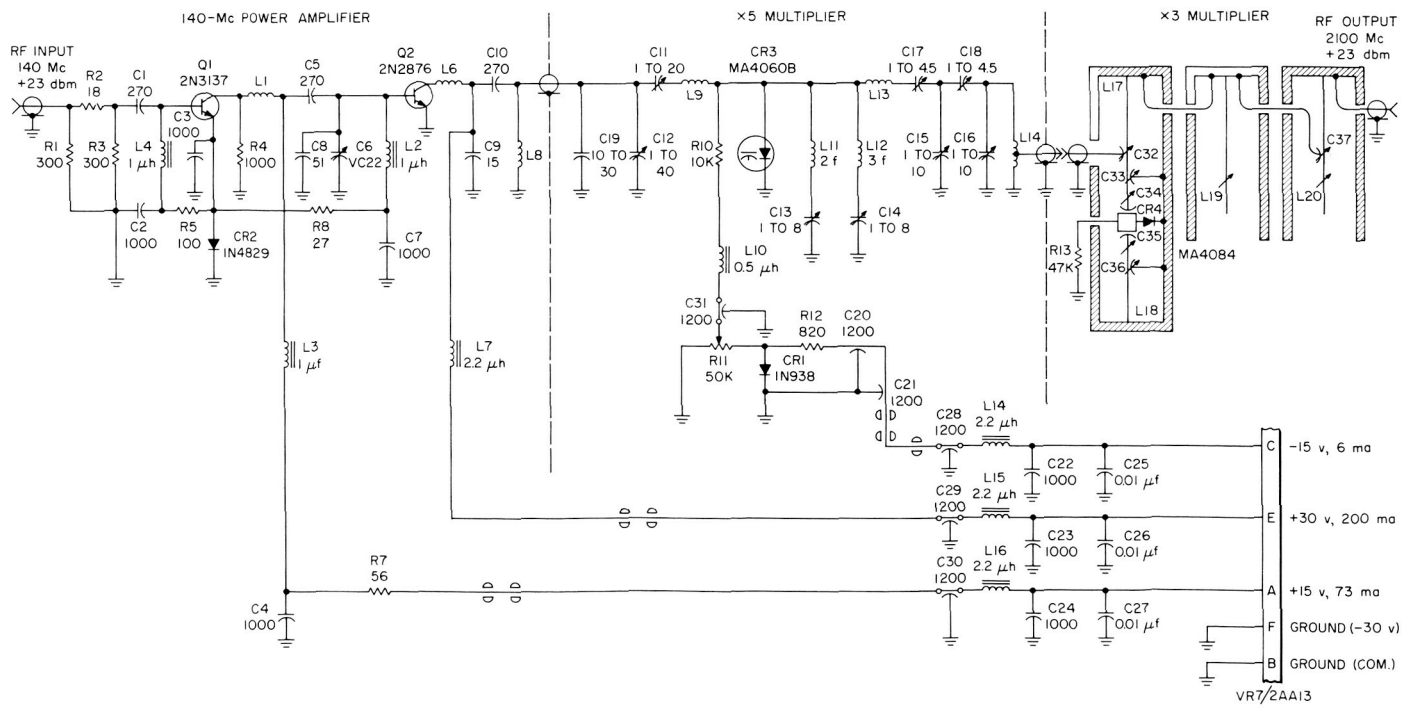


Fig. 27. Schematic diagram of ×15 frequency multiplier

d. ×15 frequency multiplier to S-band. A schematic diagram of the ×15 frequency multiplier is shown in Fig. 27; photographs of each side of the unit with cover plates removed are shown in Fig. 28. Referring to Fig. 27, a Class C VHF amplifier Q1,Q2 provides about 34 dbm of drive power to a ×5 frequency multiplier stage CR3, which in turn drives the final ×3 multiplier CR4 to produce an S-band output of 24 to 25 dbm. Resistive padding formed by R1 through R3 is used at the input of Q1 to improve the input match; temperature compensating diodes CR1 and CR2 are used for stabilizing the bias of the ×5 varactor CR3 and of the amplifiers Q1, Q2, respectively. Idler currents at two and three times the input frequency are provided for the ×5 multiplier by the low Q series resonant circuits L11 C13 and L12 C14, respectively, and the output at five times the input frequency is coupled to the input of the final ×3 multiplier via the bottom capacity coupled bandpass filter formed by L13

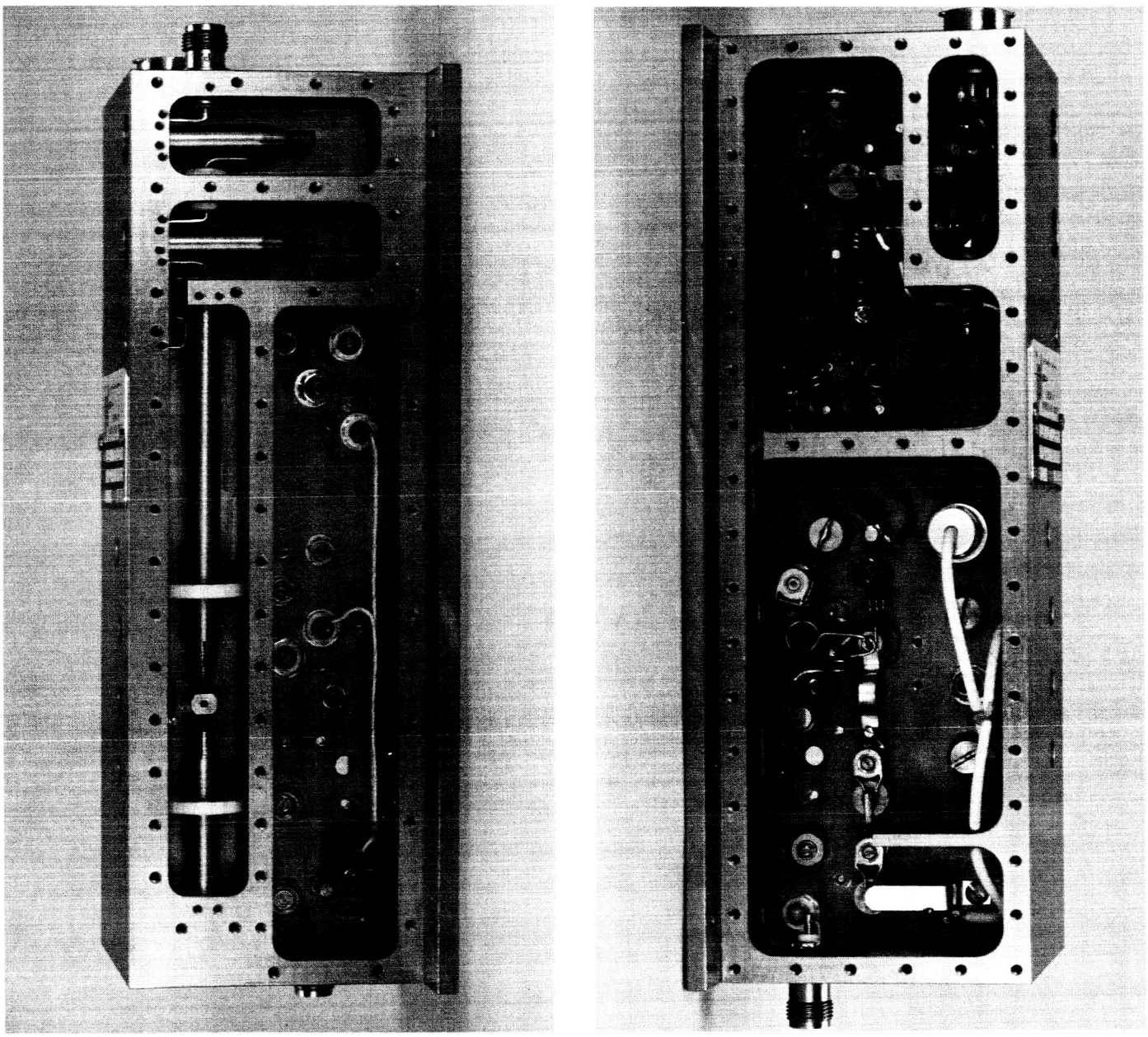


Fig. 28. ×15 frequency multiplier (both sides)

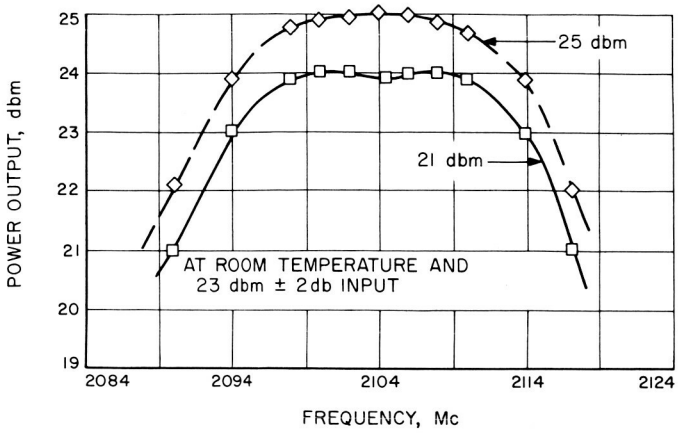


Fig. 29. Frequency response of ×15 multiplier

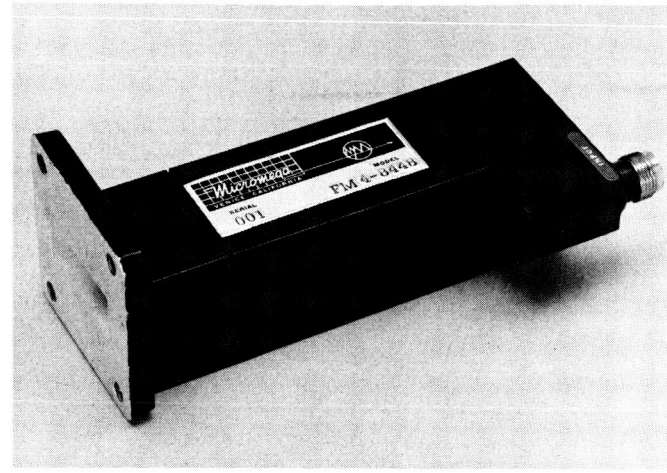


Fig. 30. ×4 frequency multiplier to X-band

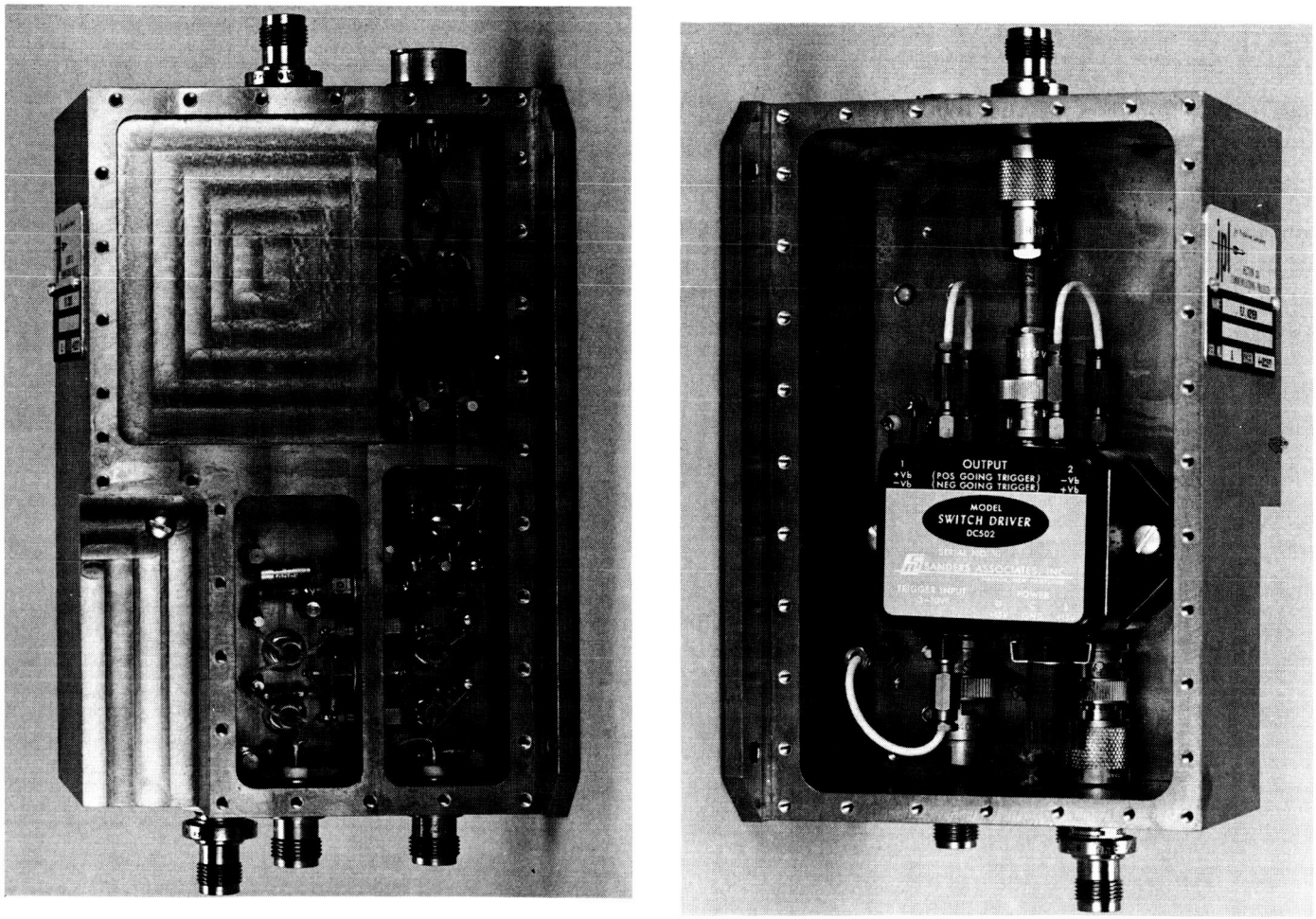


Fig. 31. RF keyer (both sides)

L14 C15 C16 C17 C18. For convenience of alignment and also for practical mechanical reasons the output impedance is matched to 50 ohms.

The final ×3 multiplier utilizes coaxial cavities for the input, idler, and output circuits. Cavity L15 operates as a fore-shortened quarter wave line at the input frequency and as a fore-shortened three-quarter wave line at the output frequency. The 50-ohm output of the ×5 multiplier is matched into the input of the ×3 multiplier via a variable capacity C32. This is coupled into L15 at a point corresponding to a voltage node at the output frequency so as to minimize the tuning effect at the output frequency. Differential tuning at the input and output frequencies is provided by C33 and C34, respectively. C34 also provides output coupling. The idler cavity L16 is a fore-shortened quarter wave line at twice the input frequency and is coupled into the varactor CR4 by C35 and tuned by means of C36. The S-band output from L15 is link-coupled to the input cavity of the output bandpass filter formed by L17 L18. These quarter wave cavities are bandpassed by means of a hybrid coupling consisting of link coupling out of L17 and combination link and adjustable capacity (C37) coupling into L18.

Table 4 indicates the range of electrical performance of the three frequency multipliers produced, and Fig. 29 the frequency response of one of the units over an input range of 23 dbm ±2 db. All units meet JPL requirements.

e. ×4 multiplier to X-band. A photograph of this unit is shown in Fig. 30. A quarter wave coaxial line is used to couple the input to a varactor diode, which is mounted in a length of H-band waveguide tuned to four times the input frequency. A short at one end of the waveguide tunes out the diode reactance, and the X-band load is coupled into the diode via a diode impedance matching section and a two-section bandpass filter.

These multipliers, as originally submitted, were not acceptable due to insufficient bandwidth and also to restricted dynamic range causing breakup and sharp discontinuities of the output. These faults were found to be due to the same cause – imperfect matching of the input and output. Insufficiencies in the basic design, which do not permit the adjustment for optimum operation of the varactor diode, hampered considerably the production of wholly acceptable units, two of which were eventually supplied, the third unit still having a tendency to break up.

f. RF keyer. Photographs of each side of the RF keyer with the cover plates removed are shown in Fig. 31. Since the switching arrangement used in this unit is identical to

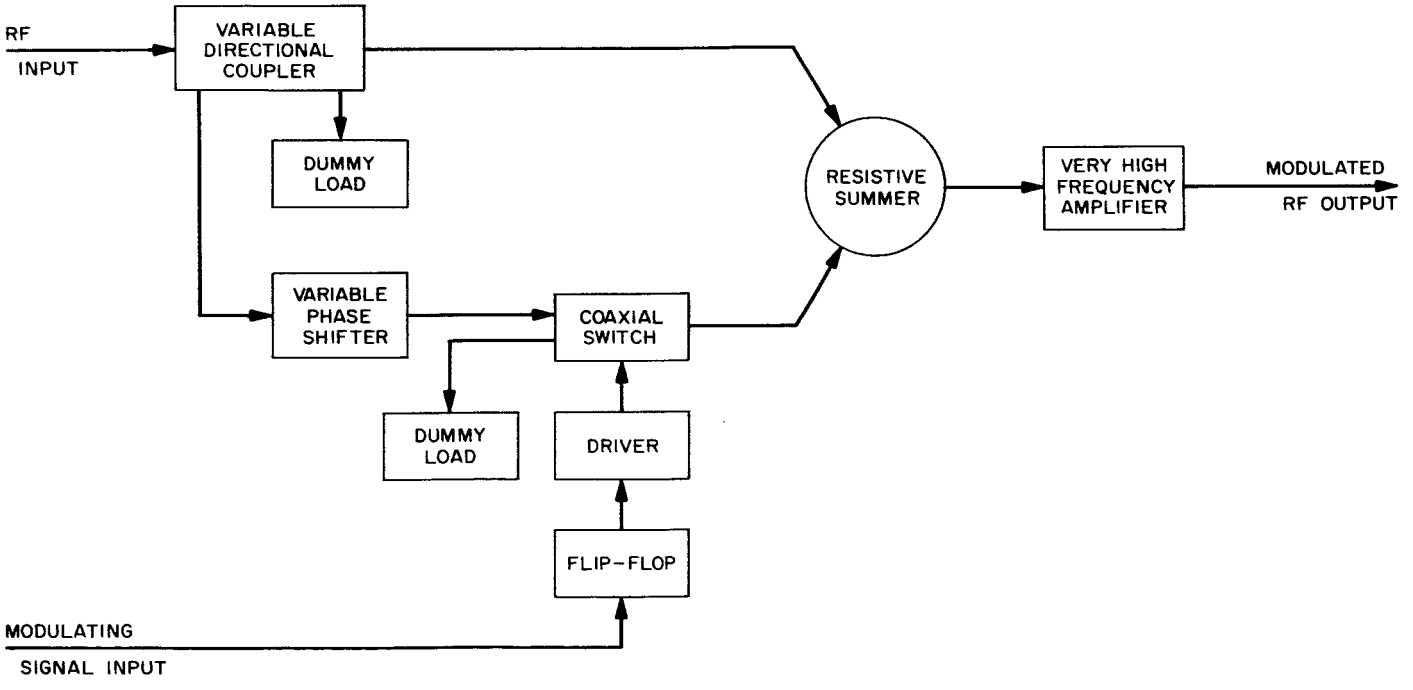


Fig. 32. Digital phase modulator

Table 4. Electrical performance of ×15 multiplier

Characteristics	Specification limits	Performance, three units
Center frequency, Mc		
Input	140.3 and 140.8	140.3 and 140.8
Output	2104.5 and 2112	2104.5 and 2112
Impedance, ohms	50	50
VSWR	<1.2	≤ 1.1
Power levels, dbm		
Input	23	23
Output	21 (minimum)	22.8 to 24.8
Bandwidth, Mc		
3 db	20 (minimum)	25 to 27
1 db	—	15 to 20
Limiting action output variation for 4-db input variation, db	1 (maximum)	0.4 to 1.0
Spurious response	−40 db (maximum)	<-45 db

that used in the digital phase modulator, a description of its operation may be found under that heading below. For test purposes and when not keying, a manually operated reset button is provided so as to ensure that the keyer is in the *on* position.

Keying takes place immediately after phase modulation at an input level of 8 dbm ±3 db, the insertion loss of the keyers varying between 0.5 and 0.7 db. Since a wide-band (400-Mc) coaxial switch is used, there is no restriction on the bandwidth. The keyers will operate at frequencies from dc to well over the 1-kc rate currently called for, the rise and fall times of the switching operation amounting to approximately 30 nsec. The minimum keying ratio is greater than the 50-db JPL requirement.

g. Digital phase modulator. A block diagram of the digital phase modulator is shown in Fig. 32; a photograph of the assembled strip line components and switching unit comprising them is shown in Fig. 33. Digital phase modulation is obtained by the addition, to the main carrier, of a suitably attenuated quadrature component at the modulating frequency by means of a switch. Amplitude and phase adjustments of the quadrature component are provided by the variable strip-line directional coupler and phase shifter, respectively. Components for the switching and summing of the signals are housed in the switching unit (Fig. 34). Switching is provided by the solid-state coaxial switch, the driver of which is actuated by a pushpull square wave modulating signal via a dc flip-flop. Summing of the signals is provided by the re-

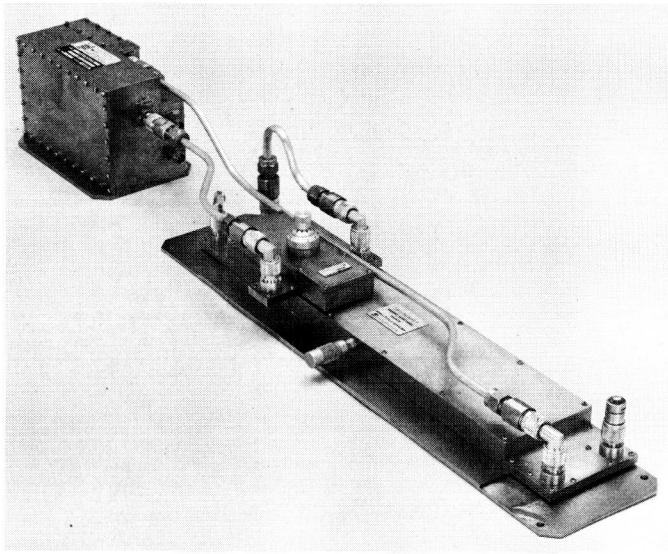


Fig. 33. Assembled phase modulator

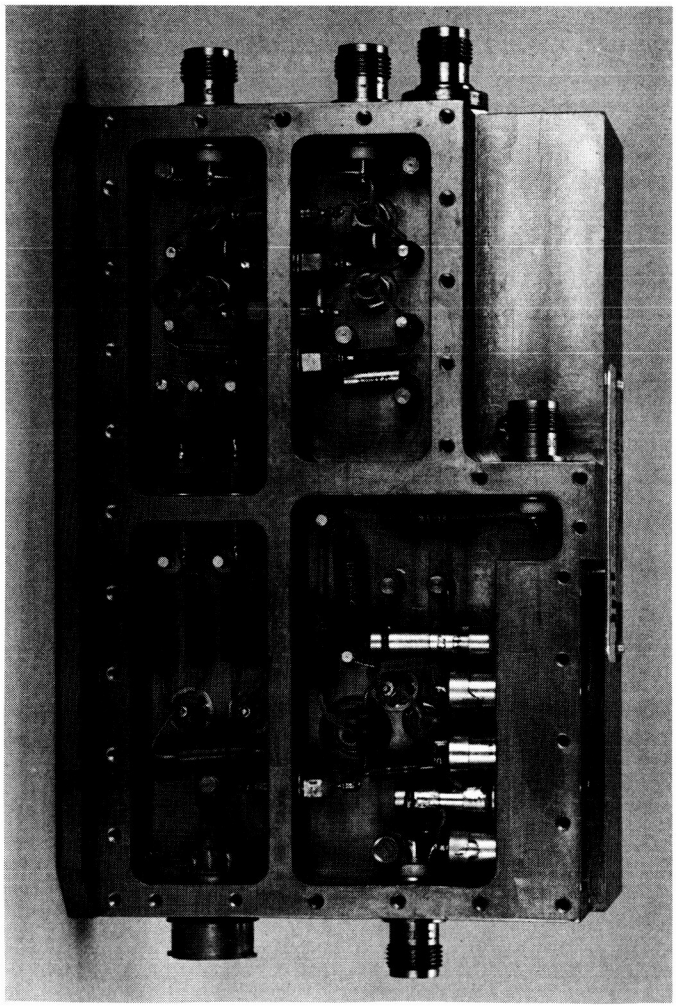


Fig. 34. Phase modulator switching unit

sistive summer, and a single-stage VHF amplifier is included to make up for the losses in the passive elements and maintain unity gain.

For reasons discussed in *SPS 37-27*, Vol. III, this equipment is required to maintain a high degree of carrier suppression when the output carrier is phase-modulated ±90 deg. A minimum carrier suppression of 50 db, requiring a deviation stability of 0.12 deg in 90 deg was considered desirable, but factors other than accuracy of modulation index can contribute toward a residual carrier. The most important of these factors include departures from unity mark space ratio and incidential modulation, particularly amplitude modulation.

With regard to the first factor, imperfections of the input modulating wave form, together with any additional degradation of the mark space ratio that may occur in the switching operation due to asymmetry of the transition characteristics, poses a grave problem. However, the suppression of a residual carrier produced in this manner can be improved by tolerating some degradation in symmetry of the output modulation sidebands by a suitable change of the modulation index. In practice, this always occurs to some extent and is limited by the degree of asymmetry considered tolerable. Incidental modulation can occur at the resistive summer in a manner discussed later, where it is shown that unwanted modulation produced in this way can be reduced to an acceptable limit.

Referring to the schematic diagram of the switching unit shown in Fig. 35, the pushpull square wave modulating signal is applied to the input of a two-stage dc coupled flip-flop Q1 through Q4, and the output from the collector of Q3 is applied to the driver of the solid-state coaxial switch which selects either the quadrature component or a 50-ohm termination. The output of the switch is added to the main signal, and the modulated carrier so obtained is amplified by Q5. Inequalities between the impedance of the 50-ohm termination and that of the quadrature component source introduced considerable amplitude modulation of the main signal when the phase modulation was set at zero. This incidental modulation could be eliminated from the main carrier during phase modulating by reapportioning the values of α and $90 + \delta$, as

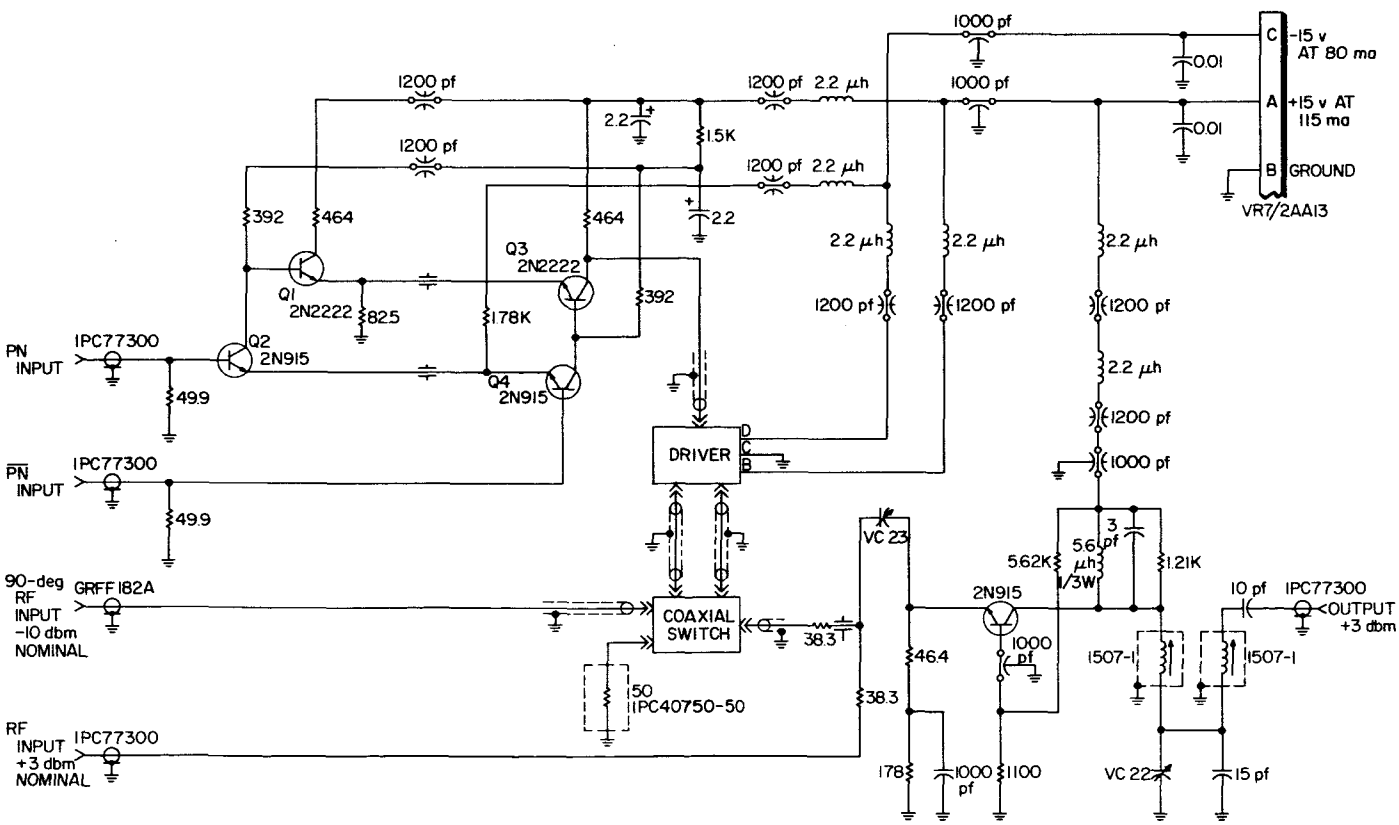
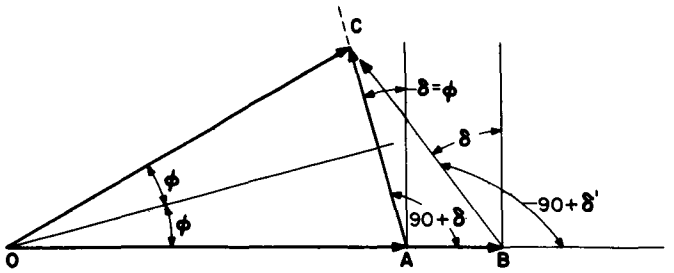


Fig. 35. Schematic diagram of switching unit



FOR PHASE MODULATION = ± φ

QUADRATURE COMPONENT FOR NO AMPLITUDE MOD

AMPLITUDE = a = AC/OA

PHASE = (90 + δ)

AND FOR AB AMPLITUDE MOD

AMPLITUDE = a' = BC/OA

PHASE = (90 + δ')

Fig. 36. Vector diagram

illustrated in Fig. 36, but it was considered more satisfactory to correct this effect by means of an impedance matching network in the quadrature connection. A small amount (about −45 db) of residual modulation could not be removed by this means and was accounted for by the open circuiting of the quadrature output when the switch was in the *off* position.

In the absence of any incidental modulation of the in-phase component, the amplitude and phase of the quadrature component required to deviate the output carrier ±90 deg at X-band are −25.6 db and 91.5 deg, respectively, and at S-band −13.5 db and 96 deg, respectively. This range in attentuation can be covered by the directional coupler used, but degradation in the VSWR at S-band necessitates readjustment of the impedance matching network. These strip line variable directional couplers, as first received, were not acceptable mechanically. Backlash and extreme stiffness of the movement made amplitude adjustments impracticable. Rework to correct this problem had to be limited by the necessity of maintaining adequate electrical contact pressure to meet electrical stability requirements. The modulator is capable of being preset to phase-modulate the S- or X-band carrier at depths ranging from ±9 to ±90 deg continuously. At the higher modulation index, the carrier can be suppressed to well under −50 db with good symmetry of the output sidebands, but can be expected to approach −40 db under adverse working conditions. The main factor, and perhaps the deciding factor, against achieving the target suppression of −50 db, is the specified quality of the input modulating signal.

D. S-Band Planetary Radar Project

1. Redesigned Cassegrain Cone

A 2388-Mc Cassegrain antenna cone has been constructed to replace the Goldstone Venus site cone damaged in September 1964. Fig. 37 shows the new cone layout. Several major improvements have been made in equipment and the cone layout:

(1) Locating the 100-kw transmitter, water load, and transmitter water load switch inside the cone.

(2) Rebuilding the old maser package with a DSIF configuration and incorporating a helium load in the maser cryogenic assembly.

(3) Replacement of the nitrogen load vacuum Dewar with a long life foam unit.

(4) Integration of the post maser receiver and monitor receiver into one package.

(5) Building in a quick-disconnect capability to allow rapid changeover to the 100-kw *Mariner C* transmitter cone.

Planetary radar tests are presently being conducted with the planets Venus and Jupiter. System tests and tests on the individual subsystems will be reported as data is accumulated.

2. Rebuilt TWM and Instrumentation

The traveling wave maser (TWM) for the 2388-Mc radar system used on the 85-ft antenna at the Venus site has been rebuilt and repackaged in the closed cycle refrigerator (CCR). The external package is basically a duplicate of the TWM/CCR units delivered to the DSIF for 2295-Mc operation. Fig. 38 shows the amplifier installed in the experimental planetary radar Cassegrain cone. A liquid helium cooled termination was included in the refrigerator for calibration purposes. This replaces the open cycle Dewar cooled load used previously. The maser instrumentation in the cone and control room was considerably simplified.

a. Closed cycle refrigerator. The CCR was modified to provide a mounting flange for the amplifier having the same dimensions as the DSIF units. Additional supports have been added to the 4.4°K station of the CCR. In the past, gain changes have been caused by mechanical movement of the amplifier microwave head,which is supported by the refrigerator and coaxial lines. Movement, which

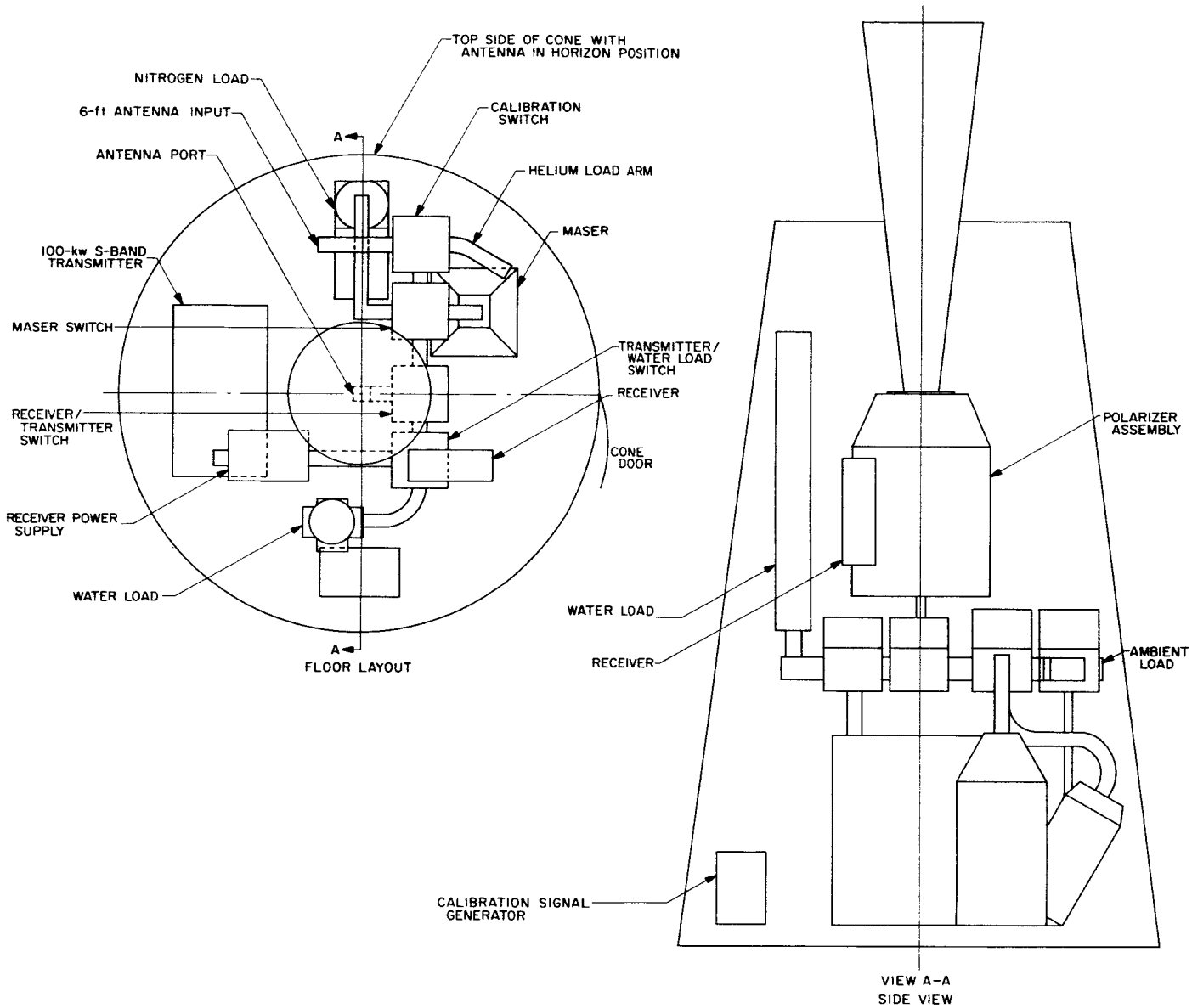


Fig. 37. 85-ft antenna, 2388-Mc R&D cone layout

occurs at the rate of the refrigeration cycle, is caused by alternating high and low pressures in the expansion engine of the CCR. This causes a corresponding gain fluctuation which has been referred to as "crosshead modulation."

Crosshead modulation in this amplifier has been reduced to the point where it is not measurable with the existing instrumentation (less than 0.02 db peak-to-peak). This improved stability has been accomplished by the use of micarta supports extending from the outer housing of the CCR to the 4.4°K heat station where the TWM microwave head is mounted. Improved support should provide better gain stability as a function of package position.

b. Traveling wave maser. The new TWM amplifier was tested in the laboratory; the following characteristics were measured:

Net gain	46 db
Electronic gain	57 db
Forward loss	11 db
Bandwidth (3-db)	12.3 db
Bandwidth (1-db)	7.5 Mc



Fig. 38. Packaged S-band maser and CCR installed in 85-ft antenna Cassegrain cone

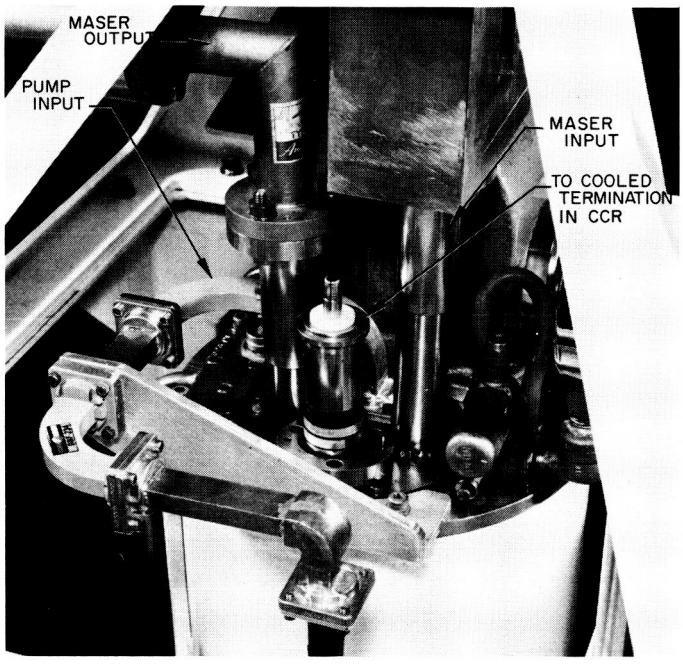


Fig. 40. RF "head" installed in CCR

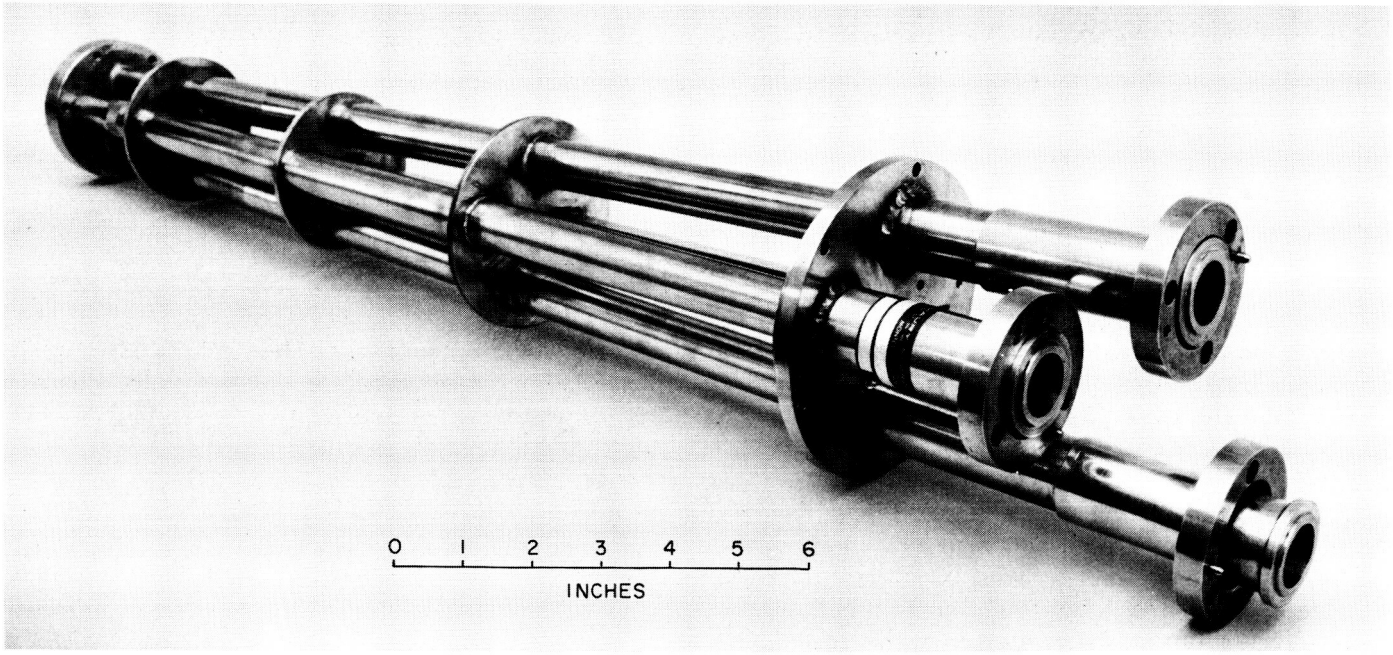


Fig. 39. RF "head" providing input and output connections to the 2388-Mc maser and a cooled reference termination

These measurements were performed at a CCR temperature of 4.4°K. The theoretical noise temperature (Ref. 2) of this amplifier is 2.3°K. The maser "head" (coaxial lines providing input and output connections to the amplifier) has been changed to be consistent with the DSIF package, and an additional ⅞-in. coaxial line has been added (Fig. 39). This line is terminated at the 4.4°K station to provide a cooled reference load for system temperature measurements. The maser input lines are shown mounted in the refrigerator in Fig. 40. The RF "head" assembly including the reference termination was fabricated by Maury Microwave Corporation, Montclair, Calif. The 4.4°F load temperature will be increased by an estimated 5.5°K due to resistive losses in the input coaxial line, the waveguide transition, and the 26-db directional coupler. The equivalent input excess noise temperature of the TWM amplifier is expected to be approximately 8°K; it has not yet been measured.

c. Maser instrumentation. A block diagram of the instrumentation used with the 2388-Mc TWM is shown in Fig. 41. Several improvements have been made since the previous installation (*SPS 37-18*, Vol. III, p. 16). The "noise box" (Figs. 38 and 42) is installed inside the maser package as in the DSIF installation. A tucor noise source is used with ⅞-in. EIA flanges. The precision signal generator does not feed through the noise tube in order to maintain calibration accuracy. It is now feasible to measure the match of the terminations and the antenna feed as seen from the maser. In the past, cooled terminations have experienced a change in VSWR with time. It has been necessary to disconnect a waveguide section to insert a

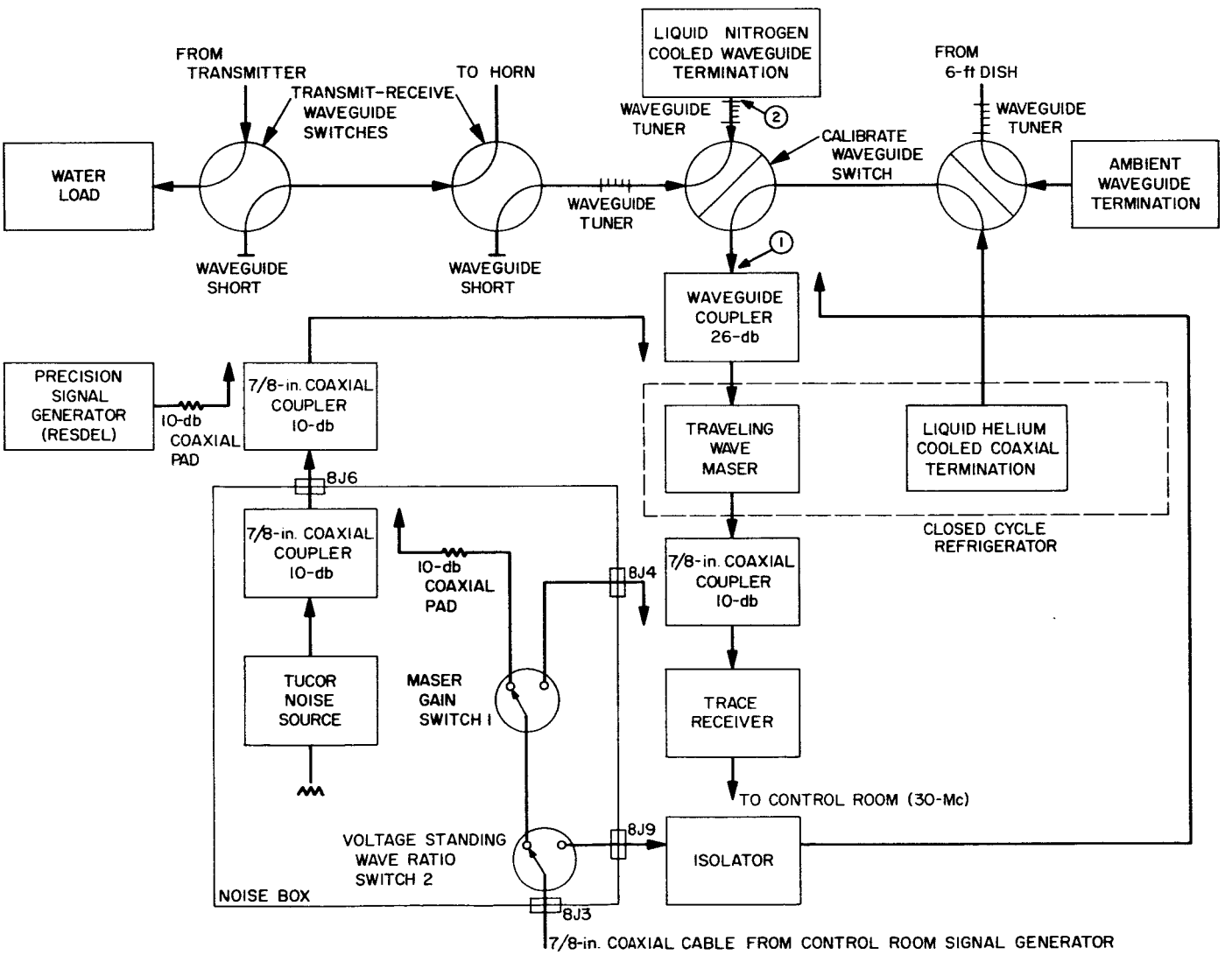


Fig. 41. Block diagram of TWM instrumentation

slotted line to measure the match. Aside from the inconvenience of disconnecting the waveguide, there is a possibility of degrading the waveguide performance when disconnecting and reconnecting the waveguide flanges. With the new configuration, the impedance match is measured on a daily basis from the maser instrumentation rack (Fig. 43) in the control room without any change to the system. Coaxial switch 2 is used to measure the VSWR using the maser input coupler as a reflectometer. A signal reference is made by setting the waveguide switch to the short position. The signal generator attenuator is set for the same output signal level when the maser input is switched to the termination under evaluation. The 26-db coupler had 37 db of measured isolation after installation.

Maser gain is measured by adjusting the signal generator attenuator for equal output level when switching the signal between the maser input and output (Fig. 41, maser gain switch 1).

The liquid nitrogen cooled waveguide termination (Fig. 41) is under construction and will be installed in a Dewar (Fig. 44) mounted in the cone at a 30-deg bias to the vertical. The liquid nitrogen life is expected to be greater than 24 hr. A liquid helium cooled waveguide termination in an open-cycle glass Dewar can be periodically (at present on a weekly basis) connected to the calibrate waveguide switch (Fig. 41) for precise absolute calibrations.

The insertion loss of the waveguide from the maser input to the liquid helium cooled termination (between points 1 and 2, Fig. 41) was measured on November 6, 1964, to be 0.029 db. The contribution from this loss is a function of its temperature. The equivalent noise temperature of the liquid helium cooled termination at the output flange (where connection is made to point 2, Fig. 41) was calibrated to be 6.2°K. The equivalent noise temperature of the liquid helium cooled termination referred to the maser input, T_H, (point 1, Fig. 41) as a function of the waveguide temperature, T_0, is

$$T_H = [0.00666\,T_0 + 6.16] \qquad ^\circ\mathrm{K}\,.$$

The other waveguide insertion loss measurements such as from the maser input to the horn, liquid helium cooled termination in the CCR, and the waveguide short have

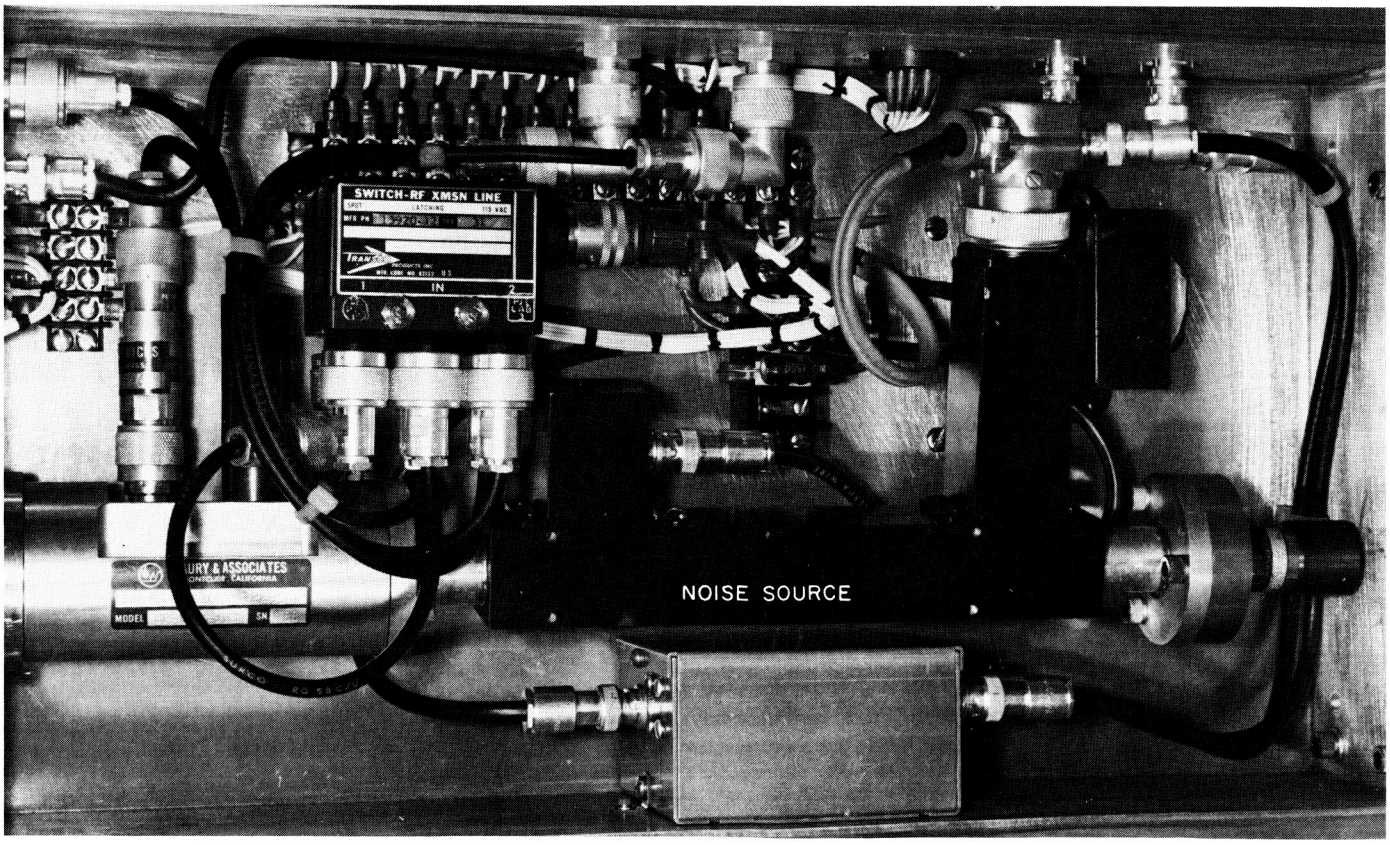


Fig. 42. "Noise box" instrumentation used with TWM

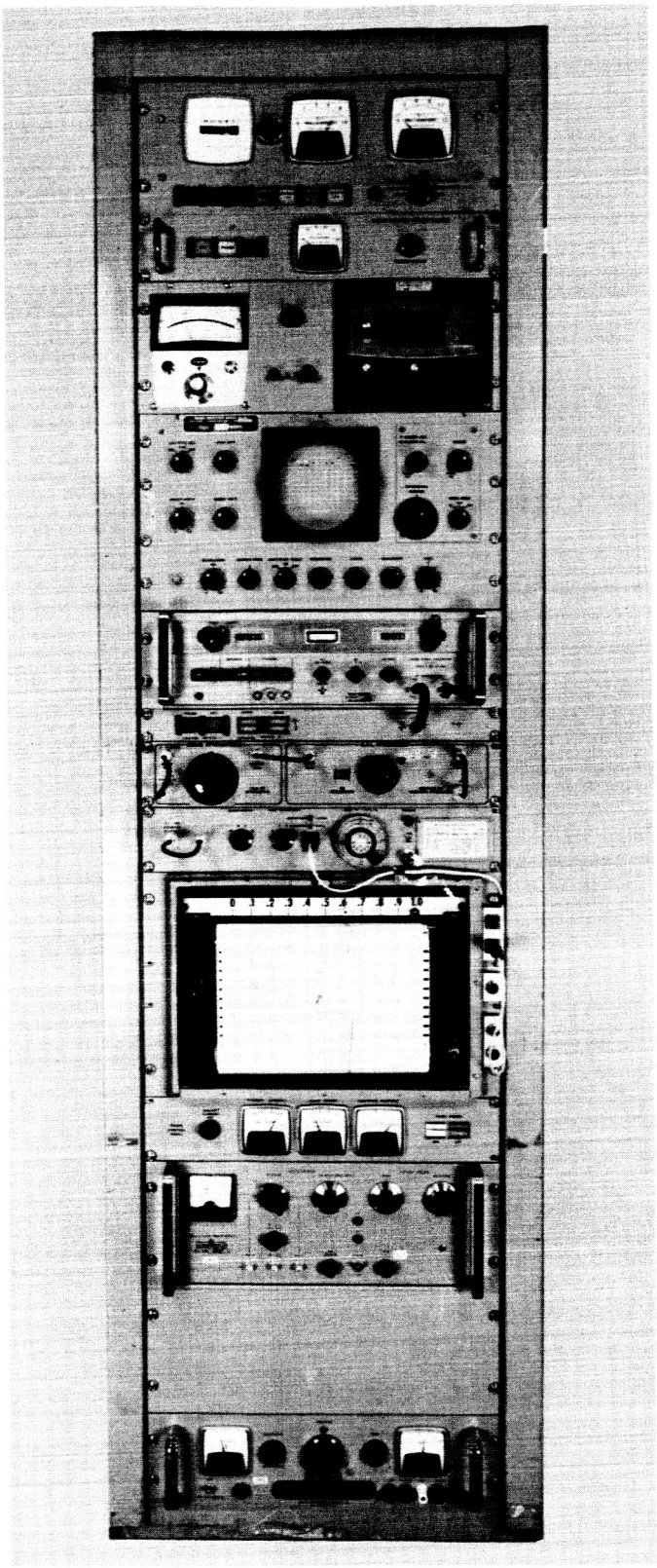


Fig. 43. S-band maser instrumentation rack located in control room



Fig. 44. Partially completed liquid nitrogen cooled waveguide termination mounted in Dewar

not yet been made. The noise source is calibrated with the ambient and liquid helium cooled termination.(See Sect. VI-F of this volume.) The liquid nitrogen cooled termination will be used to refine and verify the calibration.

The coaxial liquid helium cooled termination, installed in the CCR, and the waveguide short are also calibrated periodically (Sect. VI-F) with the cooled waveguide termination and used for calibrating the receiver system on an operating basis.

The performance of the TRACE receiver (especially amplitude gain stability) has been improved (Sect. VI-D-6) so that the monitor receiver is no longer required for noise temperature calibrations and radio astronomy experiments. Direct measurements of the maser amplifier and TRACE receiver amplitude gain stability have been made (Sect. VI-F). Also, the overall system performance is demonstrated by a very interesting total power radiometer "drift curve" taken of Jupiter (Fig. 45). No special gain stabilizing techniques were used for this recording. In this measurement, the antenna is moved ahead of the path of Jupiter and stopped. As Jupiter moves through the antenna beam, the system temperature increases as shown (Fig. 45). The total system temperature during the time of this measurement was approximately 24°K so that the

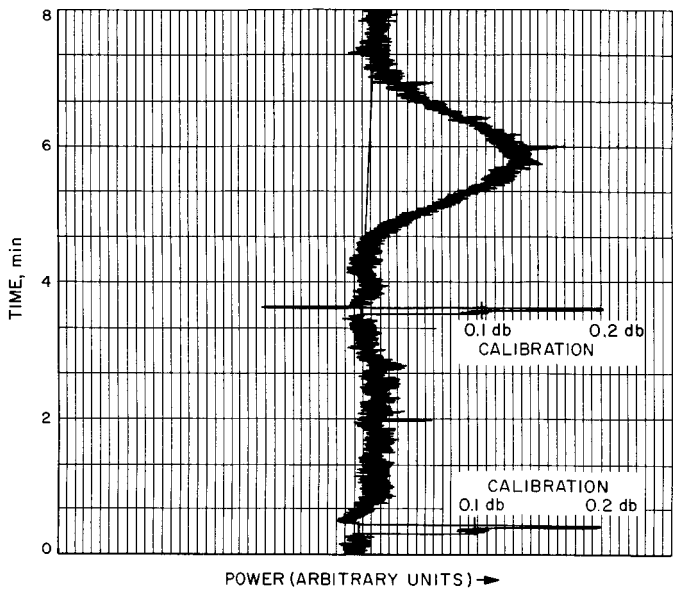


Fig. 45. 2388-Mc total power radiometer "drift curve" of Jupiter

increase in antenna temperature due to Jupiter $\Delta T_{A\psi}$ defined at the maser input calibrated from the 0.1-db (1.023 ratio) calibrations is

$$\Delta T_{A\psi} \simeq (24°\text{K})\left(\frac{17.6 \text{ divisions}}{13.3 \text{ divisions}}\right)(1.023 - 1) \simeq 0.73°\text{K}.$$

For this measurement:

Date	December 4, 1964
Time	09:28 GMT
Azimuth	261.59 deg
Elevation	39.94 deg
Frequency	2388 Mc
Bandwidth	9 Mc
Recorded time constant	0.1 sec

The apparent brightness temperature of Jupiter T_ψ is approximately (*SPS 37-10*, Vol. I. p. 61: Ω_ψ antenna beamwidth):

$$T_\psi \simeq T_{A\psi}\frac{4\pi}{G_0\Omega_\psi},$$

where

G_0 = maximum antenna gain

Ω_ψ = angular diameter of Jupiter

This results in

$$\boxed{T_\psi \simeq 760°\text{K}}$$

with

Earth – Jupiter range $\simeq 6.014 \times 10^8$ km (Ref. 3)

Jupiter semi-diameter $\simeq 7.14$ km

$G_0 \simeq 54.4$ db
(*SPS 37-24*, Vol. III, p. 24)

The accuracy of the above is probably about $\pm 10\%$ and represents only a preliminary measurement.

3. Planetary Tracking Program

a. Summary. A multipurpose program has been written, for use on the Mod III stored program controller at the Venus site at Goldstone, which automates all phases of the current planetary tracking experiments, and which provides coder control during the planetary mapping experiments. This article is intended to explain the construction and operation of the program.

b. General program characteristics. In the following discussion, it will be assumed that the reader has an awareness of:

(1) The structure and organization of the Mod III stored program controller and its language, as outlined in *SPS 37-21*, Vol. III, pp. 62–71.[1]

(2) The operation of the planetary coders, as described in *SPS 37-27*, Vol. III, pp. 70–79.

(3) The philosophy of the tracking system implemented by the Planetary Tracking Program, as given in *SPS 37-28*, Vol. III, pp. 55–61.

The Planetary Tracking Program can be divided into four major components:

(1) Initialization and tape synchronization routine.

(2) "One-second loop."

(3) "Twenty-millisecond loop."

(4) Data acquisition and display routine.

The functional structure of these four components and the order of their relationships is displayed in Fig. 46.

[1]See also Baugh, Harold W., "Mod II Ranging Equipment," Technical Report No. 32-337, Jet Propulsion Laboratory, September 15, 1962.

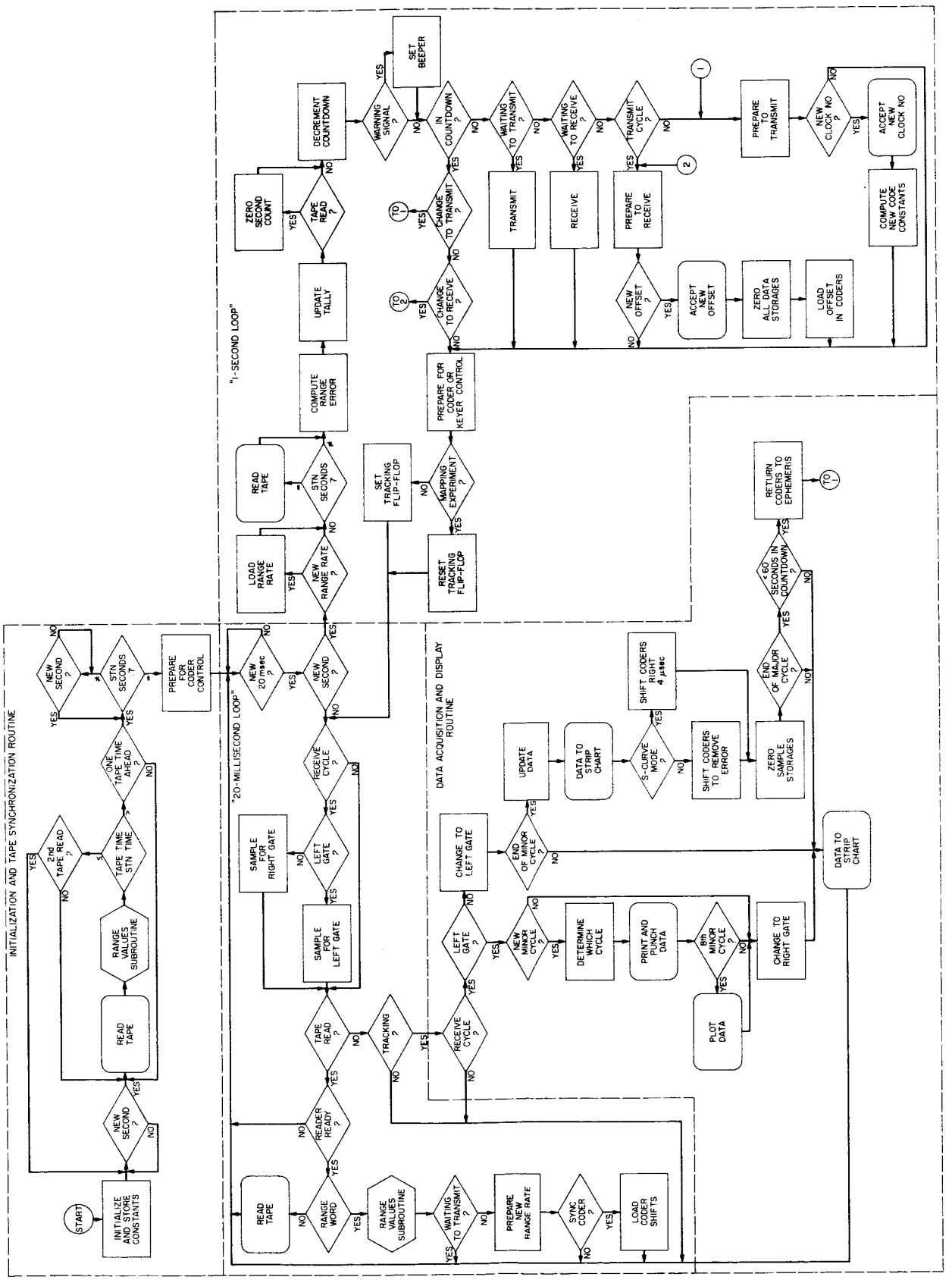


Fig. 46. Functional flow diagram of Mod III Planetary Tracking Program

The initialization and tape synchronization routine is a first-time-in structure which provides for the initial state of the Mod III and its external subsystems, and which synchronizes the tape reading and other real-time processes to the station time. The "one-second loop" is the minor timing loop, and its main purpose is to oversee the external control functions of the machine. The "twenty-millisecond" loop is the major timing loop, and is concerned essentially with controlling the internal state of the machine. Finally, the data acquisition and display routine has the task of ordering the sampled data internally and presenting this data through the various display devices of the Mod III. More comprehensive descriptions of the four program components follow.

c. Initialization and tape synchronization. A detailed flow chart of the initialization and tape synchronization routine is given in Fig. 47. The initialization portion of the routine is straightforward, consisting as it does of clearing internal lines and preparing constants. The tape synchronization portion of the routine consists of a tape search, in which the Mod III compares time words on the tape to station time until the first time word ahead of the station time is found, followed by a positioning of the tape for entrance into the program. Note that as each time word is read, the "range-values" subroutine, displayed in Fig. 48, is entered and range values are computed. Since the tape reader cannot process more than two time word–range word pairs per second, this practice

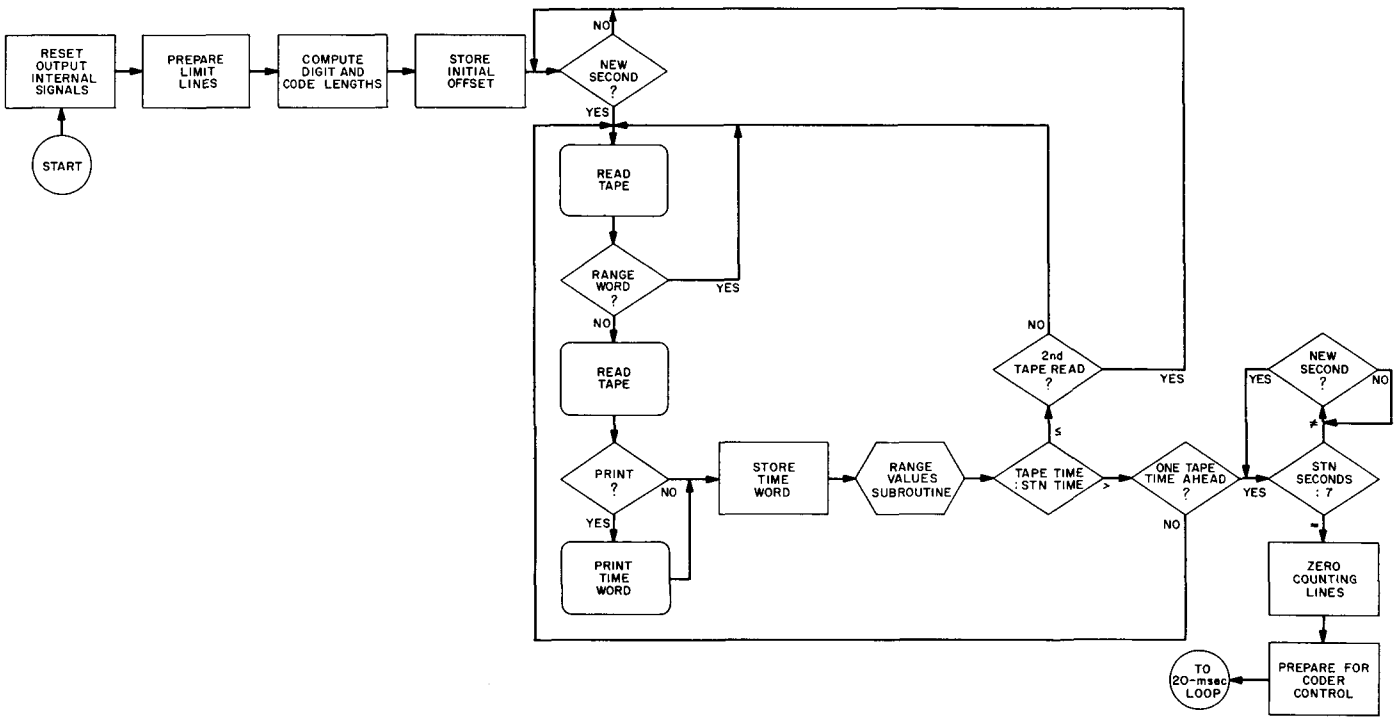


Fig. 47. Detailed flow chart of initialization and tape synchronization

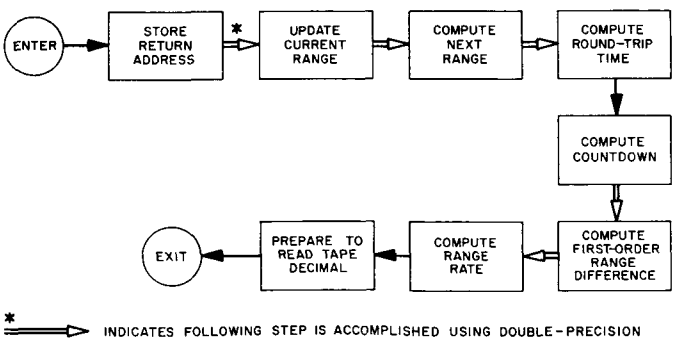


Fig. 48. Detailed flow chart of range values subroutine

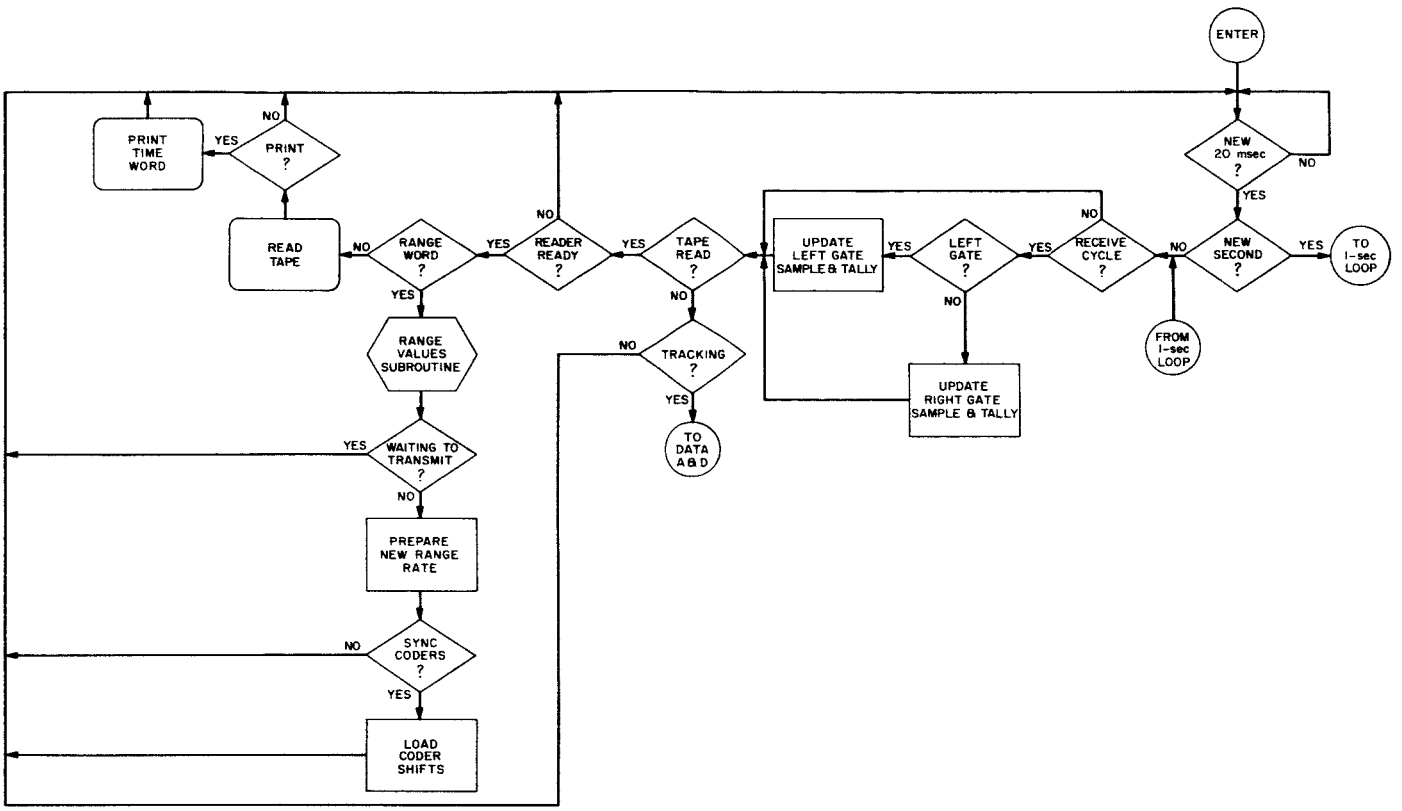


Fig. 49. Detailed flow chart of "twenty-millisecond loop"

enables the machine to make use of time that would otherwise be spent in waiting for the tape reader to recover.

d. "Twenty-millisecond loop." The "twenty-millisecond loop" is detailed in Fig. 49. After the initial entrance to the loop from the initialization and tape synchronization routine, all further program control is accomplished through this loop. A check is made each 20 msec to see if a new second has been entered and, if such is the case, control is passed to the "one-second loop." If a new second has not been entered, or if the "one-second loop" has returned control to the "twenty-millisecond loop," a check is made to see if the program is in the *receive* state and, if such is the case, the analog-to-digital converter is sampled and the data stored in either the left- or right-gate sample storage. Once the sampling is complete, or if the program were in a state other than *receive*, a check is made to see if a tape-read sequence has been initiated by the "one-second loop." If such a sequence has not been started, control goes to the data acquisition and display routine when the program is in the tracking mode, or to the beginning of the "twenty-millisecond loop" when the program is in the mapping mode. When a tape-read sequence has begun, the tape is read for range, and, when the print-time breakpoint is on, the time is printed. Control then returns to the beginning of the "twenty-millisecond loop." The next time through the loop, the range-values subroutine is entered and, if the program is in the *waiting-to-transmit* state, the tape-read sequence is completed and control returns to the beginning of the "twenty-millisecond loop." If the program is in some state other than *waiting-to-transmit*, a new range rate is prepared and when the *waiting-to-receive* part of the cycle has been entered, the coders are synchronized. The tape-read sequence is then completed and control returns to the beginning of the "twenty-millisecond loop."

e. "One-second loop." The organization of the "one-second loop" is detailed in Fig. 50. Entrance to this loop is from the "twenty-millisecond loop," and exit is back to the "twenty-millisecond loop." The loading of the range rate, calculated in the "twenty-millisecond loop," takes place here, as well as the initiation of the tape-read sequence. The range error (the difference between the actual shift present in the planetary coder and the shift reported by the coder counter) and the tally-mod-code-length (the Mod III's record of what the shift in the

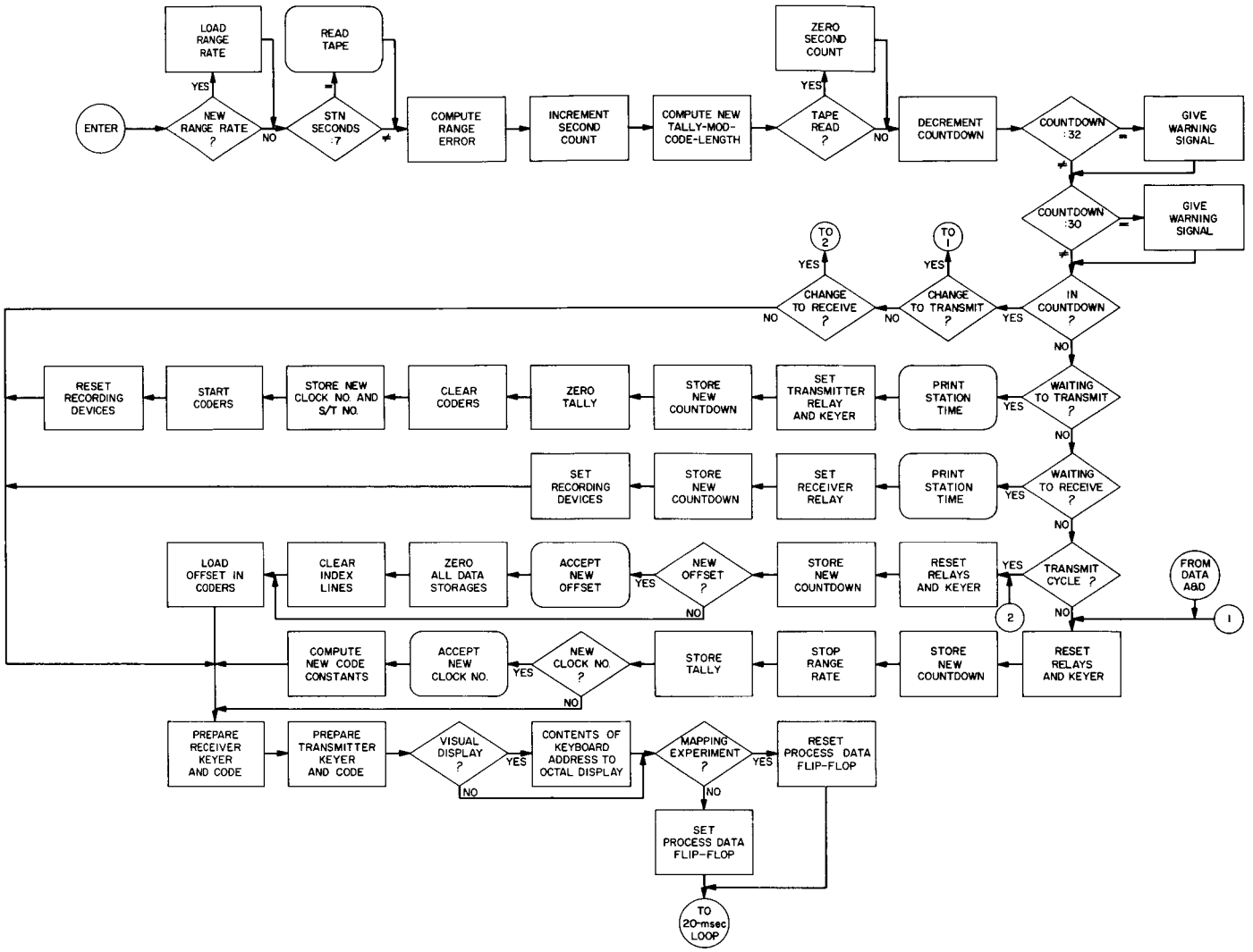


Fig. 50. Detailed flow chart of "one-second loop"

planetary counter should be) are calculated in the "one-second loop." A 1-sec count is used to interpolate between range values. The countdown number (initially set to the round-trip-time-minus-4-sec for both the *transmit* and *receive* portions of the cycle, and set to 8 sec for the *transmit–receive* changeover) is used to count time in each of the four states: *waiting-to-transmit*, *transmit*, *waiting-to-receive*, and *receive*. An operator-warning signal is given when there are 32 sec left in a *receive* or *transmit* state, and again 2 sec later. While the Mod III is counting down, a check is made each second to see if the operator has entered (by means of break-points) instructions to change cycles. Once the Mod III is through counting down, the next state of operation is determined and then entered.

A check is made each second by the Mod III to determine if the operator has indicated (by means of break-points) that transmitter or receiver control should be given to the keyer or coder. Also, a check of the break-points is made to see if an octal display of the contents of any of the Mod III addresses is desired, and to see if the mode of program operation, i.e., tracking versus mapping, is to be changed. The *waiting-to-transmit* state may also be entered, under conditions explained in Part *f* of this article, from the data acquisition and display routine.

f. Data acquisition and display. A detailed flow chart of the data acquisition and display routine is given in Fig. 51. The routine is entered from the "twenty-millisecond loop," and exits to either the "twenty-milli-

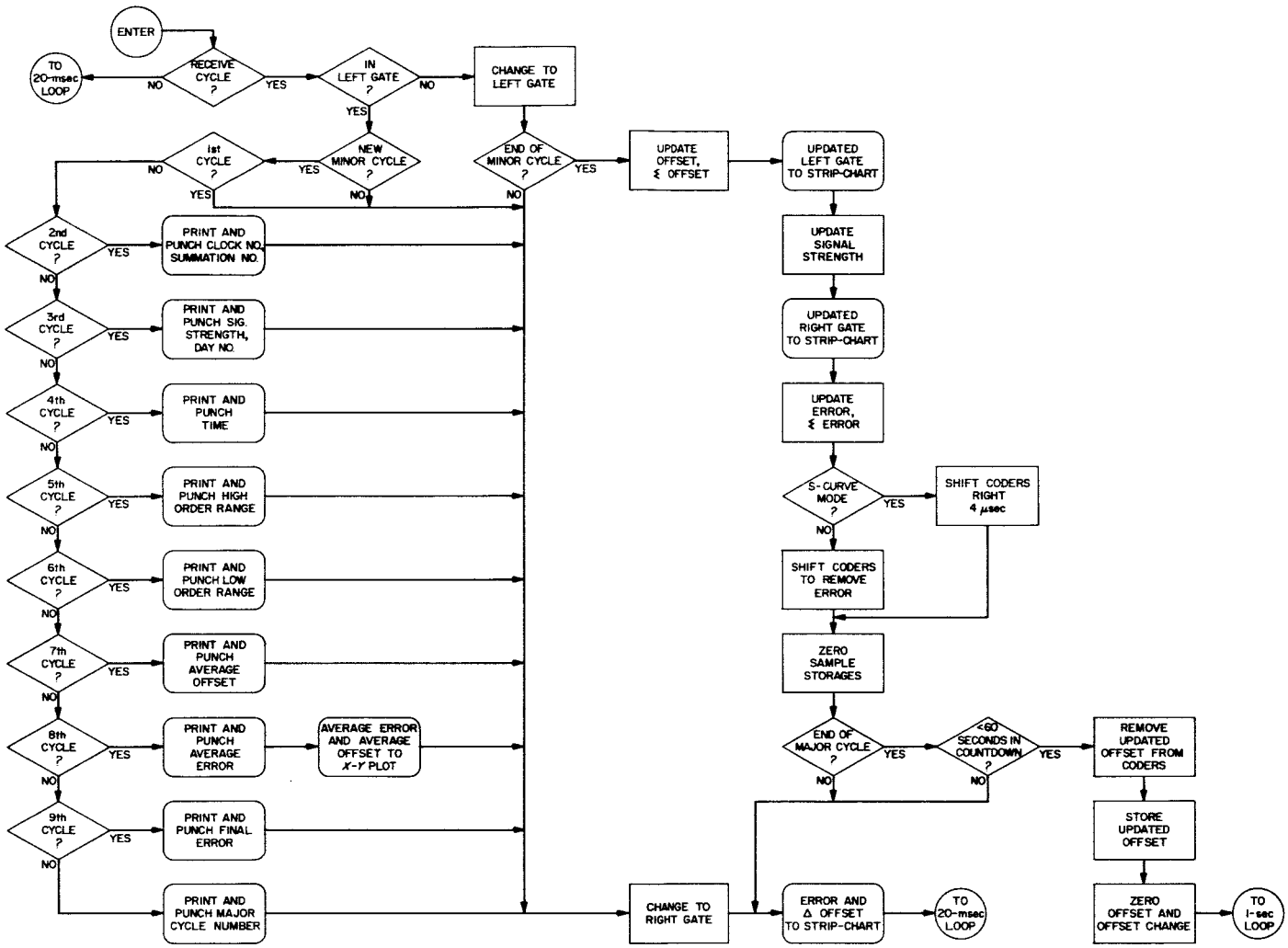


Fig. 51. Detailed flow chart of data acquisition and display

second loop" or to the "one-second loop." The data acquisition and display routine operates only during *receive* portions of the cycle. It is controlled by both minor and major timing loops, the minor loop being 6 sec in length, and the major loop being 60 sec long.

At the beginning of each minor cycle, one of nine pieces of data is printed and punched, except during the first minor cycle, when a blank is printed. At the end of each minor cycle, the data sampled over the preceding 6 sec is processed and displayed, and the coders are shifted in response to the data results. If the routine is in an S-curve mode, as dictated by the operator through a break-point, the coders shift right 4 μsec as part of a scan into the planet.

At the end of each major cycle, a check is made to see if there are more than 60 sec left in the countdown and, if such is the case, control is returned to the beginning of the "twenty-millisecond loop." If there are less than 60 sec left in the countdown, since there is not time enough to complete a major cycle, control goes to the *waiting-to-transmit* portion of the "one-second loop." A complete explanation of the order and method used by the data acquisition and display routine to display the data is given in the following article.

4. Data Processing

a. Summary. The 1964 Venus Tracking Experiment, now concluded, for over 2 mo produced data of high accuracy and precision. It is the purpose of this article to document the data acquisition and reduction procedures, and to indicate the steps that have been, or are being, taken in the analysis of the data.

b. Data acquisition and display. As indicated in the first report on the 1964 tracking experiment, which described the analysis and calibration of the system (*SPS 37-28*, Vol. III, pp. 55–61), data acquisition and display is one of the several functions performed by the Mod III stored program controller on site at Goldstone. Fig. 46, a functional flow diagram of the Mod III Planetary Tracking Program, shows the relationship of the data processing routine to the other functions of the program. The routine is detailed further in Fig. 51.

Real-time constraints are placed on data acquisition and display by the control functions of the machine, and it is a combination of these constraints, together with the relatively slow speed of the associated output devices, that has dictated the segmented nature of the data acquisition and output.

Data display is in the form of a print-out, a punched paper tape, a strip-chart, and an x-y plot. The print-out, strip-chart, and plot are used for on-the-spot engineering monitoring, while the punched tape is used as the initial source of permanent data. The following data items are recorded on both the print-out and the punched paper tape:

(1) *Clock number.* The number of 125-μsec blocks that compose a digit in the 511 PN code. With the exception of the first 2 days, a clock number of one was used throughout the experiment.

(2) *Summation number.* The number of seconds spent in each gate before the difference of the gates is examined to determine the appropriate phase shift in the receiver coder. Twice this number defines the length of a minor cycle. Throughout the experiment, the summation number was three.

(3) *Signal level.* The average signal plus noise level present in the left gate over each major cycle, a major cycle being ten minor cycles. The duration of a major cycle throughout the experiment was 60 sec.

(4) GMT day number.

(5) Greenwich Mean Time.

(6) *Range.* Ephemeris round-trip time in microseconds.

(7) *Average offset.* The average tracking-induced phase-shift in the receiver coder over each major cycle.

(8) *Average error.* The average gate difference over each major cycle.

(9) *Final error.* The gate difference during the last minor cycle of each major cycle.

(10) *Sample number.* The major cycle number.

It should be noted that, because the different data are acquired and recorded at differing intervals, each data item represents the state of the system at some unique time. The time relationships between the items, often pertinent to the analysis of the data, are shown in Table 5.

Table 5. Time–type relationship

Data type	Time, sec
Clock number and summation number	$t - 12$
Signal level and day number	$t - 6$
Greenwich Mean Time	t
High-order range	$t + 6$
Low-order range	$t + 12$
Average offset	$t + 18$
Average error	$t + 24$
Final error	$t + 30$
Sample number	$t + 36$

The x-y plot displays average offset on the x-axis against average error on the y-axis, thus forming a graph of the S-curve. This curve enables the engineer in charge to determine what initial offset is necessary in order to lock on to the planet for tracking. The strip-chart records total left gate signal on strip 1, total right gate signal on strip 2, average error on strip 3, and change in average offset on strip 4.

c. Octal-to-decimal conversion. The data, as it appears on paper tape from the Mod III, is in octal or quasi-octal form. In order to make the data amenable to hand and machine analysis, it is necessary to convert it to decimal form. This is done by first generating octal cards, one card per major cycle, from the punched paper tape, and then using these cards as input data to either an IBM 1620 or an IBM 7094 program which handles the octal-to-decimal conversion.

The octal cards are generated through the use of a modified IBM-047 tape-to-card punch located at the Echo site, Goldstone. The modification, made necessary because of the nonstandard paper tape format of the Mod III, consists of a disabling switch at the back of the machine which removes the parity check. A special board for the 047 is also necessary because of the tape format.

The 1620 Monitor I program for converting the octal cards to decimal cards and print-out, called *digital inter-*

preter, is shown in Fig. 52 as a functional flow diagram. The 7094 program follows the same logic and bears the same name, but is written in Fortran IV in order to accommodate the large range word without using double precision.

The conversion of the data from octal to decimal is complicated by the fact that the day number and time word are in the Mod III as binary-coded-decimal (BCD), but are punched on the paper tape as if they had been octal. The *digital interpreter* converts these words to decimal by first going through octal-to-decimal conversion procedure, and then taking the result and performing a hexadecimal conversion. The resulting number is the decimal equivalent of the original BCD word.

A second form of quasi-octal data is found in the range word. It is necessary to handle range in double precision within the Mod III; hence, when the range word is punched, the sign bit of the low-order half is the least significant binary bit of the next highest octal digit. This causes the entire high-order word to be shifted right by 1 binary bit. The problem is easily remedied by converting the high-order half from octal to decimal in the usual way, multiplying the result by two, and then adding the sign bit of the low-order half.

The output of the *digital interpreter* is in the form of decimal cards and print-out. The format of both the cards and the print-out was changed after Day 189, the difference being that through Day 189 the fields labeled "Average Offset" and "Average Error" actually contained, during the S-curve mode, the final offset and average offset, respectively. Before Day 156, range was measured to the left-gate rather than the mid-gate, and the signal strength was not recorded. Any non-zero entries in the signal field during the period before Day 156 were entered by hand to indicate bad data.

d. Data analysis. The data described in this article is being used in two major studies. One of these studies uses the S-curve data to determine the Venus backscattering law. The other uses the tracking data, in conjunction with older tracking data and all available doppler data, to

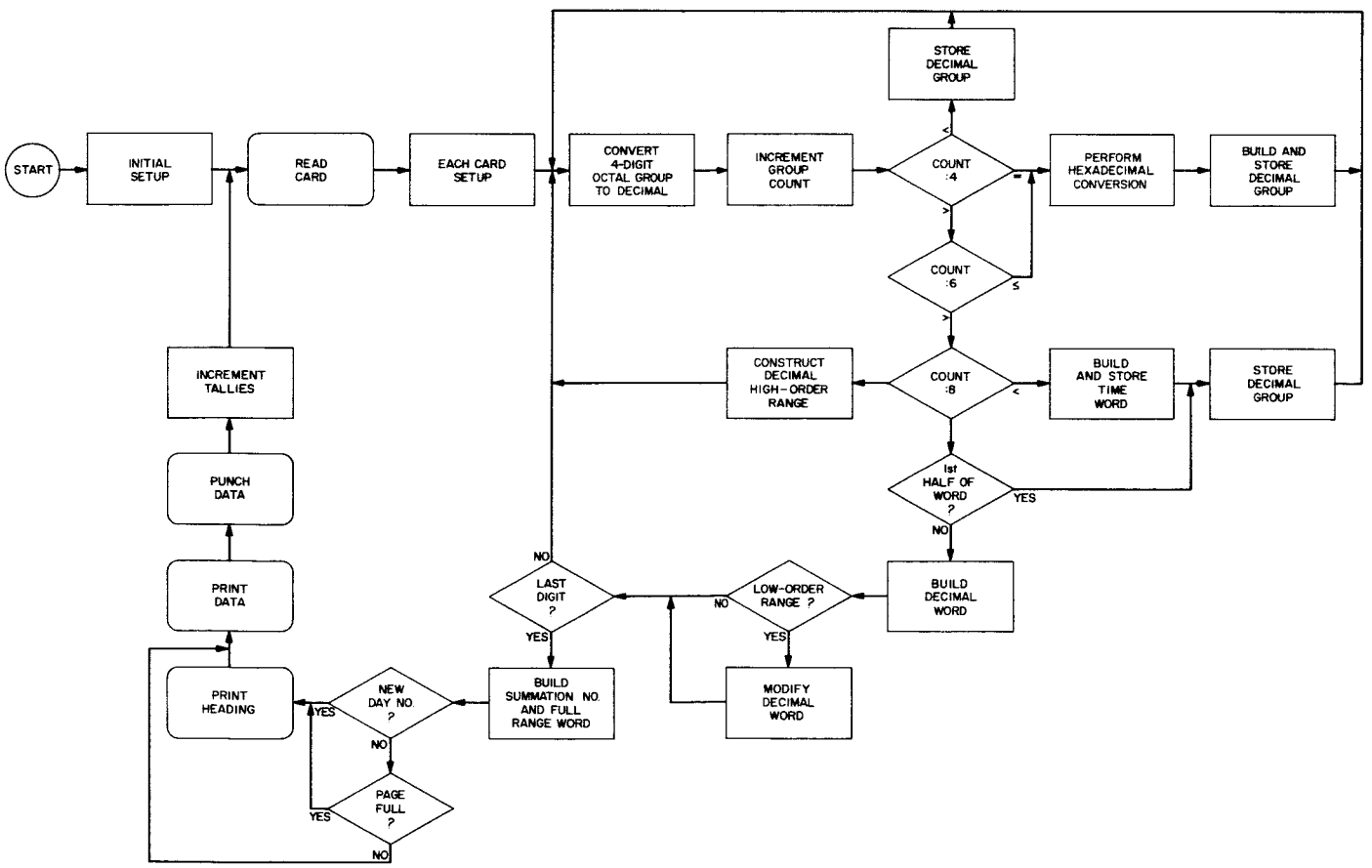


Fig. 52. Functional flow diagram of *digital interpreter*

better determine various astronomical constants used in the calculation of the orbit of Venus and Earth. Both of the projects demand further processing of the decimal data obtained from the *digital interpreter*.

Each study requires high-resolution S-curve plots in order that the distance to the sub-Earth point can be accurately determined. For this purpose, a 1620 program, called *data plot*, and a 7094 program have been written. Fig. 53 is a functional flow diagram of *data plot*. The 7094 program uses the Stromberg–Carlson plotter to produce x-y plots, while the 1620 program takes advantage of the "PLOT" subroutine to produce x-y plots on the high-speed printer. Examples of plots of the same data from each of the programs are given in Figs. 54 and 55.

For the backscatter study, a 1620 program has been written to normalize all the S-curve data and fit appropriate sections of the resulting curve with polynomials. The astronomical constants study requires edited data with range given to the sub-Earth point rather than the left- or mid-gate. The ephemeris range, printed during the minor cycles $t + 6$ and $t + 12$ (Table 5) is actually an ephemeris prediction of the range 8 sec past the minute in question; in order to have the equivalent measured range, it is necessary to interpolate linearly between the two range measurements that bound this minute. A 1620

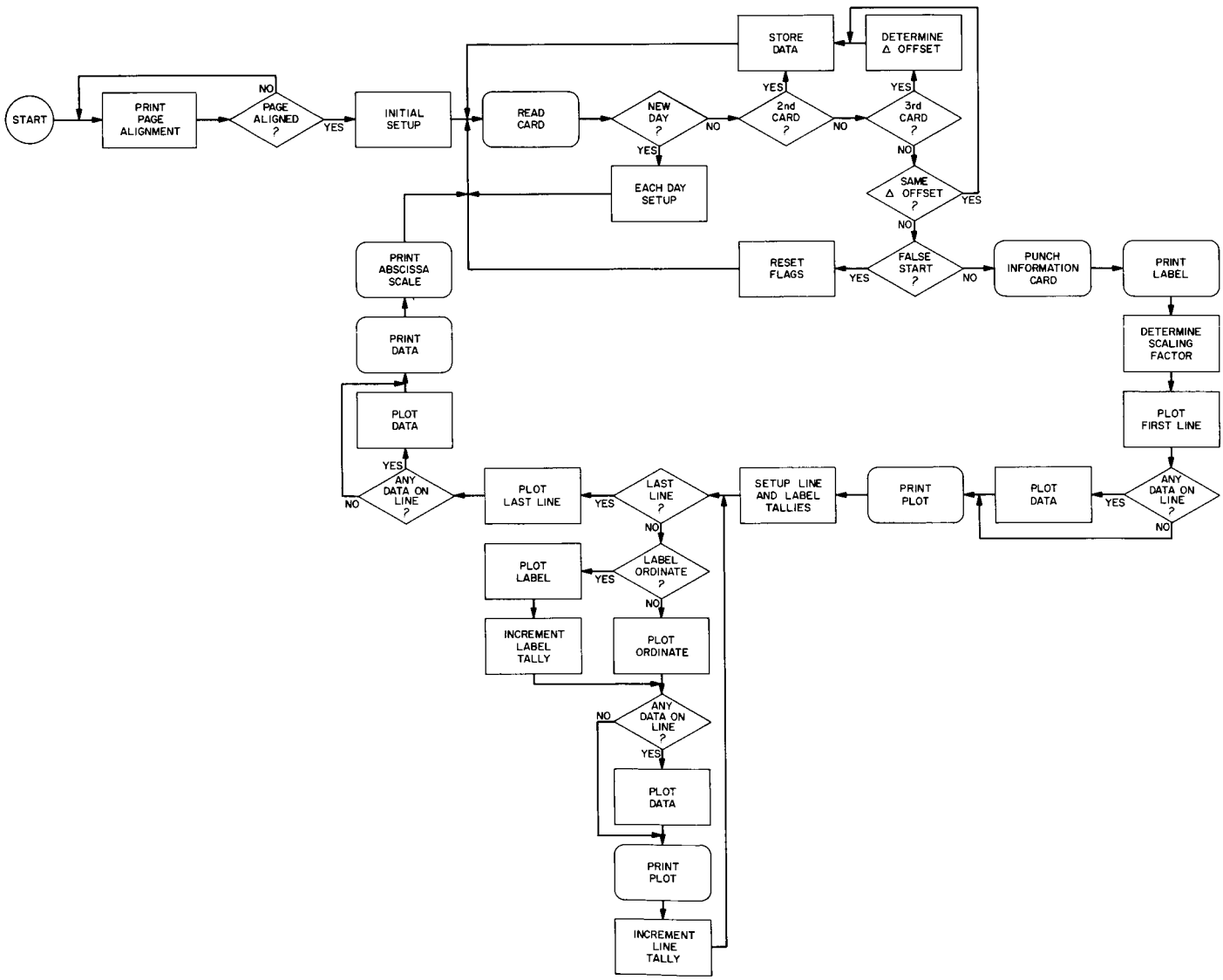


Fig. 53. Functional flow diagram of *data plot*

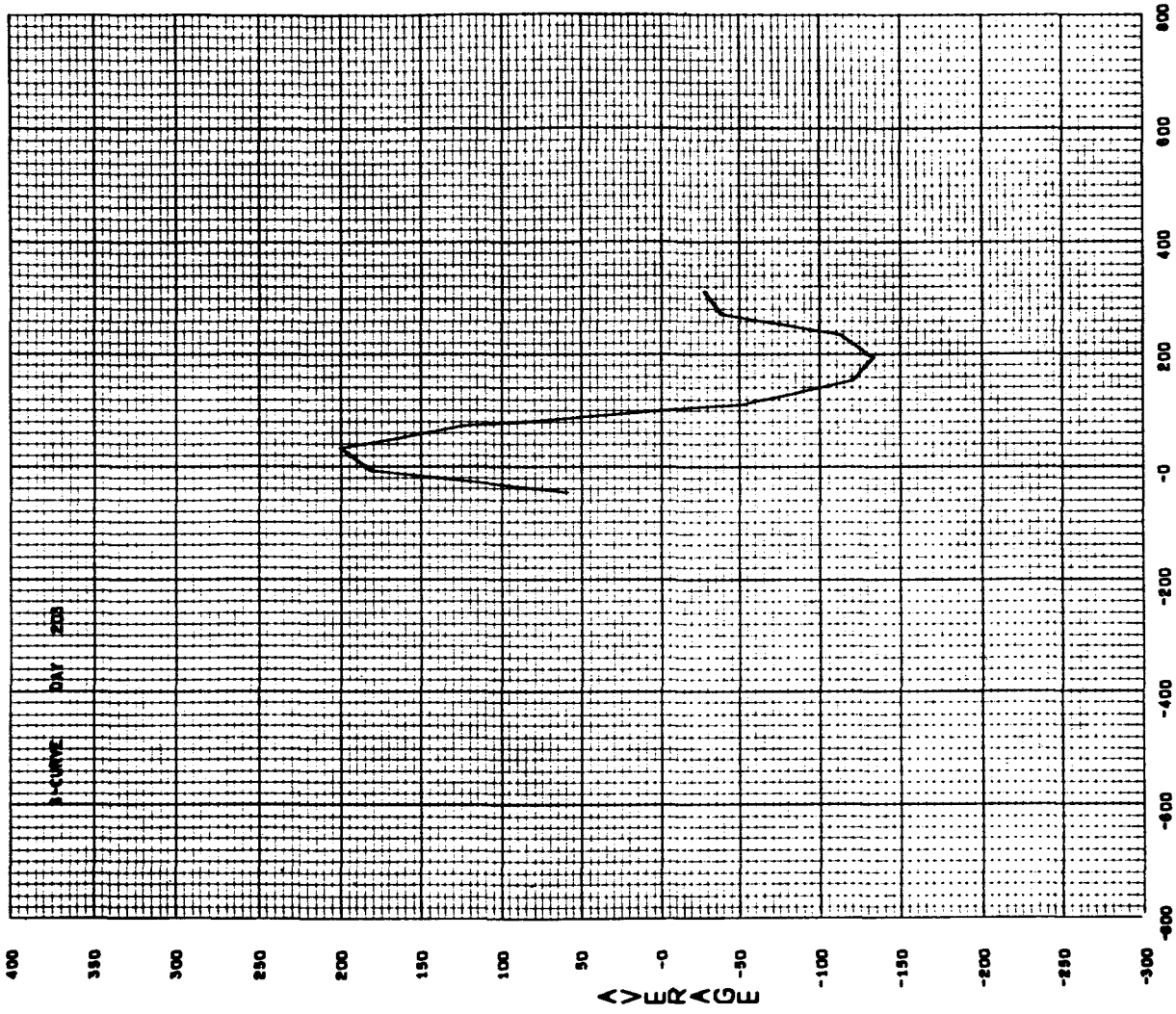


Fig. 55. Typical 7090 plot of S-curve (July 21, 1964)

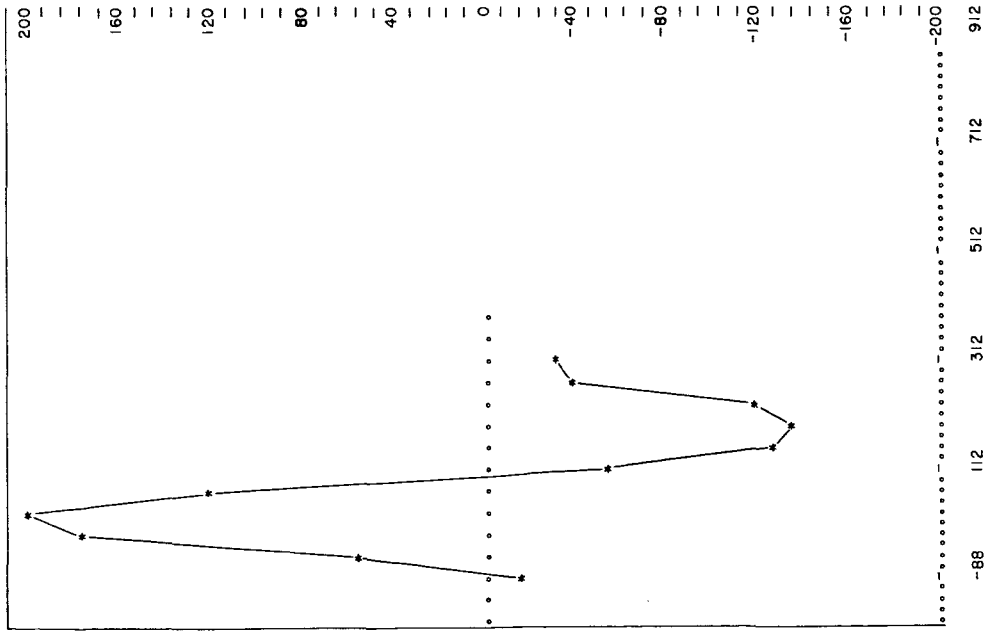


Fig. 54. Typical data plot S-curve (July 21, 1964)

program, called *tracking data,* has been written which performs the described interpolation and converts the resulting range to a distance-to-front-face measurement. Output of the program is in the form of punched cards and print-out. Fig. 56 is a functional flow diagram of *tracking data.*

Since the astronomical constants project uses as input edited points only, plots of the tracking data are necessary in order to determine when planetary lock-up occurred. The 7094 program that produces S-curve plots produces tracking plots simultaneously; an example is given in Fig. 57. A similar 1620 program is being written.

e. Future data. The 1964 Venus Tracking Experiment has aptly demonstrated the capabilities of the present system. Modifications are now being made which will allow the same basic system to be used in lunar ranging. The major hardware modification will be the installation of coders capable of providing digit lengths as small as 1 μsec. The major software modification involves changing the data acquisition scheme so that all data will be sampled at a specified time, buffered, and then distributed over minor cycles for output.

5. 100-kw S-Band Transmitter

a. Radio frequency interference. Installation of the 100-kw S-band transmitter in the R&D cone does not appear to have increased the receiving system noise temperature significantly. The noise temperature with the receiver switched to the antenna was increased 0.01 db when the transmitter beam voltage was on. This confirms the measurements and analysis made prior to the installation and previously reported (*SPS 37-30,* Vol. III). The power density at the maser input flange was measured to be −44.4 dbm (average) with the transmitter radiating +80 dbm into the RF load. This is slightly better than the predicted −42.5 dbm; the RF leakage from the transmitter and waveguide joints has been reduced by carefully machining and lapping the flanges.

6. S-Band Planetary Radar Receiver

a. Introduction. One of the objectives of the new S-band cone installation was the combining of the front end (antenna-mounted) portions of the maser instrumentation and radiometer functions with that of the planetary radar. This reduction, from two receivers to one, results in considerably less hardware and a simpler system configuration. On the other hand, neither existing receiver (*SPS 37-18,* Vol. III, Fig. 16; and *SPS 37-21,* Vol. III, Figs. 47, 49, and 52) possessed the combined requirements of coherent local oscillator, balanced mixing, and wideband, high-gain, stable amplification at 30 Mc. Therefore, a rather extensive modification of the radar converter was accomplished to meet these objectives.

b. Description. Fig. 58 depicts the combined configuration in a simplified manner. (For a more detailed

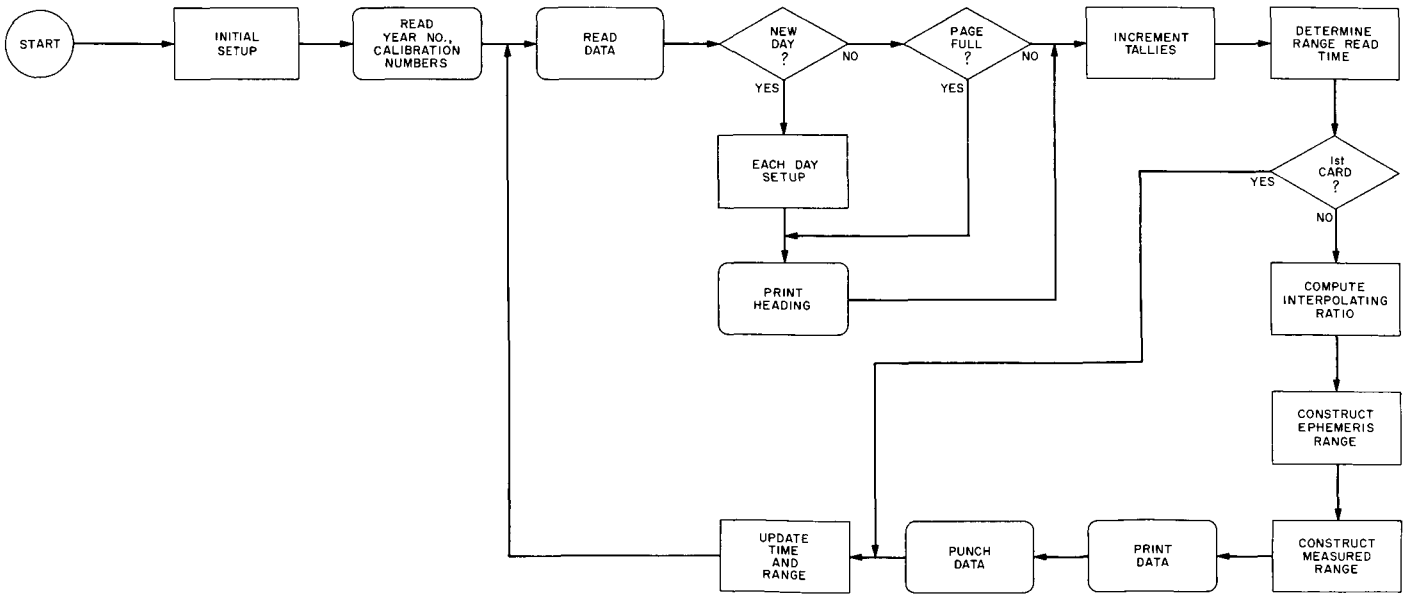


Fig. 56. Functional flow diagram of *tracking data*

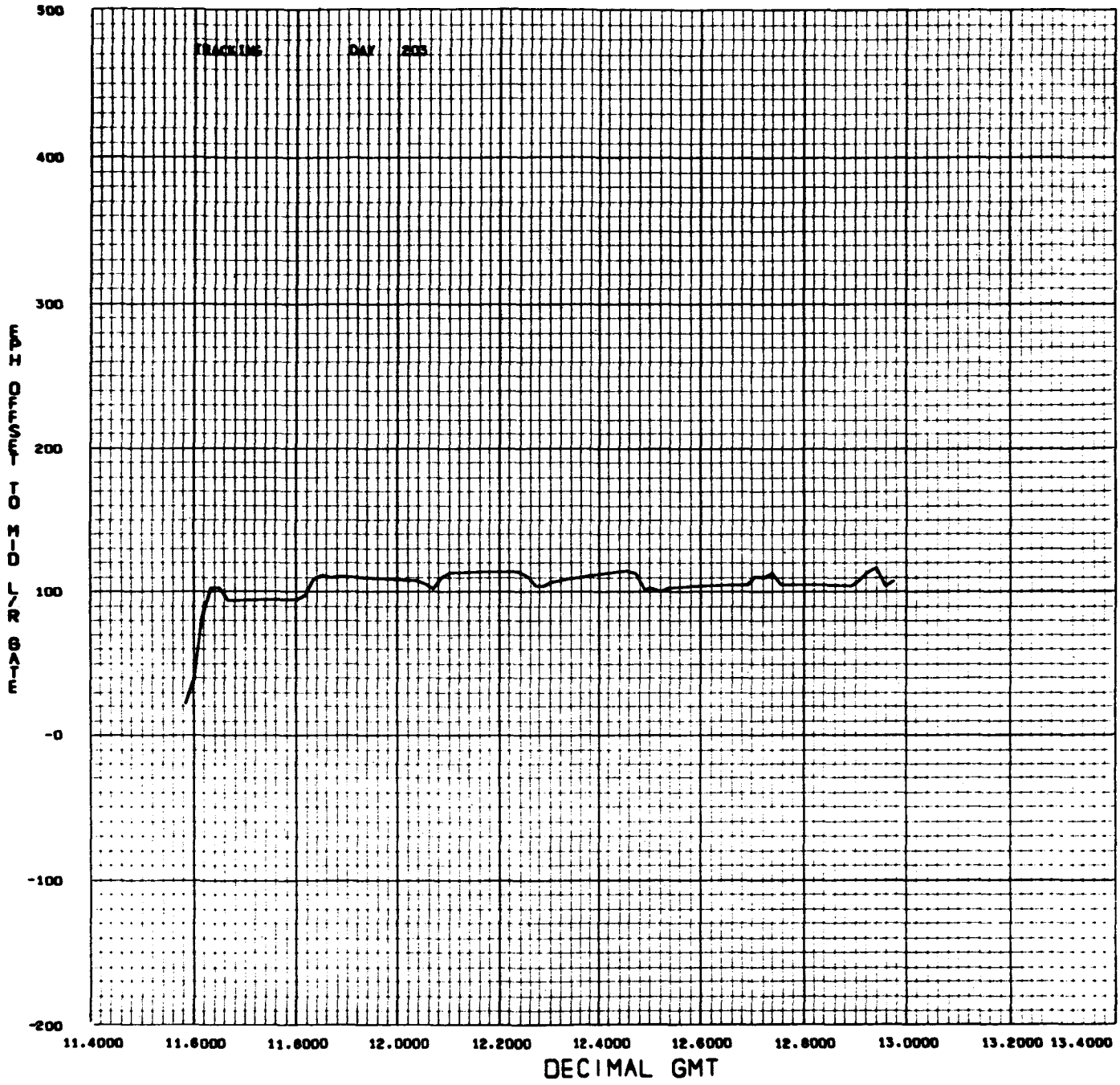


Fig. 57. Typical 7090 plot of tracking data (July 21, 1964)

description of the maser system, see Sect. VI-D-2 of this volume.) Fig. 59 is a detailed block diagram of the converter; photographs of the unit appear as Fig. 60. Although a selected combination of existing mixers and preamplifiers could have been utilized, prior experience with gain stability problems indicated that the weak point of previous systems was the control room mounted filament supply for the vacuum tube preamplifier. Gain sensitivity to filament temperature variations suggested the use of a solid-state preamplifier with a well regulated power supply. A combination of commercially available units (Figs. 59 and 60) provided the required gain and bandwidth. Modification of the units prior to incorporation included line filtering and self-contained, low-temperature-coefficient, zener regulators for double regulation of supply voltage, as well as RFI shielding

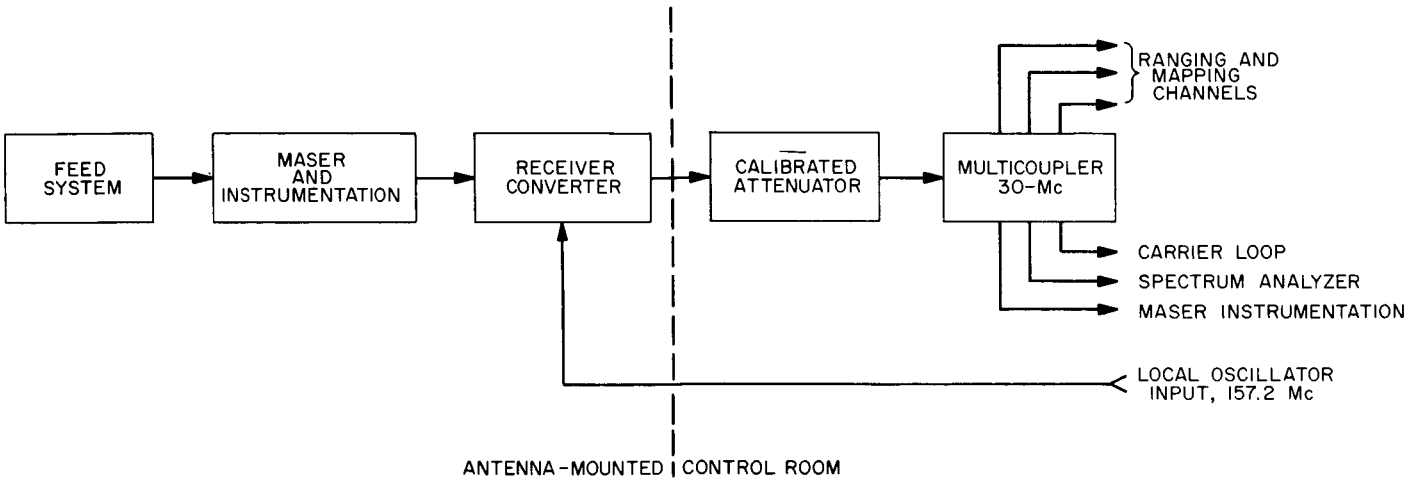


Fig. 58. Combined S-band radar and maser instrumentation receiver front end

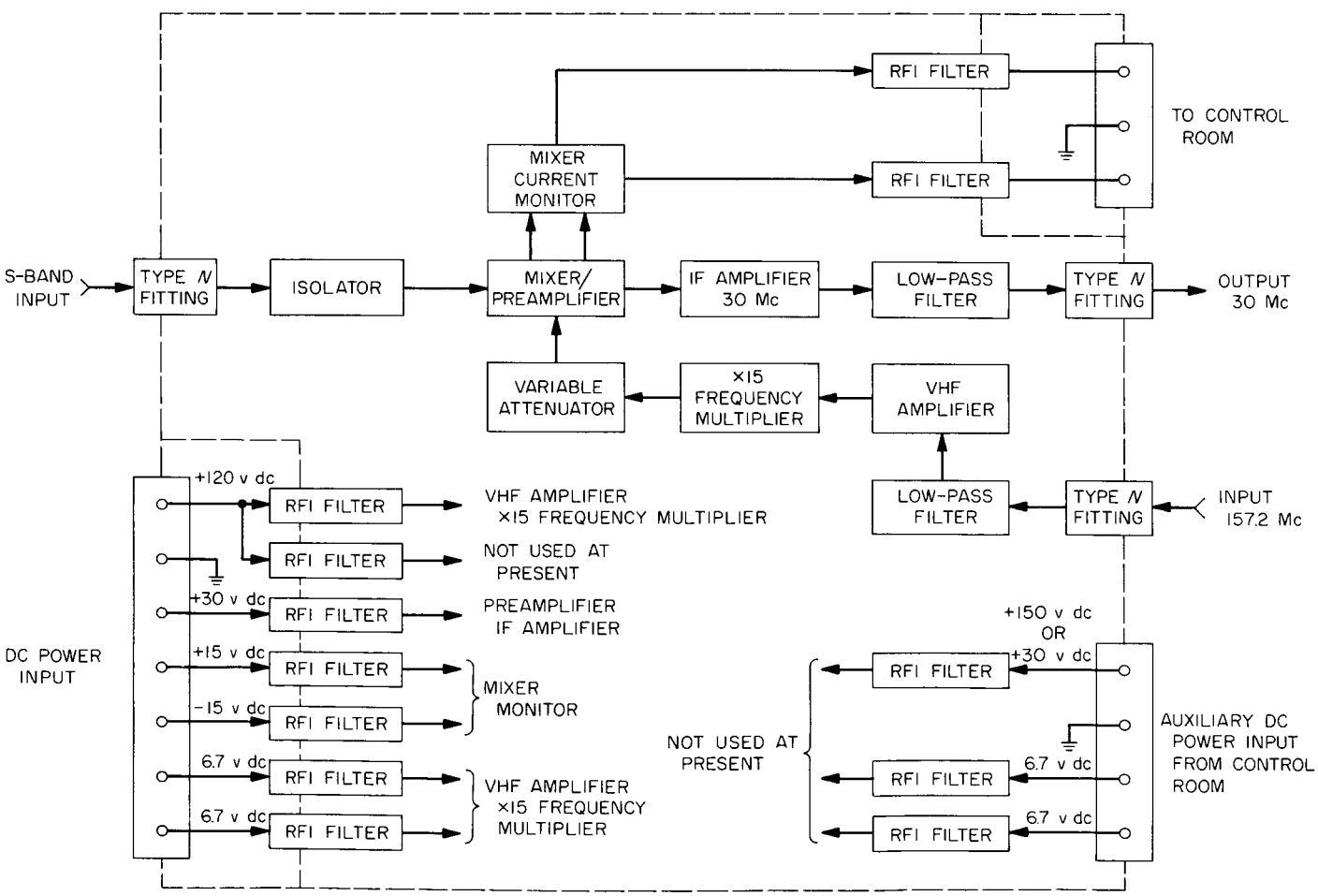


Fig. 59. 2388- to 30-Mc converter

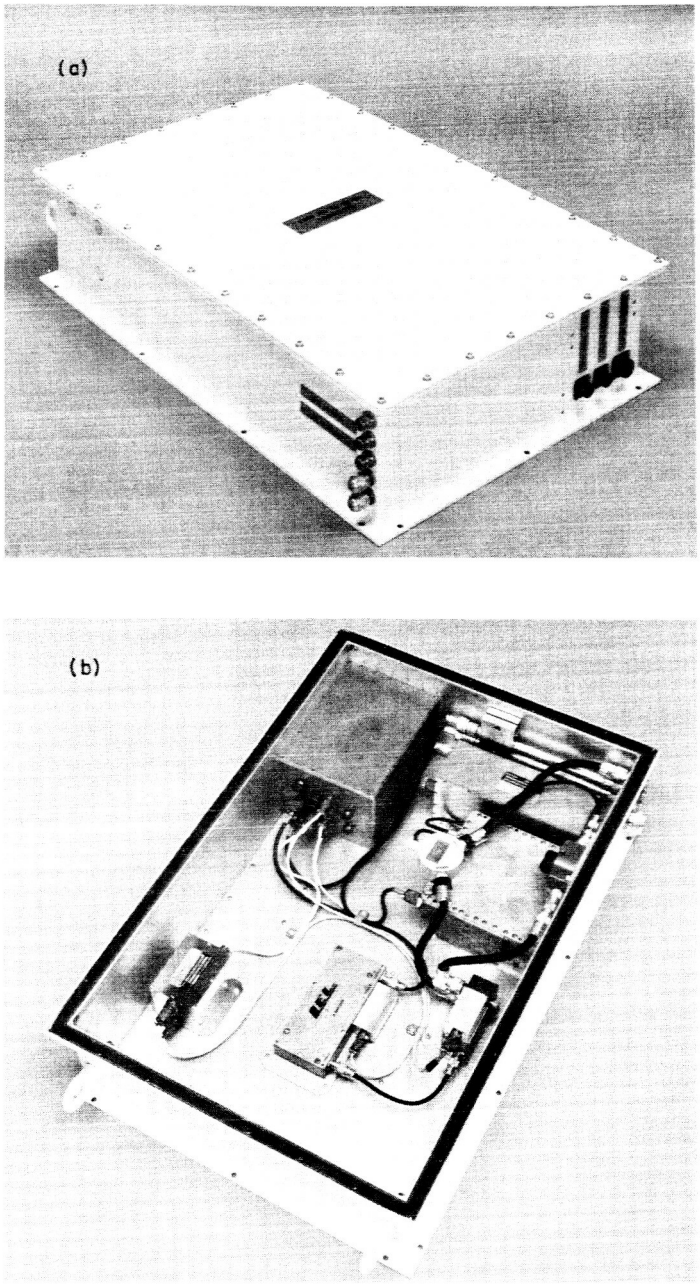


Fig. 60. 2388- to 30-Mc converter: (a) with cover and (b) with cover removed

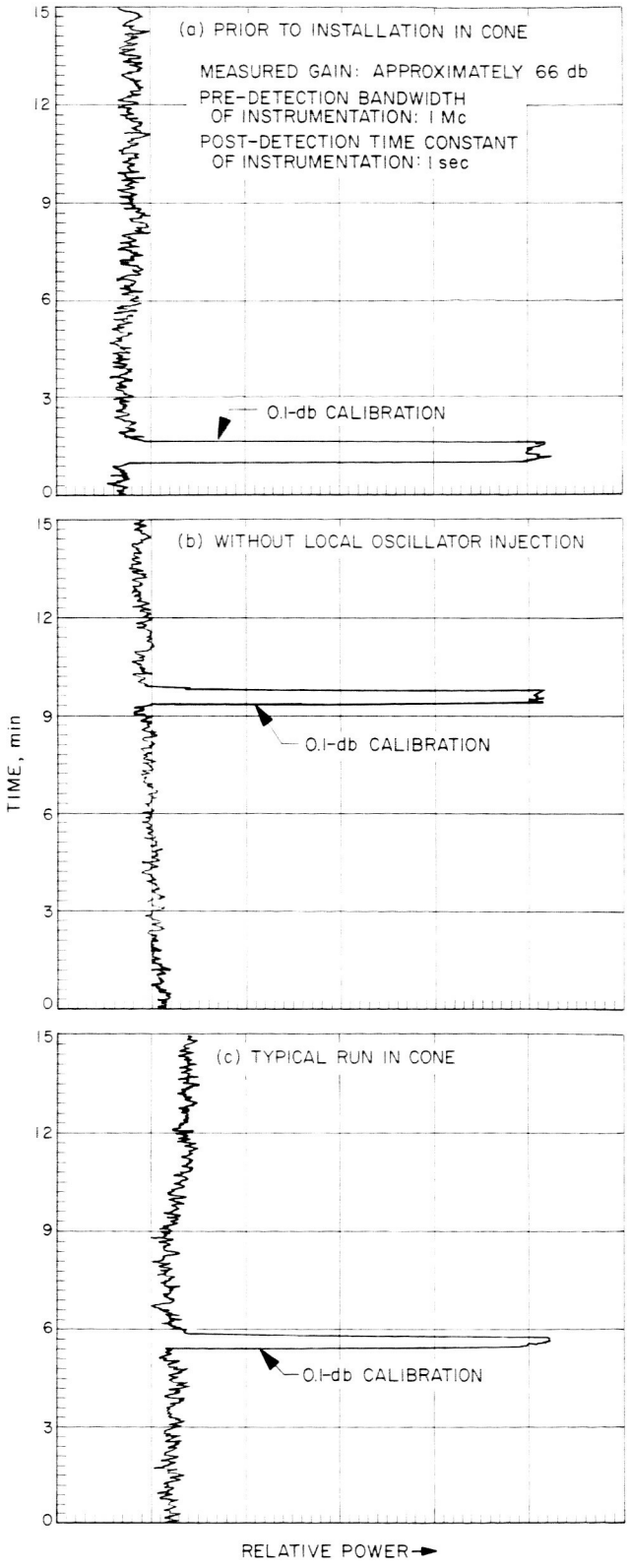


Fig. 61. 2388- to 30-Mc converter gain stability recordings

and mounting adapters with special consideration for module temperature stability. Not shown in the photograph is a ½-in.-thick copper base plate, thermally insulated from the outer housing, which replaced the thin aluminum plate of the IF amplifier prior to final data.

c. Test results. The completed converter was tested as a unit both before and after installation in the cone at the Laboratory with results described below. Although field operations (including maser calibration, radiometer star track and spectrum analysis of planet Jupiter radar returns) indicate satisfactory receiver performance, a full S-band retest of the modified (*SPS 37-30*, Vol. III) receiver has not been accomplished. This is due primarily to scheduling difficulties and to spurious operation of the cone-mounted S-band test signal generator. This difficulty was not in evidence during laboratory test prior to reinstallation, and is presently under investigation.

The converter test data follows:

Conversion gain	65.5 db
Noise figure, double sideband	7.0 db
Bandwidth (3-db)	12.5 Mc
Gain sensitivity to +30-v supply change	0.002 db/0.05%
Mixer balance (relative immunity to local oscillator self-detection)	30.5 db
Short-term gain stability (10 min)	<0.005 db peak-to-peak

Supporting test data for gain stability appears in Fig. 61. Comparison of the samples bears out the conclusion that, under normal (temperature and voltage stabilized) operating conditions, the local oscillator is now the limiting factor in gain stability. When solid-state multiplier chains become available (similar to those recently implemented at X-band, *SPS 37-29*, p. 86) for S-band, further improvement in this area is a likely prospect.

E. Error Statistics of Inter-DSN Teletype Channels

This article continues the teletype-error-correction study last reported in *SPS 37-30*, Vol. III, pp. 91–93. The problem of transmission of command messages to a spacecraft is two-fold. The first is the need for correct transmission and interpretation of messages, and the second is that the first be accomplished as speedily as possible. Previous Summaries (*SPS 37-26*, Vol. IV, pp. 223–225; *SPS 37-29*, Vol. III, pp. 95–99; and *SPS 37-29*, Vol. IV, p. 299) discussed a procedure to be used to decode messages, and detect and correct errors induced into the messages from the Earth environment before transmission to the spacecraft. By the implementation of the techniques discussed in those Summaries, it was possible to correct as many as 10 teletype symbol errors in a block of 63 message symbols. If the communication channel had probability of error of 0.02 per symbol, and errors occur independently, then the correction routine would drop the error probability to less than 10^{-8} per symbol. In order to determine the statistics of the channel more exactly, a program was written for the SDS 910 at the Venus site, GTS, to analyze messages that had been sent through the DSIF Stations. It is on that program that we report here. The program is now running, and messages are being sent.

1. Test Message

A program was written to encode a long pseudo-random test message to be sent over the DSIF communication links. After the return message is to be received, the received message would be compared to the message that was sent. Since the SDS computer was used for the encoding procedure and since a (nearly as possible) random message of teletype symbols was to be sent, a shift register sequence defined by the binary primitive recursion $x^{23} + x^5 + 1 = 0$ was used. Teletype symbols were determined from the standard Baudot code. The SDS has data word length 23 with 1 extra bit for sign, so the choice of the degree 23 polynomial was a natural one.

There are 5 bits used to encode each unit of information in the teletype code; this corresponds to a similar code in the SDS computer. The elements of the sequence were placed in the 5 highest order bits of each of the four 6-bit blocks in a data word, and then punched onto paper tape for sending in the teletype machine.

2. Channel Error Counter

The next step in the program was to design a program to determine varieties of errors occuring in the channel. Fig. 62 is a flow diagram of the error counting program. The program relies heavily on the shift and logical operations of the computer. The program utilizes 75 counters

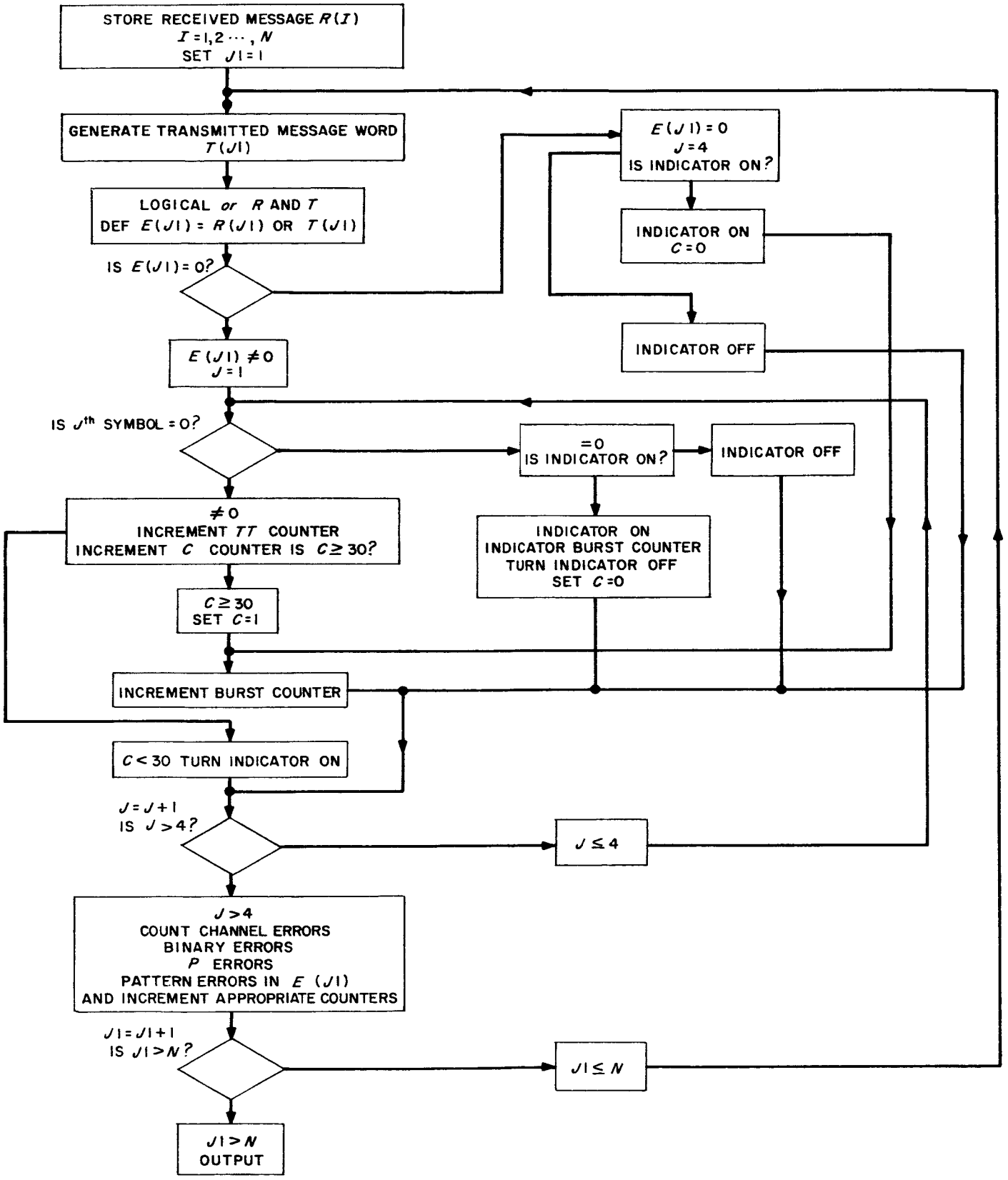


Fig. 62. Flow diagram of error checking routine

to indicate the frequency of errors. These counters and their number are:

Teletype symbol errors	(1)
Total binary errors	(1)
Binary channel errors	(5)
Number of errors per symbol	(6)
Pattern errors	(32)
Burst errors	(30)

Since not all of these counters are independent, a check can be made between them for quality of operation.

The teletype symbol counter counts every occurrence of an error in the teletype symbols themselves. The binary error counter counts every transition of a *zero* into a *one* or a *one* into a *zero* in the Baudot binary representation. The five channel counters break this count down to determine in which of the five "channels" these errors are taking place in the teletype symbol. The six counters tell the number of times 0, 1, 2, 3, 4, and 5 errors have occurred in each teletype symbol. The 32-error-pattern counters generalize the work of the six counters immediately above. While they count the number of errors in a teletype symbol, they also tell which of 32 possible error vectors have been added to the teletype symbol.

The 30 burst error counters are the most interesting. These counters tell how long a string of teletype errors occurred between reception of two symbols which were not in error. It is conceivable that there could occur a string of more than 30 symbols all of which are in error. The probability of such an occurrence is so small (less than 10^{-50}) that it can be ignored.

3. Program Checkout

The operation of the program was checked out with a series of two experiments. First, the received message was taken to be the message of all *zeros*. This was compared with the message which was generated in the computer during the error check program. By comparing this with a null message, every *one* which occurred as an output of the sequence generator would be interpreted as a binary error in the analysis of the data by the program. Given the starting vector 100 · · · 0, the sequence generator ground out 1000 bits, that is, 200 teletype symbols. The values of the various counters agreed with a hand calculation of the values that would be obtained.

For the second test, the transmitted message was inserted into the computer as the received message with no errors introduced. In this case there were to be no discrepancies between corresponding elements of the two sequences; again the program functioned correctly, indicating that no errors had occurred.

On December 14, 1964, there began to be sent a series of messages to the DSIF Stations over the *Mariner IV* link. With these messages went the instructions to retransmit the message back to JPL and to send a copy of the received tape via normal mail routes. With copies of the tapes which were sent to compare against those which were received, the statistics for the errors in the channel can be determined. If the error probabilities of the different kinds of errors fall within acceptable limits, the design of an error correcting program, as defined in previous Summaries, can go on as described.

F. Venus Site Operations: Experimental Activities

1. Current Experiments

a. X-band lunar experiment. An X-band lunar radar experiment was conducted at the Venus site for 11 days in the period from October 22 to November 11, 1964. A total of 74 hr of good data was obtained during this period. The X-band radar experiment operated at 8448 Mc using the 30-ft parabolic antenna with Cassegrain feed. A nine-cavity maser was used to obtain a system temperature of approximately 65°K. The 7-kw transmitter was phase-modulated with a pseudonoise code of length 16,383. Except for the RF equipment used, the ranging experiments conducted were identical to those performed earlier with the S-band system on the 85-ft antenna at the Venus site. The X-band system gave a much better signal-to-noise ratio (Fig. 63). The data from the ranging experiment is still being reduced, but preliminary results confirm the range obtained with the S-band system. Range-gated spectrum analysis was also obtained on one day during this period with a range gate of 1 μsec.

b. S-band planetary experiments. Beginning November 20, 1964, a continuing program of radar experiments on the planets Venus and Jupiter has been carried on during their view periods. This program uses the 85-ft Az–El antenna at the Venus site in conjunction with a maser

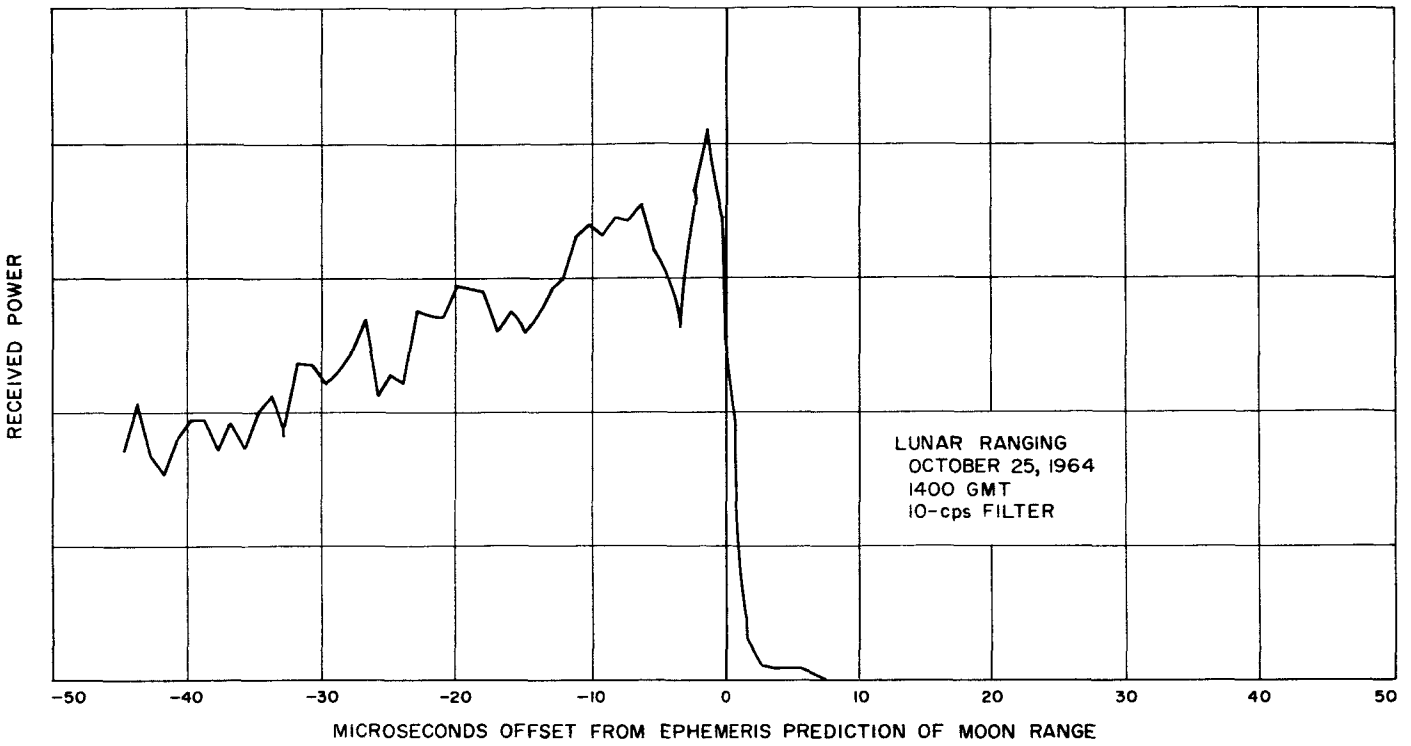


Fig. 63. Lunar ranging

and 100-kw transmitter. The primary purpose of the present experiment is to detect reflected signals from the planet Jupiter. The transmitter is amplitude-modulated 1 sec on and 1 sec off. The received signal is processed in a digital correlator to obtain the spectrum. On Jupiter the received signal is broken up into 12-min segments, so that only a small part of the surface will be observed on one spectrum. This procedure is necessary because of the high rotation rate of Jupiter. At the end of December, when the experiment is concluded, all the spectra obtained from a particular segment of the Jupiter surface will be averaged together in an attempt to detect a returned signal. Since Venus is easily detected in one round-trip time, the same experiment is run in a similar fashion on Venus primarily to check the operation of the system.

c. Star tracking. A continuing program of optical and radio star tracks has been carried on with the 85-ft S-band system and the 30-ft X-band system. These experiments are necessary to check the performance of the antennas.

d. 23-Gc radiometer. Beginning December 1, 1964, the Space Sciences Division has been conducting radiometer experiments at 23 Gc on the 30-ft antenna. The primary observation is Jupiter, but the Sun and radio star sources are also observed for calibration purposes.

A summary of Venus site activities is given in Table 6.

Table 6. Summary of Venus site experimental activity[a]

Experiment	Hours
Primary experiments	
Planetary radar	322
Lunar radar	74
Secondary experiments	
Radio and optical star track	55
Testing, calibration, construction, and maintenance (scheduled)	804
Down time (equipment failure, includes unscheduled maintenance)	147
Holidays	62
Total	1464

[a]For the period October 20, 1964 to December 19, 1964.

2. Subsystem Performance

a. 100-kw transmitter (operation). The 100-kw transmitter was refurbished and installed in the R&D Cassegrain feed cone. The cone was installed on the 85-ft antenna, and tracking operations began on November 20, 1964.

The transmitter was operated at powers lower than 100 kw at the start of the experiment due to operation of the reflected power protective devices at full power.

This problem was found to be caused by improper installation of component parts and was corrected. The system was shut down on November 30, 1964, because of burned and scored slip rings on the 1-Mw synchronous motor generator. Tracking resumed on December 9, 1964, after the slip rings had been resurfaced and new brushes installed. Other shutdowns of the transmitter were caused by operation of Vac-Ion, back power and arc detector interlocks, caused by the "outgassing" of the klystron tube.

b. 7-kw X-band transmitter (operation). The X-band transmitter was operated on the 30-ft antenna as part of the Lunar Ranging Experiment from October 22 through November 11, 1964. During this period, the transmitter varied in power output from 2.8 to 9.4 kw, with an average output of 6.2 kw over the entire experiment.

Transmitter problems causing downtime included failure of a coaxial switch, low cooling water flow, monitoring circuit failure, water leaks, low output from the traveling wave tube (TWT) driver, and recurring back power cutoffs caused by improper operation of the waveguide switches.

At completion of the X-band experiment, the transmitter was removed from the antenna and installed on the ground for testing of the new beam keyer, presently under design and construction.

c. S-band receiver. In bringing the modified S-band receiver to an operational status, several difficulties were encountered. Limiting on strong signals occurred in the 30-Mc postamplifier of the receiver 2388- to 30-Mc converter. This limiting produced nonlinearity and was eliminated by installing 10 db of attenuation between the preamplifier and the post amplifier in the converter.

The second conversion mixer in the AM channel had insufficient bandwidth for the Jupiter experiment. It was modified to obtain the required 40-kc bandwidth. The AM channel 455-kc IF amplifier also had insufficient bandwidth and was realigned for 32-kc bandwidth.

The Resdel signal generator failed and is being repaired. Without this generator, absolute measurement of receiver sensitivity cannot be made. Two channels only are presently being used: the AM channel for planetary experiments and the SUM channel for testing and calibration.

d. Programmed local oscillator. Due to the modifications made to the programmed local oscillator (PLO) as described in *SPS 37-30*, the reliability of the system has been improved and the operation has been simplified. During the recent X-band experiment and present S-band experiment, the system has operated with only minor difficulties of a faulty power supply and incorrect setup procedures. In a further modification to improve reliability and simplify operation, the only remaining phase-locked loop has been replaced with a balanced mixer and crystal filter.

e. X-band receiver. During the X-band lunar experiment, the receiver operated normally except for the failure of the $\times 4$ frequency multiplier in the 8448- to 30-Mc converter. This unit was a new experimental model; when it was replaced, the system was restored to operational status. A detailed description of the X-band receiver conversion is covered in *SPS 37-30*, Vol. III. It should be noted that no absolute receiver sensitivity measurements were made during the lunar experiment because of the lack of a suitable X-band signal generator.

f. S- and X-band central frequency synthesizer. No failures have occurred and no modifications have been made to this system during this period. It has been observed that whenever the refrigeration unit which supplies cold water to the power supply cold plates fails, the temperature of the cold plate rises to 42°C. This condition has existed for several days at a time with no apparent ill effects. The refrigeration unit has failed many times in the past and is presently being modified to provide more reliable operation.

g. Collimation tower. During a recent windstorm, the waveguide run between the signal generator and the antenna was damaged, and waveguide pressurization was lost. The waveguide has now been repaired, and is being inspected for internal contamination. VSWR and loss measurements will also be made. Additional and more rigid supports for the waveguide run are also being installed.

h. Digital equipment. Two problems have marred the otherwise satisfactory performance of digital equipment during this reporting period. The SDS 910 computer made occasional errors during program operation that could not be made to recur by standard diagnostic analysis. These errors were only cured when an intermittent transistor in a main register failed completely and permitted itself to be found. Continuing temperature problems led to intermittent failures also in the Mod III stored program controller (SPC) and digital PLO. Brute-force increases in air supply have suspended these failures, but leave a simple answer yet to be found.

Rework of the Control Building refrigerated air supply has increased the supply and decreased the temperature of underfloor air; it is probably correct to say that sufficient capacity exists to handle the present equipment heat load. For digital equipment using germanium components, however, the situation is still marginal. Internal rack layout and small underfloor pressure differential combine to allow localized hotspots, and logic failures follow.

During shutdown, Mod III SPC was reworked to make better use of the available supply of cooling air; bottoms were completely cut out of both logic racks; one-half the carriage slides were removed from top and bottom of mounting frames to decrease air resistance. Initially, louvered tops were installed in the racks. When logic dropouts began to occur, these tops were removed completely, allowing greater flow. When the dropouts continued, 500-ft^3/min fans were installed in rack tops and the trouble ceased. However, the margin is small; a 3 to 4°F rise in input temperature can again initiate dropouts.

Room exhaust air is initially chilled to 55°F, pumped, baffled, silenced, and delivered underfloor at 62 to 64°F. Air exhausted from Mod III logic racks can run as high as 84°F under these conditions. Since this temperature does not greatly change with or without fans, it is reasonable to suppose that fans remove some heat that normally stays trapped in the structure with convection cooling only, and that better scavenging, rather than increased flow, is the reason for improvement. Since further rework of Mod III is impractical at this time, the fans have been retained for the immediate future.

A significant addition to the digital installation has been the increase in memory of the SDS 910; it now contains 4096 randomly accessible cells constituting 7777 (octal) programmable addresses. Of these, the lower 217 (octal) are reserved for special program functions.

The Mod III SPS input/output bay also has been rebuilt to allow easier and simpler connection to and from the computer. This is useful when operational programming changes demand quick additions or changes to the computer proper.

Programs have been written for use on the SDS 910 permitting expansion of polynomial curve fits to provide angle, range, and doppler ephemerides. Eighth-order fits are sufficient to describe range and doppler, but tenth-order are necessary to fit azimuth and elevation within the requisite error over a 12-hour span. Throughout the X-band lunar ranging experiment, the 30-ft antenna was driven to the lunar ephemeris using the angle portion of this program. Although doppler and range expansions have been programmed and checked, they have not yet been employed in actual operations.

The attempt to provide these same programmed functions for Mod III SPC has been abandoned as unprofitable. With only 1777 (octal) programmable addresses, Mod III memory is insufficient to contain program and subroutines for an operation of this size, and expansion of the memory is considered unjustified.

Continual updating of operational programs is continuing.The Jupiter AM spectrum program has had four major changes in the course of the experiment to permit immediate changes in operational method. This experiment is being conducted using the 85-ft antenna with the Jupiter millimeter wave experiment being conducted simultaneously on the 30-ft antenna. Since both use the Mod III SPC for operational control of their systems, and since both have somewhat similar timings, the programs were rewritten and merged; both experiments are now under simultaneous control from Mod III. Antenna drive for the 85-ft is provided by the angle tape puller (ATP) and digital differencing junction (DDJ) using drive tapes generated at the Laboratory; 30-ft commands come from the SDS 910 using the sidereal clock program manually updated hourly. It is of interest here that predetermined offsets for the 30-ft antenna are entered and removed from the SDS 910 by control from the Mod III—a first step in directly integrating the operation of the two computers.

i. 30-ft antenna (operations and modifications). Using the X-band radar system installed during the previous reporting period, Venus site operations were carried out on a 24-hr/day schedule. No major modifications were made to the antenna during this period, since it was constantly in use for the experiments. Normal maintenance and minor equipment modification were performed during the few periods when experiments were not being conducted. A ½-ton electric hoist was purchased and installed on the antenna to facilitate the installation and removal of equipment.

At the conclusion of the listed experiments, the X-band radar equipment was removed and a radiometer, together with its associated equipment, was installed on the antenna and in the operations control room. This is essentially the same equipment which had been used during the Venus millimeter experiment, conducted at this site during June and July. The antenna in this configuration is currently being used to gather data for experiments

being conducted by the Space Sciences Division. Support and maintenance functions are being performed by site personnel during this operation.

j. 85-ft antenna (operations and modifications). The only major modification to the 85-ft antenna during the present reporting period was the removal of the *Mariner* equipment cone and its replacement with the redesigned and rebuilt S-band research and development cone. This cone interchange allowed further training of site personnel in the methods of cone installation. A step-by-step written procedure for this operation has been developed and distributed to all site personnel. It is felt that the use of this procedure and further practice by site personnel will not only enhance the safety of this operation, but will also reduce the time required for its performance. Normal maintenance continues; the antenna has been completely lubricated and all hydraulic filters have been replaced. A difficulty in switching from low to high speed in elevation has been cured by the replacement of a servo valve. Finally, all surplus and no longer used cabling has been removed from the antenna structure.

The 85-ft antenna operations during this period have consisted exclusively of the Jupiter and Venus tracking experiments. These experiments are currently in progress and will continue into January.

k. X-band maser. The X-band multiple cavity maser was operated as part of the X-band lunar radar system during the period October 22 to November 11. The system temperature, when connected to the antenna, was approximately 65°K. Some trouble was experienced maintaining normal maser gain toward the end of the operating period; this was presumably due to continual frosting of the waveguide input structure during liquid helium filling. The maser has been returned to the Laboratory for overhaul in preparation for the next operating period.

During the X-band radar experiments, weekly calibrations of the microwave gas tube noise sources were made. The gas tube noise sources are the means by which the daily measurements of system noise temperature are made; they must be accurately calibrated to provide reliable measurement of system temperature.

The calibration technique (*SPS 37-30*, Vol. IV, p. 230) used microwave terminations at known temperatures for standard noise sources. The initial calibration of the noise sources was performed on October 24, 1964. The calibrating sources used were waveguide loads maintained at liquid helium, liquid nitrogen, and ambient temperatures. After correction for waveguide losses and ambient temperature effects, the equivalent noise temperatures at the maser input flange were 32.6, 97.5, and 297°K, respectively, for the helium, nitrogen, and ambient loads. The results of this calibration are shown in Table 7.

Table 7. Characteristics of noise sources used for X-band system temperature measurement

Noise source	Terminations used for calibration	Calculated excess noise T_e, °K	Probable error, °K	Weighted average, °K
Data taken October 24, 1964				
Experimental gas tube (neon)	Helium, nitrogen	25.6	0.88	26.1
	Helium, ambient	25.6	1.0	
	Nitrogen, ambient	28.5	1.5	
High-power gas tube	Helium, nitrogen	34.8	1.0	34.7
	Helium, ambient	34.6	1.1	
	Nitrogen, ambient	34.5	1.5	
Low-power gas tube	Helium, nitrogen	3.86	0.69	3.84
	Helium, ambient	3.71	0.93	
	Nitrogen, ambient	4.06	1.4	
Data taken October 31, 1964				
High-power gas tube	Helium, nitrogen	34.6	0.8	33.9
	Helium, ambient	33.4	0.9	
	Nitrogen, ambient	33.0	1.2	

l. S-band maser. The rebuilt S-band maser was shipped to the Venus site on November 14, 1964. During November 14 and 15, the maser was installed in the Cassegrain feed cone and the associated waveguide and hardware was installed and connected; the main closed cycle refrigerator (CCR) compressor and interconnecting helium lines were leak-tested and vacuum-pumped; and all necessary preparations were made for installation of the maser on the antenna.

On November 16, 1964, the Cassegrain feed cone was installed on the 85-ft antenna; the helium lines from the CCR compressor were connected to the maser and again vacuum pumped. The lines were then charged with dry, oil-free helium gas, and the maser "cool-down" was begun, using temporary instrumentation because the new simplified maser instrumentation rack was not completed. The maser instrumentation rack was delivered during the "cool-down" period and was partially operational on November 20, 1964, at which time the radar experiment on Venus and Jupiter was begun. On December 8, 1964, the maser "warmed up" due to a vacuum leak, possibly due to improper seating of an O-ring within the maser Dewar. The maser was again cooled down and is presently operational.

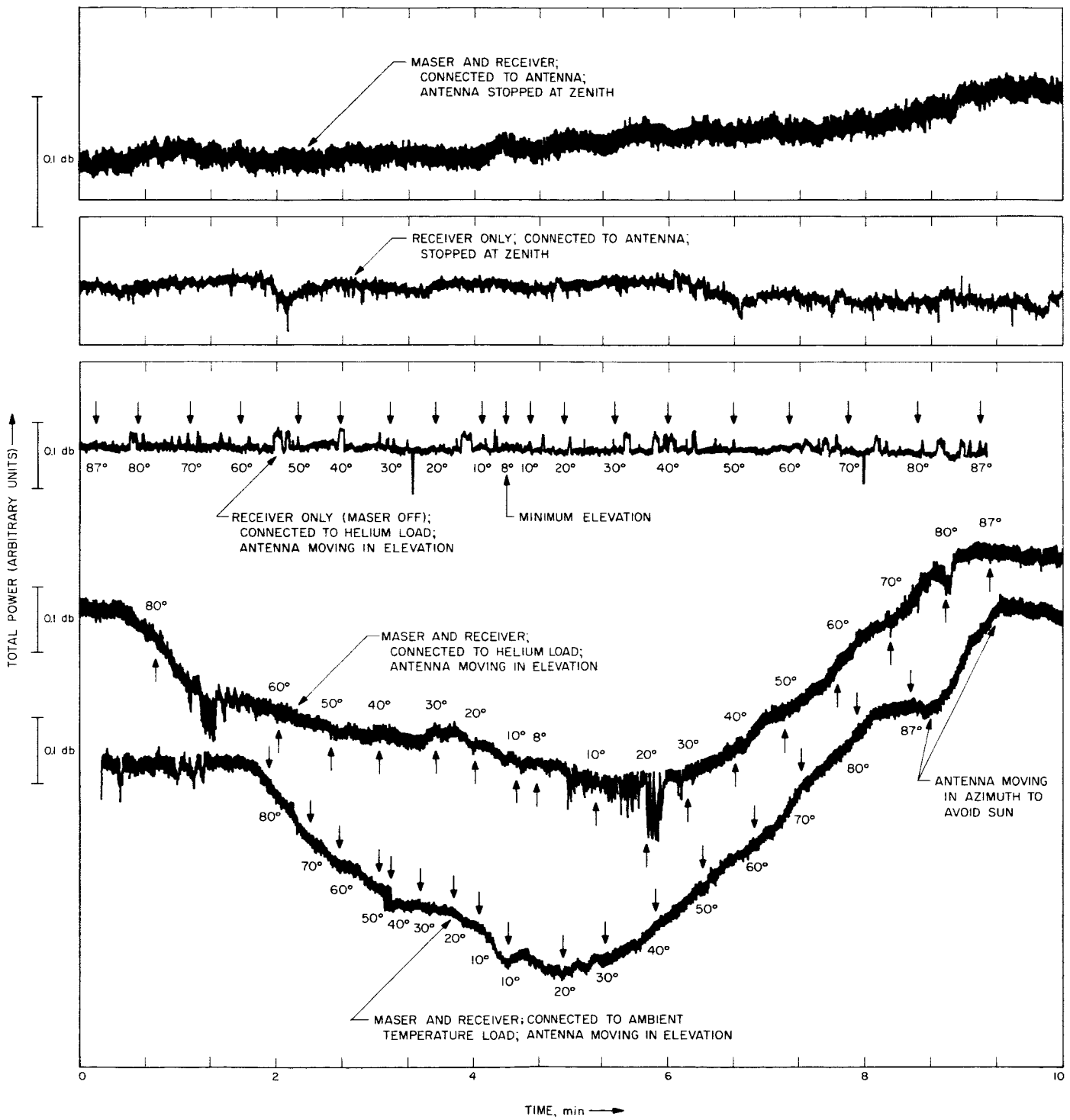


Fig. 64. S-band (2388 Mc) receiving system gain stability under various conditions

The instrumentation for this maser provides for injecting a signal into the maser input waveguide in a direction away from the maser input. This permits reflectometer measurements to be made on the various terminations (i.e., antenna, cold loads, etc.) to which the maser can be connected. These measurements have indicated that the impedance of the various terminations is fairly stable; current parameters are tabulated in Table 8. Measurements have been made of the short-term maser gain stability with the antenna stationary and with the antenna moving, while the maser and receiver were connected to various input terminations. A typical recording, covering a 10-min period, is illustrated in Fig. 64. Note that, with the antenna stopped at zenith position, the system gain changes only 0.05 db during a 10-min period. In order to evaluate the effect upon system gain of moving the antenna, the antenna was moved in elevation at a slow constant rate from zenith to 8 deg and back again. The maximum gain changes were 0.4 to 0.5 db. Measurements of long-term gain stability have not yet been made. Weekly calibrations of the gas tube noise source have been made on the S-band system. The calibrating terminations used are a liquid helium and an ambient temperature load. The first calibration was performed on December 5 and resulted in an excess noise for the gas tube of 48.7°K with a probable error of plus or minus 0.8°K. The next calibration, performed on December 12, 1964, resulted in a calculated excess noise of 51.4°K, with a probable error of plus or minus 0.9°K. The latter figure checks more closely with estimates made by other techniques; it is being used in system temperature calculation. Additional calibrations will be made at regular intervals. The gain and noise temperature of the S-band maser system are shown in Fig. 65 for the recent operating period.

Table 8. Source impedance match for S-band maser

Termination	Apparent VSWR
Helium load	1.05
Antenna (A-arm)	1.06
Antenna (B-arm)	1.06
Ambient load	1.07

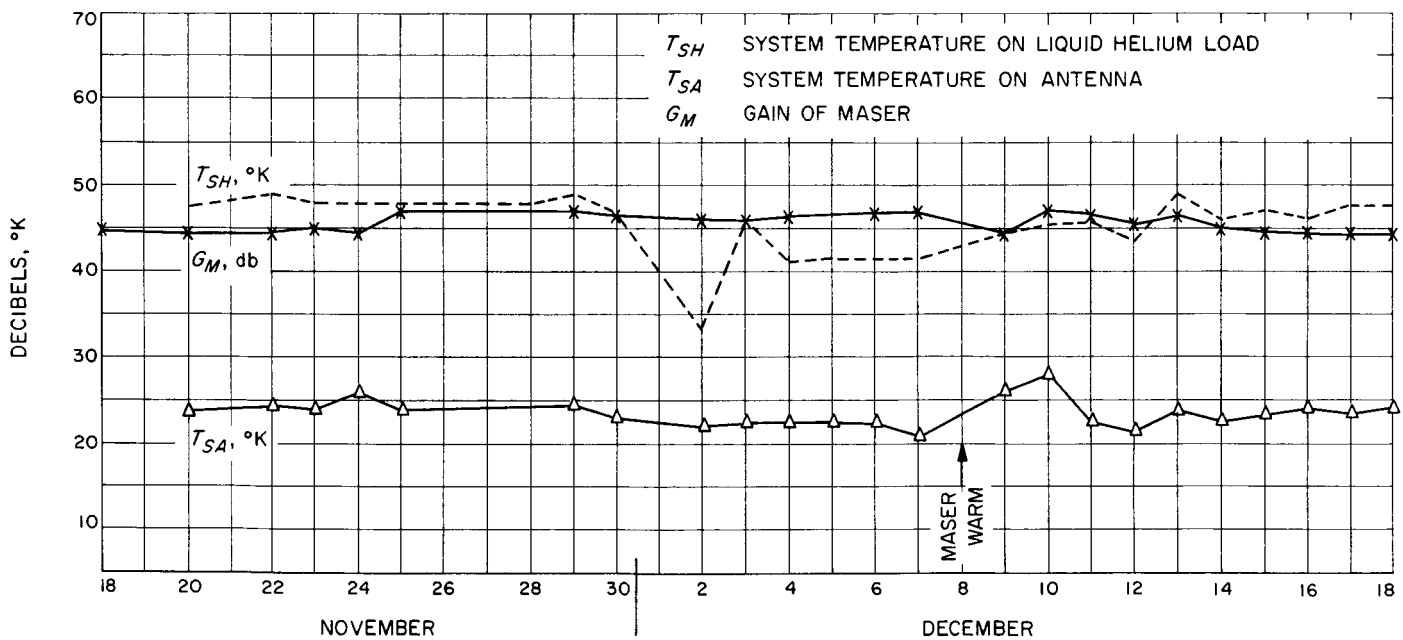


Fig. 65. S-band maser operating characteristics

References

1. Silver, S. ed., "Microwave Antenna Theory and Design," *MIT Radiation Lab Series*, Vol. 12, p. 195, McGraw-Hill Book Co., New York, 1949.

2. Higa, W. H., "Noise Performance of Traveling Wave Masers," *IEEE Transactions on Microwave Theory and Techniques*, Vol. MTT-12, No. 1, January 1964.

3. Allen, C. W., "Astronomical Quantities," p. 156, University of London, The Athlone Press, 1955.

VII. Advanced Antenna System

A. Synopsis

A 210-ft-D Advanced Antenna System (AAS) is being designed and constructed for the Mars Site of the Goldstone Space Communications Station. This AAS is designed specifically for deep space communications and will be integrated with related systems and equipment of the Deep Space Instrumentation Facility (DSIF).

The work progress on the AAS project has been reported regularly in this *SPS*. The project is generally on schedule, and it is expected that the end dates for erection and project completion will be met. Fig. 1 depicts the on-site progress as of November 16, 1964.

1. Progress Summary

The detail design and material procurement phases for the structural and drive components is essentially complete, and all components are either being fabricated at various locations or are being erected at the Mars Site.

The presently planned utility installations are complete except for inter- and intra-site communications. The diesel-electric power system was completed on November 28, 1964.



Fig. 1. Advanced Antenna System construction progress

Work is in progress on the development and procurement of the tracking feed, the optical boresight equipment, the operational optical instrumentation for alignment of the reflector and structure and the servo, hydrostatic bearing, and antenna gain instrumentation. Measurement equipment, such as film height measuring equipment, is being installed in pace with the AAS construction.

The preliminary design for the optical mount for the Precision Data System (master equatorial) has been completed, and final design has begun. The layouts and error analysis indicate that the goals of the system specifications can be met. Gravity deflections are not expected to exceed 0.6 arc sec, and indications are that the total pointing error can be held within 5 arc sec. Procurement actions are in progress for other components of the Precision Data System.

System integration work continues and the component test results are being compared with design requirements as the work progresses.

2. AAS Structural and Drive Components

The concrete structural work on-site has been accomplished and the A&E interior work in the pedestal, where two floors of equipment and work area are provided, is over 90% complete.

Construction of the cooling system of AAS is nearing completion (Fig. 2). The system includes a ground-level cooling tower and the required piping and circulating pumps to circulate water to all heat exchange equipment. From the pedestal to the alidade, the coolant is circulated through hoses on the cable wrapup.

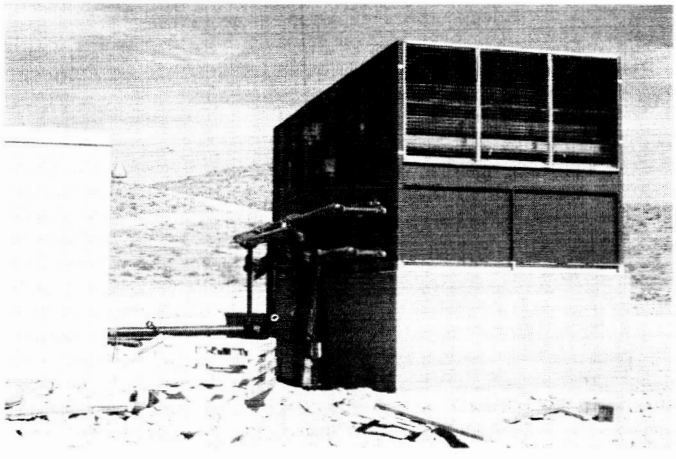


Fig. 2. Advanced Antenna System cooling tower

Air conditioning is provided in the electronic equipment rooms on a heat-dissipation basis of 50 w/ft² of floor area, and in the offices and shop spaces on the basis of 10 w/ft². All air conditioning equipment is based on maintaining a maximum temperature of 85°F and a minimum temperature of 65°F in the enclosed areas with the outside air ranging from 10°F to 115°F with 12% relative humidity at the upper limit.

Electrical duct heaters provide heat for the pedestal and alidade and provide three levels of operation. The same ducting system is utilized for both air conditioning and heating. Sufficient capacity is provided to maintain a temperature of 65°F minimum.

Installation of the steel portions of the instrument tower is being accomplished on-site. The steel tower will be thermally protected and air conditioned. A Precision Data System Astrodome will be mounted on a windshield surrounding the tower which will be mounted on, and rotate with, the alidade structure. Fig. 3 shows one of the sections of the steel instrument tower being sprayed with foam insulation prior to erection. The insulation is rigid urethane foam that is Freon-blown to a minimum thickness of 1.25 in. and a density of 2 lb/ft³. The purpose of this insulation is to prevent radiant heating through the windshield and to maintain the instrument tower at a uniform temperature, thereby maintaining a stable ground

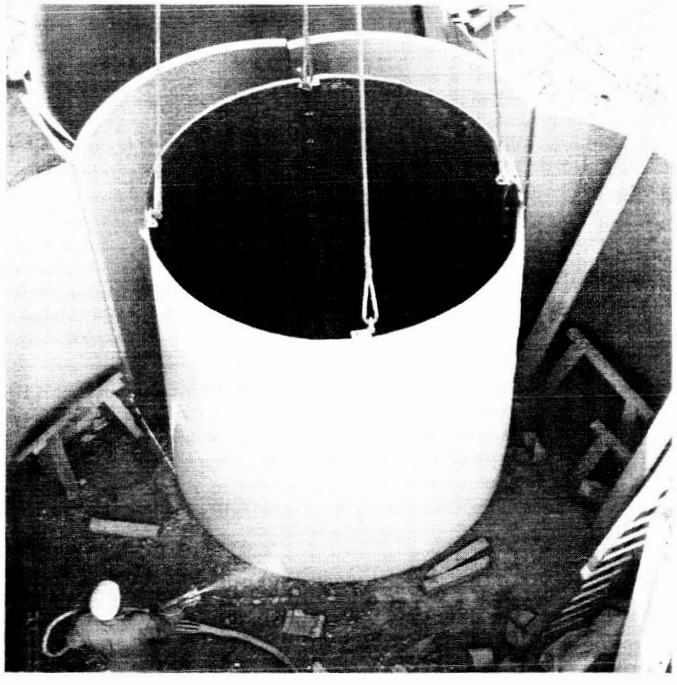


Fig. 3. Insulation of the steel instrument tower

reference position. Fig. 4 shows the bottom section of the windshield installed at the rotating alidade floor level.

The steel alidade structure of the AAS has been erected, and work is nearing completion on the alidade building structure, cable wrapup and alidade structure walkways and ladders. A general discussion of the basic alidade structure was contained in *SPS 37-30*, Vol. III, pp. 97–110.

The azimuth motion components, consisting of the azimuth hydrostatic thrust bearing, azimuth radial bearing and azimuth bull gear and drives, have been installed. Checkout of the components is in progress. General discussions of these components were contained in *SPS 37-30*, Vol. III, pp. 97–110; *SPS 37-28*, Vol. III, pp. 90–93; *SPS 37-29*, Vol. III, pp. 106–109.

A major milestone was passed on December 4, 1964 when a successful hydrostatic "liftoff" and azimuth rotation was accomplished. All three pads of the azimuth hydrostatic bearing, with the weight of the large alidade structure upon them, were lifted and floated. Rotation through 30 deg was accomplished in a successful trial of the component. Further rotation occurred on December 5 and 6, 1964, when detailed measurement of the film thickness was verified during a 340-deg rotation.

The two massive elevation bearing assemblies have been fabricated and have been motor-shipped to the Mars Site. The elevation gears and drives have been fabricated and are being held at Philadelphia Gear Corporation, Philadelphia, Pennsylvania, pending on-site erection need dates in early 1965.

Fabrication of the elevation wheel, its backup structure and counterweights is nearing completion at Rohr Corporation, San Diego, California, and will soon be shipped to the Mars Site for erection.

The primary reflector structure, quadripod, subreflector (Figs. 5 and 6), feed cone and primary reflector panels are also being fabricated at Rohr Corporation.

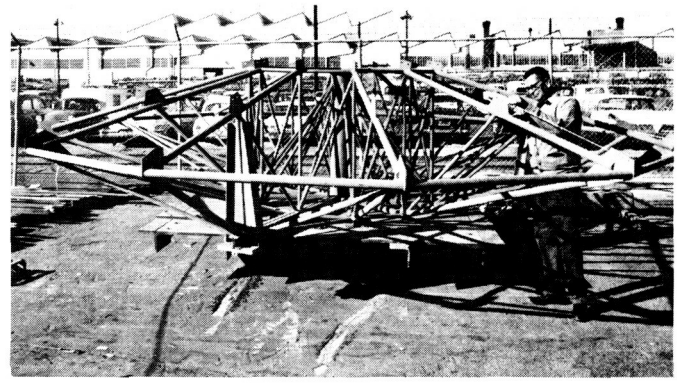


Fig. 5. Fabrication of the subreflector backup structure

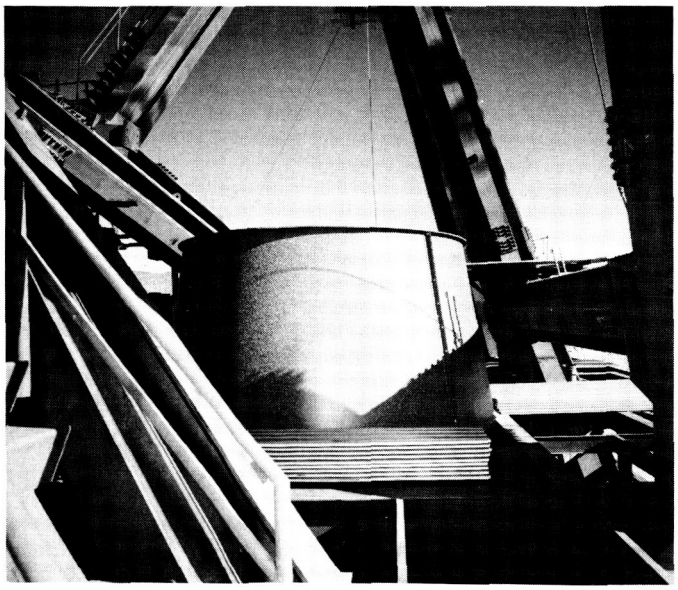


Fig. 4. Bottom section of the instrument tower windshield

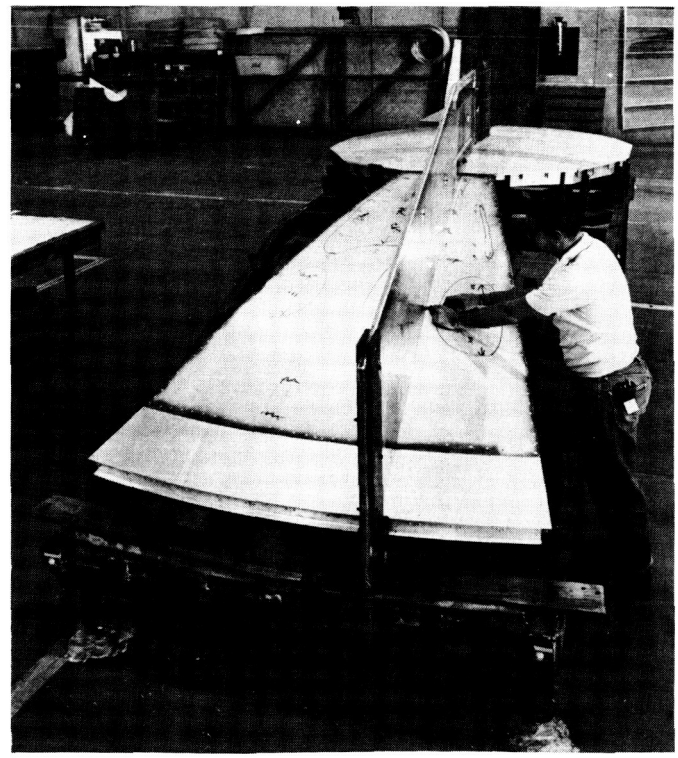


Fig. 6. Fabrication of the subreflector panels

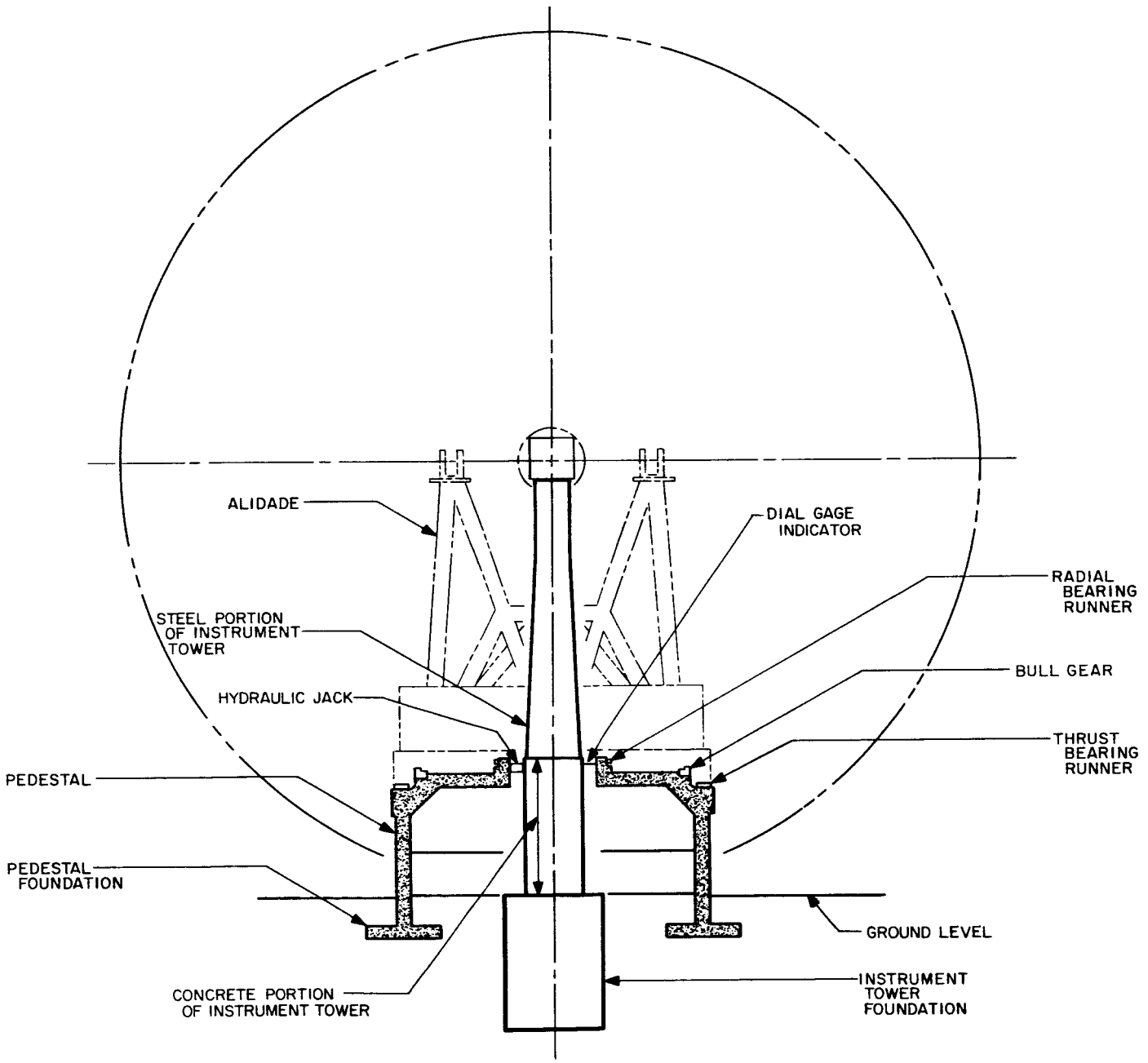


Fig. 7. Static deflection test of instrument tower

The servo and control components are being fabricated at Dalmo Victor Company, Belmont, California, and testing of the components will begin soon. Initial on-site installation work has begun.

B. Static Deflection Test of Instrument Tower to Determine Foundation Modulus

The AAS instrument tower provides a mounting surface for the AAS Precision Data System (master equatorial), an instrument which establishes reference coordinates for the antenna. The tower is mounted on its own foundation, separate from the antenna foundation, in order to minimize the force interactions between the tower and the antenna structure.

In order that the antenna servosystem bandwidth can have its required value, it is necessary that the lowest natural frequency of the instrument tower be made sufficiently high. Analyses have been made which established this frequency in terms of the weight of the Precision Data System and supporting floor structure, and the foundation modulus. The effective modulus is a function of the soil properties and the geometry of the foundation. The calculated frequency range corresponding to the range of parametric values used was from 3.68 to 6.08 cps, the lower limit being considered a tolerable value.

Upon completion of the concrete portion of the instrument tower, a static deflection test was performed in order that the foundation modulus could be evaluated. A hydraulic force-measuring jack was placed between the top of the concrete portion of the instrument tower and the antenna pedestal as shown in Fig. 7. On the opposite side from the jack, a dial gage indicator was attached to the antenna pedestal. Since the stiffness of the pedestal is so very much greater than that of the tower, the dial gage indicated to a high degree of accuracy the deflection of the tower. In Fig. 8, the test results are shown from which the effective foundation modulus can be determined.

Using this experimentally established foundation modulus, together with the known weight of the Precision Data System and its supporting floor structure, the current vibrational analysis yields a first-mode natural frequency of 4.5 cps. This frequency is near the middle of the range predicted before the Precision Data System weight and the foundation modulus were known. The results of this test indicate that the instrument tower will perform its function satisfactorily.

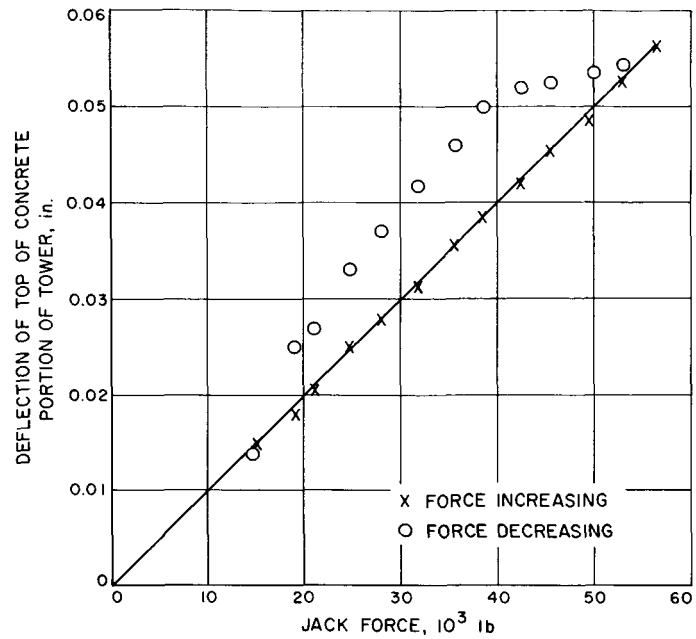


Fig. 8. Total deflection versus jack force

C. AAS Elevation Bearing Assemblies

The tipping parts of the antenna structure are supported by two elevation bearing assemblies mounted atop the alidade. Each bearing assembly consists of two split housings, supporting bases, two self-aligning spherical roller bearings, a stub shaft, a reflector support casting and associated shaft seals and alignment and adjustment components (Figs. 9, 10). Each bearing assembly is approximately $14 \times 11 \times 10$ ft, and weighs 135,000 lb.

The two elevation bearing assemblies have been delivered to the Mars Site of the Goldstone Tracking Station, one on November 24 and the other on December 2, 1964.

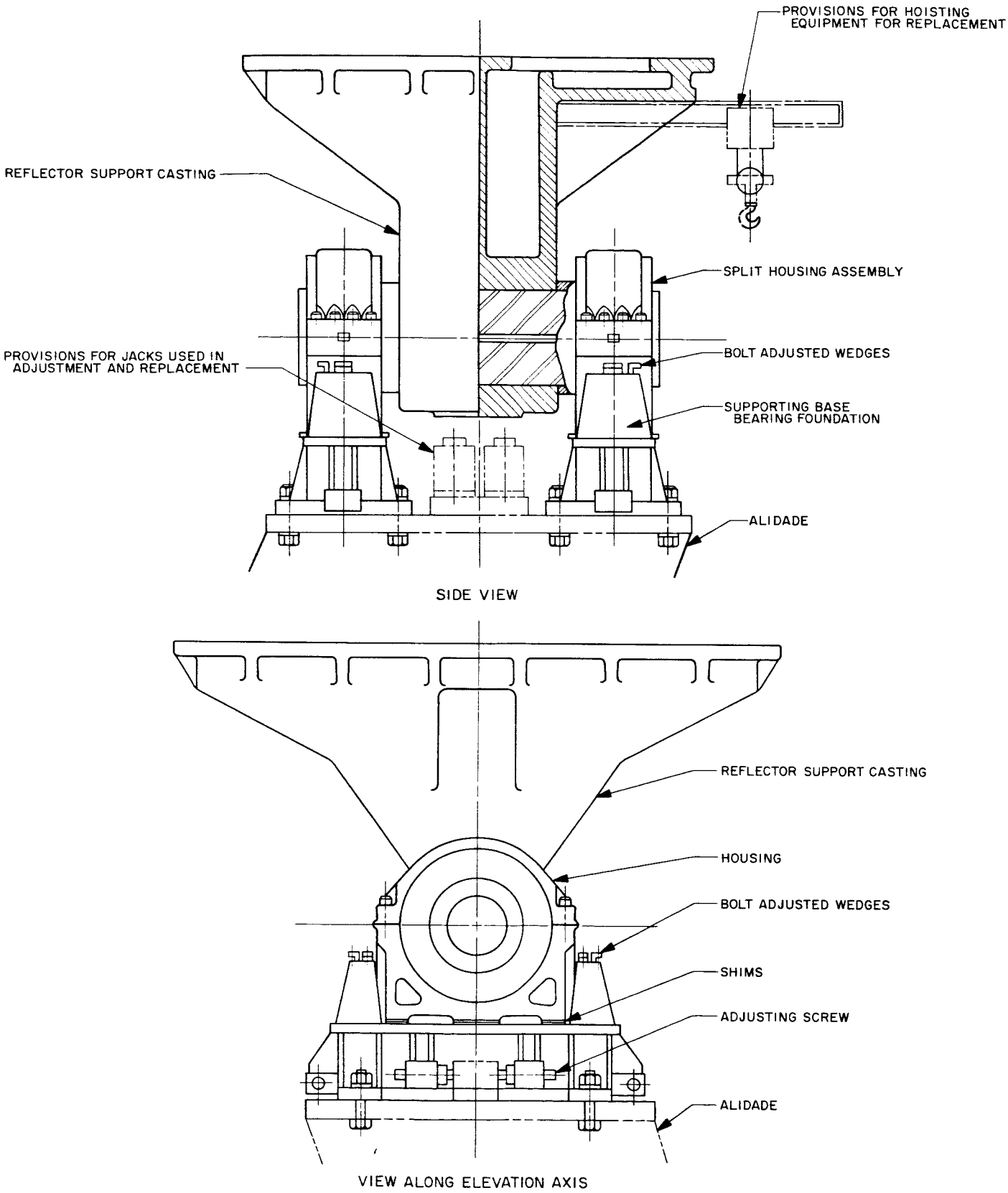


Fig. 9. Elevation bearing assembly, side and end views

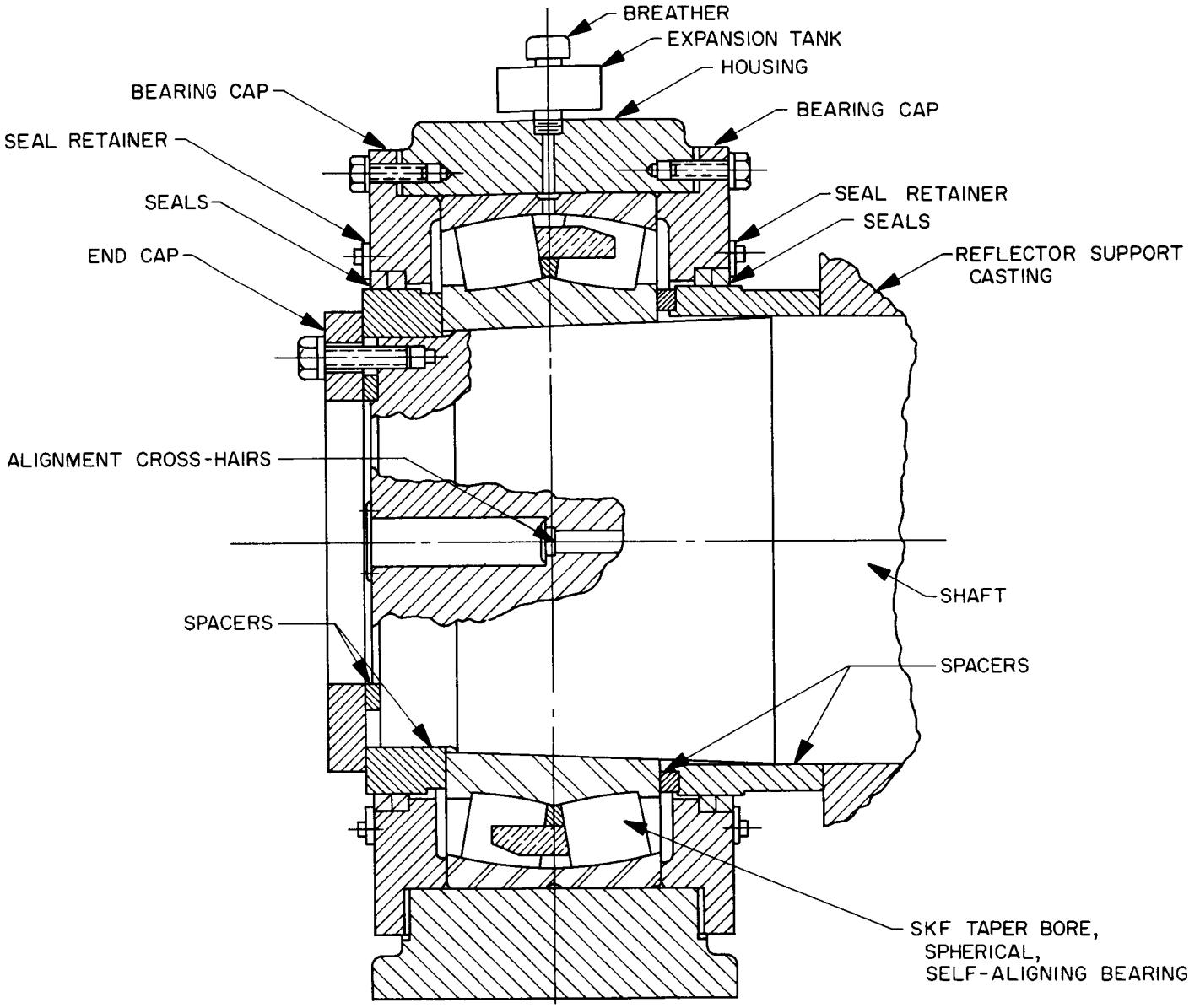


Fig. 10. Elevation bearing assembly, section through housing

The assemblies were fabricated by National Steel and Shipbuilding, San Diego, California, under subcontract to Rohr Corporation. SKF Industries, Los Angeles, California, provided the bearings. Bethlehem Steel Company, Bethlehem, Pennsylvania, made the reflector support castings. Fig. 11 is a photograph of one of the elevation bearings being delivered to the Mars Site. The portion shown on the photograph was motor-shipped from San Diego and is the heaviest single piece (approx 50 tons) to be shipped to the AAS site.

1. Design Requirements

Load requirements, including dead-load, for each of the four elevation bearings are:

50 mph wind, operating	690 Kips
70 mph wind, reflector in any position	750 Kips
120 mph wind, survival	820 Kips, radial 150 Kips, axial

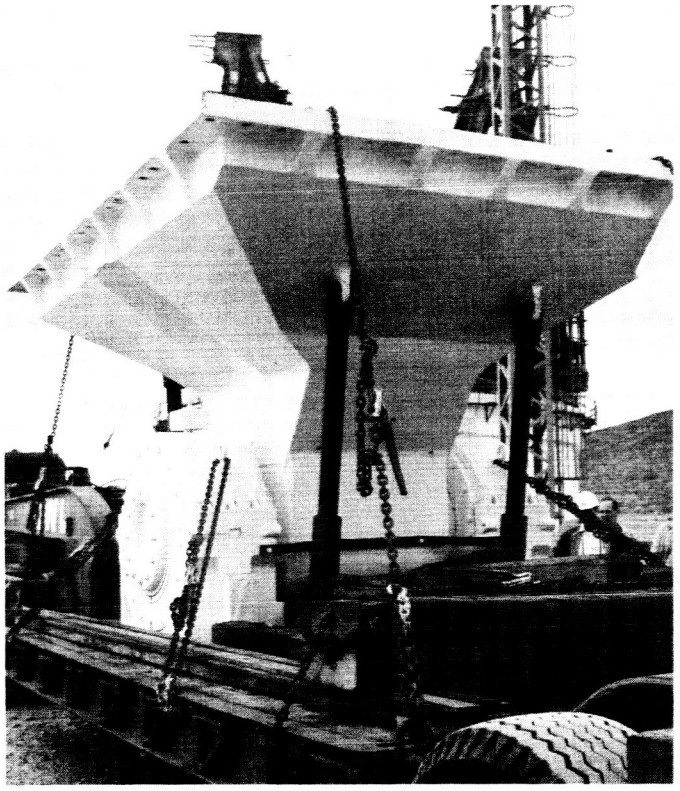


Fig. 11. Delivery of an AAS elevation bearing assembly

Early designs for the elevation bearing assembly proposed a single spherical roller bearing mounted in a one-piece housing. This arrangement is used successfully on many smaller antennas, but the large bearing and heavy parts required on the AAS introduced serious problems of assembly, maintenance and replacement and preclude this design.

2. *Description of Bearing Assembly*

The present design has the two bearings of an assembly mounted on each end of a shaft pressed into the reflector support casting (Fig. 9). With the bearings on the outside of the structure, many of the assembly and replacement problems are solved. Provisions are made for mounting hoisting equipment to the reflector support casting to accomplish bearing replacement. Each bearing is mounted in a cast-steel bearing housing which is split for ease of assembly and bearing replacement. A key is provided between the cap and housing for the transfer of axial shear. Lugs on the housing are slid into vertical grooves in the support base. Vertical alignment is accomplished by the use of shims between the housing and the support bases. The vertical lugs thus serve to restrain the housings horizontally while they are free for vertical movement while shimming. Provisions are made for using hydraulic jacks for lifting and supporting the weight of the reflector during adjustment or bearing replacement. After alignment, bolted wedges serve to lock the housings in the bearing supports.

The support bases are steel weldments bolted to the alidade top. They provide the horizontal adjustment for the bearing assembly. Large holding and adjustment screws are provided for moving the bearing supports on the alidade top. Recesses in the bottom of the bearing support provide for hydrostatic floating during horizontal adjustments. After oil pressure is introduced to the hydrostatic recesses, movement is accomplished by the adjusting screws. After alignment, the screws are used as locking devices.

The stub shaft is a 25-in.-D steel forging approximately 8 ft long. This shaft is pressed into the steel reflector support casting, and these two parts, in combination, form the elevation rotating connection for the reflector and backup structure.

Seals and seal retainers are split as required to permit their replacement without major disassembly of the bearing assembly. The bearings are SKF 231/600 CAK/CI spherical roller bearings with a static capacity of over 2 million lb each (Fig. 10).

D. AAS Elevation Wheel and Primary Reflector Structure

The elevation bearings, discussed above, support the tie truss, elevation wheel trusses and the wheel bracing members. The AAS elevation gears are mounted on the circumference of the elevation wheel. The elevation wheel structure supports the primary reflector structure, which in turn supports the reflector surface panels, quadripod and attached subreflector, feed cone and feed cone hoist.

The tie truss, the tie-truss end weldments, and the elevation wheel trusses support the rectangular girder of the primary reflector structure. The center hub of the AAS rests on the tie truss. The primary reflector structure

consists of rib trusses radiating from the center hub and interconnected by the rectangular girder and circular hoop trusses.

1. Design Requirements

The accuracy of the primary reflector surface is governed by the deflection of the panel attachment points on the reflector structure and by the quality of the manufactured surface panels. The design of the elevation wheel and primary reflector structures requires consideration of errors from gravity, wind, thermal differentials, fabrication and field setting to meet a 0.250-in. design rms of one-half the RF path length errors. In addition, the rms of one-half the RF path length errors of the peripheral panel support point deflections, due to gravity in the zenith position, was to be 0.050 in. or less. The panel support point deflections and member stresses were to be calculated by three-dimensional static analysis.

2. Design Achievements

System integration studies subdivided the design rms of half the RF path length errors (rms) into design goals for various error sources, specifically gravity, wind, thermal differentials, fabrication, field setting and safety factor. The elevation wheel and the primary reflector structures were assigned a 0.065-in. rms design goal for gravity loading. The results of design calculations were 0.068-in. rms for gravity load, the antenna at zenith, panels set at 45 deg and a 0.064-in. rms for gravity load, the antenna at horizon, panels set at 45 deg. A balanced design was achieved as is shown by the nearly equal rms values for perpendicular gravity conditions. Three-dimensional static analysis using the "STAIR" computer program showed that the rms results were optimum. The rms for peripheral panel point deflections due to gravity in the zenith position of the antenna was 0.019 in.

3. Design Detail

a. Elevation wheel. The elevation wheel trusses are designed to support the counterweights, accept the elevation gear loads and meet the over-all deflection requirements of the reflector surface. The wheel trusses are attached to the short sides of the rectangular girder and supported by the tie truss and by the wheel bracing members attached to the tie truss and the tie-truss end weldments.

The elevation wheel trusses are primarily welded construction with bolted connections between subassemblies. The circumferential members of the wheel trusses are built up from steel billets and plates; these large billets, weighing from 2 to 6 tons, also serve as a large portion of the counterweight. The remainder of the wheel trusses and the wheel bracing members is made of structural steel shapes and plates. Fig. 12 shows the general shape of the elevation wheel and tie truss. Fig. 13 is a detail of the counterweight. Fig. 14 depicts the initial stages of welding the counterweight section of the wheel truss.

b. Tie truss. The tie truss supports the elevation wheel and the primary reflector center hub and is structurally integrated with the primary reflector structure. The reflector rectangular girder is supported by the tie truss and tie-truss end weldments. The tie truss transfers the

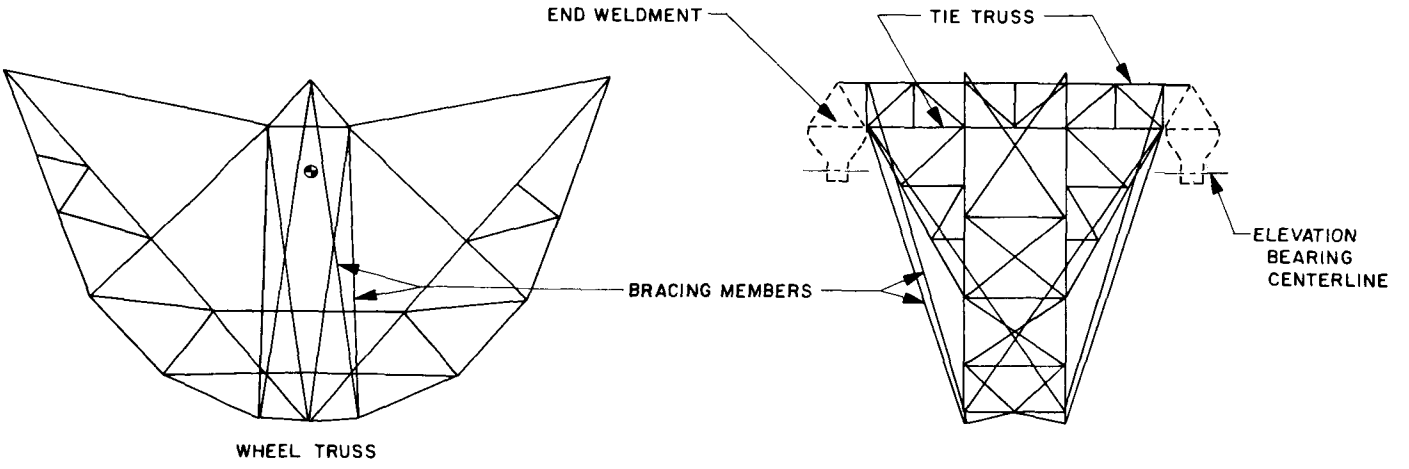


Fig. 12. General outline of elevation wheel and tie truss

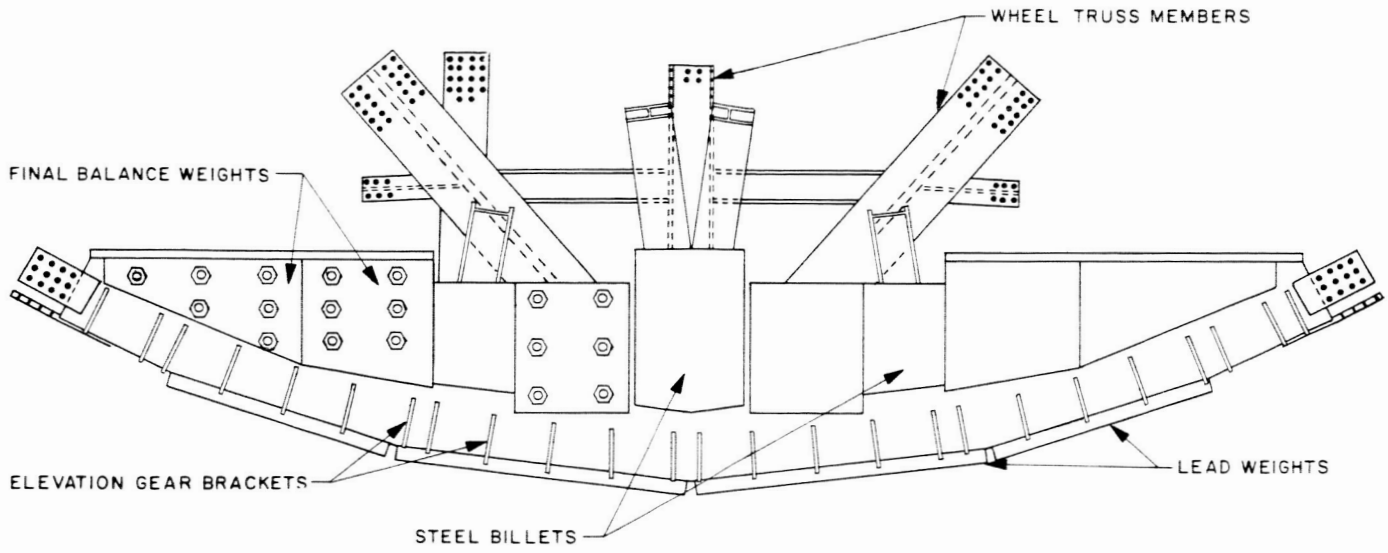


Fig. 13. Elevation wheel counterweight detail

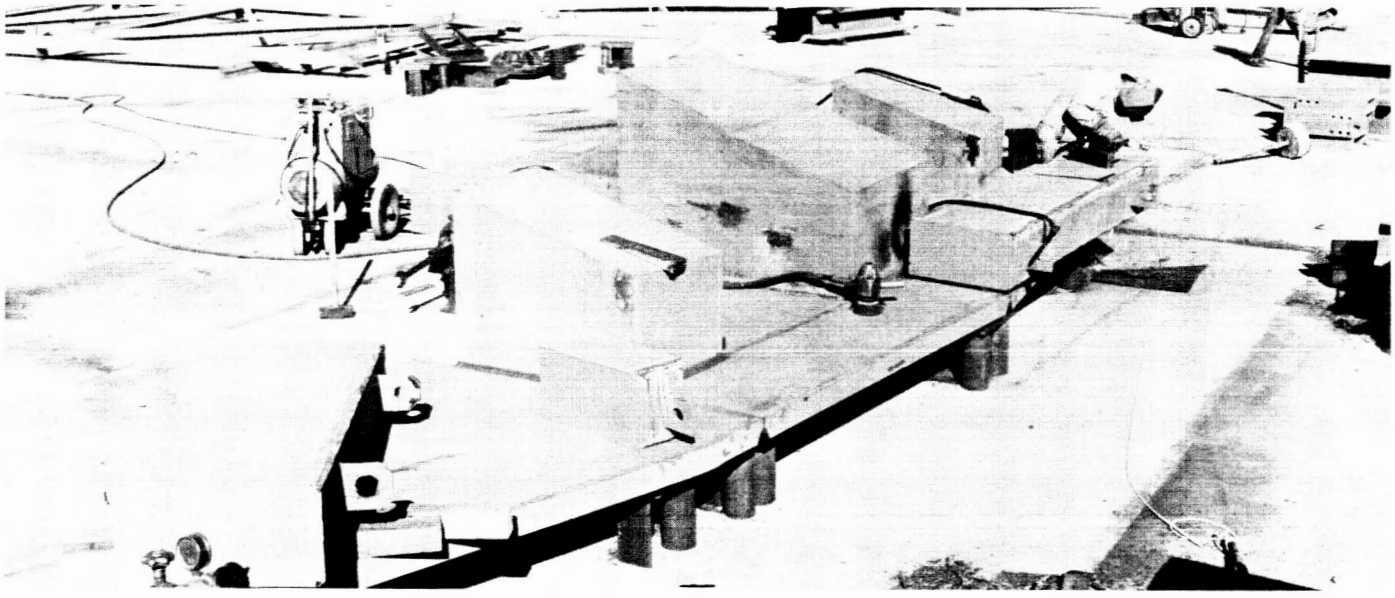


Fig. 14. Welding the counterweight section

entire weight of the elevation wheel and reflector structure to the elevation bearing assemblies. Bracing members which supply transverse stiffness to the elevation wheel trusses are connected directly to the tie-truss end weldments.

The tie truss is a welded truss of triangular cross section. The bottom chords are 12-in. diameter pipe; the remainder of the truss is made from structural steel shapes. The end weldments are made from steel billets, rod and plates. Fig. 15 shows the tie-truss end weldments in detail.

Fig. 16(a) shows the tie-truss end weldment in the initial stages of fabrication. Shown are 10-in. rods in the weld jig prior to welding outside plates. To the right of the photograph, welders are working on base members. Fig. 16(b) shows the tie truss inverted for welding on the bottom side.

c. Center hub. The center hub rests directly upon the tie truss, and the two are joined by a bolted connection. The center hub supports the feed cone and houses the optical instrument for monitoring the reflector surface. The reflector rib trusses radiate from the center hub.

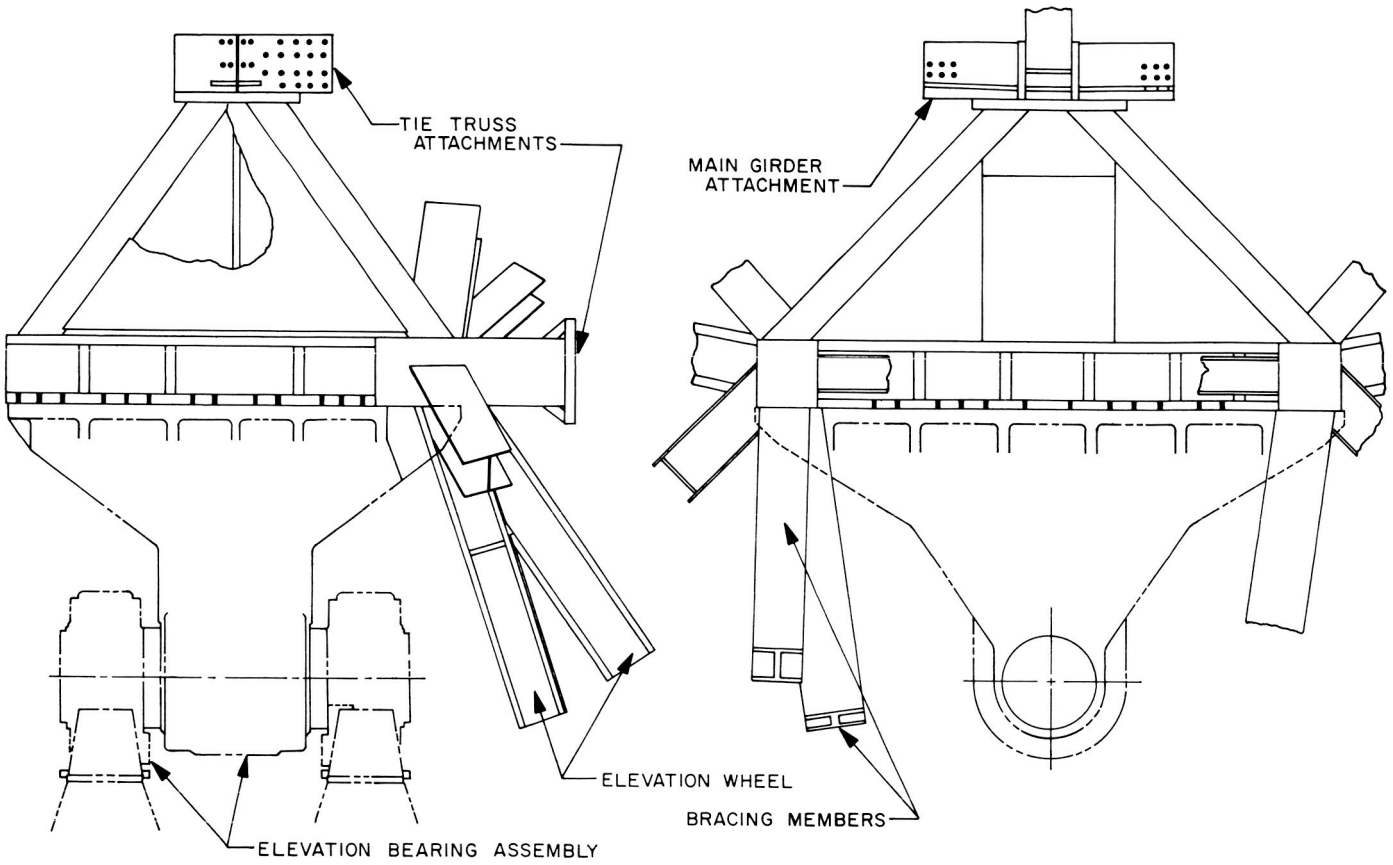


Fig. 15. Tie-truss end weldment detail

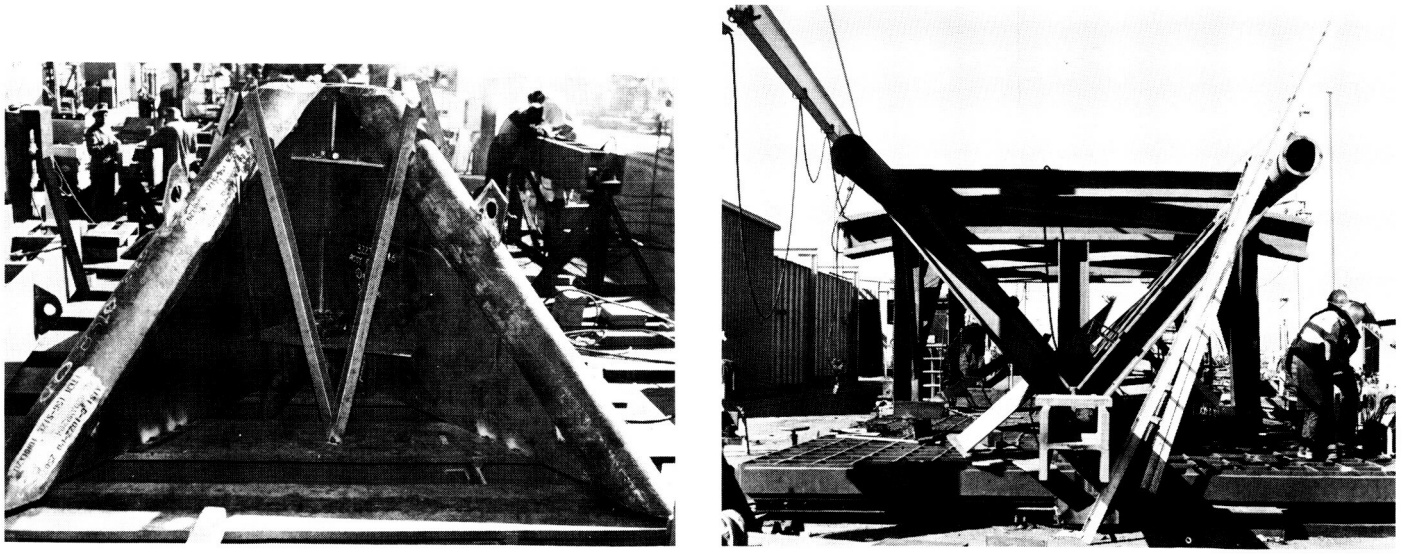


Fig. 16. Fabrication of the tie truss

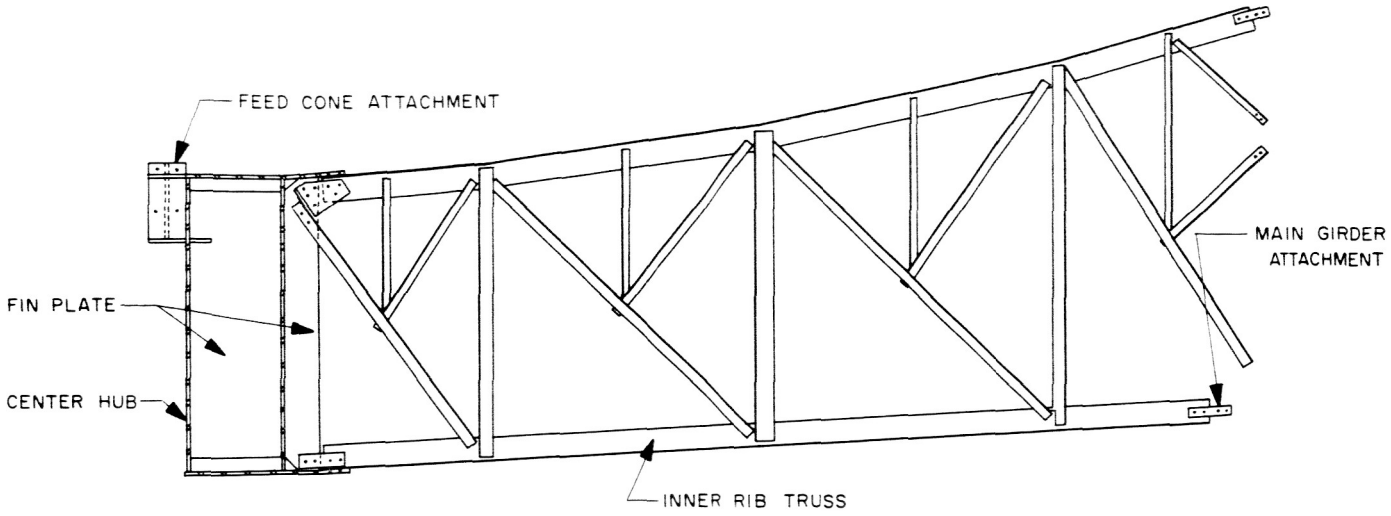


Fig. 17. Center hub and inner rib detail

The center hub is a doughnut-shaped structure of rectangular cross section. The hub is intersected by 48 fin plates which stiffen the hub and provide means for attachment of the rib trusses. The entire hub is made of structural steel plate. Fig. 17 is a cross-sectional view of the center hub. A rib is shown mated to the hub fin plate. Fig. 18 depicts the initial stage of welding the center hub. Typical fin plates and the notch for splice to the tie truss can be seen.

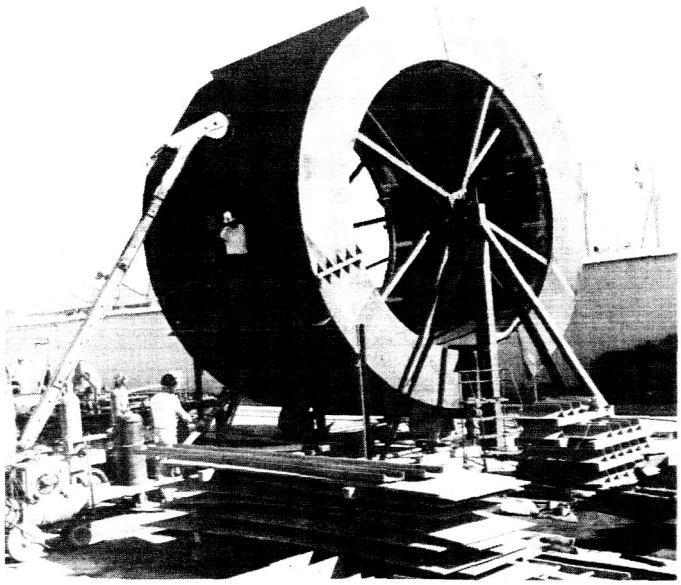


Fig. 18. Welding the center hub

d. Rectangular girder. The rib trusses are supported by the rectangular girder. The vertical members of the girder are also vertical members of the rib trusses. The main girders are attached to the tie-truss end weldments and are stiffened by knee braces connected to the base of the tie-truss end weldments. The wheel girders connect the ends of the wheel trusses and support the intersecting ribs. The quadripod is attached at the corners of the rectangular girder. Fig. 19 shows one-half of the main girder. The wheel girder is similar in detail. The main girder, being fabricated, is shown in Fig. 20.

e. Rib trusses and hoops. The 48 rib trusses are supplemented by 48 partial or intermediate rib trusses beneath the outer 50-ft portion of the reflector surface. The rib trusses are interconnected by the center hub and ten circular hoop trusses.

Through the rib-hoop interconnection, the reflector loads are carried by the rectangular girder. Fig. 21 shows one-quarter of the reflector in the plan view.

The rib trusses have been divided into inner ribs and cantilever ribs. The inner ribs are that portion from the center hub to the 56 ft-0 in. radius (Hoop 7). The cantilever rib extends from Hoop 7 to the reflector edge. The welded rib assemblies are made from structural steel tees and angles. The rib assemblies are bolted to the center hub and rectangular girder. The hoop trusses are bolt-connected to each rib. Fig. 17 is a typical inner rib in detail. The cantilever rib is similar. Figs. 22 and 23 show the inner rib and cantilever rib in the weld jigs. The center hub can be seen in the background in a later stage of fabrication. All fin plates of the hub have been welded.

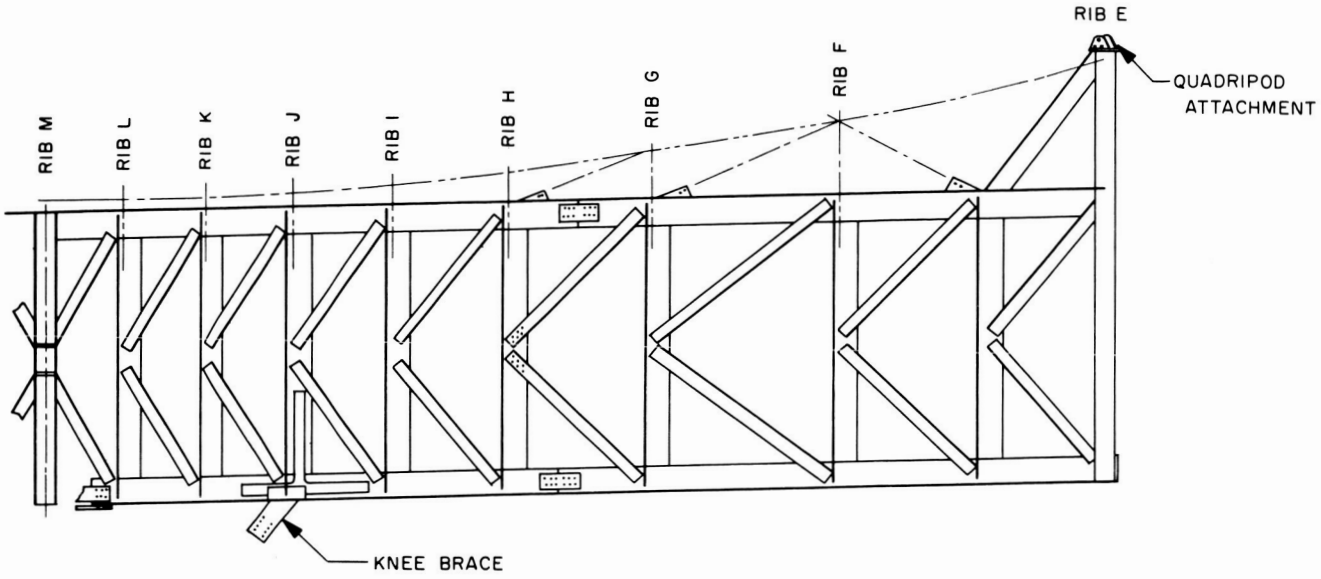


Fig. 19. Rectangular girder, main girder detail

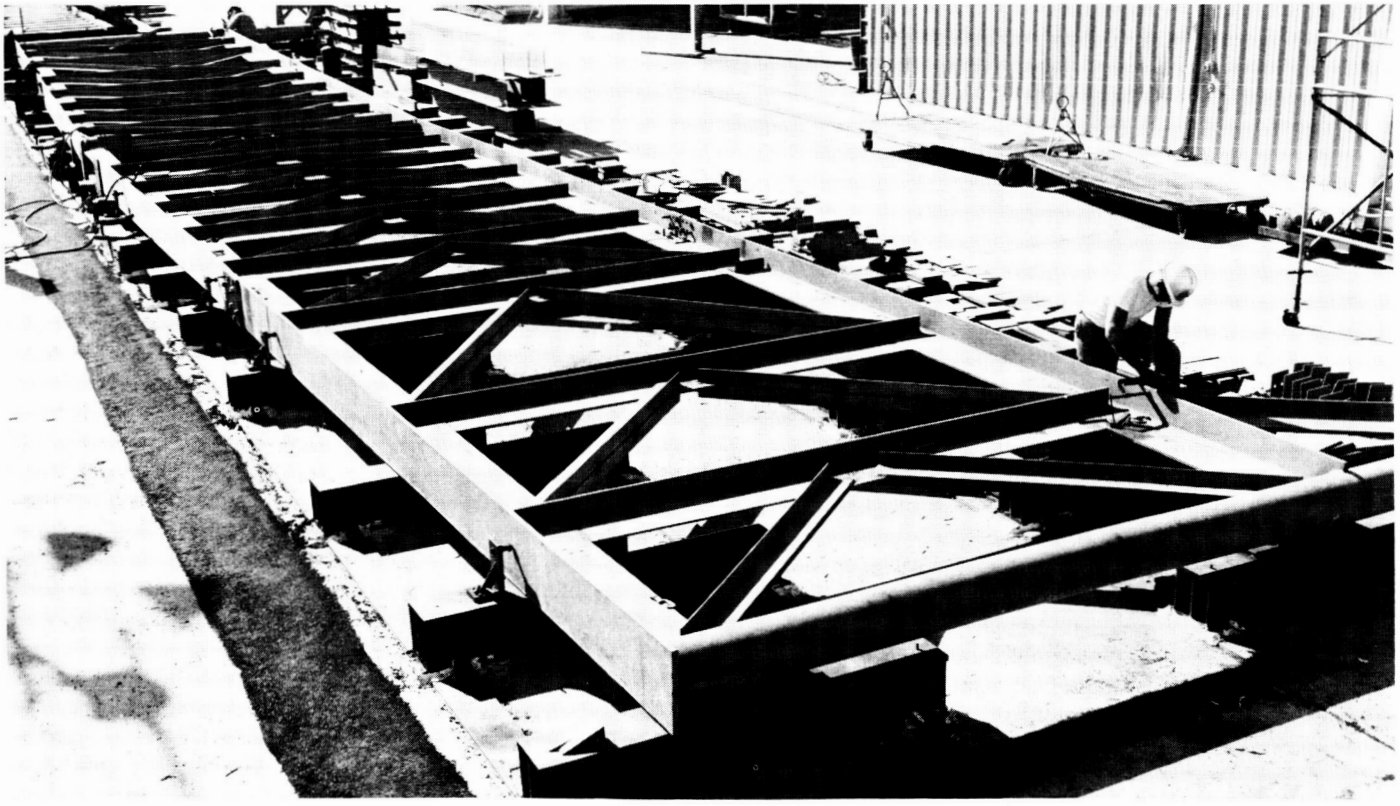


Fig. 20. Main girder in the weld jig

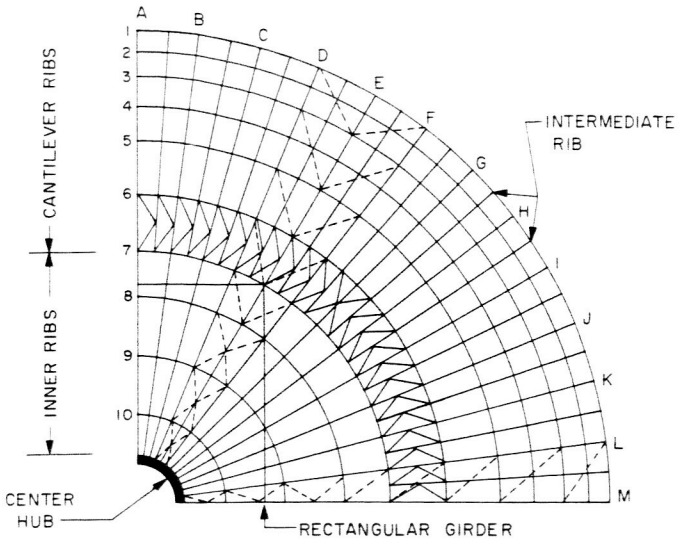


Fig. 21. Primary reflector structure, quarter reflector plan view

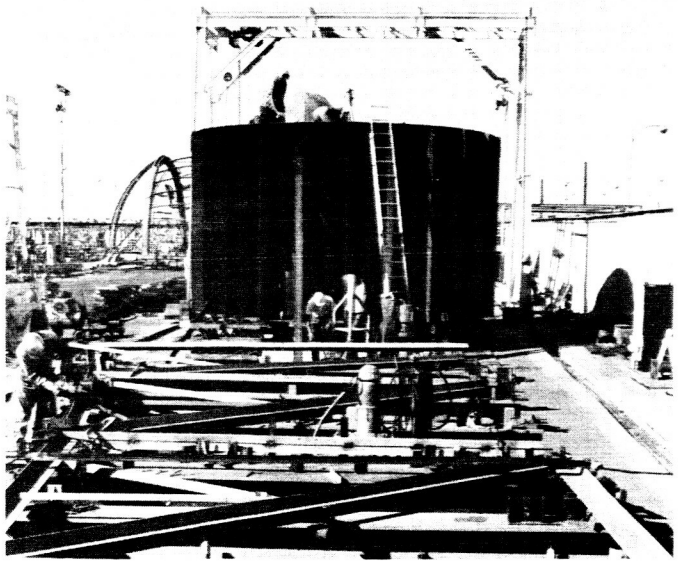


Fig. 22. Fabrication of inner ribs

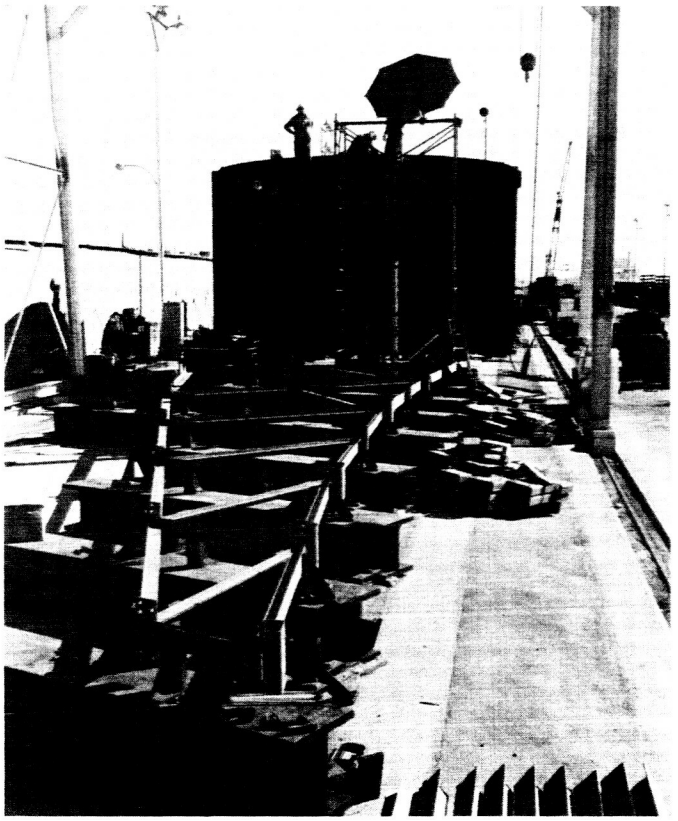


Fig. 23. Fabrication of cantilever rib

E. 1/7-Scale Model Feed for AAS

a. Summary. To date the K_u-band 16,330-Mc scale model studies of the feeds for the 210-ft AAS have consisted of primary patterns of the feeds and secondary patterns of the Goldstone 30-ft reflector illuminated by the feeds. Primary patterns of the feeds, obtained with Mesa antenna range facilities were presented in *SPS 37-29*, Vol. III, p. 109, for the original monopulse feed. Secondary patterns of the 30-ft reflector, obtained using the Tiefort Mountain collimation facility were reported in *SPS 37-30*, Vol. III, p. 110–115. In this reporting, some of the preparations for Phase II studies will be described.

b. Recent work. Phase II scale model studies of the feeds for the 210-ft AAS include the use of a very accurate model quadripod assembly to be installed on the Goldstone Venus Site 30-ft reflector. A contract has been awarded to Rohr Corporation for the construction of the model quadripod. Some of the specifications for the model structure which consists of trusswork legs include structural member cross sectional tolerances of ± 0.010 in. and structural member locational tolerances of ± 0.030 in. relative to the focal point. An attempt is being made to avoid possible problems caused by periodicity of non-exact items such as weld fillets and structural bar corners by specifying these items on the basis of electrical (RF) and mechanical compromise. Detail design is proceeding satisfactorily.

Fabrication of the hyperboloid positioner has begun and is 50% completed. This positioner, which is capable

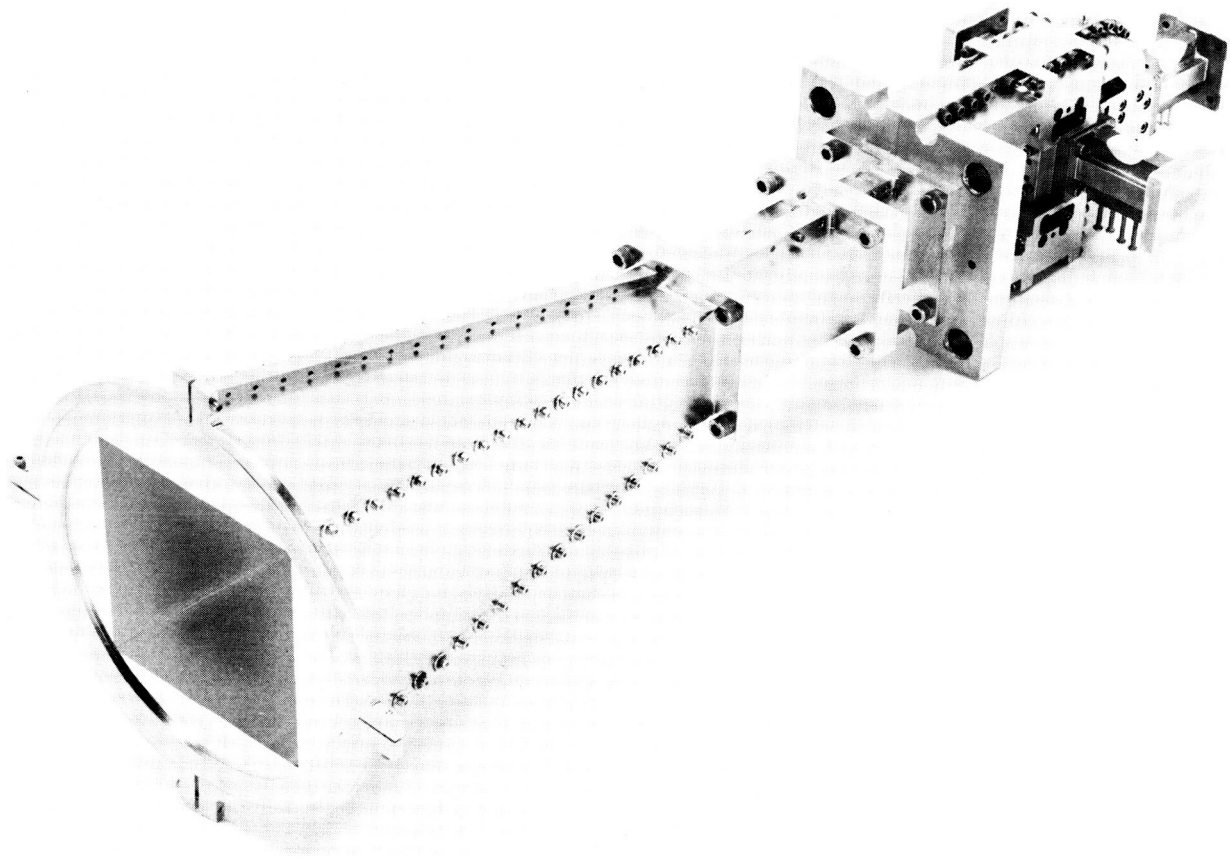


Fig. 24. Assembly of the waveguide bridge, horn and mode generator-control section

of axial (focus) and tilt motions, will be mounted on the model quadripod apex.

As mentioned in *SPS 37-29*, Vol. III, p. 109, the model monopulse feed with modifications will exhibit suppressed sidelobe action. A model of the S-band prototype horn throat region has been fabricated and is now being tested. Fig. 24 shows the assembly of the waveguide bridge, horn and mode generator-control section. Additional subreflector-scattered pattern data will be obtained for a possible vertex plate and offset feed patterns. Offset feed pattern data will allow a more accurate prediction of gain loss caused by structure deformation to be made via JPL developed computer programs.

Fig. 25 shows the exterior and interior of the 1/7-scale Cassegrain feedcone used for the feed evaluations. Fig. 25(b) shows the dual mode horn installed as well as two waveguide switches, and two traveling wave tubes. Ancillary equipment such as waveguide isolators, filters, couplers and mixers are all contained within the upper rotatable cylinder.

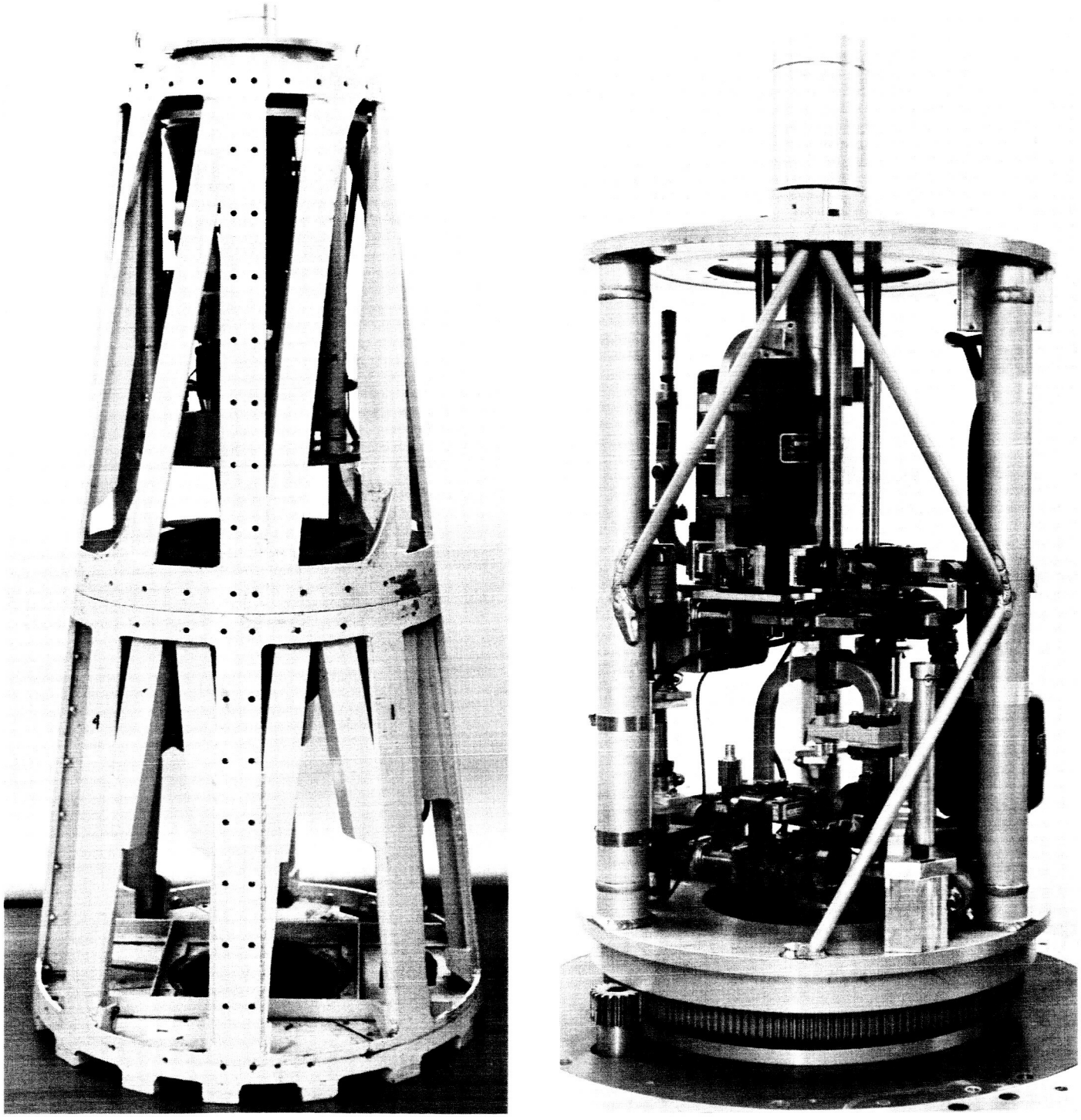


Fig. 25. Exterior and interior views of the 1/7-scale Cassegrain feedcone used for the feed evaluations